CFD MODELLING OF STIRLING ENGINES WITH COMPLEX DESIGN TOPOLOGIES

ATHANASIOS ALEXAKIS

Ph. D.

2013

CFD Modelling of Stirling Engines with Complex Design Topologies

Athanasios Alexakis

A thesis submitted in partial fulfilment of the requirements of the University of Northumbria at Newcastle for the award of Doctor of Philosophy

Research undertaken in the Mechanical and Construction Engineering Department of the Faculty of Engineering and Environment

June 2013

Declaration

I declare that the work contained in this thesis has not been submitted for any other award and it is all my own work. I also confirm that this work fully acknowledges opinions, ideas and contributions from the work of others.

Name: Athanasios Alexakis

Signature:

Date: June 2013

Acknowledgements

First, I would like to express my gratitude to Prof. K. Mahkamov for his invaluable support, guidance and care over the duration of this project and during the whole course of my studies in the UK. Special thanks are due to my beloved parents for their continuous psychological and financial support over the course of my academic journey. Furthermore I would like to thank my brother, Dr V. Soulis for his genuine interest about my research and his loving support throughout its course. Special thanks of course are due to my loving partner in life, Miss Nelly Stavropoulou for her unconditional love, support, care, and patience since the beginning of this work. Moreover, I would like to express my gratitude to the friends and colleagues I had the pleasure to meet in the UK: Mr G. Gkounis, Dr K. Kraitong, Dr S. Pardalis, Dr G. Gkafas, Mr P. Theodoropoulos, Dr C. Lim, Dr G. Airoldi, Mr B. Belgasim, Mr M. Al-Maghalseh, Dr I. Mahkhamova and the staff at AVID Technology Ltd to name but a few. Additionally, I would like to thank my beloved friends in Greece, Greg, Theo, Marina, Thomas and Alex. Also, thanks are due to my friends and colleagues who I met and bonded with during my first degree. Finally, I would like to thank Mr P. Gangwar for his valuable contribution in the development of the user-defined function for the numerical simulation of the Wankel-type rotary machine.

This work has received partial financial support from Hannover Housing Association, the Northumbria University Alumni fund and the KTP personal development budget.

Abstract

This research is in the field of CFD modelling of heat engines, particularly the advanced CFD methodologies for the performance characterization of solar Stirling Engines with complex geometrical topologies. The research aims to investigate whether these methods can provide a more inclusive picture of the engine performance and how this information can be used for the design improvement of Stirling engines and the investigation of more complex engine topologies.

In the first part of the research the performance of a Solar Stirling engine with a cavity-type heater was investigated by means of a second order mathematical model and an optimization procedure was carried out using Genetic Algorithms. In the second part of this study the global 3D CFD modelling was performed for the performance analysis of the solar Stirling engine. The predicted engine performance was in good agreement with previous data and revealed complex flow patterns and heat transfer processes not addressed in previous research. Finally, a Stirling machine topology was modelled which uses a Wankel-type rotary piston arrangement instead of the common reciprocating piston configuration. The complex flow character and associated computational mesh problems were addressed by means of a user-defined function (UDF) embedded in the solver. The simulation results indicate that for the cases when the rotors are shifted by 90 and 180 degrees the machine works as a heat pump / cooling machine. Further study is required to establish a suitable shift angle for the machine to produce power.

Table of Contents

List of Figures

List of Tables

Nomenclature

A = a factor $\left(\tau^2 + 2\tau\kappa\cos\alpha + \kappa^2\right)^{1/2}$

Ar = Working area (m^2)

A_{str} = Piston stroke (m)

B = a factor $\left(\tau + \kappa + 2S\right)$

b = Width of rotor (m)

C = Constants

C_2 = Inertial resistance coefficient

C_p = Heat capacity at constant pressure

C_v = Specific heat at constant volume

Diss = Dissipation

e = Eccentricity (m)

E = Energy (J)

f = Cyclic frequency of engine

F = Total force

Fitnessvalue = Fitness value

g = Gravitational acceleration

G_b = Generation of kinetic energy due to buoyancy

G_k = Generation of turbulent kinetic energy due to mean velocity gradients

h = Sensible Enthalpy (J)

h = Cell height (m)

J = Flux

K = constant

k = Turbulent kinetic energy

k_{eff} = Effective thermal conductivity (W/mK)

k_{ij} = Spring constant

L = Connecting rod length

M = constant mass of the working fluid

M_T = Total mass (kg)

m = Mass in each space (kg)

m = Number of rotor apexes

m = Moment arm

maxvalue = Maximum value of chromosome

M_{t0} = Turbulent viscosity without swirl

N = machine speed (RPM)

N_{keep} = Surviving chromosomes to form next generation

N_{pop} = Number of chromosomes

N_{var} = Number of variables

p = Pressure (Pa)

P = engine output (W)

P_l = Piston location (m)

P_{mass} = P / RT_{e}, power parameter based on the mass of fluid

$p_{\max}$ = maximum cycle-pressure (Pa)

$P_{\max}$ = $P / (p_{\max} V_{\text{T}})$, power parameter based on the maximum pressure and swept volume

p_{mean} = mean cycle-pressure (Pa)

$p_{\min}$ = minimum cycle-pressure (Pa)

Q = heat transferred to the working fluid in the expansion space, the heat lifted;

Q_{mass} = Q / RT_{c}, dimensionless cooling parameter based on the mass of the working fluid;

$Q_{\max}$ = $Q / (p_{\max} V_{\text{T}})$, dimensionless heat lifted based on the maximum cycle pressure;

r = Volume ratio V_{max} / V_{min}

R = characteristic gas constant of the working fluid, 287 J/kgK

R = Generating radius of peritrochoid (m)

r_{ef} = Effective radius (m)

S = Entropy

S = $(2X\tau) / (\tau + 1)$, reduced dead volume;

S_h = Heat from any volumetric sources

S_m = Mass source

T = Temperature (K)

Trq = Total torque (Nm)

t = Time (s)

T_C = temperature of the working fluid in the compression space, generally assumed to be 300K;

T_D = temperature of the working fluid in the dead space (K)

T_E = temperature of the fluid in the expansion space (K)

u = Velocity (m/s)

V = Volume (m^3)

v = y velocity component (m/s)

value = Value of chromosome

V_C = swept volume in the compression space (m^3)

V_D = dead volume (m^3)

V_E = swept volume in the expansion space (m^3)

V_T = $(V_C + V_E) = (1 + \kappa)V_E$, combined swept volume (m^3)

V_W = $\frac{1}{2}V_E(1+\cos\varphi)+\frac{1}{2}V_C[1+\cos(\varphi-a)]+V_D$, volume of total working space (m^3)

V_{Wmax} = maximum volume of total working space (m^3)

W = Work (J)

w = z velocity component (m/s)

X = V_D / V_E, dead volume ratio;

X_{rate} = Mutation rate

Yj = Mass fraction of species j

Y_M = Contribution of fluctuating dilatation in compressible turbulence to overall dissipation rate

Subscripts

C, c = Compression- Cold Space

d = Dead Space

E, e = Expansion Space

eff = Effective

pop = population

r = Regenerator

T = Total

var = Variable

w = Wall

H, h = Hot space

K = Cooler

Greek Characters

α = phase angle [Degrees)

α_c = Layer collapse factor

α_p = Permeability [m^2)

α_s = Layer split factor

α_{sw} = Swirl constant

δ = $(\tau^2 + \kappa^2 + 2\tau\kappa \cos\alpha)^2 / (\tau + \kappa + 2S)$;

ε = Turbulence dissipation rate

z = Scalar property

ζ = Porosity of medium

θ = $tan^{-1} ((\kappa \sin\alpha) / (\kappa + \kappa \cos\alpha)$;

μ = Viscous stress (Pa)

μ_{eff} = Effective viscous stress (Pa)

μ_t = Turbulent viscosity (Pa s)

ρ = Density (kg/m^3)

σ_ε = Turbulent Prandtl number for dissipation rate

σ_κ = Turbulent Prandtl number for turbulence

τ = Temperature ratio T_{min}/ T_{max}

$\bar{\bar{\tau}}$ = Stress tensor (Pa)

φ = crank shaft angle (Degrees)

ω =rotational velocity (rad/s)

Ω = Characteristic swirl number

Acronyms

BC	= Boundary Condition
COP	= Coefficient of Performance
FDM	= Finite Difference Method
FEM	= Finite Element Method
FVM	= Finite Volume Method
GA	= Genetic Algorithm
IC	= Internal Combustion
LTD	= Low Temperature Difference
mCHP	= micro-Combined Heat and power
MTD	= Medium Temperature Difference
ODE	= Ordinary Differential Equations
RANS	= Reynolds Averaged Navier-Stokes
UDF	= User-defined Function
WRSM	= Wankel Rotary Stirling Machine

Chapter 1 Introduction

The energy crisis is a multi-faceted reality which affects the world's population. It is manifested in the decreasing reserves of fossil fuels, the increasing price of energy, the increase of energy demand, but most importantly in the carbon footprint of energy to the environment. To tackle this crisis, there has been a great drive for deploying alternative energy solutions, primarily renewables, like solar, wind, wave and tidal energy.

A Stirling engine is a type of heat engine which can utilize any source of heat input supplied externally. The principle of operation of Stirling engines is based on a closed regenerative thermodynamic cycle in which the process of expansion of the working fluid (usually helium, hydrogen or air) takes place at elevated temperature levels due to heat being supplied through a special heat exchanger – a heater. To minimize the required compression work, the process of compression occurs at lower temperature levels due to heat being rejected from the working fluid in another special heat exchanger, the cooler. To separate the expansion and compression processes in space, the internal gas circuit of the engine is divided into separate expansion and compression spaces (cylinders) which usually have their own pistons, in order to maintain the heater and cooler at constant high and low temperatures, respectively. These pistons provide displacement (flow) and correct distribution of the working fluid between the expansion and compression space. The two pistons are shifted by a phase angle of 90^{o} to ensure that most of the gas is inside the expansion cylinder during the expansion process, and inside the compression cylinder during the compression process, respectively. In order to avoid direct contact between the heater and cooler and corresponding heat losses, a third special heat exchanger is introduced between the heater and the cooler which is called a

regenerator. One of the first Stirling engines designed by R. Stirling in the 19th century is shown in Figure 1.1.

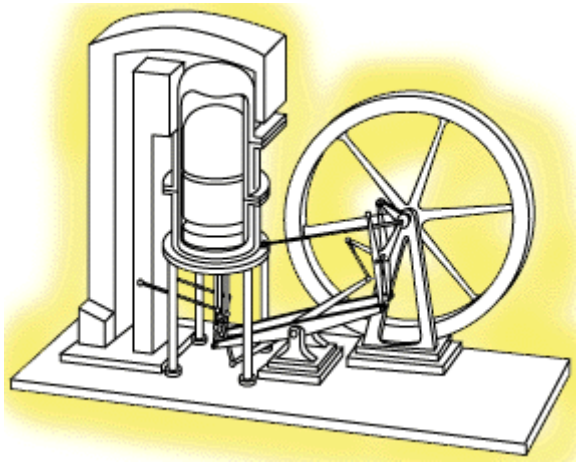

Figure 1.1: Stirling engine design by R. Stirling in the 19th century [1]

The theoretical advantage of the Stirling cycle is that it has the same thermodynamic efficiency with the Carnot cycle for the same temperature and pressure boundaries. The main advantages of practical Stirling engines are primarily their multi-fuel capability, their quiet operation, their high heat recovery efficiency and their reliability. Their multi-fuel capability in particular has led to the deployment of Stirling engines in a range of applications including solar power plants, biomass plants, micro-Combined Heat and Power plants (mCHP), artificial hearts, space power applications and submarine applications.

With regards to solar applications, a number of Dish/ Stirling plants have been developed, in which the hot end of a Stirling engine receives heat in the form of concentrated solar radiation reflected by an array of parabolic mirrors. Such plants have been developed in Europe and the U. S. and have performed favourably in terms of reliability and efficiency.

These possibilities have triggered a rebirth of scientific interest to Stirling-cycle machines. The research and development work carried out during the 1980s had already provided researchers with initial tools and methods to design, analyse and improve the performance of Stirling engines. However, these methods could not provide detailed information about the flow patterns and the complex heat transfer processes taking place inside the engine and thus provided limited capabilities to the designer and restricted designs from reaching a feasible commercial potential. With the recent developments in computing and commercially available Computational Fluid Dynamics (CFD) codes, a Stirling engine designer can comprehend and evaluate the several design possibilities in a fast and convenient way while avoiding building and testing expensive prototypes.

This research work aims to further extend the application of global CFD modelling of Stirling engines by developing a more detailed numerical model which incorporates the solid walls of the engine. Furthermore, CFD is used to model the working process of an alternative mechanical arrangement of a solar Stirling system that uses a Wankel-type rotary piston arrangement instead of the reciprocating piston configuration of conventional Stirling engines. This idea was born during the 1980s and has been patented in several permutations but very little theoretical and experimental research was done. With the vast capabilities of CFD and the amount of documented knowledge on Stirling engines, such ideas and possibilities can now be tested and possibly lead to new ideas and designs which can be implemented in novel and renewable energy solutions.

1.1 Research objectives

The objectives of the investigations presented in this text are:

1. To simulate a solar Stirling engine using a recently developed advanced second-order mathematical model.
2. To further develop the global 3D CFD model of a Stirling engine, originally developed by Prof. Mahkamov. This model takes the thickness of the solid material of the engine into consideration along with the internal gas circuit, effectively representing both the solid and gas domains of the engine, whereas previous models specified thermal boundary conditions across the boundary surfaces of the gas domain.
3. To assess the performance and possible advantages of the developed global 3D CFD model compared against second-order mathematical modelling and 2D axi-symmetric modelling.
4. To develop a CFD model of the system's gas circuit in order to assess the theoretical performance of a rotary Stirling machine employing a Wankel-type configuration.

1.2 Research methodology

The work was carried out in several stages which are outlined below:

1. The performance of the alpha-type solar Stirling engine was analysed by means of a recently developed second-order mathematical model which takes into account thermal, hydraulic and mechanical losses during the engine cycle.
2. The above mathematical model was coupled to a Genetic Algorithm (GA) optimization code and optimal design parameters were obtained within practical design and manufacturing constraints.

3. The global 3D CFD model originally developed by Prof Mahkamov which includes both the solid and the gas domain of the engine was further developed.
4. Numerical results were obtained from the global 3D CFD model and the results were analyzed and compared against results from the second-order mathematical model and works published previously.
5. A solar Stirling design arrangement was developed using Wankel-type rotary piston configuration instead of the conventional reciprocating piston design of the original engine.
6. A simple 2D CFD model was developed for the gas circuit of the rotary solar Stirling engine.
7. The performance of the solar rotary Stirling machine was estimated using results of the above 2D CFD model.

1.3 Contribution to knowledge

The novelty of this research mainly stems from the global 3D CFD model of the solar Stirling engine. To the author's knowledge, most Stirling engine investigations have been carried out by means of second-order mathematical models and the few CFD investigations have mainly focused on the gas circuit of the engine. The global 3D CFD approach which was originally introduced by Prof. Mahkamov and is further developed and presented in this work, offers the ability to analyse complex flow and heat transfer interactions in detail and enables engineers to more accurately determine the engine's performance.

Another aspect of this work which may be considered as an advancement compared to previous research is the CFD modelling of the Wankel-type rotary Stirling machine (WRSM). The concept of Wankel-type Stirling machine topologies is not new. However, the

operational principle of this type of system cannot be proven without CFD modelling which provides information on flow patterns inside the gas circuit. Using such approach it was demonstrated in this study for the first time that the WRSM design cannot produce useful power output when the shift angle between the rotors is 90 and 180^{o}.

1.4 Thesis structure

This section presents the sequence of the investigation stages described previously and provides a brief presentation of the thesis outline. The thesis is split into the following eight chapters.

Chapter 1 Introduction: This chapter briefly highlights the scope of the research, the applied research methodology, and highlights the contribution to knowledge and thesis structure.

Chapter 2 Literature review: In this section previous works related to the development and modelling of Stirling and Wankel engines are critically reviewed. The chapter presents published results on designing, experimental testing and simulations of Stirling and Wankel engines.

Chapter 3 Theory and application of Stirling and Wankel engines: This chapter describes the theory behind the operation of Stirling and Wankel engines, their applications and summarizes the main modelling techniques. The main principles of Genetic Algorithms are discussed here as well.

Chapter 4 General principles of CFD modelling: In this chapter the governing equations of CFD modelling are described including sections referring to more specific CFD techniques used in Stirling engine modelling such as porous media and dynamic mesh modelling.

Chapter 5 Mathematical modelling and design optimization of a solar Stirling engine: This chapter discusses the results obtained by the second-order mathematical model and GA optimization code developed by Kraitong and Mahkamov [2] at Northumbria University at Newcastle. The model provided details of gas flow patterns and pressure and temperature variation throughout the cycle along with the estimation of the theoretical power output of the engine. These results were compared against previous analytical results for the same engine. Moreover, optimal geometric dimensions were obtained for the annular gap of the cavity-type heater and the length of the cooler and the regenerator by means of the GA code coupled to the mathematical model

Chapter 6 Results of the global 3D CFD modelling of the solar Stirling Engine: Here, the results obtained by the global 3D CFD modelling are described and compared against previous results from thermodynamic and CFD modelling of the same engine. The variation of working parameters of the engine throughout the cycle is described and analyzed for each section of the engine including its solid walls. This was possible to carry out by setting data monitoring points inside the gas and solid regions. An estimation of the theoretical power output was also carried out along with a quantification of power losses associated with pressure drop.

Chapter 7 CFD Simulation of the Wankel-type Rotary Solar Stirling Machine: This chapter describes the proposed engine mechanical arrangement for the system. The discussion continues by describing the 2D CFD model of the gas circuit of the system. The 2D CFD model was also enhanced by a user-defined function incorporated into the solver to simulate the operation of gas seals installed on the tips of the triangular-shaped pistons. Preliminary results were presented with information on indicated pressure-volume diagrams in the expansion and compressions spaces of the machine.

Chapter 8 Conclusions and recommendations for future work: In the last chapter the main findings and observations from this work are summarized along with recommendations for further development of engine modelling techniques.

Chapter 2 Literature Review

2.1 Introduction

In this Chapter previous works related to the development and modelling of Stirling and Wankel engines are critically reviewed. The chapter presents published results on designing, experimental testing and simulations of Stirling and Wankel engines.

2.2 Empirical performance evaluation

The simplest method to carry out a performance estimation of Stirling engines is by using empirical correlations obtained from experimental observations. Such correlations have been introduced by Professors Beale (Beale number) and by West (West number) [3]. Prieto and Stefanovsky introduced a parameter called "the characteristic Stirling number" that could be used for analyzing the impact of engine speed on leakage and mechanical power losses in [4]. Kongtrapool and Wongwises investigated the applicability of empirical design parameters like Beale and West formulae on the design of gamma type LTD engines and concluded that the mean pressure power formula derived from the Beale number concept can used as a useful empirical design formulation for any temperature ratio [5].

2.3 Thermodynamic modelling

Three main Stirling engine modelling categories have been described in [6], [1] and [7]. These are namely the first, second and third order models. The methods included in those categories are based on one-dimensional flow models. The order ranking denotes level of the

complexity rather than order of differential equations used to describe the operation of engines.

2.3.1 First order modelling

First order modelling is based on an idealised, loss-free thermodynamic analysis described using algebraic equations [3]. A more advanced method is the one established by Schmidt and presented in [3]. The Schmidt analysis is a more advanced thermodynamic analysis which considers the harmonic variation of volumes. Erbay and Yavuz [8] introduced polytropic processes in their thermodynamic calculations in order to obtain a more realistic regenerator design by considering the maximum power density as the primary design condition. Costea et al. [9] introduced irreversibilities associated with the pressure drop in the regenerator and mechanical friction losses for the moving pistons of a dish Stirling engine. They concluded that the real cycle efficiency is half of that of the ideal cycle. Hsu et al. investigated the heat transfer characteristics of a free piston engine running on incinerator waste heat in [10]. The authors introduced the heat leak parameter which accounted for the conduction loss between hot and cold parts and through the working medium due to its extreme temperatures in either end. Kongtrapool and Wongwises carried out a thermodynamic analysis based on the isothermal assumption which included dead volumes in [11]. Among their conclusions, they reported on the engine power decreasing with increasing dead volume whilst the heat input and engine efficiency decrease with increasing dead volume and decreasing regenerator effectiveness. Martaj et al. [12] presented an isothermal thermodynamic analysis of a LTD gamma-type engine which also considered irreversibilities due to imperfect regeneration and heat transfer in the two heat exchangers. The developed model revealed causes of entropy generation and exergy loss and results obtained were in close agreement with experimental results. Puech and Tishkova applied an isothermal model

including volume variations for the thermodynamic analysis of Stirling engines in [13] and reported that the magnitude of the regenerator dead volume has a negative effect on the engine efficiency only under imperfect regeneration.

2.3.2 Second order modelling

Second order modelling is based on a simplified thermodynamic analysis using a set of ordinary differential equations. Here losses are then deducted to obtain a more realistic performance approximation [7]. This type of modelling is also subdivided in to 4 main categories, the isothermal, adiabatic, semi-adiabatic and quasi-steady analysis [7]. For the second order modelling the engine is divided in to the main working spaces and ordinary differential equations of the mass and energy conservation equations are formulated for each space along with algebraic expressions of losses and the gas state equation. Then, a simple numerical procedure is used to solve the set of equations iteratively [7]. This section presents a brief bibliographical review of the published scientific developments in Stirling engine second order mathematical modelling in chronological order.

The first documented adiabatic second order nodal analysis of Stirling engines was performed by Filkenstein and was described in [14]. The model assumed adiabatic working spaces while the heat exchangers remained isothermal. Urieli and Berchowitz [14] further developed Filkenstein's analysis and presented an adiabatic model with non-ideal heat exchangers. In this model, the heat exchanger walls and the gas contained inside the heat exchangers remain isothermal whereas the gas temperatures inside the working spaces change due to adiabatic expansion and compression. The model was solved by implementation of a fourth order Range-Kutta algorithm. Furthermore, the authors introduced the quasi-steady model in which heat transfer in heat exchangers was calculated using heat transfer correlations and this model

was tested against experimental data from the GPU-3 engine. The disagreement between the two sets of results was attributed to losses unaccounted for by the model and the steady flow correlations used for heat transfer and pressure drop. Schulz and Schwendig [15] developed a similar approach to [14] in which the heat transfer and pressure drop correlations for oscillating flow were derived theoretically. The developed algorithm generated acceptable results in comparison to experimental data. Prieto et al [16] suggested a new design method which combined the quasi-steady state analysis and dynamic similarity using dimensionless parameters obtained in [17]. The proposed method was applied to provide performance indications of GPU-3 engine derivatives. Makhkamov and Ingham analysed the working process and mechanical losses of a 1 kW_e solar alpha-type engine in [18]. The engine was subdivided into five chambers and the analysis was implemented to include heat transfer in all chambers and pressure losses in heat exchangers. The principle assumptions of the analysis were the isothermal walls of each chamber and the ideal regenerator. The temperature of gas in the heat exchangers was obtained by the energy balance equation. The model predicted an indicated power of 3.19 kW and the overall mechanical losses were estimated at 50% of the engine indicated power with most losses attributed to the mechanical friction between the sealing rings and cylinders and the sealing of the crank shaft. Ataer and Karabulut [19] performed a thermodynamic evaluation on a V-type Stirling engine refrigerator based on the ideal adiabatic model where the pressure drop was assumed uniform and the heat transfer coefficients were constant. The novelty of this approach was the subdivision of the engine into 14 sub-domains, 2 for each heat exchanger and 8 for the regenerator. The algorithm was implemented as a FORTRAN program. Andersen et al. performed a numerical study of an improved regenerator design for the SM5 9 kW_e beta-type engine in [20, 21]. For the second order model, the engine was split into multiple sub-domains. It was reported that the predicted temperature oscillations in the regenerator had

particular effects on the power output and the efficiency of the engine. Karabulut et al. [22] further developed the model described in [19]. The improved model was used to simulate a beta-type Stirling engine which was split into 103 sub-volumes for further accuracy. The heat transfer coefficients were again assumed to be constant and the effects of regenerator area and charging fluid mass were investigated. Tlili et al. [23] used the quasi-steady method to analyse the performance of a MTD solar engine. The model was configured to include two sub-domains of the regenerator space and included internal and external heat conduction dissipation and shuttle losses. The model was used for obtaining a set of optimised parameters for a new engine design. Timouni at al. used a very similar approach for the design and performance optimization of the GPU-3 engine in [24]. Abbas et al. reported on the mathematical modelling of a gamma-type solar engine in [25]. The mathematical model was run as a FORTRAN code. The regenerator was split into 3 subdivisions and losses were taken into account. The results demonstrated the importance of proper sealing and high regenerator effectiveness. Granados at al. [26] applied mathematical modelling on the Eurodish solar Stirling plant which also included the concentrator side. This approach presented advancements on the estimation of heat transfer coefficients and friction factors in the form of Reynolds number correlations. The obtained results were not validated but were reported to be within reasonable range. Similar work on the Eurodish plant was carried out by Nepveu et al. in [27]. The heat exchangers of the modelled engine were configured into 8 cells for the heater and 10 for the cooler and the regenerator. The Colburn heat transfer correlation was used for the heater and cooler and a correlation given by Lemrani (cited in [27]) was used for the regenerator. The numerical results were in acceptable agreement to experimental data and revealed losses in the cavity. Gheith et al. applied a quasi-steady model to investigate the performance of a beta-type engine under driving and receiving modes in [28]. Parlak et al. [29] used a quasi-steady analysis to investigate the performance of a

gamma-type engine. The numerical data had not been validated with experimental results. Invernizzi investigated the real gas effects on the performance of Stirling engine in [30]. The mathematical formulation was based on the simple model presented in [14] but also included the compression and expansion efficiency factors to account for viscous effects, along with an expression to make the gas density temperature-dependent. Tekin and Ataer performed second order mathematical modelling for a V-type Stirling engine refrigerator in [31]. In the analysis, different working fluids and regenerator matrix materials were evaluated. Strauss and Dobson developed a quasi-steady model based on the original model presented in [14] and [32]. However, the authors modified the code so that the simulated losses were subtracted from the power output and added to the heat dumped by the cooling system. The model was used to simulate the GPU-3 engine and results were compared to experimental data. The modified code provided more accurate predictions of heat flows to and from the engine, however, under-predicted the power output and efficiency. Cheng and Yu [33] combined the quasi-steady approach presented in [7] with a dynamic model to account for the kinematics of the beta-type engine also described in [7]. The authors investigated a range of operating conditions and found a dependency of the power output on the inertial moment of the flywheel and a tendency of the engine to lose power at higher levels of pressurization in the crank case. In a similar work, Karabulut [34] combined a dynamic and a quasi-steady model and reported on the effect of spring constant and damping coefficient in relation to the geometrical features of the engine. Arias et al. [35] performed second order isothermal, simple adiabatic and quasi-steady analyses to design a low cost V-type engine prototype. The results were then used for a technical feasibility study in order to evaluate the installation potential of such engine in remote areas. Cheng and Yang [36] reported on the successful development of a second order lumped-mass mathematical model with imperfect regeneration to evaluate the performance of an alpha engine prototype with regards to its

operating speed. It was found that at higher speeds the shaft power output decreases due to lower temperature difference between the two working spaces. Kraitong and Mahkamov developed a combined quasi-steady-dynamic model for LTD and MTD Stirling engines in [2]. The model was compiled in MATLAB and offered the possibility of modelling any type of engine providing a variety of heat transfer and friction factor correlations as well. The model was validated against experimental results found in [37] and 3D CFD for gamma-type LTD engines with very close agreement between the experimental and theoretical sets of results. For MTD engines the model over-predicted the power output, however, the results were considered of acceptable agreement with experimental results.

2.3.3 Third order modelling

Third order modelling is a more advanced modelling approach for the performance evaluation of Stirling engines. The concept of volume partitioning still applies but the governing equations are partial differential equations rather than ordinary and require more advanced solution methods.

Examples of such models have been reviewed by Dyson et al. in [38]. Gedeon developed GLIMPS in 1986, a third order tool employing finite difference grids for spatial discretization and solution of the governing equations. In 1994, the successor of GLIMPS was created, SAGE, which included a friendly user interface and an optimization algorithm based on GA. NASA has used the SAGE model for analyzing their engine and validating their CFD models. Another third order model is the H-FAST developed by Huang (cited in [38]). Zhu and Mothubara [39] presented a third order method for the thermodynamic analysis of regenerators. The model was solved by the control volume method and was deemed suitable for the regenerator analysis of all engines of the Stirling family. Choi et al. developed a third

order model for the analysis of regenerator pressure drop in pulse tube cryocoolers in [40]. The model benefited from accurate correlations obtained from experiments. Abdullah et al. applied a third order model for the design and optimization of a gamma-type solar LTD engine in [41]. Andersen presented a one-dimensional model which included the compressibility effects of the gas flow in [42]. The results of the model were in acceptable agreement with experimental results of the SM5 engine, however, it was noted that more accurate heat transfer correlations were required.

2.3.4 Multi-dimensional modelling

Ibrahim et al. [43] performed a numerical analysis employing a 2D CFD code, namely the modified CAST code. The model was tested for the case of a free-piston Stirling engine and was compared against experimental results and numerical results obtained by the commercial CFD package CFD-ACE+. Both CFD tools provided acceptable agreement with experimental results for the gas spring hysteresis loss. For heat transfer predictions the agreement between the experimental and numerical results was limited to particular conditions. Wilson et al. [44] reported on the development of a multi-dimensional CFD code and used results from SAGE 1D software for comparison. The results were obtained at an early stage of the computations and discontinuities in results indicated that the solution was still at an early stage and had not reached periodic steady state. Dyson et al. [38] stressed the importance of multi-dimensional CFD simulations for Stirling engine modelling and commented that proper CFD investigations would assist in obtaining information such as numerical coefficient correlations, better understanding of 2D and 3D turbulence effects and fluid-structure interaction that cannot be obtained by simpler mathematical models or cannot be physically measured at particular regions in an experimental set-up. In a following publication, Dyson et al. [45] performed the first fully converged, axi-symmetric 2D CFD simulation of a free-

piston Stirling engine. The predicted power output and efficiency were in close agreement with two sets of experimental data obtained from 2 engines.

Mahkamov [46] performed an axi-symmetric 2D CFD simulation of a 1 kW_e, V-type solar Stirling engine employing a cavity type heat exchanger. The engine was fitted on a solar concentrator as a part of a dish-Stirling power plant. Numerical results provided a more accurate prediction than [18] for the power output and revealed the non-uniform pressure distribution in the compression space and the inhomogeneous temperature and pressure distribution within any given component at a given time instance. It was reported that for the physical phenomena taking place in the working space of Stirling engines, 2D CFD simulations can provide more reliable performance predictions than thermodynamic models. However, the implications of three-dimensional flow physics were by definition neglected.

A 3D CFD model for the simulation of a biomass, gamma-type Stirling engine was performed by Mahkamov [47]. The numerical model predicted areas for improvement, namely the low porosity of the regenerator which increased hydraulic resistance, the non-uniform flow inside the heater tubes affecting overall heat transfer and the entrapment of the gas in the pipe connecting the two compression chambers by the piston, and the size of the pipe adding to the "dead" volume of the engine. As with regards to the accuracy of the results, the 3D CFD model provided accuracy on the levels of 12% - 18% compared to a mathematical model of 30% accuracy. In a similar context, Mahkamov and Eid [48] performed 3D CFD simulations of the heater of a cross-shaped, V-type Stirling engine employing double expansion and compression spaces to investigate whether the necessary heat could be supplied to the engine by synthetic oil heated up in evacuated tube solar collectors. The numerical results confirmed that such a set-up was indeed functional for the particular engine.

More recent work includes an axi-symmetric 2D CFD simulation of a pulse tube refrigerator by Chen et al. [49]. The obtained numerical results provided more conclusive evidence about the processes that the working gas undergoes in the system. Ashwin et al. [50] performed an axi-symmetric 2D CFD simulation of a pulse tube refrigerator in which the wall thickness was also taken into consideration. This was, to the author's knowledge, the first CFD model to account for the wall thickness of the engine structure and investigate the effects of axial heat conduction in the performance of the pulse-tube refrigerator. Finally, Kraitong and Mahkamov performed 3D simulations of 2 LTD and MTD gamma-type engines in order to validate the optimal engine parameters predicted by a GA code in [2].

2.4 Optimization of Stirling engine design

This section provides a literature survey of the scientific advancements in the field of Stirling engine design optimization.

Blank and Wu [51] applied a finite time thermodynamic approach for the optimization of an extra-terrestrial Stirling engine operating on solar heat supply. The optimum power and the corresponding engine efficiency were calculated for an endo-reversible thermodynamic cycle. Costea and Feidt reported on the effect of the heat transfer coefficient variation on the optimum design of a Stirling engine in [52]. The results were not consistent for all the investigated cases and it was noted that further research was required. Costea et al. [9] reported on the optimization of operating temperature ratio for a solar engine. The approach was based on a simple thermodynamic analysis which included irreversibilities. The optimization was achieved by solving a system of non-linear equations using Langrangian Multipliers. Wu et al. reported on the design optimization of a Stirling engine using a quantum thermodynamics approach in [53]. In a following publication [54], Wu et al.

investigated the optimum performance of an endo-reversible Stirling engine using finite-time thermodynamics for an isothermal Stirling cycle analysis. A sensitivity analysis revealed that the optimum power output of an engine depends on the heat conductance between the engine and the two heat reservoirs, and the regenerator effectiveness. Kaushik and Kumar also applied a finite time thermodynamics approach for the performance evaluation of irreversible Stirling and Ericsson engines in [55]. Their research demonstrated the dependence of maximum power output on the effectiveness of the hot and cold heat exchangers while the regenerator effectiveness has an effect only on the thermal efficiency. The latter observation disagrees with [54]. Senft [56] used the Schmidt analysis for the optimization of a gamma-type Stirling engine aiming at maximum brake power rather than indicated power. He argued that previous optimization work might produce engines that will not function due to high unaccounted mechanical losses. The fact that shaft work decreases with increasing swept volume ratio and the deleterious effect of dead volume were stressed among other results. Feidt et al. [57] investigated the optimum heat transfer design of the heat exchangers in Stirling engines when the heat transfer area was at a minimum. The proposed methodology was successful in determining the optimal operating temperature ratio and heat transfer distribution among the machine components. Rogdakis et al. [58] performed a design optimization analysis on the stable performance of free piston Stirling engines. Their methodology was based in the Schmidt isothermal analysis and a dynamic analysis. Abdullah et al. described a design optimization methodology based on the Schmidt analysis and a third order mathematical model in [41], for a alpha-type solar engine. Among several findings, the analysis showcased that there is an optimum engine speed for a particular temperature difference and that swept volume needs to be high for high indicated power output. Andersen et al. [21] used the numerical results of their developed mathematical model to investigate the regenerator effectiveness with regards to temperature oscillations. Their analysis led to

regenerator with a higher fill factor towards the ends than in the middle section which amplified the positive heat pumping effect of temperature oscillations while it reduced the temperature oscillations effect induced by inflow to the matrix. The optimized regenerator design increased the efficiency of the engine, however, reduced the power output by 3%. Martaj et al. [59] proposed an advanced first order mathematical model including exergy analysis and finite-time thermodynamics for the optimum heat transfer area allocation corresponding to the objective functions of maximum power, efficiency, exergy efficiency and minimum entropy generation. It was concluded that the heat transfer area should be equally distributed between the hot and cold end although an increase in the cold area could be beneficial. Hsieh et al. presented a performance optimization model for a free piston engine supplied with heat by a waste incinerator in [60]. The proposed methodology was based on a simple thermodynamic analysis and an optimization approach using Lagrangian Multipliers. The analysis demonstrated that such a plant could be a feasible technical solution. Timouni et al. performed an optimization study of the performance of the GPU-3 beta-type engine in [61]. The analysis was based on a second order mathematical model and a parametric study. The modelled engine employing the optimized design configurations provided higher efficiency and power output. A similar approach can be also found in Timouni et al. in [61]. de Boer presented a one-dimensional model for the analysis of the regenerator in Stirling engines in [62]. The optimization provided optimal values for the regenerator conductance and phase angle for the maximum power output. Zarizhang and Yarmahmoudi [63] performed a parametric analysis using a second order mathematical model for the design optimization of the heat exchangers in an alpha-type Stirling engine. The optimised data sets were then fed to STRENG, a third order mathematical model, for confirmation. Results demonstrated that 20 kW of power were achievable at optimum engine design. Cheng and Yu [33] performed a parametric study based on a second order

mathematical model for a rhombic drive beta-type Stirling engine. The power output and efficiency were investigated with regard to the displacer gap. It was demonstrated that both power output and efficiency decreased with increasing annular gap. Formoza and Despesse [64] presented an optimization methodology based on the classic Schmidt analysis enhanced to consider various losses. The results were validated using experimental data from the GPU-3 engine. Yaqi et al. [65] used a finite-time thermodynamics approach for the performance optimization of a solar dish/Stirling engine. The results demonstrated that there are optimal values of absorber temperature and contractor ratio after which the efficiency of the plant decreases. Kraitong and Mahkamov performed an optimization of a LTD and a MTD gamma-type Stirling engine using Genetic Algorithms in [2]. The GA was coupled to an advanced second order mathematical model including various loss mechanism and dynamic calculations. The optimization results were confirmed by the mathematical model by means of parametric analysis and, most importantly, by 3D CFD modelling.

2.4.1 Optimization using Genetic Algorithms

The Genetic Algorithm (GA) method optimization is now widely used for Stirling Engine optimization and is a common addition in most commercial Stirling engine modelling software like SAGE mentioned previously. The method has also been applied in other engineering fields, with thermal systems being amongst them. This section presents a bibliographical review of such applications in chronological order.

Homaifair et al. [66] performed an optimization study on turbofan engines using GA. The optimization criteria were the overall efficiency and thrust per unit of mass which were optimized using compressor pressure ratio, fan pressure ratio, Mach number and bypass ratio as optimization parameters. The results demonstrated acceptable agreement with previous

studies. Tayal and Diwekar compared the results of GA against simulated annealing optimization approach with regards to heat exchangers optimization in [67]. The authors reported that both methods were successful in providing an optimal design with less computational effort. Moreover, they commented that GAs have an advantage over other methods in terms of their ability to provide multiple solutions with consistent quality, thus providing more flexibility to the designer. Tofolo and Lazzaretto [68] reported on the successful application of an evolutionary algorithm (EA) for the multi-objective energetic and economic optimization of thermal systems, particularly a cogeneration plant. Mirzaeian at al. [69] performed an optimization study using fuzzy GA for the design of a switched reluctance motor design. The algorithm successfully provided optimum design values for efficiency and torque ripple. Kesgin [70] demonstrated the application of GA for the design optimization of a natural gas engine. The GA was coupled to an existing model for predicting NO_x emissions and engine efficiency; these parameters were set as the objective functions for optimization. Shopova and Bancheva [71] introduced a GA called BASIC which was easily adjustable to a variety of engineering problems. The developed algorithm was tested against a number of previous results obtained by GA or other techniques and the solutions presented acceptable agreement. Cuncas [72] reported on the application of fuzzy GA on the design optimization of induction motors using full load torque and manufacturing cost as objective functions. As in [69], the application of the algorithm was successful in providing a set of design parameters which resulted in lower manufacturing cost and better torque performance compared to an existing motor. Mohageshi and Shayegan [73] performed optimization work using GA for the determination of the optimal design parameters of heat exchangers in a heat recovery steam generator (HRSG) of a combined cycle gas turbine (CCGT). The authors commented that the GA was a suitable approach due to the non-linearity of the system. Ponce-Ortega et al. determined optimized design layouts of shell and tube heat exchangers

using GA in [74]. The GA approach was suitable because of the increased nonlinearity of the Bell-Delaware method used for designing heat exchangers. The objective function was the minimization of the cost of the heat exchangers. A number of designed parameters were used including number of tube passages, tube layout and pitch, and number of strips among others. The authors also reported on the ability of the GA to provide global rather than local optimum solutions. An extensive review regarding the application of GA methods to heat transfer problems can be found in the work of Gosseling et al. [75]. Finally, Kraitong and Mahkamov [2] used GA algorithm for the design optimization of low temperature difference (LTD) and medium temperature difference (MTD) Stirling engines. The GA algorithm was coupled to a developed second order quasi-steady thermodynamic model and was run in MATLAB. The objective functions were the maximization of power output and efficiency. The obtained results were confirmed by 3D CFD simulations.

2.5 Stirling engine design prototypes

This section presents a review of some Stirling engine prototypes and conversions using mathematical modelling and experimental investigations. The reviewed designs are grouped by the engine configuration namely alpha, beta, and gamma.

Batmaz and Ustun [76] described the manufacturing of a V-type engine using double heaters for solar power generation in Turkey. The engine was designed using thermodynamic modelling and was tested. The engine generated less power than designed due to leakages and high dead volume. Le'an et al. [77] applied a V-type design to develop a domestic Stirling engine refrigerator system. The engine was analysed using the Schmidt analysis and was also tested experimentally under different operating conditions and working fluids. Yosof et al. [78] reported on the successful conversion of a diesel engine into a V-type

Stirling engine using a swirl heater. The engine was modelled using the Beale number concept and was also experimentally tested. An alpha type engine employing elbow-bent heater and cooler was presented by El-Ehwany et al. in [79]. It was found that this type of heat exchangers reduced hydraulic losses but added to the dead volume of the engine. Nonetheless, a gain of 13% in power output was achieved.

Cinar et al. designed a beta-type Stirling engine operating on air under atmospheric conditions in [80]. The engine achieved 5.98 W at 208 rpm and 1000 ºC. Karabulut et al. presented the design of a beta-type Stirling engine with a novel driving mechanism by means of a lever along with some theoretical and some initial experimental results in [81]. The engine generated 14.72 W operating on atmospheric air and 260 ºC hot end temperature. Some design improvements leading to higher power generation from the same concept engine were described by Karabulut et al. in [82]. Karabulut et al. [83] performed tests on the same engine running on helium. A power output of 183 W was obtained by experiments. Sripakagorn and Shrikam [84] developed and tested a medium temperature (MTD) beta-type engine. The engine design was based on the analysis described by [14] and the empirical West formula. A power output of 95.4 W at 360 rpm was reported. Brandhorst and Chapman reported on the development of a 5 kW free piston engine for space applications in [85]. The H-FAST analytical tool was used for the design in addition to CFD modelling. Design parameters sets were compared with such obtained by the SAGE tool and close agreement between all design methods was reported.

As with regards to gamma-type engines, Cinar and Karabulut reported on the manufacturing and testing of a 276 cm^3 engine tested using helium and air as the working media in [86]. The results were considered encouraging for the development of the design to a 1 kW engine. Kongtrapool and Wongises [87] built and tested two gamma-type low temperature difference (LTD) Stirling engines with twin power pistons and four power pistons using air as a working

fluid and a gas burner as a heat supply. The two designs were later tested using a solar simulator by the same authors in [37, 88] for the twin and the four pistons respectively. Both surveys agreed on the fact that the engines' performance improved with higher solar intensity. In the field of solar power generation Tavacolpour et al. designed and tested a LTD gamma-type engine without a regenerator in [89] with promising results.

2.6 Investigation of new thermo-mechanical topologies

Stirling engine systems have several advantages such as high heat recovery efficiency and quiet operation. Still, further development is required to achieve higher electrical efficiency. Moreover, there are pressure losses in the Stirling motor because of gas leakage. This has a negative effect on the power produced by the system [90]. Additionally, more compact designs would be preferable with higher power to weight ratios. Besides, there are particular operating features that make practical Stirling engines less efficient than the theoretical Carnot Engine with which they have same theoretical efficiency. The main reasons for that is that expansion and compression processes do not take place wholly in one place because of the continuous harmonic sinusoidal piston motion. This results in a little gas being compressed in the hot (expansion) space and a little gas being expanded in the cold (compression) space [90]. Thus the four processes are not sharply defined and this has a deleterious effect on the overall performance [90]. Additionally, the processes of compression and expansion are not isothermal because the area contacting the fluid is not sufficient for the required heat transfer. Furthermore, in an engine operating at a speed, say, 1000 rpm the processes of compression and expansion would be adiabatic (no heat transfer) rather than isothermal (infinite heat transfer). This poses the need of separate heater and cooler heat exchangers which increase the engine's dead volume and aerodynamic flow

losses. Finally, the working gas is heated again before releasing its heat to the regenerator and cooled again before absorbing heat from regenerator. These two heat transfers have been considered wasteful [90]. A solution was suggested by Rallis et al. [91] who modelled a Stirling engine that would incorporate valves (or ports) through which the air would bypass the cooler after compression and the heater after expansion. This suggestion indeed resulted in an increase in efficiency however, to the author's knowledge, the engine was never built. Another design proposed as a research project to Professor Walker [3] was the modification of a Wankel type engine to operate as an external combustion engine with separate expansion and compression spaces and a regenerative heat exchanger in between. This engine would combine all the advantages of the Wankel engine such as compactness, high efficiency and high power output with the advantages of Stirling engines such as high heat recovery efficiency and multi fuel operation. This engine could be referred to as "*Rotary Stirling Engine*". Another suggestion by Kim et al. [92] was the replacement of the conventional piston compressor and expander with a scroll compressor and expander. These compressor technologies advanced during the 1980s and significant development has been achieved so far, as higher compression and volumetric efficiencies can be achieved and their operation is quieter. An important feature of this topology is that the working gas flows in a loop (one way flow) rather than in a reciprocating pattern as in a conventional Stirling engine, which poses difficulties in the regeneration effect. It has been said [3] that one-way flow Stirling engine topologies would be feasible but they would add complexity to the design.

To prove the operational feasibility of the above topologies only 2- or 3D CFD modelling techniques can be used due to the complex flow patterns involved.

2.6.1 Wankel engines

This section provides a brief bibliographical review on the field of Wankel engines. The main thematic entities are thermodynamic analysis and combustion modelling, kinematics and tribology, novel design applications and CFD studies.

In the field of Wankel engine operation analysis, Sirignano used a one-dimensional model of the spark ignition Wankel engine based on the turbulent diffusivity of heat and mass transfer in [93]. The model aimed to predict the motion of the finite thickness flame and also included heat conduction loss calculations along with the calculation of instantaneous pressure, temperature and density of the working gas. The authors claimed that the model generated reasonable results, however, those should be considered with caution if the model were to be used for the evaluation of new designs. Bracco [94] described a one dimensional model of the combustion inside a stratified two-phase Wankel engine. The model incorporated advanced techniques for the droplet formation and motion in the working chambers. The author concluded that the model had the potential to be a valuable tool in controlling the combustion process during the design stage. Shih and Schock performed a two-dimensional numerical simulation of the flow-field in a motored Wankel engine in [95]. The aim of the model was to investigate the effect of engine operation parameters such as the speed of the engine and speed of injection on the airflow and fuel-air mixing. The authors reported that the engine speed and speed of injection had a strong influence on the flow-field. Kawabara at al. [96] performed cycle-resolved measurements of the fuel concentration near a spark plug of a commercial Wankel engine by means of a laser infrared absorption method. The method was reported successful in identifying strong mixture inhomogenities during the early stage of the compression stroke. Moreover, it was stated that there was a faster concentration of fuel near the spark plug at richer mixtures.

In the field of kinematics and tribology, Pennock and Beard carried out an analysis of the forces acting on the apex seals of a Wankel rotary compressor and the effect of different engine speeds in [97]. The authors reported that the friction forces between the side of the seal and the rotor had a negligible effect and that there was considerable influence of the engine speed on the forces acting on the apex seals. Levi and Eliaz [98] performed a failure analysis using analytical ferrography on oil samples to determine the failure cause of Wankel engines. The method was tested on six engines and consistently identified the bearing needles as the cause of contact failure. Zhang and Wang investigated the effects of leakage and friction on the miniaturization of a Wankel compressor micro-cooler for electronics cooling applications in [99]. The main source of leakage was identified to be the gap between the apex seals and the rotor seal-slots.

In the field of engine design concepts incorporating Wankel-type mechanisms, Badr et al. reported on the design consideration of rotary steam expanders in [100]. The authors made specific recommendations on the selection of potential materials and means of lubrication and effective porting of the engine. Brown and Green conducted experimental investigations on a hydrogen fuelled Wankel IC engine in [101]. The tests indicated that the engine could operate under higher brake thermal efficiency at part load conditions with the benefit of negligible nitrogen oxide emissions. It was reported that the system was being further developed to a direct-injection system. Heppner et al. [102] documented the design of micro-cooler based on a Wankel rotary engine by means of lumped capacitance model. The results indicated that a COP at the level of about 4.6 was achievable and that there was potential for increased performance of the proposed design compared to thermal electric coolers. Ting et al. performed experimental studies on a miniature vapour compression refrigerator device in [103]. The experimental results indicated that the described equipment could provide 300 W of cooling at COP higher than 2.

In the field of CFD modelling of Wankel engines, Ma et al. [104] performed a two-dimensional CFD simulation in order to investigate the effect of different designs of the rotor flank contour on the flow-field. The authors were able to identify flow recirculation regions inside the engine chambers which could enhance fuel-air mixing. Chou performed 3D CFD calculations on a rotary Stirling system incorporating Wankel-type pistons in [105]. The author modelled two main layouts of the system which mainly consisted of two rotors shifted by 90º and 180º in each case, respectively. The heat exchangers were modelled by means of two connecting pipes on either side of the rotors. A constant temperature boundary condition was specified along the pipe length near the hot and the cold ends which simulated the heater and the cooler. The fluid volume of the pipe at mid-length was specified as a porous zone simulating the regenerator matrix. The computational results demonstrated that there was not sufficient pressure swing in the cycle to produce a sensible amount of indicated power.

2.7 Conclusions

From the conducted literature review it can be concluded that there has been little work carried out in the field of CFD modelling of Stirling engines, whereas there has been a considerable work on 1st and 2nd order thermodynamic modelling. The CFD approaches listed previously have focused only on the internal gas circuit of the engine with most applications using 2D and fewer using 3D CFD modelling. This shows that there is room for further development of the CFD techniques applied to Stirling engine modelling. The improvement deployed in this work is the implementation of a 3D CFD model which fully represents the engine geometry by taking the solid domain of the engine walls also into consideration, and captures the complex heat transfer processes and flow patterns which take place inside the engine.

Additionally, the conducted literature survey reveals that most design procedures in Stirling engine prototypes have relied on thermodynamic modelling and parametric analyses. Particularly with regards to the Wankel-type Stirling system, there is no sufficient information in published literature about whether this mechanical arrangement is functional or not. For this reason, 2D CFD modelling of a system employing Wankel-type pistons and full sets of heat exchangers is applied in this work as the only technique capable to assess the functionality of this system.

Chapter 3 Theory and Application of Stirling and Wankel Engines

3.1 Introduction

"Stirling engines" is a general nomenclature for a large family of engines which operate under a closed regenerative cycle, with cyclic compression and expansion of the working fluid at different temperature levels [3]. These engines vary in characteristics and include machines operating as prime movers, heat pumps and refrigerators. The main predecessor of those engines is the "air" or hot air engine" conceived by a Scottish cleric, Minister Rev. R. Stirling, in the nineteenth century. These engines demonstrated great potential as they could achieve a theoretical thermal efficiency equal to the maximum attainable efficiency of the Carnot cycle. However, their development was abandoned for nearly half a century with the widespread use of Otto and Diesel engines. Interest was again drawn on to Stirling engines during the oil crisis of the 1970s as those engines can utilise any source of heat and their deployment could be a means of limiting dependency on fossil fuels. Since then, many developments have been achieved and now Stirling engines can be used in numerous applications such as small-scale heat and power cogeneration, space applications, artificial hearts and solar electricity generation. The purpose of this chapter is to introduce the fundamental operational principles, describe the main mechanical arrangements and variations, list the potential applications and conduct an in-depth analysis of the fundamental thermodynamic principles and design considerations of Stirling engines.

3.2 Principles of operation

As mentioned in the introduction, Stirling engines operate under a closed regenerative cycle in which the flow is governed by volume changes and heat input to the cycle is supplied externally. In a simplified manner, heat is introduced to a cylinder containing a piston and the hot gases force the piston to move downwards thus creating a power stroke. The accumulated kinetic energy on the crack shaft then forces the piston to move upwards and compress the medium. This requires the cylinder to be cooled during compression. This simplified version of the engine is demonstrated in Figures 3.1, 3.2.

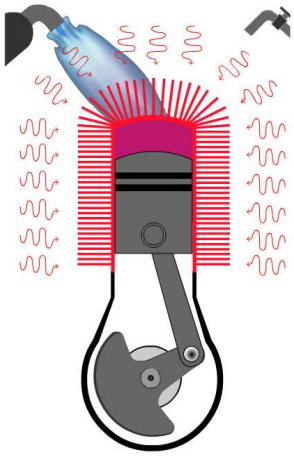

Figure 3.1: A primitive Stirling engine. Power stroke: Heat is being introduced through the walls while the piston is moving downwards [1]

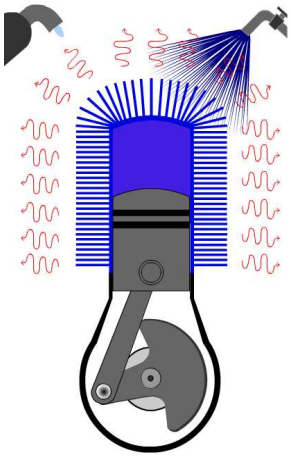

Figure 3.2: A primitive Stirling engine. Power Stroke: Heat is being rejected through the walls via water spray while piston is moving upwards [1]

A more practical alternative is to have two separate cylinders, one in which heat is supplied to (hot space) and one in which heat is removed from (cold space) as shown in Figure 3.3. The hot cylinder is kept at high temperature and the cold cylinder is kept at low temperature. The two pistons are arranged to reciprocate with a phase difference of 90^{o} - 120^{o}. The purpose of this arrangement is to contain the whole mass of the fluid in the hot space during heat input

and in the cold space during heat rejection. A further improvement to this version of the engine is to introduce two separate heat exchangers, a heater to supply heat to the hot space and a cooler to provide cooling of the cold space. This arrangement, shown in Figure 3.4, is necessary as the surface of the cylinders is not adequate to facilitate sufficient heat transfer to and from the cylinders. Furthermore, by incorporating heat exchangers, there is less exertion of alternating thermal loads on the walls of the cylinders.

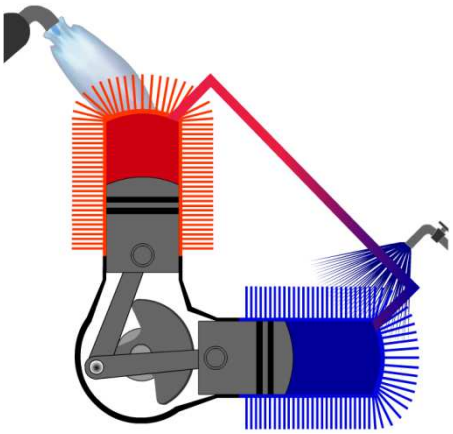

Figure 3.3: A Stirling engine with separate "hot" and "cold" cylinders [1]

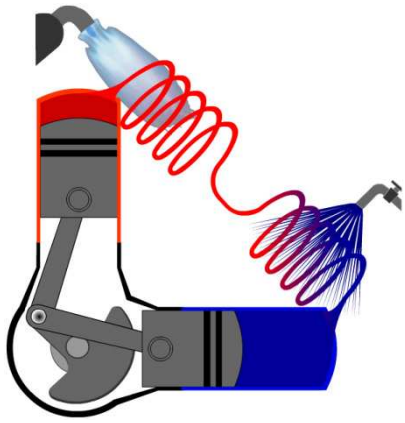

Figure 3.4: A Stirling engine with separate "hot" and "cold" cylinders and a heater and a cooler [1]

It is required that those heat exchangers have a surface-to-volume ratio as high as possible. The additional volume of the heat exchangers decreases the compression ratio (the ratio of minimum to maximum volume) and poses a negative effect on the performance of the engine. Thus the heat exchangers must be carefully designed so that the compression ratio of the engine is kept as high as possible.

In the arrangement presented in Figures 3.3, 3.4, the heater and the cooler are in direct contact which results in high heat losses from the hot to the cold zone and, ultimately, in a low thermal efficiency. In order to alleviate this, a special heat exchanger, a regenerator, is

introduced between the heater and the cooler as shown in Figure 3.5. The regenerator is essentially a porous medium enclosed in a metallic casing. This porous medium, essentially a wire mesh, is made from a material with, ideally, infinite thermal conductivity in the radial direction and zero thermal conductivity in the axial direction. The regenerator acts as a "heat-sponge" in which heat is stored as the gas flows from the hot zone to the cold zone and this heat is then retrieved by the cooled gas as it flows back to opposite direction. As a general practice, the metallic casing is thermo-insulated to avoid heat losses from the porous medium to its casing and to the surroundings.

Figure 3.6 presents examples of volume and pressure variations in the hot and the cold zone of the engine, and a cyclic pressure-volume (P-V) diagram – the indicator diagram. The 2 areas of the indicator diagram represent the work in the hot and the cold zone. Their difference provides the net indicated work of the engine. The product of the indicated cyclic work and the frequency of the engine is called the indicated power of the engine.

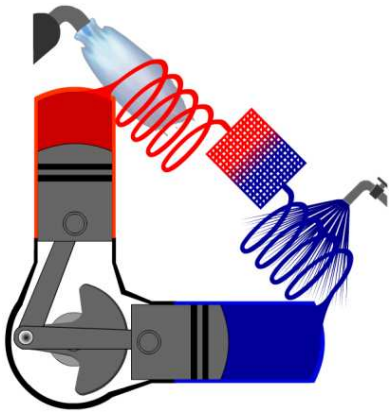

Figure 3.5: A Stirling engine with separate "hot" and "cold" cylinders, a heater, a cooler and a regenerator [1]

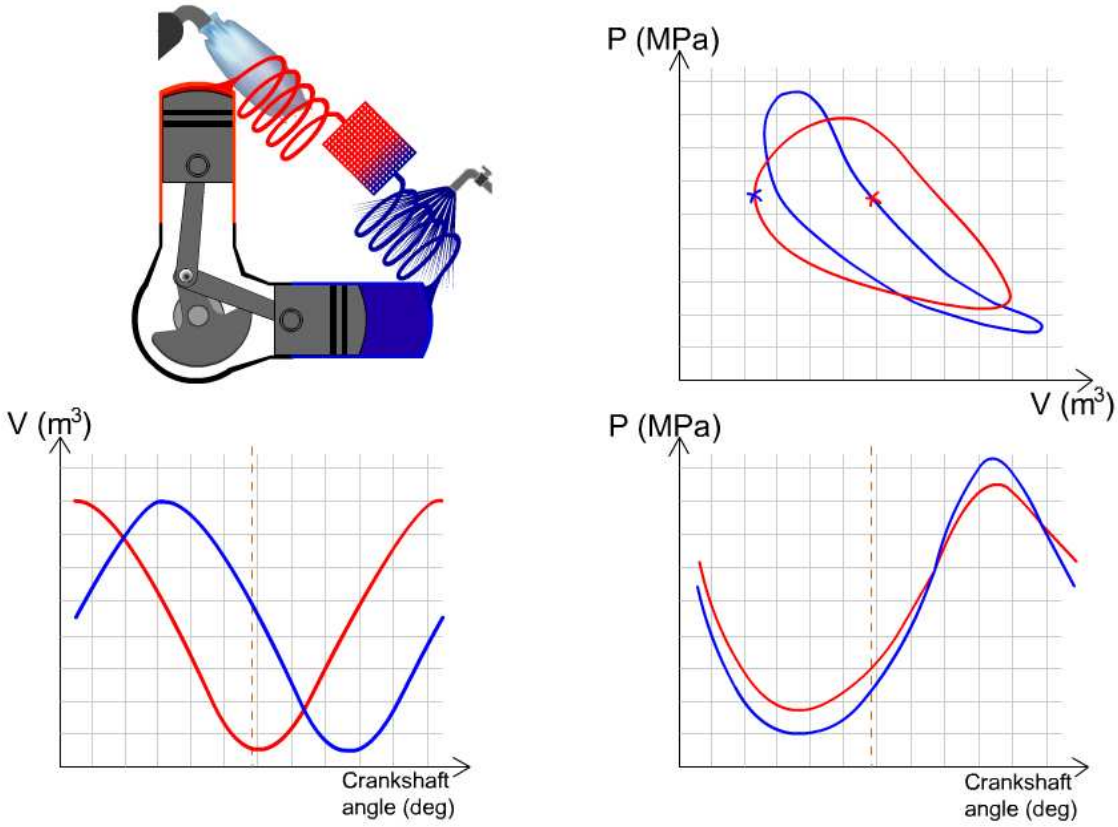

Figure 3.6: Example of volume and pressure variation in the hot and cold zone of the engine and an indicator diagram [1]

3.3 Mechanical arrangements

Stirling engines can be divided in two main categories: (a) single acting or (b) double acting engines. Single acting engines consist of expansion space, compression space and the associated heat exchangers in one or two cylinders, with two reciprocating elements of which one must be a piston [3] as shown in Figure 3.7. Double acting machines are groupings of multiple cylinders arranged such that the expansion space of one cylinder is connected to the compression space of the next cylinder through the associated heat exchangers as shown in Figure 3.8. There is one reciprocating element per cylinder, a piston-displacer [3]. The main advantage of the double acting engine is that the number of reciprocating components is half of what would be required for multiple arrangements of single-acting machines [3]. This can

lead to reduced cost due to the simplified kinematic drive [3]. The main disadvantage is the limited flexibility in design and, to a lesser extent, operating conditions. The main design consideration is the placement of the heat exchangers. In order to maintain adequate sizes for heat exchanger channels, the cylinders need to be connected in a circular or square configuration as shown in Figures 3.9, 3.10.

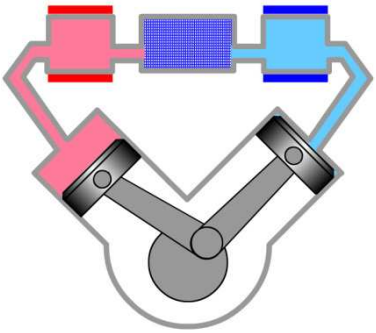

Figure 3.7: A V-type, single-acting alpha-configuration Stirling engine [1]

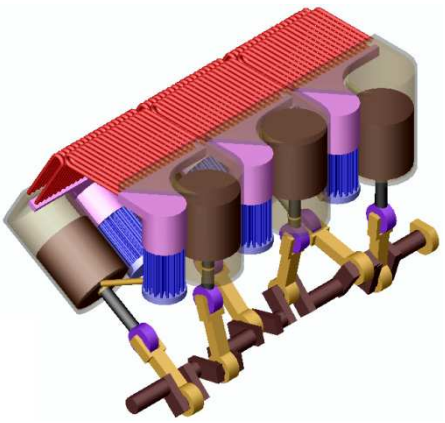

Figure 3.8: A double-acting Stirling engine [1]

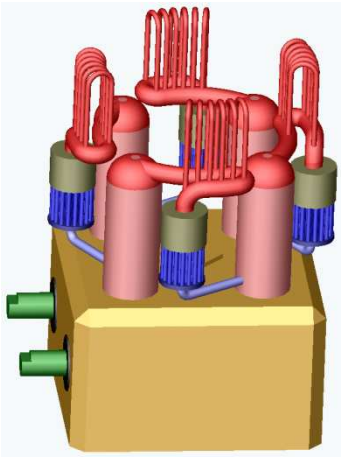

Figure 3.9: A double-acting Stirling engine with "square" location of cylinders [1]

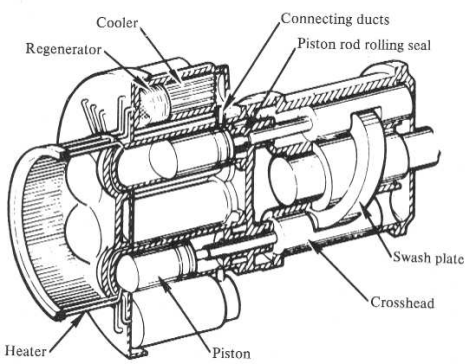

Figure 3.10: A double-acting Stirling engine with "circular" location of cylinders [1]

The previous examples of single and double acting machines were of the alpha type. The beta and gamma types can be considered as arrangements of single acting machines. Figure 3.11 presents an example of a beta type machine. The top piston is called the displacer and its function is to control flow to and from the two spaces; all work is generated from the lower piston- the power piston. The principal difference between a piston and a displacer is that there are large pressure differences between the lower and upper surface of the piston and thus sealing rings are required. A displacer, however, experiences the same pressure on its upper and lower surfaces, apart from aerodynamic losses. When it reciprocates, it does no work on the gas but only displaces it from one side of the displacer to another [3]. Another important feature of Figure 3.11 is the kinematic drive often used in this engine configuration, the rhombic drive. This mechanism provides better dynamic balance and reduces the side-forces exerted on the pistons. This leads to reduced wear on the piston rings and the seals. Furthermore, effective balancing provides less vibrations and, thus, smoother operation [1]. Finally, Figure 3.12 demonstrates an example of a so called gamma-type engine. In this configuration, the piston and the displacer are contained in separate cylinders and the compression space is split in two parts. The first part is located in the hot space and under the displacer and the second part is in the cold space and above the power piston. The two spaces are linked with channels in the casing of the cylinders or by pipes [1].

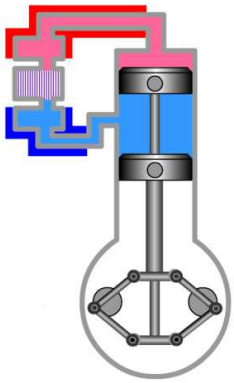

Figure 3.11: A beta-type Stirling engine [1]

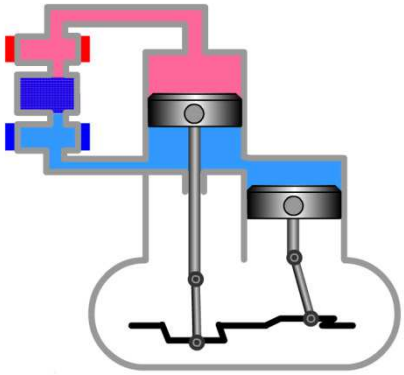

Figure 3.12: A gamma-type Stirling engine [1]

Those piston-displacer machines provide an important advantage in terms of sealing compared to multiple pistons arrangements. By rule of thumb, one fluid seal is required on each piston. In the case of displacers, an additional fluid seal is required on the displacer rod as it passes through the piston in beta type engines, and through the underside of the displacer cylinder in gamma type engines. However, the seal around the displacer rod is much smaller than the seal around the piston, with less leakage and friction. This is the main advantage of this type of engines since dynamic sealing is a challenging task, particularly when media other than air are used [3].

Although piston-displacer engines share this sealing advantage compared to the multiple pistons engines, there are also different advantages in each of the beta and the gamma types of engines. In the gamma-type engines, the compression space is divided into two parts thus requiring a connection between them. This connection adds to the dead volume of the engine and this has a negative effect on power output. The second advantage of the beta-type machines is that, in each revolution, the displacer and the piston both sweep the same part of the cylinder, although at different times. This is considered a very efficient utilization of engine-cylinder volume. Respectively, the advantages of the gamma-type machines are: the production engineering flexibility provided by the two cylinders; the separation of the displacer rod-seal to a fixed location in the displacer cylinder rather than the limited environment of the piston crown [3].

Another major category of Stirling engines are the free-piston Stirling engines. These are also piston-displacer machines but they do not include a kinematic drive. Figure 3.13 presents a schematic illustration of a free-piston machine. This engine is essentially a thermal self-oscillating system. The reciprocating motion of pistons are forced oscillations induced by the varying pressure of the working fluid in the working spaces, and forces from mechanical or

gas springs. The power piston is the reciprocating analogous of the "rotor" of the linear alternator and reciprocates relative to the stator. This motion generates electricity.

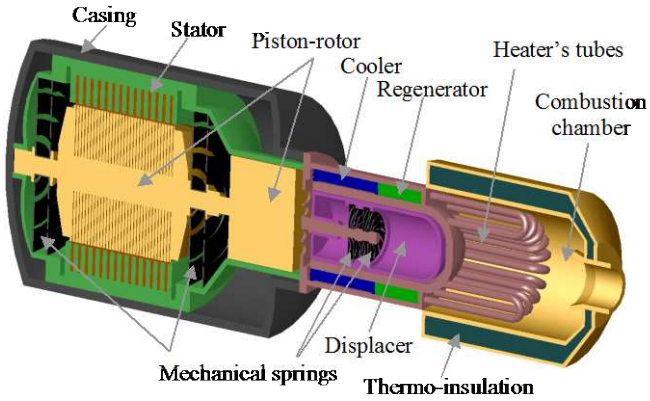

Figure 3.13: A general scheme of a free-piston Stirling Engine [1]

3.4 Applications

During the years from 1940 to 1980 there was significant development of Stirling engines in a broad area of applications including artificial hearts, small-scale power generation, automotive and space applications. At present, activities focus on space applications, heat and power generation using solar and biomass sources and conventional fuels, and back-up propulsion systems for submarines.

3.4.1 Space applications

These activities are mainly focused on the development of a radio isotope system that will replace thermo-electric generators and provide on-board electricity to the spacecraft in deep space missions by NASA. This project is carried out in the NASA Glenn Research Centre in conjunction with the US DOE. The machine under investigation is a 55-W_e free-piston

Stirling engine developed by Stirling Technology Company, Kennewick, WA (Figure 3.14). Two such engines are arranged in the dynamically-balanced opposite configuration as shown in Figure 3.15. Studies have shown a higher efficiency of the Stirling engine plant compared to the thermo-electric generators and, with radio isotope as a heat source, significant savings are achievable [1]. Similar research has been carried out in the National Space Laboratory in Japan with solar radiation used as the hot temperature heat source.

Figure 3.14: A Stirling Technology Corp., Kennewick, WA 55W_e free-piston Stirling engine for a space application [1]

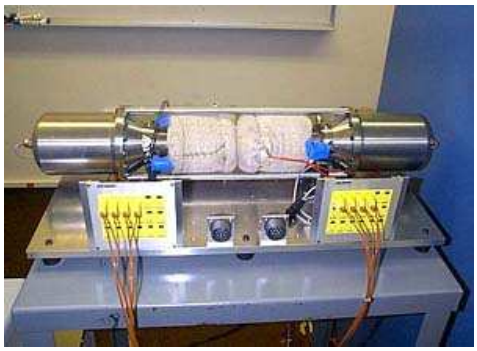

Figure 3.15: A dynamically-balanced opposite arrangement of two 55W_e free-piston Stirling engines for a space application [1]

3.4.2 Solar applications

One of the main advantages of Stirling engines is that heat can be supplied externally to the engine and, therefore, any source of heat can be utilized. This makes Stirling engines suitable for solar, biomass, and waste heat power plants.

Solar power plants employing a Stirling engine have been under development in several parts of the world. Such a concept is presented schematically in Figure 3.16. This installation

consists of a parabolic mirror concentrating dish and a Stirling engine with its hot end placed at the focal point of the concentrator. Such units usually employ a 2-coordinate tracking mechanism which allows the unit to follow the motion of the sun during daylight. Figure 3.17 demonstrates a photograph of such a plant developed by Science Applications International Corporation and STM Power Inc. This plant is based on a STM 4-120 double-acting Stirling engine with swash-plate drive mechanism. The rated power of this installation is equal to 22 kW_e, with peak and annual efficiencies equal to 20% and 14.5%, respectively. The engine consists of four cylinders with a displacement 220 cm^3 per cylinder. The operational speed is 2200 rpm and working gas is hydrogen. The engine is coupled to a three-phase 480 V induction generator. The total area of the concentrators is 113.5 m^2. A total of five such units have been built and tested. The current mean time between failures is 40 hours. Incidents include tracking system instability and hydrogen leakage among others [1].

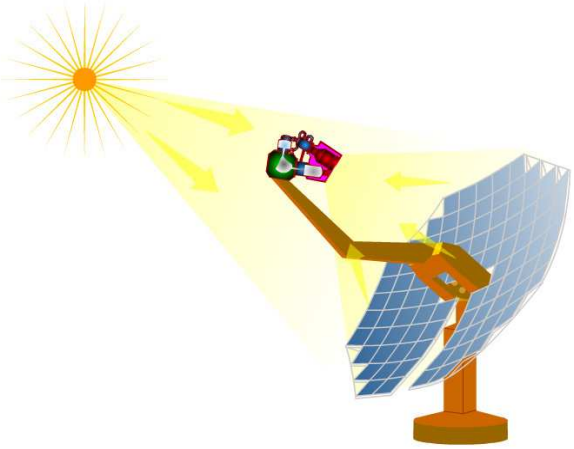

Figure 3.16: Schematic representation of a solar dish/Stirling engine power plant [1]

Another plant of this type is shown in the photograph in Figure 3.18. This plant was developed within the EURODISH project by Schlaich-Bergermann und Partner and was funded by the European Community, German/Spanish industries and DLR (Germany) and SIEMAT (Spain). Several units were installed and tested at Platforma Solar de Almeria,

Spain. The plants are based on the SOLO-161 Stirling engine developed by SOLO Kleinmotoren GmbH based in Germany. The total aperture of the receiver is 57 m^2 and the engine is of the alpha type with the cylinders arranged in a "V" configuration. The total swept volume of the engine is 160 cm^3 and the working gas is helium. The engine generates 10 kW_e of power at 1500 rpm. Such a plant was tested at Albuquerque, New Mexico, and demonstrated 15.7% annual efficiency [1].

Figure 3.17: A Science Applications International Corp and STM Power Inc. dish/Stirling engine installation [1]

Figure 3.18: A Schlaich-Bergermann und Partner GmbH and SOLO Kleinmotoren GmbH dish/Stirling engine installation at Platforma Solar de Almeria in Spain [1]

3.4.3 Biomass applications

Similar to solar radiation, another external heat supply to Stirling engines is heat generated by combustion of bio-fuels. The heat generation of such units typically ranges from 1 kW to 200 kW. This concept is presented schematically in Figure 3.19. Figure 3.19a demonstrates a bio-fuelled Stirling engine unit powered by bio-gas produced on a sewage reactor. The hot exhaust gases from the combustion chamber of the engine flow through the heat exchanger of the bio-reactor and enhance the production of the bio-gas by increasing the temperature. Figure 3.19b presents a Stirling engine unit coupled to a Dutch oven-type burner. These systems can use biomass residuals like chips, pellets and logs but can also operate with crops, straw, and other agricultural residuals. These types of plants can use commercially available burners for different types of solid bio-fuels [1]. The wood residuals or crops can be treated in special reactors to produce bio-gas to fuel the Stirling engine. This concept is presented in Figure 3.19c.

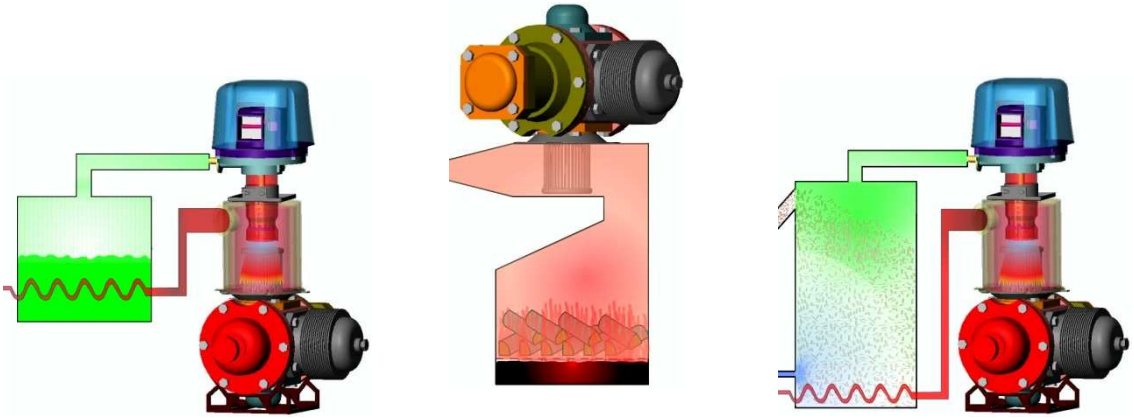

A B c

Figure 3.19:A concept of small and micro energy units on the basis of Stirling engines powered by bio-fuels [1]

Figures 3.20, 3.21 demonstrate examples of developed Stirling engine micro-combined heat and power (mCHP) bio-fuelled units. Figure 3.20 shows a SOLO-161 Stirling engine modified to operate on biomass fuel. This unit generates about 10 kW of electrical power. Figure 3.21 shows a 35 kW_e engine developed in Denmark Technological University. This engine is a four-cylinder double acting machine coupled to a built-in generator. This engine was modified to operate using wood chips and bio-gas produced from wood chips.

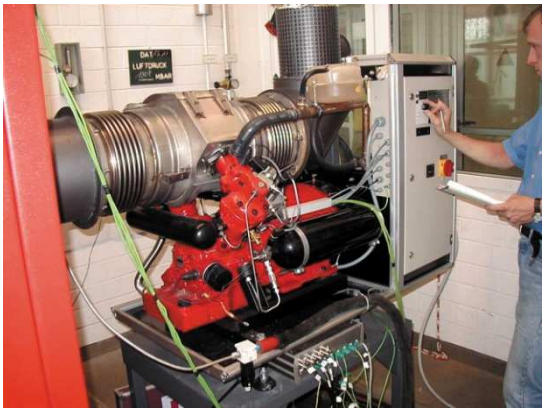

Figure 3.20: A 10-kW_e Stirling engine power unit fuelled by biomass [1]

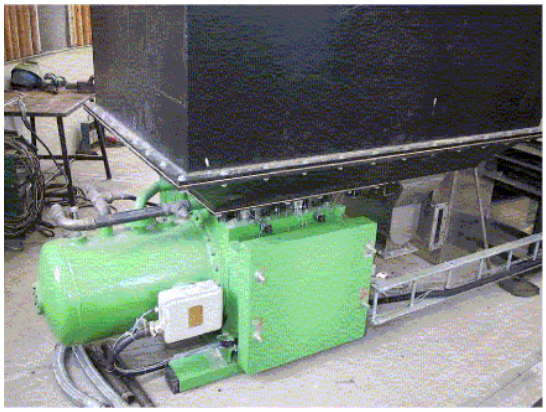

Figure 3.21: A 35-kW_e Stirling engine power unit fuelled by biomass [1]

Similar work in this field, using their own developed Stirling engines, is being performed at Joanneum Research in Austria, Sunpower Inc (the USA) and other companies in the world.

3.4.4 Commercial and domestic micro- Combined Heat and Power (mCHP) applications

Combined Heat and Power (CHP) or cogeneration refers to the conversion of the energy content of a single fuel in to two different forms of energy simultaneously, namely thermal energy and electricity. Stirling engine based CHP plants seem rather attractive for Micro-scale CHP (mCHP) in commercial and domestic buildings. The commercial target of such units is to replace the widely used gas-boilers, conventional, condensing or combination. The theoretical advantage of such installations is the increased fuel energy utilization which ultimately results in economic and environmental benefits compared to a conventional energetic scenario based on grid electricity and gas boilers. The operation principle of such plants is that hot gases from fuel combustion supply the heat to the engine which subsequently drives the coupled built-in generator, and the heat released by the cooling

process of the engine is dumped to the radiator circuit. Figure 3.22 shows a schematic illustration of the concept of domestic mCHP.

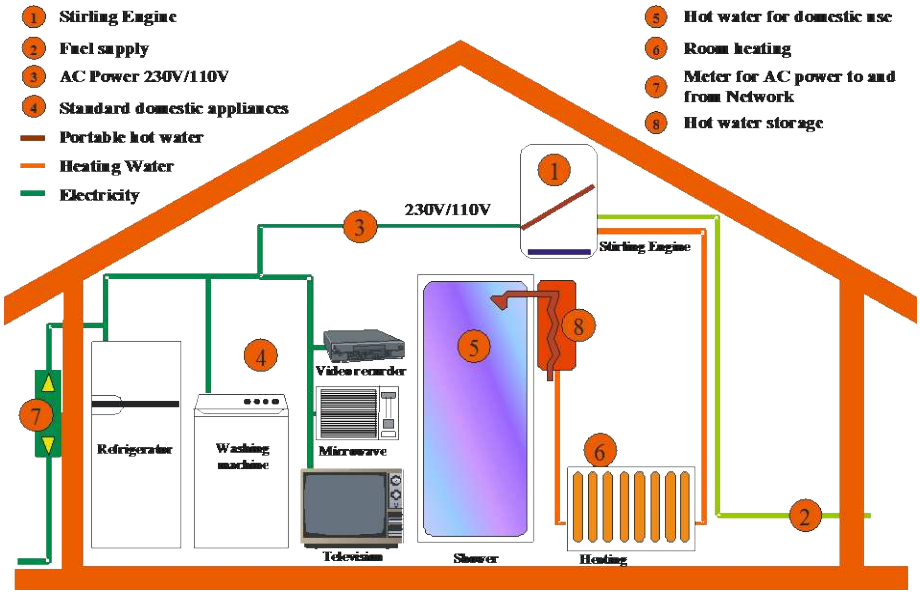

Figure 3.22: Concept of a Micro-CHP installation on the basis of a Stirling engine [1]

At present, there are two companies manufacturing Stirling engines mCHP units for commercial buildings: STM Power Inc., USA, and SOLO Kleinmotoren GmbH, Germany. STM Power Inc. have developed 25 kW_e commercial CHP units based on the STM Stirling engines. The electrical efficiency of those engines is about 30% with an aim to be further increased to 40% [1]. SOLO Kleinmotoren GmbH have developed a 10 kW_e CHP unit based on the SOLO V-161 engine [1]. This engine is shown in Figure 3.23.

Figure 3.23: A 10kW$_e$ net electric CHP unit based on the alpha V-type SOLO V-161 Stirling engine [1]

The leading manufacturers of Stirling engine-based domestic mCHP are Whisper Tech Ltd, New Zealand, and Sunpower INC, USA.

The AC WhisperGen unit developed by Whisper Tech Ltd (Figures 3.24, 3.25) was designed to supply both heat and power up to 1.2 kWe at 220 V-240 V, replacing the gas boiler and reducing carbon-intensive electricity supply from the grid. The unit was based on a four-cylinder double acting machine with a wobble-yoke kinematic mechanism (Figure 3.26). Heat to the engine was supplied by a single-point burner which sits on the top of the engine. This burner was specifically designed for the particular engine and provided multi-fuel capabilities. The Mk III version of the WhisperGen mCHP unit was capable of generating heat and power with a combined fuel utilization efficiency of 90% to 95% and financial and environmental benefits of 9.3% and 9% respectively, for a semi detached house located in the south of England [106]. The newer version of the WhisperGen, the Mk Vb, employed a secondary burner adding another 5 kW to the unit's heat generation capacity. This was an attempt to make the unit suitable for larger houses with higher heat demand. However, this practice does not lie within the concepts of cogeneration and does not generate environmental or economic savings. Moreover, experimental tests [107] showed low responsiveness of the

auxiliary burner which was attributed to its electronic controls and how those were programmed. As with regards to the performance of the unit, its combined fuel utilization efficiency was found lower than its predecessor, at about 80% to 85%. This was due to the lower heat recovery efficiency attributed to the lower pressurization of the Stirling engine. Studies including experimental tests and advanced modelling [107] indicated that the financial benefits achieved by the WhisperGen Mk Vb were mainly attributed to the recently introduced UK feed-in tariff and that environmental benefits were marginal.

Sunpower Inc. has developed a 1.1 kW_e free-piston Stirling engine-based mCHP unit with a linear alternator as the loading device, the EG-1000. The electrical efficiency of the engine is estimated at about 29%. The engine has a mass of 35 kg, a diameter of 230 mm, and a length of 440 mm. Finally, Figure 3.27 shows an "on-wall" free piston Stirling engine based mCHP plant by Microgen, based on the Sunpower 1 kW free-piston engine.

Figure 3.24: WhisperGen MK IV Micro CHP unit [1]

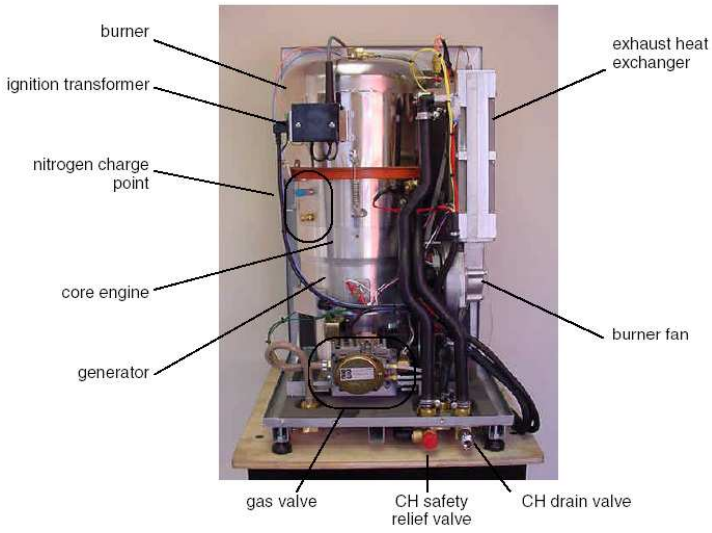

Figure 3.25: WhisperGen Micro CHP unit – casing is removed [1]

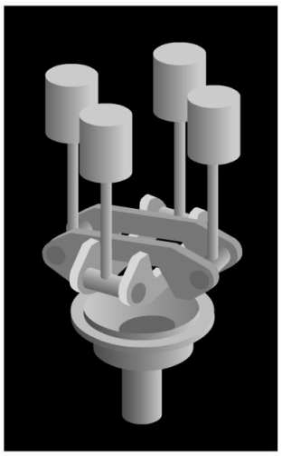

Figure 3.26: Schematic representation of the wobble-yoke mechanism [1]

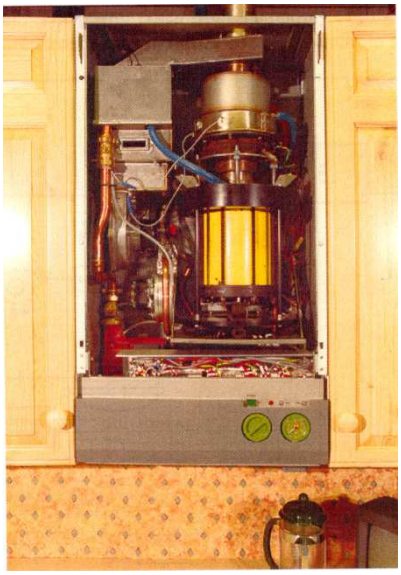

Figure 3.27: A Micro-CHP system on the basis of a SUNPOWER 1-kW free-piston Stirling engine [1]

3.5 Thermodynamic analysis

3.5.1 Ideal Stirling cycle

The ideal Stirling cycle with perfect regeneration and isothermal compression and expansion consists of four processes as shown in Figure 3.28:

Process 1-2: Isothermal compression;

Process 2-3: Isochoric heat addition from regenerator;

Process 3-4: Isothermal expansion;

Process 4-1: Isochoric heat release to regenerator.

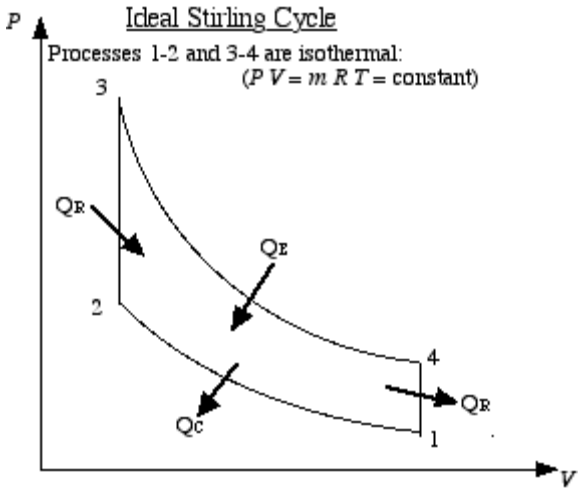

Figure 3.28: Ideal Stirling cycle thermodynamic diagram [90]

With reference to Figure 3.28 and the description of the four processes given above, the equations can be summarized as follows [3]:

Temperature ratio $\tau = T_{\min} / T_{\max}$

Volume ratio $r = V_{\max} / V_{\min}$

For a unit mass of working fluid assuming to be an ideal gas and from the characteristic gas equation

$$V_1 = \frac{RT_1}{p_1}, \tag{3.1}$$

where p denotes absolute pressure, V denotes volume, R is the universal gas constant and T denotes temperature.

- Process 1-2 - Isothermal compression

  Heat is abstracted from the working fluid and rejected from the cycle at minimum temperature. Work done on the working fluid is equal in magnitude to the heat rejected from the cycle. There is no change in internal energy, but there is a decrease in entropy.

$$p_2 = \frac{p_1 V_1}{V_2} = p_1 r\,, \tag{3.2}$$

$$T_2 = T_1 = T_{\min}.$$

  Heat transfer, Q, equals work done,

$$W = p_1 V_1 \ln\left(\frac{1}{r}\right) = RT_1 \ln\left(\frac{1}{r}\right), \tag{3.3}$$

and change in entropy,

$$(S_2 - S_1) = R \ln\left(\frac{1}{r}\right). \tag{3.4}$$

- Process 2-3 – Isochoric regenerative heat transfer to working fluid

  In this process heat is transferred from the regenerative matrix to the working medium, thus increasing the temperature from minimum to maximum. No work is done and there is an increase in the entropy and internal energy of the gas.

$$p_3 = \frac{p_2 T_3}{T_2} = \frac{p_2}{\tau}\,, \tag{3.5}$$

$$V_3 = V_{2,}$$

$$Q = C_v (T_3 - T_2)\,, \tag{3.6}$$

$$W = 0,$$

$$(S_3 - S_2) = C_v \ln\left(\frac{1}{\tau}\right). \tag{3.7}$$

- Process 3-4 – Isothermal expansion

Heat is supplied to the working gas at high temperature, T_{max}, during expansion of the working fluid. Work done by the fluid is equal in magnitude to the heat supplied. There is no change in internal energy but there is an increase in the entropy of the working fluid.

$$p_4 = \frac{p_3 V_3}{V_4} = \frac{p_3}{r}, \tag{3.8}$$

$$T_3 = T_4 = T_{\max.}$$

Heat transfer, Q, equals work done,

$$W = p_3 V_3 \ln r = R T_3 \ln r, \tag{3.9}$$

$$\Delta S_{3-4} = (S_4 - S_3) = R \ln r. \tag{3.10}$$

- Process 4-1 – Isochoric regenerative heat transfer to regenerator matrix

As the fluid flows from the hot space to the cold space, heat is transferred from the fluid to the regenerator at maximum temperature, decreasing the fluid temperature from $T_{\max}$ to $T_{\min}$. No work is done and there is a decrease in both the entropy and internal energy of the working fluid.

$$p_1 = \frac{p_4 T_4}{T_1} = p_1 \tau, \tag{3.11}$$

$$V_1 = V_{4,}$$

$$Q = C_v(T_1 - T_4), \tag{3.12}$$

$$\Delta S_{4-1} = (S_1 - S_4) = C_v \ln \tau . \tag{3.13}$$

In the regenerative processes, the heat transferred from the matrix to the working fluid (2-3) in then fully restored from the working fluid during process 4-1. There is no net gain or loss of heat by the working medium in the matrix and therefore the total heat supplied to the cycle at T_{max} is

$$Q_{in} = Q_{3-4} = RT_3 \ln r , \tag{3.14}$$

and the heat released from the cycle at T_{min} is

$$Q_{out} = Q_{1-2} = RT_1 \ln\left(\frac{1}{r}\right). \tag{3.15}$$

Hence, the thermal efficiency is defined as

$$n_{th} = \frac{Q_{in} - Q_{out}}{Q_{in}} \tag{3.16}$$

$$= \frac{(RT_3 \ln r - RT_1 \ln r)}{RT_3 \ln r} \tag{3.17}$$

$$= 1 - \tau .$$

The primary conclusion that stems from this rather simplified analysis is that the ideal Stirling cycle efficiency is the same as that of the Carnot cycle between the same temperature limits. Other than that, this type of analysis is only useful for primary calculations and comprehension of the fundamental thermodynamic principles governing the Stirling cycle.

3.5.2 The Schmidt analysis

The classical analysis of Stirling cycle machines was proposed by Gustav Schmidt (1861). This analysis accounts for the harmonic motion of the reciprocating elements. However, it remains highly idealized as it retains the major assumptions of isothermal compression and expansion processes and perfect regeneration. Nonetheless, it provides a more realistic approach than the ideal cycle analysis, and can be used as a preliminary design methodology if results are cautiously interpreted [3].

The main assumptions of the Schmidt analysis are [3]:

1. The regenerative process is perfect;
2. The instantaneous pressure is constant throughout the system;
3. The working medium obeys the characteristic gas equation, $PV = RT$;
4. There are no leakages, and the mass of the working fluid remains constant;
5. The volume variations in the working spaces occur sinusoidally;
6. There are no temperature gradients in the heat exchangers;
7. The cylinders walls and piston temperatures remain constant;
8. There is perfect mixing of the cylinders contents;
9. The temperature of the working fluid in the ancillary spaces remains constant;
10. The speed of the machine is constant;
11. Steady-state conditions are established.

3.5.2.1 Basic equations of the Schmidt analysis

In this section the basic equations of the Schmidt analysis [3] will be outlined excluding extensive derivations and algebraic manipulations.

Volume variation of the expansion space [3]:

$$V_{\mathrm{e}} = \frac{1}{2} V_{\mathrm{E}} (1 + \cos\varphi) , \tag{3.18}$$

where V_{e} is the instantaneous volume, V_{E} is the maximum volume and φ is the crank shaft angle.

Volume variation of the compression space [3]:

$$V_{\mathrm{c}} = \frac{1}{2} V_{\mathrm{C}} \left[1 + \cos(\varphi - \alpha) \right], \tag{3.19}$$

where α is the phase difference between the two spaces.

Volume of dead space, being that constant volume of the total working place is not included in the compression and expansion place [3]:

$$V_{\mathrm{D}} = X V_{\mathrm{E}} , \tag{3.20}$$

where V_{D} is the dead volume and X is the ratio of dead volume to the expansion space volume.

Mass of the working fluid in the expansion space [3]:

$$m_{\mathrm{e}} = \frac{p_{\mathrm{e}} V_{\mathrm{e}}}{R T_{\mathrm{e}}} . \tag{3.21}$$

Here, m is mass, R is the universal gas constant and T is the instantaneous temperature.

Mass of the working fluid in the compression space [3]:

$$m_{\mathrm{c}} = \frac{p_{\mathrm{c}} V_{\mathrm{c}}}{R T_{\mathrm{c}}} . \tag{3.22}$$

Mass of the working fluid in the dead space [3]:

$$m_{\mathrm{d}} = \frac{p_{\mathrm{d}} V_{\mathrm{d}}}{R T_{\mathrm{d}}}. \tag{3.23}$$

The total mass of the working fluid remains constant and is given by the expression [3]:

$$\begin{aligned} M_{\mathrm{T}} &= m_{\mathrm{e}} + m_{\mathrm{c}} + m_{\mathrm{d}} \\ M_{\mathrm{T}} &= \frac{K V_{\mathrm{E}}}{2 R T_{\mathrm{E}}} \end{aligned}, \tag{3.24}$$

where K is a constant.

The instantaneous pressure, p, is expressed by [3]:

$$\begin{aligned} p = p_{\min} &= \frac{K}{[B(1+\delta)]} \\ p = p_{\max} &= \frac{K}{[B(1-\delta)]} \end{aligned}, \tag{3.25}$$

or,

$$\begin{aligned} p = p_{\min} &= \frac{(1+\delta)}{[1+\delta\cos(\varphi-\theta)]} \\ p = p_{\max} &= \frac{(1-\delta)}{[1+\delta\cos(\varphi-\theta)]} \end{aligned}, \tag{3.26}$$

The mean cycle pressure is given by [3]:

$$p_{\mathrm{mean}} = p_{\max}\left[\frac{(1-\delta)}{(1+\delta)}\right]^{\frac{1}{2}}. \tag{3.27}$$

Here, $B = (\tau + \kappa + 2S)$; $\delta = (\tau^2 + \kappa^2 + 2\tau\kappa\cos\alpha)^2 / (\tau + \kappa - 2S)$; τ is the temperature ratio, T_C / T_E; κ is the swept volume ratio, V_C / V_E; $S = (2X\tau) / (\tau + 1)$, is the reduced dead volume.

Heat transfer and work done

Since the processes of expansion and compression occur isothermally, the heat transferred, Q, equals the work done, P. Hence [3]:

$$Q = P = \int p dV \,. \tag{3.28}$$

After manipulation the following equations can be obtained for each working space:

- expansion space [3]:

$$Q_e = \frac{\pi p_{mean} V_E \delta \sin\theta}{\left[1 + (1 - \delta^2)^{\frac{1}{2}}\right]}; \tag{3.29}$$

- compression space [3]:

$$Q_c = \frac{\pi p_{mean} V_E \kappa \delta \sin(\theta - \alpha)}{\left[1 + (1 - \delta^2)^{\frac{1}{2}}\right]}. \tag{3.30}$$

Dividing Q_c by Q_e and after manipulations [3]:

$$\frac{Q_c}{Q_e} = -\tau \,, \tag{3.31}$$

which indicates that heat transferred from the cold space is opposite in direction to the heat transferred from the expansion space and numerically different by the temperature ratio, τ. By analogy, work done in the two spaces follows the same relationship [3]:,

$$P_c = -\tau P_E \,. \tag{3.32}$$

The thermal efficiency is given by [3]:

$$n = \frac{Q_E - \tau Q_E}{Q_E} = 1 - \tau = \frac{T_E - T_C}{T_E}\,, \tag{3.33}$$

which corresponds to the Carnot efficiency as in the ideal thermodynamic cycle described earlier.

3.5.3 The ideal adiabatic model

Urieli and Berchowitz [14] investigated the contribution of heat exchangers in the ideal Stirling cycle and reached to the paradoxical conclusion that the heat exchangers were redundant. This conflicts with practical machine and effective heat exchange requirements and, therefore, an adiabatic model was proposed. The main assumption of this method was that the net heat transferred through the cycle must be provided by the heat exchangers and the working spaces tend to be adiabatic rather than isothermal [14]. This model retains the assumptions of perfectly effective heat exchangers. The equations of the ideal adiabatic model are not explicitly integrable, as for the ideal Stirling cycle model, due to the adiabatic nature of the working spaces. This poses a requirement for numerical solution methods which adds to the complexity but also allows for enhanced consideration of heat transfer and flow-friction phenomena in the heat exchangers, thus providing more realistic results.

The modelled engine is set up as a five-component serially connected model with ideal heat exchangers. Such layout is presented in Figure 3.29 [2, 14]. The gas in the cooler and heater is maintained at isothermal conditions at temperatures T_K and T_H respectively. The gas inside

the regenerator has a linear temperature distribution. The gas is assumed to flow through the cooler-regenerator interface at cooler temperature, T_K, and at heater temperature, T_H, through the heater-regenerator interface. The resulting mixed mean temperature of the gas in the regenerator is equal to the logarithmic mean temperature between T_H and T_K. The temperature of the working spaces, T_c and T_e vary through the cycle, in accordance to the adiabatic nature of these spaces. Enthalpy is transported in terms of mass flow through four interfaces, being respectively compression space-cooler cK, cooler-regenerator Kr, regenerator-heater rH, and, heater-expansion space He. The positive direction of flow is defined as being from the compression space to the expansion space. The enthalpies flowing across the interfaces cK and He carry the respective upstream temperatures which, thus, depend on the direction of flow. There is no gas leakage, hence the total mass of gas in the system remains constant and there is also no pressure drop and p represents the instantaneous pressure throughout the system. Work is done on the surrounding by means of volume variations of the working spaces, V_c and V_e respectively. Heat Q_K and Q_H is transferred between the environment and the working gas through the cooler and the heater respectively. Finally, the regenerator casing is considered adiabatic and heat Q_r is exchanged between the matrix and the working gas.

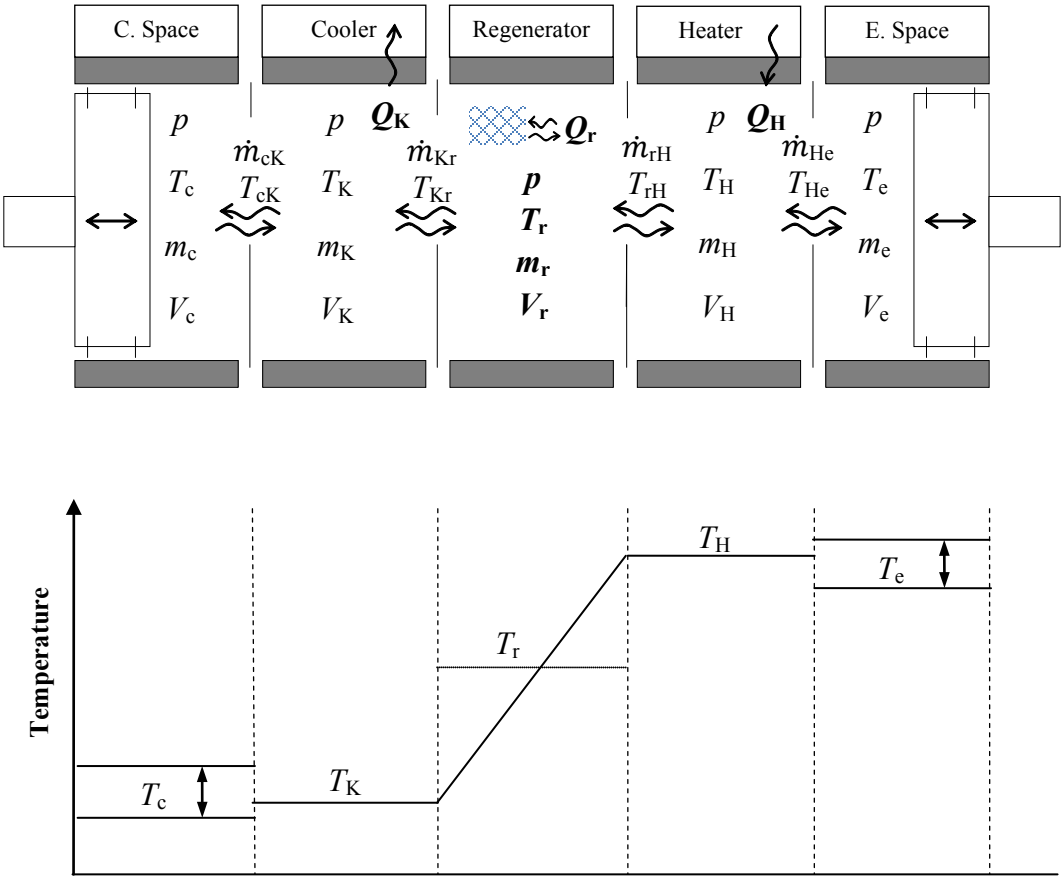

Figure 3.29: Layout of the ideal adiabatic model

3.5.3.1 Basic equations of the ideal adiabatic model

The main approach for deriving the necessary differential and algebraic equations is to apply the energy and gas state equations to each of the five components which are considered as the control volumes, and link the results by applying the continuity equation across the entire system. The final equations required for the solution are presented below [14].

Pressure:

$$Dp = \frac{-\gamma p\left(\frac{DV_c}{T_{cK}} + \frac{DV_e}{T_{He}}\right)}{\frac{V_c}{T_{cK}} + \gamma\left(\frac{V_K}{T_K} + \frac{V_r}{T_r} + \frac{V_H}{T_H}\right) + \frac{V_e}{T_{He}}}, \tag{3.34}$$

where γ is the isentropic index.

Masses:

$$Dm_{\mathrm{c}} = \frac{pDV_{\mathrm{c}} + V_{\mathrm{c}} \dfrac{Dp}{\gamma}}{RT_{\mathrm{cK}}}; \tag{3.35}$$

$$m_{\mathrm{K}} = \frac{pV_{\mathrm{K}}}{RT_{\mathrm{K}}}; \tag{3.36}$$

$$m_{\mathrm{r}} = \frac{pV_{\mathrm{r}}}{RT_{\mathrm{r}}}; \tag{3.37}$$

$$m_{\mathrm{H}} = \frac{pV_{\mathrm{H}}}{RT_{\mathrm{H}}}; \tag{3.38}$$

$$m_{\mathrm{e}} = M - (m_{\mathrm{c}} + m_{\mathrm{K}} + m_{\mathrm{H}} + m_{\mathrm{r}}) . \tag{3.39}$$

Temperatures:

$$T_{\mathrm{c}} = \frac{pV_{\mathrm{c}}}{Rm_{\mathrm{c}}}; \tag{3.40}$$

$$T_{\mathrm{e}} = \frac{pV_{\mathrm{e}}}{Rm_{\mathrm{e}}}; \tag{3.41}$$

Mass accumulation and flows:

$$Dm_{\mathrm{K}} = m_{\mathrm{K}} \frac{Dp}{p}; \tag{3.42}$$

$$Dm_{\mathrm{r}} = m_{\mathrm{r}} \frac{Dp}{p}; \tag{3.43}$$

$$Dm_{\mathrm{H}} = m_{\mathrm{H}} \frac{Dp}{p}; \tag{3.44}$$

$$\dot{m}_{\mathrm{cK}} = -Dm_{\mathrm{c}}; \tag{3.45}$$

$$\dot{m}_{\mathrm{Kr}} = \dot{m}_{\mathrm{cK}} - Dm_{\mathrm{K}}; \tag{3.46}$$

$$\dot{m}_{\mathrm{rH}} = \dot{m}_{\mathrm{Kr}} - Dm_{\mathrm{r}}; \tag{3.47}$$

$$\dot{m}_{\mathrm{He}} = \dot{m}_{\mathrm{rH}} - Dm_{\mathrm{H}}; \tag{3.48}$$

Energy:

$$DW = p\left(DV_{\mathrm{c}} + DV_{\mathrm{e}}\right); \tag{3.49}$$

$$DQ_{\mathrm{K}} = \frac{V_{\mathrm{K}} Dpc_{\mathrm{v}}}{R} - c_{\mathrm{p}}\left(T_{\mathrm{cK}}\dot{m}_{\mathrm{cK}} - T_{\mathrm{Kr}}\dot{m}_{\mathrm{Kr}}\right); \tag{3.50}$$

$$DQ_{\mathrm{r}} = \frac{V_{\mathrm{r}} Dpc_{\mathrm{v}}}{R} - c_{\mathrm{p}}\left(T_{\mathrm{Kr}}\dot{m}_{\mathrm{Kr}} - T_{\mathrm{rH}}\dot{m}_{\mathrm{rH}}\right). \tag{3.51}$$

The calculation requires the simultaneous solution of the pressure and $\dot{m}_{\mathrm{c}}$ equations with the algebraic equations. The other four energy derivatives can be solved afterwards. If it is decided to solve all six main differential equations simultaneously, it is preferable to formulate the problem as an initial-value problem and use a numerical technique like the fourth order Range-Kutta method. The ideal adiabatic model, however, is a boundary-value problem rather than an initial-value problem as the working space temperature which results from adiabatic processes are unknown [14]. Nonetheless, the cyclic nature of the model permits the formulation of the problem as an initial-value problem by assigning arbitrary initial values and iterate the solution process until convergence has been established [14]. The

transient period of the simulation is equivalent to the "warm-up" period of an actual machine. The compression and expansion space temperature values initially defined are T_K and T_H respectively [14].

3.5.4 The quasi-steady flow model

The quasi-steady flow model, described in [14] is another useful addition to the Stirling engine mathematical modelling field. This methodology is widely used by researchers, enhanced with improvements, modifications, and often coupled with optimization techniques. It is based on the ideal adiabatic model; however, it is more inclusive as it considers more realistic phenomena such as temperature variation and pressure drop due to frictional drag in the heat exchangers. Furthermore, the model assumes that the walls of the heat exchangers are isothermal and heat is transferred to the working medium by means of forced convection. This showcases the importance of the convection heat transfer coefficients which are defined empirically as they are dependent on temperature, flow regime, and heat exchanger geometry. The regenerator is divided in to two control volumes with an interface in between and is assumed to have infinite thermal conductivity across the direction of the flow and zero conductivity in the bulk flow direction. Additionally, heat loss through the matrix and its casing in assumed negligible. The effect of pressure drop in the heat exchangers is accounted for by virtue of dissipation terms. The assumption here is that heat is generated when the gas is forced to flow against friction. This increases the gas temperature and, as a result, less heat is transferred to the gas. Overall, this pressure drop in the heat exchangers has a negative effect on power output. A layout of the quasi-steady flow model is presented in Figure 3.30 [2, 14]. Lower case "w" characters denote wall temperatures.

The heater and cooler walls are maintained isothermal but the regenerator wall temperatures, Twr1, Twr2, are calculated from energy considerations. The enthalpies flowing across the interfaces cK, Kr, rH, He carry the respective adjacent upstream temperatures and, therefore, temperatures are conditional on the flow direction as in the ideal adiabatic model.

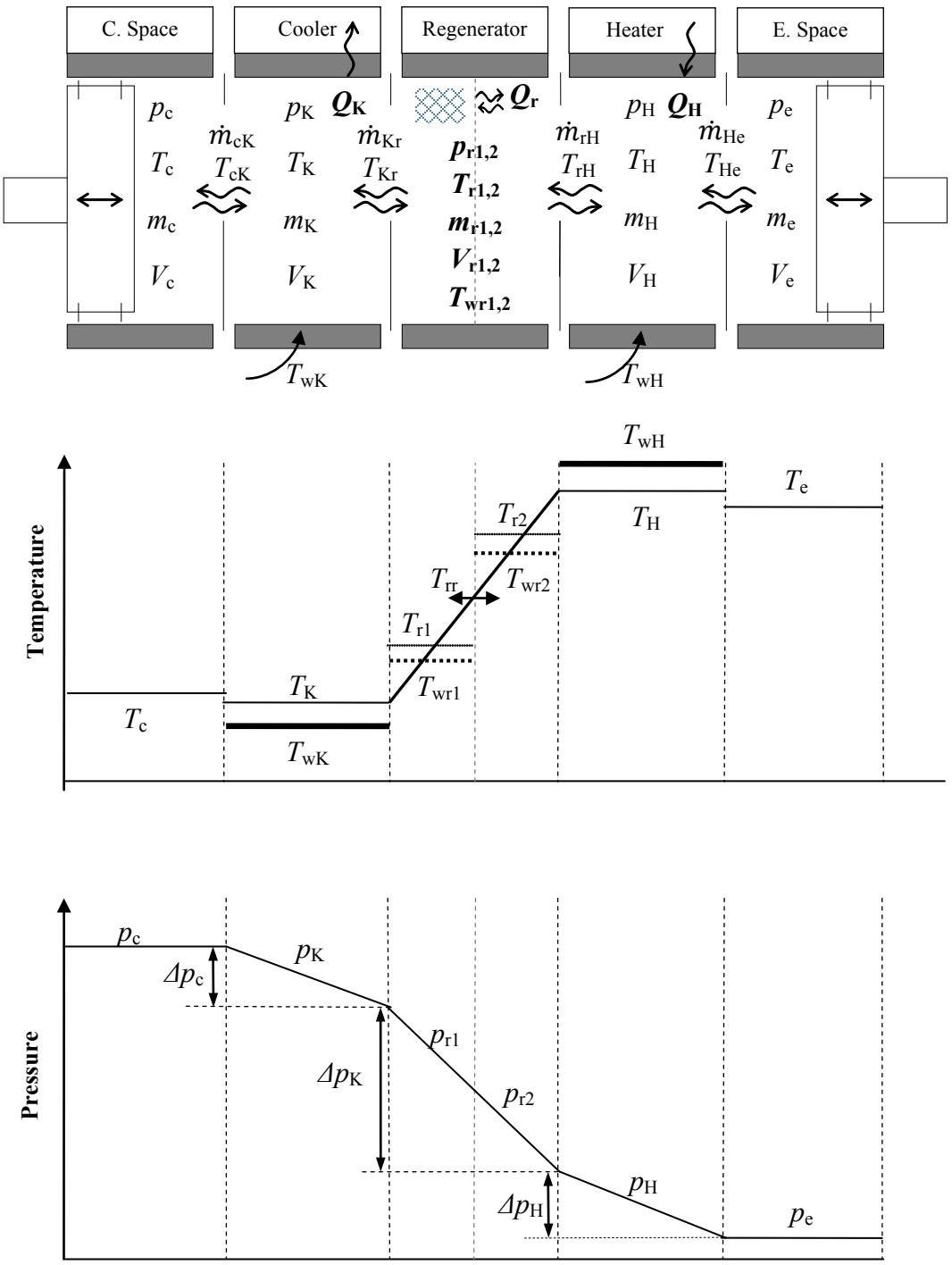

Figure 3.30: Layout of the quasi-steady flow model

3.5.4.1 Basic equations of the quasi-steady flow model

The approach used to derive equations for the quasi-steady flow model is similar to the one used for the ideal adiabatic model. However, the energy balance equations have been modified to include the flow dissipation terms, and heat flow is evaluated in terms of heat transfer equations rather than of energy balance. Thus, enthalpy and the associated mass flows are determined by the energy equation. The set of differential and algebraic equations for the quasi-steady flow model is presented next [14].

Pressures:

$$p_{\mathrm{K}} = p_{\mathrm{c}} + \frac{\Delta p_{\mathrm{K}}}{2}; \tag{3.52}$$

$$p_{r1} = p_{\mathrm{K}} + \frac{\left(\Delta p_{\mathrm{K}} + \Delta p_{\mathrm{r1}}\right)}{2}; \tag{3.53}$$

$$p_{\mathrm{r2}} = p_{\mathrm{r1}} + \frac{\left(\Delta p_{\mathrm{r1}} + \Delta p_{\mathrm{r2}}\right)}{2}; \tag{3.54}$$

$$p_{\mathrm{H}} = p_{\mathrm{r2}} + \frac{\left(\Delta p_{\mathrm{r1}} + \Delta p_{\mathrm{H}}\right)}{2}; \tag{3.55}$$

$$p_{\mathrm{e}} = p_{\mathrm{H}} + \frac{\Delta p_{\mathrm{H}}}{2}. \tag{3.56}$$

Mass in the expansion space:

$$m_{\mathrm{e}} = M - \left(m_{\mathrm{c}} + m_{\mathrm{K}} + m_{\mathrm{r1}} + m_{\mathrm{r2}} + m_{\mathrm{H}}\right). \tag{3.57}$$

Gas temperatures:

$$T_{\mathrm{c}} = \frac{p_{\mathrm{c}} V_{\mathrm{c}}}{R m_{\mathrm{c}}}; \tag{3.58}$$

$$T_{\mathrm{K}} = \frac{p_{\mathrm{K}} V_{\mathrm{K}}}{R m_{\mathrm{K}}}; \tag{3.59}$$

$$T_{\mathrm{r1}} = \frac{p_{\mathrm{r1}} V_{\mathrm{r1}}}{R m_{\mathrm{r1}}}; \tag{3.60}$$

$$T_{\mathrm{r2}} = \frac{p_{\mathrm{r2}} V_{\mathrm{r2}}}{R m_{\mathrm{r2}}}; \tag{3.61}$$

$$T_{\mathrm{H}} = \frac{p_{\mathrm{H}} V_{\mathrm{H}}}{R m_{\mathrm{H}}}; \tag{3.62}$$

$$T_{\mathrm{e}} = \frac{p_{\mathrm{e}} V_{\mathrm{e}}}{R m_{\mathrm{e}}}. \tag{3.63}$$

Regenerator interface temperatures:

$$Tr_{\mathrm{k}} = 1.5 T_{\mathrm{r1}} - 0.5 T_{\mathrm{r2}}; \tag{3.64}$$

$$T_{\mathrm{rr}} = 0.5 \left(T_{\mathrm{r1}} + T_{\mathrm{r2}} \right); \tag{3.65}$$

$$Tr_{\mathrm{k}} = 1.5 T_{\mathrm{r2}} - 0.5 T_{\mathrm{r1}}. \tag{3.66}$$

Energy:

$$DW = p_{\mathrm{c}} DV_{\mathrm{c}} + p_{\mathrm{e}} DV_{\mathrm{e}}; \tag{3.67}$$

$$DQ_{\mathrm{K}} = h_{\mathrm{K}} A_{\mathrm{wgK}} \left(T_{\mathrm{wK}} \quad T_{\mathrm{K}} \right); \tag{3.68}$$

$$DQ_{\mathrm{r1}} = h_{\mathrm{r1}} A_{\mathrm{wgr1}} \left(T_{\mathrm{wr1}} \quad T_{\mathrm{r1}} \right); \tag{3.69}$$

$$DQ_{\mathrm{r2}} = h_{\mathrm{r2}} A_{\mathrm{wgr2}} \left(T_{\mathrm{wr2}} \quad T_{\mathrm{r2}} \right); \tag{3.70}$$

$$DQ_{\mathrm{H}} = h_{\mathrm{H}} A_{\mathrm{wgH}} \left(T_{\mathrm{wH}} \quad T_{\mathrm{H}} \right). \tag{3.71}$$

For the heat transfer coefficient inside the heater and the cooler the Dittus-Boelter Nusselt number correlation was used [108],

$$Nu = 0.029 Re^{4/5} Pr^{n}, \tag{3.72}$$

where $n = 0.4$ for heating and 0.3 for cooling.

For the heat transfer coefficient inside the regenerator the Nusselt number coefficient was used by Tanaka et al. [109],

$$Nu = 0.33 Re^{0.67}, \tag{3.73}$$

where Re is the Reynolds number [108]:

$$Re = \frac{\rho u D}{\mu}, \tag{3.74}$$

and Pr is the Prandtl number [108]:

$$Pr = \frac{C_p \mu}{k}. \tag{3.75}$$

Regenerator matrix temperatures:

$$DT_{\mathrm{wr1}} = -\frac{DQ_{\mathrm{r1}}}{c_{\mathrm{mr}}}; \tag{3.76}$$

$$DT_{\mathrm{wr2}} = -\frac{DQ_{\mathrm{r2}}}{c_{\mathrm{mr}}}, \tag{3.77}$$

where c_{mr} is the heat capacity of each matrix control volume.

Derivation of pressure equation in the compression space:

$$DQ = DQ_{\mathrm{K}} + DQ_{\mathrm{r1}} + DQ_{\mathrm{r2}} + DQ_{\mathrm{H}}; \tag{3.78}$$

$$V = V_{\mathrm{c}} + V_{\mathrm{K}} + V_{\mathrm{r1}} + V_{\mathrm{r2}} + V_{\mathrm{H}} + V_{\mathrm{e}}; \tag{3.79}$$

$$Diss = Diss_{\mathrm{K}} + Diss_{\mathrm{r1}} + Diss_{\mathrm{r2}} + Diss_{\mathrm{H}}; \tag{3.80}$$

$$Dp_{\mathrm{c}} = \frac{\left[R\left(DQ - Diss\right) - c_{\mathrm{p}} DW\right]}{c_{\mathrm{v}} V}. \tag{3.81}$$

Mass in the compression space:

$$Dm_{\mathrm{c}} = \frac{\left(p_{\mathrm{c}} DV_{\mathrm{c}} + \frac{V_{\mathrm{c}} DP_{\mathrm{c}}}{\gamma}\right)}{RT_{\mathrm{cK}}}; \tag{3.82}$$

Mass flows:

$$\dot{m}_{\mathrm{ck}} = -Dm_{\mathrm{c}}; \tag{3.83}$$

$$\dot{m}_{\mathrm{Kr}} = \frac{\left(c_{\mathrm{p}} \dot{m}_{\mathrm{cK}} T_{\mathrm{cK}} - DQ_{\mathrm{K}} - \frac{c_{\mathrm{v}} V_{\mathrm{K}} Dp_c}{R} - Diss_{\mathrm{K}} \right)}{c_{\mathrm{p}} T_{\mathrm{Kr}}}; \tag{3.84}$$

$$\dot{m}_{\mathrm{rr}} = \frac{\left(c_{\mathrm{p}} \dot{m}_{\mathrm{Kr}} T_{\mathrm{Kr}} - DQ_{\mathrm{r1}} - \frac{c_{\mathrm{v}} V_{\mathrm{r1}} Dp_c}{R} - Diss_{\mathrm{r1}} \right)}{c_{\mathrm{p}} T_{\mathrm{rr}}}; \tag{3.85}$$

$$\dot{m}_{\mathrm{rH}} = \frac{\left(c_{\mathrm{p}} \dot{m}_{\mathrm{rr}} T_{\mathrm{rr}} - DQ_{\mathrm{r2}} - \frac{c_{\mathrm{v}} V_{\mathrm{r2}} Dp_c}{R} - Diss_{\mathrm{r2}} \right)}{c_{\mathrm{p}} T_{\mathrm{rH}}}; \tag{3.86}$$

$$\dot{m}_{\mathrm{He}} = \frac{\left(c_{\mathrm{p}} \dot{m}_{\mathrm{rH}} T_{\mathrm{rH}} - DQ_{\mathrm{к}} - \frac{c_{\mathrm{v}} V_{\mathrm{H}} Dp_c}{R} - Diss_{\mathrm{H}} \right)}{c_{\mathrm{p}} T_{\mathrm{He}}}; \tag{3.87}$$

Masses:

$$Dm_{\mathrm{K}} = \dot{m}_{\mathrm{cK}} - \dot{m}_{\mathrm{Kr}}; \tag{3.88}$$

$$Dm_{\mathrm{r1}} = \dot{m}_{\mathrm{Kr}} - \dot{m}_{\mathrm{rr}}; \tag{3.89}$$

$$Dm_{\mathrm{r2}} = \dot{m}_{\mathrm{rr}} - \dot{m}_{\mathrm{rH}}; \tag{3.90}$$

$$Dm_{\mathrm{H}} = \dot{m}_{\mathrm{rH}} - \dot{m}_{\mathrm{He}}. \tag{3.91}$$

The problem is again formulated as an initial value problem and the set of differential equations are integrated over several cycles until steady state has been reached. The time required for convergence is dependent on the thermal capacitance of the regenerator matrix [14]. In order to accelerate the solution, the thermal capacitance of the matrix can be set at a high value so that temperatures T_{mr1}, T_{mr2} will not vary significantly. Another option would be to check the heat balance at the end of every time step and change the matrix temperatures so that the net heat transferred between the matrix and the working gas is zero [14].

3.5.5 Empirical modelling

This section describes two empirical concepts used to estimate the performance of a Stirling engine, namely the Beale number and the West number.

The Beale number is given by [3]:

$$B_n = \frac{P}{p_{mean} V f}, \tag{3.92}$$

where P is the power output of the engine, p_{mean} is the mean operating pressure (Pa), V is the swept volume of the expansion space (m^3) and f is the cyclic frequency (Hz).

Common values for the Beale number range from 0.11 to 0.15 where higher values correspond to engines with higher temperature differential.

The West number is given by [3]:

$$W_n = B_n \frac{T_H + T_K}{T_H - T_K} \tag{3.93}$$

where B_n is the Beale number and T_H, T_K are the gas temperatures inside the hot and cold spaces respectively.

A variety of engines can be characterized by a West number of approximately 0.25 whereas engines with high temperature differentials may have a West number of up to 0.35

3.6 Main principles of Genetic Algorithm optimization

This section provides a general overview of the general principals used in the Genetic Algorithm (GA) optimization method with a focus on the code developed in [2]. This procedure was used to obtain an optimum set of design parameters for the solar Stirling engine.

3.6.1 Introduction

Genetic algorithms are stochastic optimization methods essentially mimicking the evolutionary mechanism of species survival, evolution and adaption. This theory was presented by Holland in 1975 and was successfully applied in engineering problems by Goldberg in 1989. The GA methodology follows nature's "survival of the fittest" rule over a population of individuals (solutions) and aims to generate a new population of better offspring. A useful attribute of GAs is that they can reach a global optimum by operating over a random population, whilst the analytical step-methods may be limited to providing local optimum solutions. The advantages of GAs are listed in Haupt as cited in [2] among other sources, with some of them being:

- Ability to use continuous or discrete variables;
- Can consider large numbers of variables;

- Can be run in parallel computing with the benefit of reduced solution times;
- The objective function can be analytical, in numerical form based in experimental data.

The procedure for implementing GAs is outlined in Goldberg as cited in [2]. The optimization is achieved by means of the natural selection process and thus the problem needs to be formed in a biological expression. The procedure starts by randomly forming the initial population of individuals. Each individual or chromosome contains various combinations of genetic information (optimization parameters) that are potential solutions to the problem. Each chromosome is initially evaluated by the fitness function which controls which individuals are fit to be considered as parents for the next generation. The chromosomes that meet the fitness requirements are allowed to reproduce and exchange genetic information by recombination and crossover. The genetic material can be also altered by mutation. Mutation can alter the genetic material in a more random fashion according to a usually low mutation probability rate. The resulting offspring are checked again for fitness (potential to solve the problem) and the procedure iterates until the optimum individual has been generated. The genetic information (parameters) stored in this chromosome are effectively the optimum solution to the problem.

3.6.2 Genetic algorithm procedure for the optimization of Stirling engines

The method used in this work is the one deployed in [2]. This procedure was laid out in such way as to be incorporated in a detailed second order mathematical model for the performance evaluation of Stirling engines. That model was developed in [2].

The method uses the binary GA, in which the variable is translated into a bit number by the encoding process and reverted by the decoding process. In order to avoid computational intensity and quantitative limitations, the continuous or real-value GA is used in which the

variables are represented by a single floating point number (Haupt cited in [2]). The details of the procedure are presented in the following sections.

3.6.2.1 Definition of the objective function for Stirling engine optimisation

As mentioned earlier, the engineering problem needs to be expressed in biological terms. Hence, a set of engine geometrical features are defined as the genetic information for each chromosome. A chromosome or individual in this case is considered an engine with any combination of the design parameters. The objective function in this case was the maximization of indicated power.

The engine design parameters used in this study were the annular flow section of the cavity-type heater, the length of the cooler and the length of the regenerator. Thus, a chromosome or individual can be represented as [2]:

$$\text{Chromosome} = (D_h; L_k; L_r), \tag{3.94}$$

where D_h is the annular gap of the heater (m); L_k is the length of the cooler (m); L_r is the length of the regenerator (m).

These parameters are set to vary with a specific range based on manufacturing practicality. For the solar engine under investigation, the primary limitation was the design of the cavity-type heater and most importantly its inner heated surface. This was, in turn, sized based on optical consideration and requirements of the solar dish the engine is mounted on. Therefore the inner heater diameter and hence the diameter of the regenerator and cooler could not be modified. The engine efficiency was not a primary concern as the engine operates on solar radiation. The objective function is [2]:

$$\text{Indicated power} = \text{f (chromosome)} = \text{f}\,(D_h; L_k; L_r). \tag{3.95}$$

3.6.2.2 Generation of the initial population

As was described earlier the initial population (group of potential engine configurations) is formed in a random way as [2]:

$$\text{population} = \text{rand}\ (N_{pop};\ N_{var}), \tag{3.96}$$

where N_{pop} and N_{var} are the number of chromosomes and parameters respectively. The size of the population has been found to affect the speed of convergence and therefore practical numbers of chromosomes have been defined in the range of 30 - 100 (Zalzala et al. cited in [2]). For this work, the selected number of chromosomes was 30 per generation.

3.6.2.3 Evaluation

The indicated power calculation for each generation is performed in the second order mathematical model developed in [2]. The chromosome value is then assessed by the fitness function and the fitness value is calculated by [2]:

$$Fitnessvalue = \frac{1}{1 + \max value - value}, \tag{3.97}$$

where max*value* is the maximum value of the chromosome and *value* is the value of chromosome.

3.6.2.4 Selection process

Once the fitness values of each chromosome have been calculated, they are ranked in descending order. The surviving chromosomes which will form the next generation are determined by [2]:

$$N_{keep} = X_{rate} N_{pop}, \tag{3.98}$$

where X_{rate} is the selection rate equal to 0.5 and N_{keep} is the number of surviving chromosomes. The parents for the next generation are selected randomly from the fitness ranking list using a random pairing selection procedure achieved by the rank weighting technique described in Haupt as cited in [2].

3.6.2.5 Mating process

During the mating process the parents are handled by the reproduction operator to produce offsprings for the next generation. A common operator for this is the single point crossover with a random position which is applied to a couple of parents. During the crossover process the two parents exchange genetic information or - in this case - values of engine parameters.

3.6.2.6 Mutation process

In order to avoid a local maximum which usually results after a fast solution, an additional reproduction operator called the mutation is used as means to ensure a global optimum point. During the mutation process some engine parameters are randomly changed. It is considered that a mutation rate of 0.2 is a practical value to ensure a global solution, albeit at the expense of slower convergence.

3.6.2.7 Convergence check

During this stage it is examined whether the termination condition has been met. The maximum numbers of generation was set to 80 to allow enough headroom for the solution to

converge. The convergence criteria are met when the difference between the indicated power of one generation and the subsequent has remained constant for 20 generations in a row.

The optimization code used in this work was developed in [2] and was based on a continuous GA code documented in Haupt as cited in [2]. The different procedures described previously were implemented in MATLAB. The second order mathematical model of the solar Stirling engine was incorporated into the GA code and the program was run for the same boundary conditions available in literature. It is worth mentioning that the particular code has proven to be a valid method as its results were then modelled in 3D CFD in [2].

3.7 Rotary Stirling engine (Wankel configuration)

This is another promising topology for a Stirling-cycle engine. It was first proposed by Zwiauer [3] but was never reduced to practice. A schematic is shown on Figure 3.31. Two Wankel type rotary engines are coupled on the same shaft and two or three regenerators are arranged symmetrically around the axis. One Wankel unit acts as a compressor and the other as an expander. As it will be explained later, this configuration allows for two cycles per revolution for each component and it is believed that it can be a compact and high specific output machine [3].

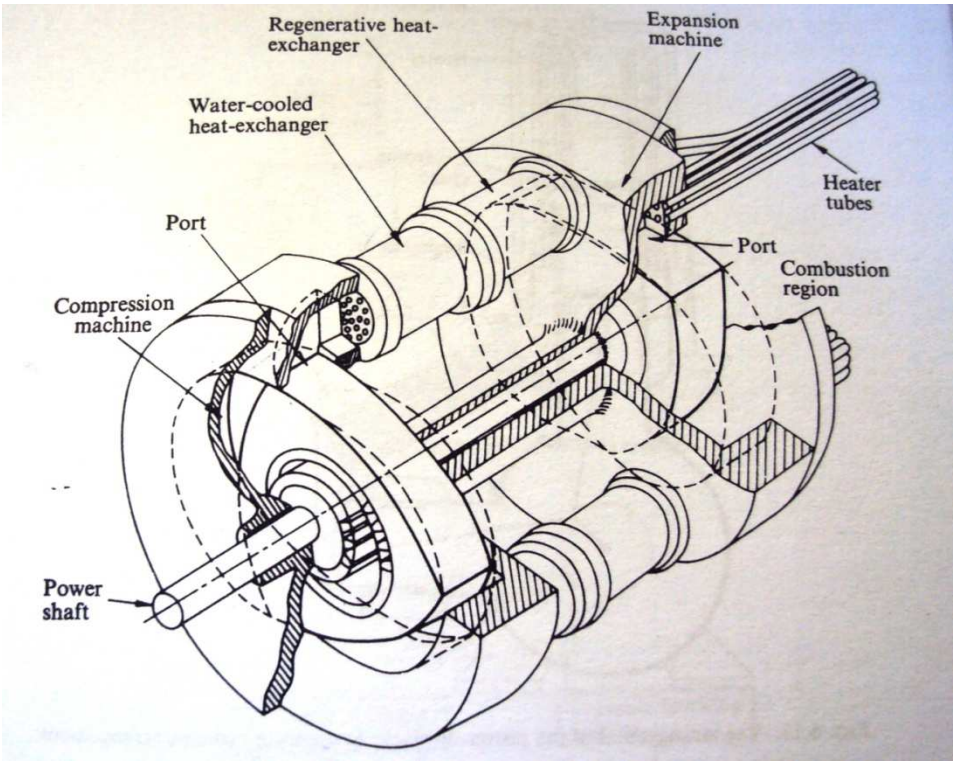

Figure 3.31: Rotary – Wankel-type Stirling engine [3]

3.7.1 Wankel engine theory

The original Wankel engine operation follows the Otto cycle principle. The main requirements that distinguish a merely rotary piston from a rotary piston – rotary combustion machine are [110]:

1. Port areas and all aspects of port timing must be such that efficient working cycles are possible. Cross-sectional areas of ports must control gas speeds within efficient design limits;
2. It must be possible to accommodate sensible gas sealing systems;
3. Adequate cooling must be possible;
4. The engine must not be heavier or larger or more expensive to produce than reciprocating engines generating the same power;

5. Power output and fuel consumption should at least approach figures which the best reciprocating piston engines can attain and a rotary design should be capable of substantially exceeding the performance of the equivalent reciprocating piston engine in at least one of the factors of comparison, and preferably in more. Particularly, it should demonstrate significant advantages in weight and space requirements for a given power output and the potential power output of the rotary piston engine should be greater than that of a conventional piston engine.

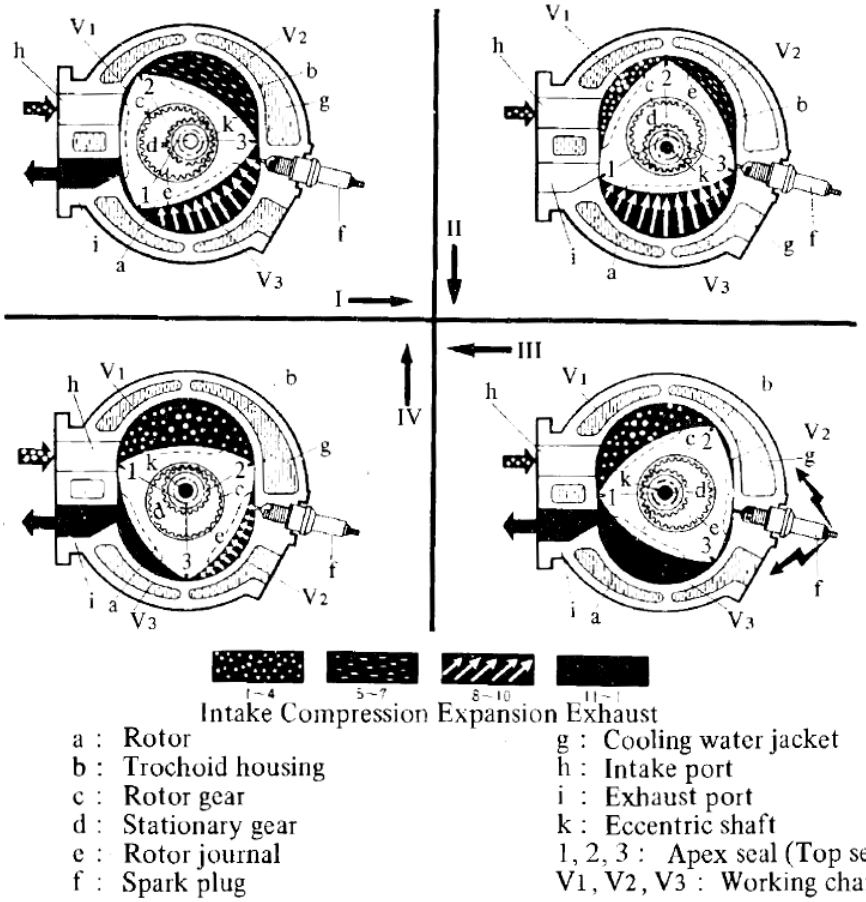

Figure 3.32: Thermodynamic processes of the Wankel engine [110]

Figure 3.32 shows the principal Wankel engine components and the 4 processes of an IC engine. During succeeding 90° rotor turns the expansion and exhaust phases will occur

sequentially. In detail, a complete thermodynamic cycle is realized in every one of the three chambers while the rotor rotates through 360°.

3.7.2 Geometrical properties of the Wankel mechanical configuration

3.7.2.1 Equation of the peritrochoid

The peritrochoid constitutes of the inner surface of the rotor housing. Theoretically, the peritrochoid curve is defined as a locus of point P on the segment $\overline{O_B P}$ fixed on a revolving circle B (radius q), which rolls in an inscribed manner on the outer circumference (x, y) of a circle A (Figure 3.33). The coordinates of point P are given by [110]:

$$\begin{cases} x = e\cos a + R\cos \alpha/m \\ y = e\sin a + R\sin \alpha/m \end{cases}, \tag{3.99}$$

where $\alpha = \omega t$; e is eccentricity; R is the generating radius of the peritrochoid, m is the number of apexes or flanks (arc-shaped contours) of the inner envelope (rotor shape) described later.

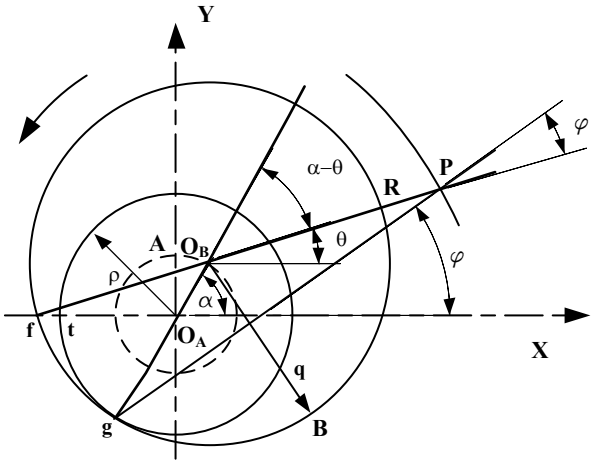

Figure 3.33: Geometrical definition of the Peritrochoid [111]

The number of peritrochoidal lobes; *n*, equals *m-1*; therefore, a 2-lobe-shaped housing corresponds to a 3-flank rotor.

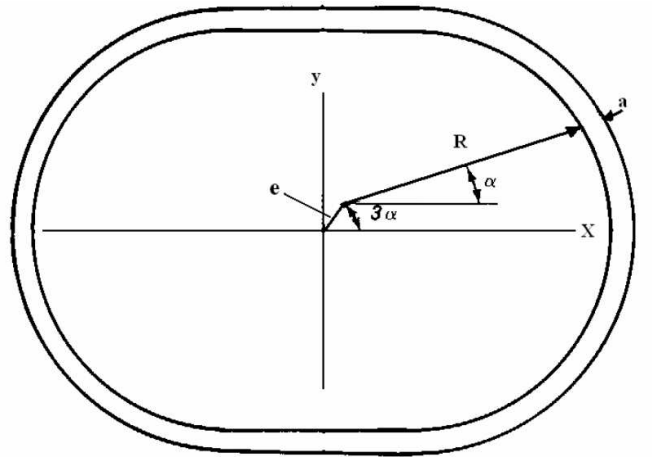

Figure 3.34: Peritrochoidal curve of rotor housing

3.7.2.2 Volumetric variation and displacement volume

The volume of the working chamber is given by the product of the area between a rotor flank and the area surrounded by the peritrochoid. The variation of the volumetric change, as described by Yamamoto [111], is as follows:

$$V = \frac{3\sqrt{3}}{2} eRb\left[1 - \sin\left(\frac{2}{3}a + \frac{\pi}{6}\right)\right] \tag{3.100}$$

The displacement area is given by the maximum of Eq. (3.102):

$$V_{\mathrm{H}} = 3\sqrt{3}eRb\,, \tag{3.101}$$

where *b* is the width of the rotor.

And the corresponding area:

$$F_{\mathrm{H}} = 3\sqrt{3}eR\,. \tag{3.102}$$

At the early stages of design, the geometric definitions of a Wankel engine can be obtained by using those definitions and nomograms like the one demonstrated below.

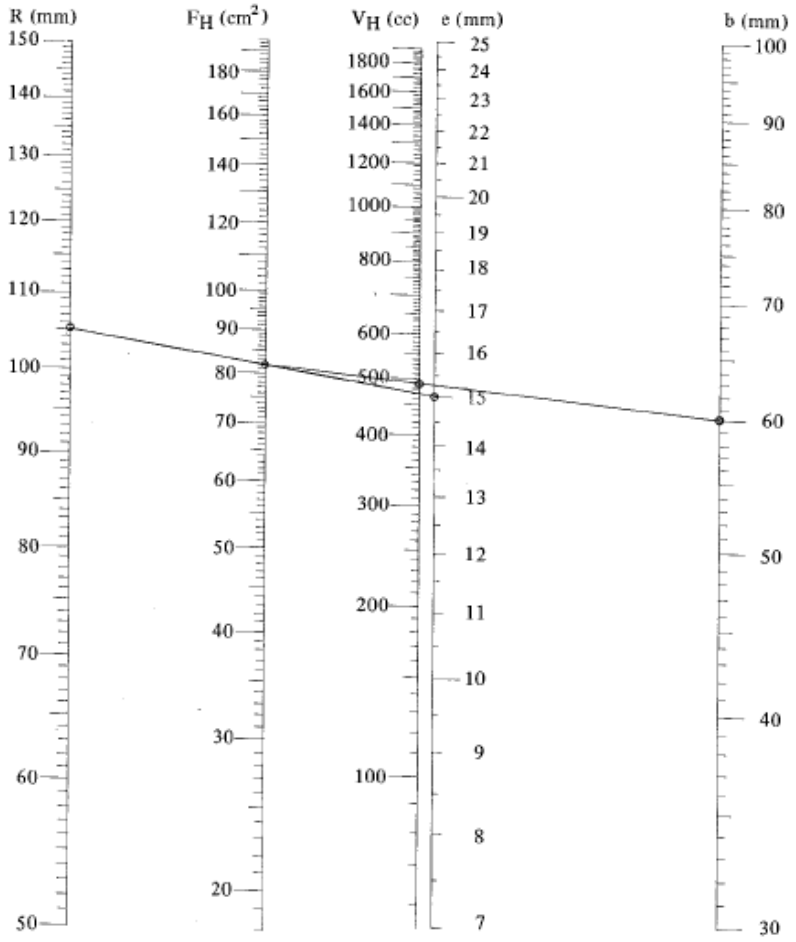

Figure 3.35: Nomogram for the calculation of the displacement volume [111]

Finally, another useful way of determining the initial geometrical dimensions of a Wankel engine is by using tables like Table 3.1 found in [111].

Table 3.1: Example of basic dimensions [111]

VH [cm^3]	e [mm]	b [mm]
60	7.6	32
125	9.5	40
150	10.5	41
250	11	52
400	14	59
500	14	67
500	15	60

3.7.2.3 Performance calculation of the Wankel engine

ANSYS FLUENT requires that the deforming domain in a dynamic mesh model is a single volume rather than three split sub-domains as would be the reality on a Wankel rotor. For the scope of this work and due to those dynamic mesh limitations the volume variation in each working chamber was performed algebraically using equation (3.100). The indicated power was calculated by power-volume diagrams, similar to a conventional Stirling engine. An alternative method was provided by Ansdale [110]. In his book, Ansdale presented a method for calculating the power output of the engine based on the pressure forces acting on each of the rotor flanks. Converting the pressure into forces the resulting torque can be calculated. For this calculation an effective radius is required for each flank which is given by [110]:

$$r_{\mathrm{ef}} = e\sin(2a)\,; \tag{3.103}$$

Then, for each flank the moment arms are [110]:

$$m_1 = e\sin 2a\,; \tag{3.104}$$

$$m_2 = e\sin\left(\frac{\pi}{3} - 2a\right); \tag{3.105}$$

$$m_3 = e\sin\left(\frac{\pi}{3} + 2a\right). \tag{3.106}$$

The total torque exerted on the rotor is given by [110]:

$$T = Ae\left[P_1\sin\left(\frac{\pi}{3} + 2a\right) + P_2\sin 2a + P_3\sin\left(\frac{\pi}{3} - 2a\right)\right], \tag{3.107}$$

where P_1, P_2, P_3 are the pressures exerted on each flank respectively and A is the equivalent area of a rotor flank stretching from apex seal to apex seal and is equal to [110]:

$$A = \sqrt{3}Rb\,. \tag{3.108}$$

In reality the flank area may vary as the spring apex seals move but the variance is considered too little and can be neglected.

In summary, there is a range of possibilities for the prediction of power output that help to overcome the limitations posed by ANSYS FLUENT. There are two common methods for the prediction of the indicated power output. The first method is by means of pressure-volume (PV) diagrams where pressure is plotted against volume for each space. The second method is by means of a torque diagram from equation (3.105). The power output of the rotor can then be calculated by the product of the mean torque and the angular velocity or areas of pressure-volume diagrams and frequency of rotation of the rotors.

Chapter 4 General Principles of CFD Modelling

4.1 Introduction

Computational Fluid Dynamics (CFD) is a powerful Computer Aided Engineering (CAE) tool for the analysis of mechanical equipment. Indicative applications include aerospace, aerodynamics, turbo machinery and combustion engines. For all flows, ANSYS FLUENT solves conservation equations for mass and momentum [112]. For flows involving heat transfer or compressibility, an additional equation for energy conservation is solved. For viscous flows this system of equations is called the "complete Navier-Stokes equations system" [113]. For flows involving species mixing or reactions, a species conservation equation is solved or, if the non-premixed combustion model is used, conservation equations for the mixture fraction and its variance are solved. Additional transport equations are also solved when the flow is turbulent.

4.2 Governing differential equations

The differential equations that describe the flow express a conservation principle. Each of them employs a particular physical quality as its dependent variable and implies that there must be a balance among the factors affecting the variables [114]. The dependent variables are usually expressed per unit mass; they are *specific* properties. If φ is a specific property and ρ is the density, then $\rho\varphi$ denotes the amount of the corresponding property contained in a unit volume. Hence the term $\partial(\rho\varphi)/\partial t$ is the rate of change of φ per unit volume [114].

A relevant concept is the net flux per unit volume.

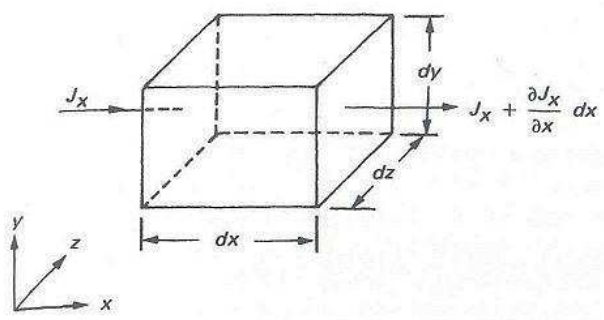

Figure 4.1: Flux balance over a control volume [114]

In Figure 4.1, J denotes a flux influencing a dependent variable φ over a control volume $dxdydz$. The x-direction component of the flux, J_x, is entering through a face of area $dydz$ and the flux is leaving the opposite face, shown as $J_x + \left(\frac{\partial J_x}{\partial x}\right) dx$. Thus, the net flux on the x-direction is $\left(\frac{\partial J_x}{\partial x}\right) dxdydz$.

If all 3 directions are considered then the net flux per unit volume equals

$$\frac{\partial J_x}{\partial x} + \frac{\partial J_y}{\partial y} + \frac{\partial J_z}{\partial z} = \nabla \cdot J \,. \tag{4.1}$$

Another important concept is the divergence of velocity, $\nabla \cdot \vec{V}$, and its physical meaning.

The mass of an infinitesimal control volume moving with the flow (Figure 4.2) is invariant whereas its overall volume and surfaces are changing with time as the element flows through regions of different density, ρ. Thus, this control volume of constant mass is constantly changing its volume and shape, depending on the characteristics of the flow. The divergence of velocity physically expresses the time rate of change of the volume of a moving fluid element, per unit volume [113].

$$\nabla \cdot V = \frac{1}{\delta v} \frac{D(\delta v)}{Dt}, \tag{4.2}$$

where δv is an infinitesimal moving fluid element.

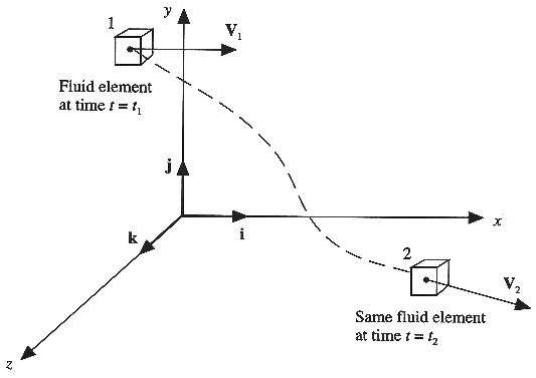

Figure 4.2: Fluid volume element moving with the flow [113]

4.2.1 Continuity equation

The equation for conservation of mass or continuity equation can be written as [112]

$$\frac{\partial \rho}{\partial t} + \nabla \cdot \left(\rho \vec{u} \right) = S_m . \tag{4.3}$$

This can be better understood if S_m is assumed to be zero and the equation is rearranged such as:

$$\frac{\partial \rho}{\partial t} = -\nabla \cdot \left(\rho \vec{u} \right)_m . \tag{4.4}$$

Equation (4.4) suggests that the total mass flow out of a control volume is equal to the time rate of change of the density.

Equation 4.3 is the general form of the mass conservation equation and is valid for incompressible as well as compressible flows. This particular form is the *conservation* form of the mass continuity equation, i.e., the fluid element is stationary and flow passes through

it. The *non-conservation* form (moving fluid element) can be obtained from Eq. 4.1 by indirect manipulation. The source S_m is the mass added to the continuous phase from the dispersed second phase (e.g., due to vaporization of liquid droplets) and any user-defined sources.

For 2D axi-symmetric geometries, the continuity equation is given by [112]:

$$\frac{\partial \rho}{\partial t} + \frac{\partial}{\partial x}(\rho u_x) + \frac{\partial}{\partial r}(\rho u_r) + \frac{\rho u_r}{r} = S_m, \tag{4.5}$$

where x is the axial coordinate; r is the radial coordinate; u_x is the axial velocity component; u_r is the radial velocity component.

4.2.2 Conservation of momentum equation

The conservation of momentum equations stem from the physical principal that

$$F = ma. \tag{4.6}$$

The conservation of momentum in a non-accelerating reference frame is given by [112]:

$$\frac{\partial}{\partial t}(\rho \vec{u}) + \nabla \cdot (\rho \vec{u}\vec{u}) = -\nabla p + \nabla \cdot (\bar{\bar{\tau}}) + \rho \vec{g} + \vec{F}, \tag{4.7}$$

where p is the static pressure; $\bar{\bar{\tau}}$ is the stress tensor; $\rho \vec{g}$ is the gravitational body force; $\vec{F}$ contains the external body forces.

This form of conservation of momentum equation is, again, the conservation form (stationary fluid element); the non conservation form of the equation can be obtained by indirect manipulation. By expanding the divergence terms, one can obtain the general Navier-Stokes equations for each direction expressed in partial derivatives [112]:

$$\frac{\partial(\rho u)}{\partial t}+\nabla\cdot(\rho u\vec{u})=-\frac{\partial p}{\partial x}+\frac{\partial \tau_{xx}}{\partial x}+\frac{\partial \tau_{yx}}{\partial y}+\frac{\partial \tau_{zx}}{\partial z}+\rho fx\,; \tag{4.8}$$

$$\frac{\partial(\rho v)}{\partial t}+\nabla\cdot(\rho v\vec{u})=-\frac{\partial p}{\partial y}+\frac{\partial \tau_{yy}}{\partial y}+\frac{\partial \tau_{xy}}{\partial x}+\frac{\partial \tau_{zy}}{\partial z}+\rho fy\,; \tag{4.9}$$

$$\frac{\partial(\rho w)}{\partial t}+\nabla\cdot(\rho w\vec{u})=-\frac{\partial p}{\partial z}+\frac{\partial \tau_{zz}}{\partial z}+\frac{\partial \tau_{xz}}{\partial x}+\frac{\partial \tau_{yz}}{\partial y}+\rho fz\,, \tag{4.10}$$

where, u, v, w, are the velocity components for the x, y, z, axis respectively; τ_{xx}, τ_{yy}, τ_{zz}, are the components of normal stress for each direction; and, τ_{ij} are the components of the shear stress acting on each direction.

The stress tensor is expressed by [112]:

$$\bar{\bar{\tau}}=\mu\left[\nabla\vec{u}+\nabla\vec{u}^{T}-\frac{2}{3}\nabla\cdot\vec{u}I\right], \tag{4.11}$$

where μ is the molecular viscosity; I is the unit tensor; and the second term on the right hand side is the effect of volume dilation.

For two-dimensional axi-symmetric geometries, the axial and radial equations of momentum conservation are as follows [112]:

$$\begin{aligned}&\frac{\partial}{\partial t}(\rho u_x)+\frac{1}{r}\frac{\partial}{\partial x}(r\rho u_x u_x)+\frac{1}{r}\frac{\partial}{\partial r}(r\rho u_r u_x)=-\frac{\partial p}{\partial x}+\frac{1}{r}\frac{\partial}{\partial x}\left[r\mu\left(2\frac{\partial u_x}{\partial x}-\frac{2}{3}(\nabla\cdot\vec{u})\right)\right]\\&+\frac{1}{r}\frac{\partial}{\partial r}\left[r\mu\left(\frac{\partial u_x}{\partial r}+\frac{\partial u_r}{\partial x}\right)\right]+F_x\end{aligned}\,; \tag{4.12}$$

$$\begin{aligned}&\frac{\partial}{\partial t}(\rho u_r)+\frac{1}{r}\frac{\partial}{\partial x}(r\rho u_x u_r)+\frac{1}{r}\frac{\partial}{\partial r}(r\rho u_r u_r)=-\frac{\partial p}{\partial r}+\frac{1}{r}\frac{\partial}{\partial x}\left[r\mu\left(\frac{\partial u_r}{\partial x}+\frac{\partial u_x}{\partial r}\right)\right]\\&+\frac{1}{r}\frac{\partial}{\partial r}\left[r\mu\left(2\frac{\partial u_r}{\partial r}-\frac{2}{3}(\nabla\cdot\vec{u})\right)\right]-2\mu\frac{u_r}{r^2}+\frac{2}{3}\frac{\mu}{r}(\nabla\cdot\vec{u})+\rho\frac{u_x{}^2}{r}+F_r\end{aligned}\,, \tag{4.13}$$

where

$$\nabla \cdot \vec{u} = \frac{\partial u_x}{\partial x} + \frac{\partial u_r}{\partial r} + \frac{u_r}{r}, \tag{4.14}$$

and u_x is the swirl velocity.

4.2.3 Turbulent flow models

Turbulent flows are characterized by fluctuating velocity fields. These fluctuations mix transported quantities such as momentum, energy, and species concentration, and cause the transported quantities to fluctuate as well. Since these fluctuations can be of small scale and high frequency, they are too computationally expensive to simulate directly in practical engineering calculations. Instead, the instantaneous (exact) governing equations can be time-averaged, ensemble-averaged, or otherwise manipulated to remove the resolution of small scales, resulting in a modified set of equations that are computationally less expensive to solve. However, the modified equations contain additional unknown variables, and turbulence models are needed to determine these variables in terms of known quantities [112].

The following options of turbulent models are available [112]:

- Spalart-Almaras model;
- *k*-*ε* model:
    - Standard *k*-*ε* model;
    - Renormalization-group (RNG) *k*-*ε* model;
    - Realizable *k*-*ε* model;
- *k*-*ω* model:

- Standard k-ω model;
- Shear-stress transport (SST) k-ω model;

- Reynolds Stress Model (RSM):
  - Linear pressure-strain RSM model;
  - Quadratic pressure strain RSM model;
  - Low-Re stress-omega RSM model;
- Detached eddy simulation (DES) model, which includes one of the following RANS models:
  - Spalart-Almaras RANS model;
  - Realizable k-ε RANS model;
  - Shear-stress transport k-ω RANS model;
- Large eddy simulation (LES) model, which includes one of the following sub-scale models:
  - Smagorinsky-Lilly subgrid-scale model;
  - WALE subgrid-scale model;
  - Dynamic Smagorinsky model;
  - Kinetic-energy transport subgrid model.

The Spalart-Almaras is the simplest and less computationally expensive model. Along with the k-ε and k-ω models it follows the Boussinesq hypothesis (Equation 4.15) to simplify the additional terms that need to be included in the Navier-Stokes equations by associating to additional viscous stress (μ_t). The k-ε and k-ω models are two equation models which require some more computational effort as they contain an additional term. The other models are more computationally intensive. The k-ε model is regarded as the most suitable model for the simulations carried out in this project and its theory is outlined below [112]:

$$-\overline{\rho u_i' u_j'} = \mu_t \left(\frac{\partial u_i}{\partial x_j} + \frac{\partial u_j}{\partial x_i} \right) - \frac{2}{3} \left(\rho k + \mu_t \frac{\partial u_k}{\partial x_k} \right) \delta_{ij}, \tag{4.15}$$

where $-\overline{\rho u_i' u_j'}$ are the Reynolds stresses that represent the effects of turbulence.

4.2.3.1 The *k-ε* model

As mentioned previously, there are three available *k* -*ε* models in the 13th version of ANSYS FLUENT: the Standard *k-ε* model, the Renormalization-group (RNG) *k-ε* model and the Realizable *k-ε* model. All three of them are regarded as the "simplest complete" two equation models and use similar transport equations for *k* (kinetic term) and *ε* (eddy dissipation).

The Standard *k-ε* turbulence model

The standard *k-ε* model is a semi-empirical model based on model transport equations for the turbulence kinetic energy, *k*, and its dissipation rate, *ε*. The model transport equation for *k* is derived from the exact equation, while the model transport equation for *ε* is obtained using physical reasoning and bears little resemblance to its mathematically exact counterpart.

In the derivation of the *k-ε* model, the assumption is that the flow is fully turbulent, and the effects of molecular viscosity are negligible. Hence, the standard *k-ε* model is valid only for fully turbulent flows. The transport equations for the standard *k-ε* model are given below [112]:

$$\frac{\partial}{\partial t}(\rho k) + \frac{\partial}{\partial x_i}(\rho k u_i) = \frac{\partial}{\partial x_j}\left[\left(\mu + \frac{\mu_t}{\sigma_k} \right) \frac{\partial k}{\partial x_j} \right] + G_k + G_b + p\varepsilon - Y_M + S_k, \tag{4.16}$$

and

$$\frac{\partial}{\partial t}(\rho\varepsilon)+\frac{\partial}{\partial x_i}(\rho\varepsilon u_i)=\left(\mu+\frac{\mu_t}{\sigma_\varepsilon}\right)\frac{\partial\varepsilon}{\partial x_j}+C_{1\varepsilon}\frac{\varepsilon}{k}(G_k+C_{3\varepsilon}G_b)-C_{2\varepsilon}\rho\frac{\varepsilon^2}{k}+S_\varepsilon, \qquad (4.17)$$

where G_k represents the generation of turbulent kinetic energy due to the mean velocity gradients; G_b is the generation of kinetic energy due to buoyancy; Y_M represents the contribution of the fluctuating dilatation in compressible turbulence to the overall dissipation rate; $C_{1\varepsilon}$, $C_{2\varepsilon}$, $C_{3\varepsilon}$ are constants; σ_k and σ_ε are the turbulent Prandtl numbers for k and ε respectively; S_ε and S_k are user-defined source terms.

The turbulent (or eddy) viscosity, μ_t, is computed by combining k and ε as follows [112]:

$$\mu_t=\rho C_\mu\frac{k^2}{\varepsilon}. \qquad (4.18)$$

The model constants, $C_{1\varepsilon}$, $C_{2\varepsilon}$, C_μ σ_k, σ_ε have the following default values [112]:

$C_1 = 1.44$, $C_{2\varepsilon} = 1.92$, $C_\mu = 0.09$, $\sigma_k = 1$, $\sigma_\varepsilon = 1.3$

The RNG *k-ε* model

The RNG *k-ε* model was derived using a rigorous statistical technique (renormalization group theory). It is similar to the standard *k-ε* model, but includes the following refinements [112]:

- It has an additional term in its ε equation that significantly improves the accuracy for rapidly strained flows;
- The effect of swirl on turbulence is included in the RNG model, enhancing accuracy for swirling flows;

- The RNG theory provides an analytical formula for turbulent Prandlt numbers, while the standard *k*-*ε* model uses user-specified constant values;

- The RNG *k*-*ε* model provides an analytically-derived formula for effective viscosity that accounts for low-Reynolds-number effects; this however requires appropriate near-wall treatment.

The RNG *k*-*ε* model has a similar form to the standard *k*-*ε* model [112]:

$$\frac{\partial}{\partial t}(\rho k)+\frac{\partial}{\partial x_i}(\rho k u_i)=\frac{\partial}{\partial x_j}\left[a_k \mu_{\text{eff}} \frac{\partial k}{\partial x_j}\right] \quad G_k \quad G_b \quad p\varepsilon \quad Y_M \quad S_k, \tag{4.19}$$

and

$$\frac{\partial}{\partial t}(\rho \varepsilon)+\frac{\partial}{\partial x_i}(\rho \varepsilon u_i)=\alpha_\varepsilon \mu_{\text{eff}} \frac{\partial \varepsilon}{\partial x_j}+C_{1\varepsilon}\frac{\varepsilon}{k}(G_k+C_{3\varepsilon}G_b)-C_{2\varepsilon}\rho\frac{\varepsilon^2}{k}-R_\varepsilon+S_\varepsilon. \tag{4.20}$$

The scale elimination procedure in the RNG theory results in a differential equation for turbulent viscosity:

$$d\left(\frac{\rho^2}{\sqrt{\varepsilon\mu}}\right)=1.72\frac{\hat{\nu}}{\sqrt{\hat{\nu}^3-1+C_{\text{v}}}}d\hat{\nu}, \tag{4.21}$$

where:

$$\hat{\nu}=\mu_{\text{eff}}/\mu; \tag{4.22}$$

$$C_{\text{v}} \approx 100.$$

The above equations can express how the turbulent transport varies with the effective Reynolds number, allowing the model to better handle low-Reynolds-number and near-wall flows.

In the high-Reynolds-number limit, Equation (4.21) gives:

$$\mu_t = \rho C_\mu \frac{k^2}{\varepsilon}, \tag{4.23}$$

where C_μ = 0.0845, derived using RNG theory; a value very close to the empirically-determined 0.09 used in the standard k-ε model.

The RNG k-ε model provides an option to account for the effects of swirl or rotation by modifying the turbulent viscosity appropriately. The modification takes the functional form below:

$$\mu_t = \mu_{t0} f\left(a_{sw}, \Omega, \frac{k}{\varepsilon}\right), \tag{4.24}$$

where μ_{t0} is the value of turbulent viscosity calculated without the swirl modification using either of Equations (4.22, 4.23); Ω is a characteristic swirl number evaluated within ANSYS FLUENT; α_{sw} is a swirl constant that takes different values according to whether the flow is swirl-dominated or mildly swirling.

The inverse Prandlt numbers, α_k and α_ε, are calculated using the following expression which is derived analytically from the RNG theory:

$$\left|\frac{a-1.3929}{a_0-1.3929}\right|^{0.6321}\left|\frac{a+2.3929}{a_0+2.3929}\right|^{0.3679} = \frac{\mu_{\text{mol}}}{\mu_{\text{eff}}}, \tag{4.25}$$

where $\alpha_0 = 1$; $\alpha_k = \alpha_\varepsilon \approx 1.393$ in the high-Reynolds-number limit ($\mu_{\text{mol}}/\mu_{\text{eff}} << 1$).

The additional term, R_ε, in the ε equation is given by:

$$R_\varepsilon = \frac{C_\mu \rho \eta^3 \left(1 - \eta/\eta_0\right)}{1 + \beta \eta^3} \frac{\varepsilon^2}{k}, \tag{4.26}$$

where $\eta \equiv Sk/\varepsilon$; $\eta_0 = 4.38$; $\beta = 0.012$.

Finally, the model constants $C_{1\varepsilon}$ αnd $C_{2\varepsilon}$ are derived analytically by the RNG theory and in ANSYS FLUENT are:

$$C_{1\varepsilon} = 1.42,\ C_{2\varepsilon} = 1.68.$$

The Realizable *k-ε* model

The Standard *k-ε* model and the Renormalization-group (RNG) *k-ε* model use an empirical and a statistical approach respectively, which is less realistic. The Realizable *k-ε* model uses a new formulation for the turbulent viscosity and a new transport equation for the dissipation rate, *ε*, which has been derived from an exact equation of the mean-square vorticity fluctuation. These qualities of the Realizable *k-ε* model have made it a preferable choice in industrial flow and heat transfer problems. The *k* and *ε* transport equations for the Realizable *k-ε* model are presented below.

$$\frac{\partial}{\partial t}(\rho k) + \frac{\partial}{\partial x_j}(\rho k u_j) = \frac{\partial}{\partial x_j}\left[\left(\mu + \frac{\mu_t}{\sigma_k}\right)\frac{\partial k}{\partial x_j}\right] + G_k + G_b - \rho\varepsilon - Y_M + S_k; \tag{4.27}$$

$$\frac{\partial}{\partial t}(\rho \varepsilon) + \frac{\partial}{\partial x_j}(\rho \varepsilon u_j) = \frac{\partial}{\partial x_j}\left[\left(\mu + \frac{\mu_t}{\sigma\varepsilon}\right)\frac{\partial \varepsilon}{\partial x_j}\right] + \rho C_1 S_\varepsilon - \rho C_2 \frac{\varepsilon^2}{k + \sqrt{\nu\varepsilon}} + C_{1\varepsilon}\frac{\varepsilon}{k} C_{3\varepsilon} G_b + S_\varepsilon, \tag{4.28}$$

where G_k is the generation of turbulent kinetic energy due to mean velocity gradient; G_b is the generation of turbulent kinetic energy due to buoyancy;

$$C_1 = \max\left[0.43, \frac{n}{n+5}\right], \tag{4.29}$$

$$n = S\frac{k}{\varepsilon}, \tag{4.30}$$

where S is the modulus of the mean rate stress tensor:

$$S = \sqrt{2S_{ij}S_{ij}}\ ; \tag{4.31}$$

$$\mu_t = \rho C_\mu \frac{k^2}{\varepsilon}; \tag{4.32}$$

$$C_\mu = \frac{1}{A_0 + A_s\dfrac{kU^*}{\varepsilon}}. \tag{4.33}$$

4.2.4 Energy conservation equation

The conservation of energy is given by [112]:

$$\frac{\partial}{\partial t}(\rho E) + \nabla\cdot(\vec{u}(\rho E + p)) = -\nabla\cdot\left(k_{\text{eff}}\nabla T - \sum_j h_j\vec{j}_j + (\overline{\overline{\tau}}_{eff}\cdot\vec{u})\right) + S_h. \tag{4.34}$$

In Equation (4.34):

k_{eff} is the effective thermal conductivity which includes turbulent thermal conductivity defined by the selected turbulent model; $\vec{j}_j$ is the diffusion flux of species j and S_h includes heat from reaction and any other volumetric heat sources defined by the user. The first three terms of the right hand side represent conductive heat, species diffusion and viscous dissipation, respectively.

$$E = h - \frac{p}{\rho} - \frac{u^2}{2}, \tag{4.35}$$

where sensible enthalpy is defined for ideal gases as:

$$h = \sum_j Y_j h_j , \tag{4.36}$$

and for incompressible flows as:

$$h = \sum_j Y_j h_j + \frac{p}{\rho} . \tag{4.37}$$

In equations (4.36) and (4.37), Y_j is the mass fraction of species j and

$$h_j = \int_{T_{\text{ref}}}^{T} Cpj dT , \tag{4.38}$$

where T_{ref} is 298.15K.

4.2.5 Porous media conditions

The porous media model can be used for a wide variety of single phase and multiphase problems. When this model is used, the definition of a cell zone in which the porous media model is applied is required and the pressure loss in the flow is determined by the user's inputs as described in subsection 4.1.5.2. Heat transfer through the medium can also be represented, subject to the assumption of thermal equilibrium between the medium and the fluid flow as described in subsection 4.5.1.3.

4.2.5.1 Limitations and assumptions of the Porous Media model

The porous media model incorporates an empirically determined flow resistance in the region of the model defined as "porous". Essentially, this model is an added momentum sink in the governing momentum equations. Hence the following modelling assumptions and limitations must be recognised [112, 115]:

- The volume blockage that is physically present is not represented in the model. Thus, by default ANSYS FLUENT uses and reports a superficial velocity inside the porous medium, based on the volumetric flow rate, to ensure continuity of the velocity vectors across the porous medium interface. As a more accurate alternative the user can instruct ANSYS FLUENT to use the true (physical) velocity inside the porous medium;
- the effect of the porous medium on the turbulence field is only approximated;
- the ANSYS FLUENT porous medium model generally assumes the porosity is isotropic and it can vary with space and time;
- the interactions between a porous medium and shock waves are not considered.

4.2.5.2 Momentum equations for Porous Media

Porous media are modelled by the addition of a momentum source term to the standard fluid flow equations. The source term is composed of two parts: a viscous loss term (Darcy, the first term on the RHS of Equation 4.39), and an inertial loss term (the second term on the RHS of Equation 4.39).

$$S_i = \left(+ \sum_{j=1}^{3} D_{ij} \mu u_j \quad \sum_{j=1}^{3} C_{ij} \frac{1}{2} \rho |v| v_j \right), \tag{4.39}$$

where S_i is the source term for the i^{th} (x, y or z) momentum equation; $|\upsilon|$ is magnitude of the velocity; D and C are prescribed matrices.

This momentum sink contributes to the pressure gradient in the porous cell, creating a pressure drop that is proportional to the squared velocity in the cell.

For the case of simple homogenous porous media:

$$S_i = \left(+ \frac{\mu}{\alpha_{\mathrm{p}}} \upsilon_i \quad C_2 \frac{1}{2} \rho |\upsilon| \upsilon_i \right), \tag{4.40}$$

where α_{p} is permeability; C_2 is the inertial resistance factor.

4.2.5.3 Treatment of the energy equation in Porous Media

ANSYS FLUENT solves the standard energy transport equation in porous media regions with modifications to the conduction flux and the transient terms only. In the porous medium, the conduction flux uses an effective conductivity and the transient term included the thermal inertia of the solid region of the medium. The equation of energy in porous medium is [112]:

$$\frac{\partial}{\partial t}\left(\gamma \rho_f E_f + (1-\zeta)\rho_s E_s\right) + \nabla \cdot \left(\vec{\upsilon}\left(\rho_f E_f + p\right)\right) = \nabla \cdot \left[k_{\mathrm{eff}} \nabla T - \left(\sum_i h_i J_i \right) + \left(\overline{\overline{\tau}} \cdot \vec{\upsilon} \right) \right] + S_f^h, \tag{4.41}$$

where E_f is the total fluid energy; E_s is the total solid medium energy; ζ is the porosity of the medium; k_{eff} is the effective thermal conductivity of the medium; S_f^h is the fluid enthalpy source term.

The effective thermal conductivity of the medium, k_{eff}, is calculated by ANSYS FLUENT as the volume average of the fluid conductivity and the solid conductivity:

$$k_{\mathrm{eff}} = \zeta k_f + (1-\zeta) k_s, \tag{4.42}$$

where k_f is the fluid phase thermal conductivity (including the turbulent contribution, k_t); k_s is the solid medium thermal conductivity.

4.3 Dynamic mesh theory

ANSYS FLUENT allows transient simulations to be carried out by updating the position of moving boundaries at each time step. To use the dynamic mesh model, the user needs to provide the initial volume mesh and specify the motion of the moving zones in the model. The motion can be described either by using boundary profiles, user-defined functions (UDFs), or the Six Degree of Freedom Solver (6DOF) [112].

Three groups of mesh motion methods are available in ANSYS FLUENT to update volume mesh in the deforming regions subject to the motion defined at the boundaries:

- smoothing methods;
- dynamic layering;
- local remeshing methods.

4.3.1 Spring based smoothing method

In the spring-based smoothing method, the edges between any two mesh nodes are idealized as a network of interconnected springs. The initial spacing of the edges before any boundary motion constitutes the equilibrium state of the mesh. A displacement at a given boundary node will generate a force proportional to the displacement along all the springs connected to the node. Applying Hooke's Law, the force on a mesh node can be expressed as [112]:

$$\vec{F}_i = \sum_j^{n_i} k_{ij} \left(\Delta \vec{x}_j - \Delta \vec{x}_i \right), \tag{4.43}$$

where $\Delta \vec{x}_i$ and $\Delta \vec{x}_j$ are the displacements of node *i* and its neighbour, *j*; n_i is the number of neighbouring nodes connected to node *i*; K_{ij} is the spring constant (stiffness) between node *i* and its neighbour, *j*.

The spring constant for the edge connecting nodes *i* and *j* is defined as:

$$k_{ij} = \frac{1}{\sqrt{\left|\vec{x}_i - \vec{x}_j\right|}}. \tag{4.44}$$

At equilibrium, the net force on a node due to all the springs connected to the node must be zero. This condition results in an iterative equation such that

$$\Delta\vec{x}_i^{m+1} = \frac{\sum_j^{n_i} k_{ij}\Delta\vec{x}_j^m}{\sum_j^{n_i} k_{ij}}. \tag{4.45}$$

After boundary node positions have been updated and displacements are known, Equation (4.45) is solved using a Jacobi sweep on all interior nodes. At convergence, the positions are updated such as that

$$\vec{x}_i^{n+1} = \vec{x}_i^n + \delta\vec{x}_i^{m,\,\text{converged}}, \tag{4.46}$$

where $n+1$ and n denote the node positions at the next and current time steps, respectively.

4.3.2 Boundary layer smoothing method

The boundary layer smoothing method is used to deform the boundary layer during a deforming-moving mesh simulation. For models that have a mesh-motion UDF applied to a face zone with adjacent boundary layers, the boundary layer will deform according to the UDF while preserving the cell height of each boundary layer. This method can be applied to all types of mesh [112].

4.3.3 Dynamic layering method

Dynamic layering can be used to add or remove layers of cells adjacent to moving boundaries, based on the height of the layer adjacent to the moving surface. The layer of the cells adjacent to the moving boundary (layer *j* in Figure 4.3) is split or merged with the layer of cells next to it (layer *i* in Figure) based on the height, (*h*), of cells in layer *j*.

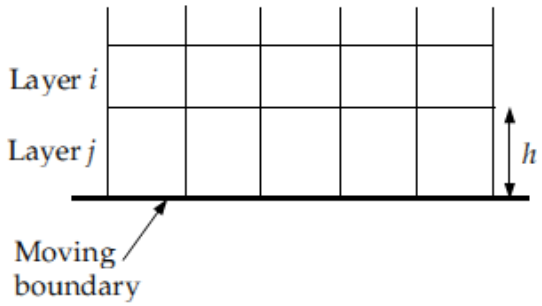

Figure 4.3: Dynamic layering [112]

If the cells in layer *j* are expanding, the cell height is allowed to increase until:

$$h_{\min} > (1 + a_s) h_{\text{ideal}}, \tag{4.47}$$

where $h_{\min}$ is the minimum cell height of cell layer *j*; h_{ideal} is the ideal cell height; α_s is the layer split factor.

h_{ideal} can be defined either as a constant value or a value that varies as a function of time or crank shaft angle.

If the cells in layer *j* are being compressed, they can be compressed until:

$$h_{\min} > a_c h_{\text{ideal}}, \tag{4.48}$$

where α_c is the ideal layer collapse factor.

When the above condition is met, the compressed layer of cell is merged into the layer of cells above it; i.e., the cells in layer *j* are merged with those in layer *i*.

4.3.4 Remeshing methods

On zones with triangular or tetrahedral meshes, the spring-meshed smoothing method is normally used. When the boundary displacement is large compared to the local cell sizes, the cell quality can deteriorate or the cells can become degenerate. This will invalidate the mesh (i.e., negative volume cells) and, consequently, lead to convergence problems when the solution is updated to the next time step. Thus, careful definition of the time step size is required in addition to quality mesh creation. To tackle this issue, ANSYS FLUENT agglomerates cells that violate the skewness or size criteria and locally remeshes the agglomerated cells or faces. If the new cells or faces satisfy the skewness and quality criteria, the mesh is locally updated with the new cells. Otherwise, the new cells are discarded.

ANSYS FLUENT includes several remeshing methods that include local remeshing, local face remeshing (limited to 3D flows), face region remeshing, and 2.5D surface remeshing (limited to 3D flows). Those methods apply for triangular-tetrahedral zones and mixed zones where the non-triangular/ tetrahedral elements are skipped.

4.3.4.1 Local remeshing method

Using the local remeshing method, ANSYS FLUENT marks cells based on cell skewness value and minimum and maximum length scales as well as an optional sizing function. The software evaluates each cell and marks it for remeshing if it meets one or more of the criteria below:

- It has skewness that is greater than a specified maximum skewness;
- It is smaller/ larger than a specified minimum/ maximum scale;
- Its height does not meet the specified length scale.

4.3.4.2 Local face remeshing method

The local face remeshing method only applies to 3D geometries. ANSYS FLUENT marks the faces (and adjacent cells) on the deforming boundaries based on face skewness. With this method ANSYS FLUENT is able to remesh locally at deforming boundaries, however, it is not possible to remesh across multiple face zones.

4.4 In-Cylinder utility

ANSYS FLUENT provides a specialised tool for piston-engines applications in the dynamic mesh menu, the In-Cylinder option. The user is required to define the crank shaft speed, the starting crank shaft angle and the crank period which are used to convert between crank shaft angle and flow time. Additionally, the specification of the time step is required at this stage. The software then uses a built-in function to calculate the location of the piston as a function of crank shaft angle. This function requires the specification of piston stroke and connecting rod length. The piston location is calculated by [112, 115].

$$p_l = L + \frac{A_{\text{str}}}{2}\left(1-\cos\left(\varphi_{\text{c}}\right)\right) - \sqrt{L^2 - \frac{A_{\text{str}}^2}{4}\sin^2\left(\varphi_{\text{c}}\right)}\,, \tag{4.49}$$

where p_{st} is the piston location (0 at top-dead-centre (TDC) and A_{str} at bottom-dead-centre (BDC)); L is the connecting rod length; A_{str} is the piston stroke; φ_{c} is the current crank shaft angle.

The current crank shaft angle is calculated using

$$\varphi_c = \varphi_s + t\Omega_{shaft}, \tag{4.50}$$

where φ_s is the starting crank shaft angle and Ω_{shaft} is the crank shaft speed.

The Piston Stroke Cutoff is used to control the actual values of the piston stroke Cutoff such that

$$p_{sc} = \min\left(p_s^c, p_s^{\min}\right), \tag{4.51}$$

where p_s^c is the stroke calculated from Equation (4.49); $p_s^{\min}$ is the piston stroke Cutoff.

4.5 Discretization methods

"Discretization is the process by which a closed-form mathematical expression, such as a function or a differential or integral equation involving functions, all of which have a continuum of values throughout a domain, is approximated by analogous (but different) expressions which prescribe values at only a finite number of discrete points or volumes in the domain" [113].

There are several ways to obtain the discretized equations and those will not necessarily be unique. Those equations are expected to give the same results over a large number of grid-points; what is different is the profiles used to obtain these equations [114].

There are 3 general discretization methodologies which differ in the selection of profiles and the methods of derivation. These methods are namely the *finite-difference* method, the *finite-element* method, and the *finite-volume* method.

4.5.1 The finite-difference method

This method uses Taylor expansion series to approximate the derivatives with difference terms. Hence, for a grid like Figure 4.4 with points 1, 2, 3 such that $\Delta x=x_2-x_1 = x_3-x_2$ [114],

$$\varphi_1 = \varphi_2 - \Delta x\left(\frac{d\varphi}{dx}\right)_2 + \frac{1}{2}(\Delta x)^2\left(\frac{d^2\varphi}{dx}\right)_2 - \ldots, \tag{4.52}$$

and

$$\varphi_3 = \varphi_2 + \Delta x\left(\frac{d\varphi}{dx}\right)_2 + \frac{1}{2}(\Delta x)^2\left(\frac{d^2\varphi}{dx}\right)_2 - \ldots. \tag{4.53}$$

After manipulation [114],

$$\left(\frac{d\varphi}{dx}\right)_2 = \frac{\varphi_3 - \varphi_1}{2\Delta x}, \tag{4.54}$$

and

$$\left(\frac{d^2\varphi}{dx}\right)_2 = \frac{\varphi_1 + \varphi_3 - 2\varphi_2}{2\Delta x}. \tag{4.55}$$

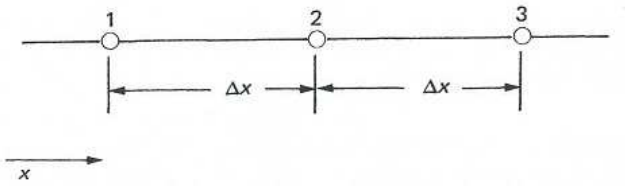

Figure 4.4: Successive gird points used in the Taylor-series expansion for the FDM [114]

4.5.2 The finite-element method

The finite element method for obtaining the discretization equations is based on the calculus of variations. As described in [116], a very common variation of the FEM is the Galerkin version based on weighted residuals. Considering the governing equation [116]:

$$\Gamma \frac{d^2\varphi}{dx^2} + S_\varphi = 0, \tag{4.56}$$

in non-conservation form, the computational domain is subdivided in N-1 elements corresponding to N nodes. $\bar{\varphi}$ denotes an approximation to φ and therefore there will be a residual R expressed as [116]:

$$R = \frac{d^2\bar{\varphi}}{dx^2} + S_\varphi . \tag{4.57}$$

The method calculates φ so that:

$$\int_{domain} W_j R dx = 0 . \tag{4.58}$$

The variation of $\bar{\varphi}$ is defined by a shape function, Nj(x). The Galerkin method requires that the weight functions are zero in the vicinity of each node of interest and non-zero everywhere else. Additionally, the weight function must equal the shape function. This method is popular with stress analysis. Its algebraic complexity and limited applicability make it less suitable for CFD applications [116].

4.5.3 The finite-volume method

The finite volume method is derived by splitting the calculation domain into sub-domains and setting $W = 1$ for each finite volume of interest and $W = 0$ for all the rest at a time. The

control volume variation of the weighted residuals method implies that the integral of the residual on each control volume must become zero [114]. The domain is sub-divided into non-overlapping control volumes in such way that the each control volume contains one grid point and the differential equation is integrated over each control volume. The variation of φ between each grid point is expressed by piecewise polynomials. As a result, the discretization equation contains the values of φ for a group of grid points. This equation expresses the conservation principal of φ for the finite control volume.

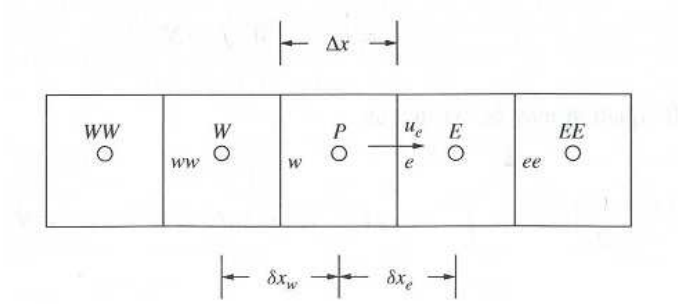

Figure 4.5: Arrangement of control volumes [116]

Figure 4.5 shows an arrangement of control volumes. Discrete values of the dependent variable φ are stored in the cell centroids denoted by W, P, and E. The cell faces are denoted by w and e and the face areas are assumed to be unity. Converting the governing equation in conservation form and integrating over the cell P yields [116]:

$$\int_w^e \frac{d}{dx}\left(\Gamma\frac{d\varphi}{dx}\right)+\int_w^e S dx = 0\,, \tag{4.59}$$

and after integration [116]:

$$\left(\Gamma\frac{d\varphi}{dx}\right)_e-\left(\Gamma\frac{d\varphi}{dx}\right)_w+\int_w^e S dx = 0\,. \tag{4.60}$$

Then, φ is assumed to vary in a piecewise linear fashion between cell centroids [116],

$$\frac{\Gamma_e(\varphi_E - \varphi_P)}{\delta x_e} - \frac{\Gamma_w(\varphi_P - \varphi_W)}{\delta x_w} + \overline{S}\Delta x = 0\,, \tag{4.61}$$

where $\overline{S}$ is an average value of S in the control volume.

Rearranging, eq (4.61) becomes [116]:

$$a_P\varphi_P = a_E\varphi_E + a_W\varphi_W + b\,, \tag{4.62}$$

where

$$a_E = \frac{\Gamma_e}{\delta x_e}; \tag{4.63}$$

$$a_W = \frac{\Gamma_w}{\delta x_w}; \tag{4.64}$$

$$a_P = a_E + a_W; \tag{4.65}$$

$$b = \overline{S}\Delta x\,. \tag{4.66}$$

Equations similar to Equation (4.63) above may be formulated for all cells of the domain, providing a set of algebraic equations that can be solved directly or iteratively. The FVM discretization method, unlike the FDM and FEM, applies the principle of conservation over the cell. The calculated cell values of φ satisfy this conservation statement [116].

4.6 CFD Solution outline

The solution of CFD problems involving the use of a particular software like ANSYS package, involves the following main steps [117]:

1. The computational domain is defined and the computational grid (mesh) is generated; the domain is subdivided into many smaller elements called cells. For 2D problems the cells are areas whereas for 3D the cells are volumes. Each cell is a control volume for which the discretized governing equations are solved. The quality of the computational grid is important. Figure 4.6 presents an illustration of two types of grid.
2. Boundary conditions are specified on each edge of the computational domain (2D problems) or face (3D problems).
3. The type of fluid is specified, along with its properties. Most CFD packages have built-in materials databases.
4. Numerical parameters and solution algorithms and calculation schemes are selected.
5. The solution is initialized by assigning starting values for all flow field variables for each cell. These values may not necessarily be correct but are required as a starting point for the iterative solution. For transient state calculations it is useful to provide as accurate initial conditions as possible to achieve faster convergence and a reliable solution. These conditions may come from previous experimental data or other mathematical models.
6. Beginning with initial guess values, the discretized governing equations are solved iteratively. The solution is considered converged when then a term called the residual is as close to zero as possible. The residual of a scalar variable φ is defined as the imbalance in the scalar transport equation, weighted for all cells. Practically, however, there is no universal metric for convergence and the user must specify particular criteria which vary for different problems. As a rule of thumb, a quantity of interest is selected for monitoring during the solution; when the solution is converged the value of this quantity should settle to some realistic constant value along with a small value for the residuals. For time-dependent calculations, this procedure is looped for each time step.

7. Once the solution has been established, flow field variables of interest are plotted and analyzed graphically. The user can provide algebraic relations to evaluate custom functions formed by flow field variables. For time-dependent solutions the user may choose to output data at each time step in order to post-process and evaluate results over a certain time period.

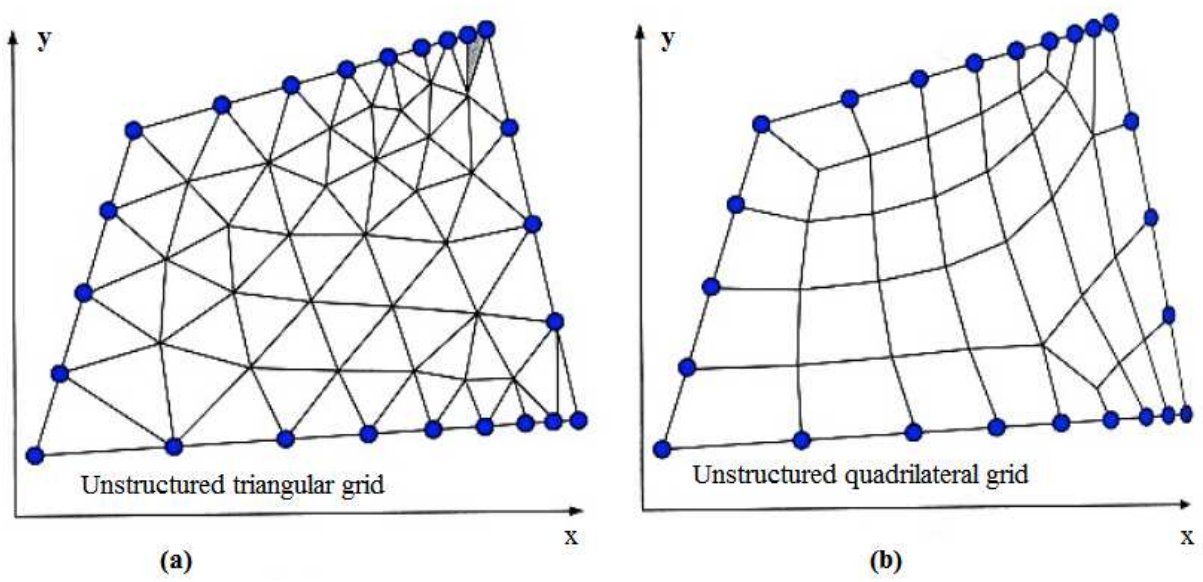

Figure 4.6: Types of computational grids: (a) Unstructured triangular grid; (b) Unstructured quadrilateral grid [117]

Chapter 5 Thermodynamic Modelling and Design Optimization of an α-type Solar Stirling Engine

5.1 Introduction

This chapter presents the results of the second order mathematical model and design optimization of an α-type solar Stirling engine. This model was developed by Kraitong in [2] and is an enhanced revision of the ODE modelling formulation introduced by [14] and developed in further publications like [23, 24, 61]. This particular model incorporates a number of different mathematical expressions for the calculation of heat transfer and friction coefficients for each heat exchanger component and can be coupled to the GA optimization technique introduced in [2]. The optimization was carried out by implementation of the GA technique presented in [2] and the optimized engine parameters were compared against those obtained by parametric analysis using the mathematical model and validated. The first section describes the results obtained by the second order numerical simulation developed in [2] for the Solar Stirling engine described in section 4.1. The characteristics of the working process are described in detail. The second section presents the results of the GA optimization technique. The rational optimized engine parameters are discussed along with their validation - comparison against a parametric study using the numerical model.

5.2 Description of the solar Stirling engine under investigation

Figure 5.1 shows a schematic illustration of a solar power plant which was developed at the Physical and Technical Institute in Tashkent. The plant consists of a solar concentrator and the 1 kW_e Stirling Engine. The metallic base of the contractor is of a parabolic form with a focal path of 3.5 m and 89 separate quadratic spherical mirrors of 0.5 m x 0.5 m are installed on it. A tracking mechanism enables the concentrator to follow the position of the sun.

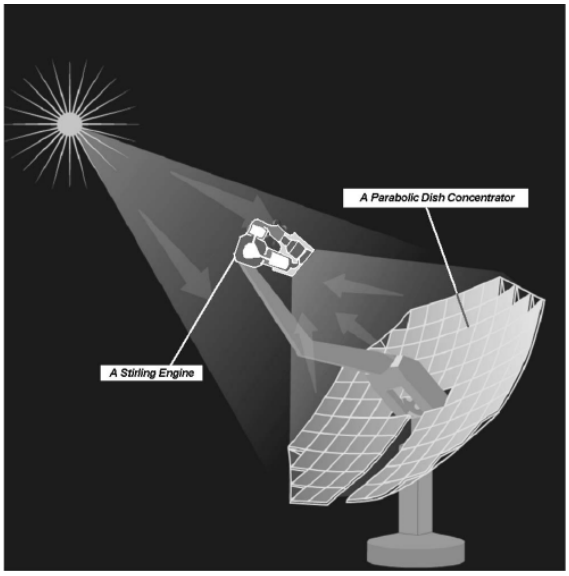

Figure 5.1: Schematic diagram of a 1kW_e Dish/ Stirling engine solar power plant [46]

Figure 5.2 shows a schematic design of the 1 kW_e Stirling Engine installed on the solar power plant. The engine is of the *α*-type configuration and consists of cylinders for the expansion (*16*) and compression (*10*) spaces which are installed on a pressurized crankcase (11) which contains a conventional crank mechanism. The two cylinders are arranged in a "V" configuration at an angle of 90º between them with the hot piston leading the cold piston. The engine has a cylindrical cavity - type heater (*3*) and the surface (*1*) of the cavity receives the heat input due to insolation from the concentrator. In order to improve the temperature

distribution on the surface of the cavity, it is fully covered by a 5 mm layer of stainless steel wire mesh. The regenerator (*4*) of the machine is cylindrical in shape and is filled with mesh gauzes which have been manufactured from stainless steel. The cooler (*7*) was made by a bank of tubes. The water jacket of the cylinder and the cooler are connected by the tubes (*5, 6*) of the cooling system. To reduce heat losses, the heater, regenerator and the upper part of the expansion cylinder (*17*) are surrounded by thermal insulation (*2, 15*). The piston of the expansion space (*14*) and the piston of the compression space (*9*) have guiding and sealing rings which are made from a fluoroplastic type of material. The drive mechanism shaft has a sealing brush made from the same material at the exit from the crankcase and the fly-wheel set on the nozzle of the shaft. Rolling bearings are used in the ends of the connecting rods (*12, 13*) and in the bearings of the crank mechanism. The working gas of the engine is helium and an external belt-driven alternator acts as a loading device. The displaced volume is 250 cc and the engine speed is 1200 rpm. More detailed specifications of the engine can be found in Table 5.1.

Table 5.1: Specifications of the Stirling engine [18]

Working fluid	Helium
Maximum working fluid pressure	41.77 bar
Frequency	20 Hz
Diameter of hot and cold cylinders	0.095 m
Stroke of the pistons	0.033 m
Diameter / width of the flywheel	22.3 m / 0.04 m
Length of connecting rods	0.165 m
Minimum volume of crankcase	0.004 m^3

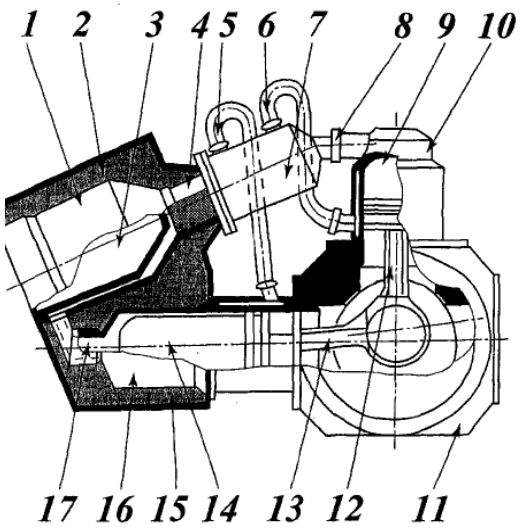

Figure 5.2: Sketch of the α-type Stirling engine. 1. The external surface of the heat receiver; 2. the thermal insulation; 3. the cavity of the heat receiver; 4. the regenerator; 5, 6. the tubes of the cooling system; 7. the cooler; 8. the joint between the cooler and the "cold" cylinder; 9. the piston in the compression space; 10. the cylinder of the compression space; 11. the engine case; 12, 13. the connecting rod; 14. the piston in the expansion space; 15. the thermal insulation; 16. the cylinder of the expansion space; 17. the joint between the "hot" cylinder and the heater [18]

5.3 Results obtained using the second-order mathematical model

Analytical results for the particular *α*-type solar Stirling engine were obtained by simulating the working process of the engine in [18]. For the current investigation, the model developed by Kraitong [2] was used. The geometry and specifications of the engine were presented in section 5.1. For the hot side of the engine, namely the heat input to the heater, a constant temperature boundary condition was used, similar to [118]. The heater temperature was specified at 1000 K. The thermal conductivity of steel was set to 27.5 W/mK which is the average thermal conductivity of steel between the two temperature limits of the engine. Similarly, the operation of the cooling heat exchanger was described by a constant temperature specification of 333 K. The working medium was helium and the regenerator matrix was made of steel with a porosity of 70% and a wire diameter of 0.0003 m. The engine ran at the speed of 1200 rpm (20 Hz).

5.3.1 Analysis of the working process

The operation of the engine is described in terms of volume, pressure and temperature variations which are presented in graphical form in addition to indicated power output predictions. The volume variations in the expansion and compression spaces are shown in Figure 5.3 as a function of the crank shaft angle. It can be seen that the 2 curves are of sinusoidal form and are in a 90 degree phase shift. The volume of the compression space, Vc, is calculated by the swept volume of the cold piston with addition of the dead volume of the cooler-connector pipe. Respectively, the dead volume of the heater-connector pipe is added to the swept volume of the hot piston for the calculation of the volume of the expansion space, Ve. A volume ratio of 2 was calculated.

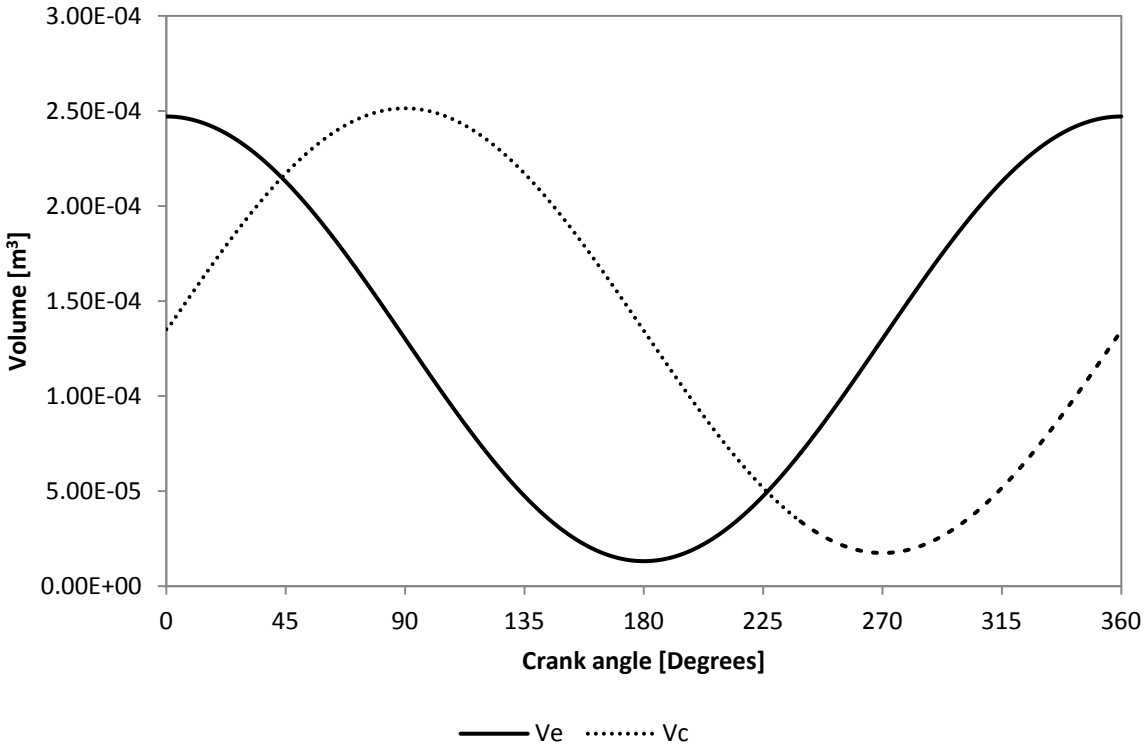

Figure 5.3: Volume variation of compression and expansion spaces

Figure 5.4 presents the variation of pressure inside the engine versus the crank shaft angle. The maximum pressure over the cycle is 41 bar at a crank shaft angle of 250º degrees. The minimum pressure is 19 bar at an angle of 55 degrees. The pressure ratio over the cycle is 2. It can be seen that the pressure is higher in the cold space and lower in the hot space. This is due to the pressure drop inside the heater and the regenerator and is represented graphically in Figure 5.5. The pressure drop in the heater is attributed to the geometry of the annular gap with a hydraulic diameter of 3 mm and the attributed friction losses. It should be noted however that the mathematical model predicted a significant amount of pressure drop in the regenerator which is due to hydraulic resistance losses attributed to the porosity of the matrix.

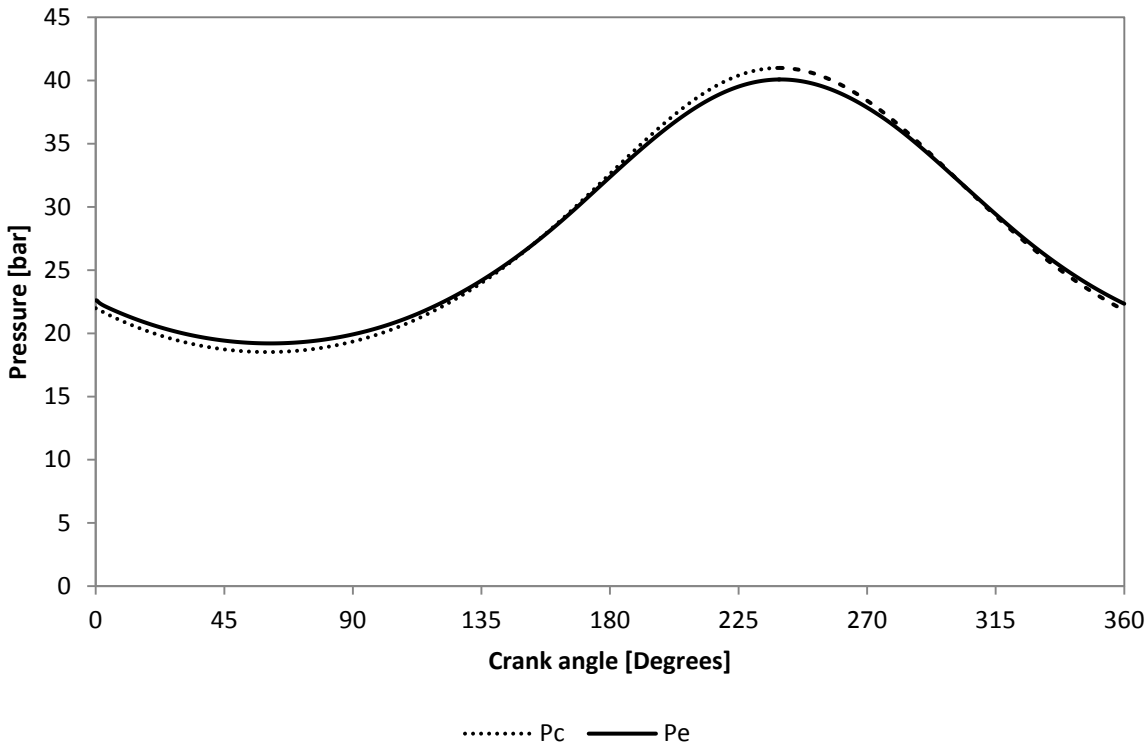

Figure 5.4: Variation of pressure inside the engine

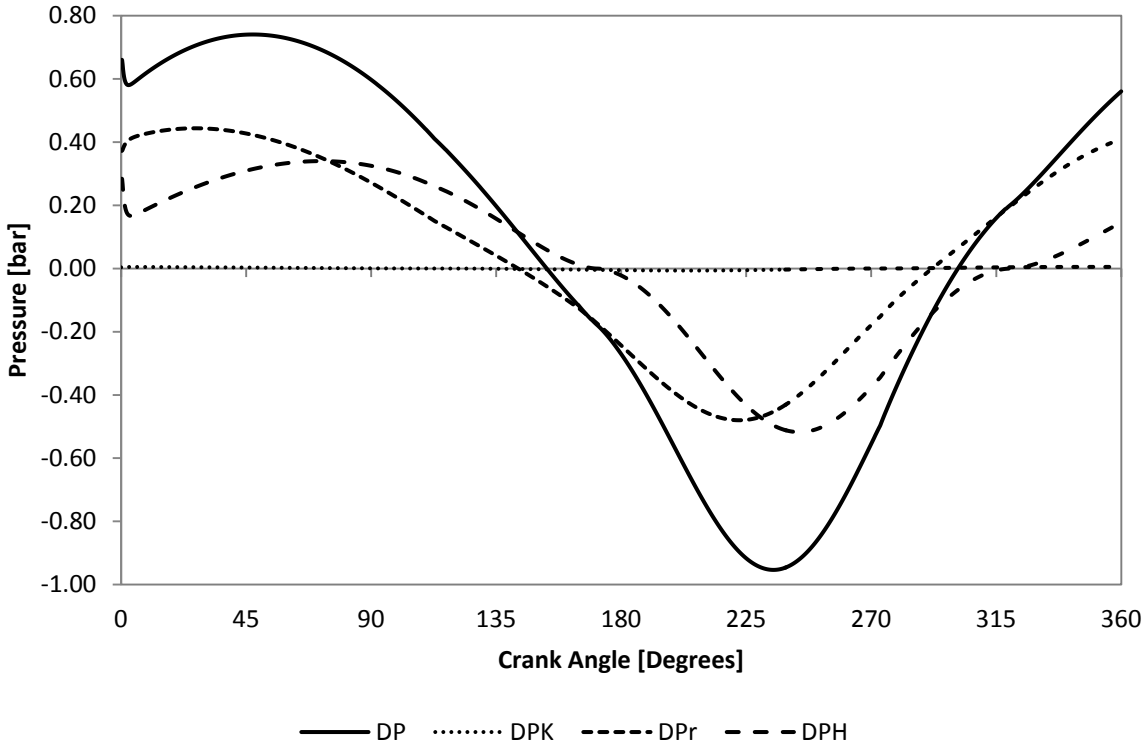

Figure 5.5: Distribution of pressure drop inside the engine

The pressure drop curves plotted in Figure 5.5 suggest that during the first 75º degrees of shaft rotation and as the fluid moves from the cold towards the hot space, the pressure drop in the regenerator is dominant. Then, the pressure drop in the heater becomes dominant until the shaft is at 225º degrees, after which point the fluid moves back towards the cold space and pressure drop in the regenerator is again higher. This can be also observed with respect to the mass flow variation throughout the dead volume during the cycle as shown in Figure 5.6. Moreover, the Reynolds number variation in Figure 5.7 suggests that the friction coefficient is higher during the same time interval. The overall pressure drop is 0.8 bar and amounts of approximately 2.5% of the maximum pressure of the engine. This amount of pressure loss poses a deleterious performance effect.

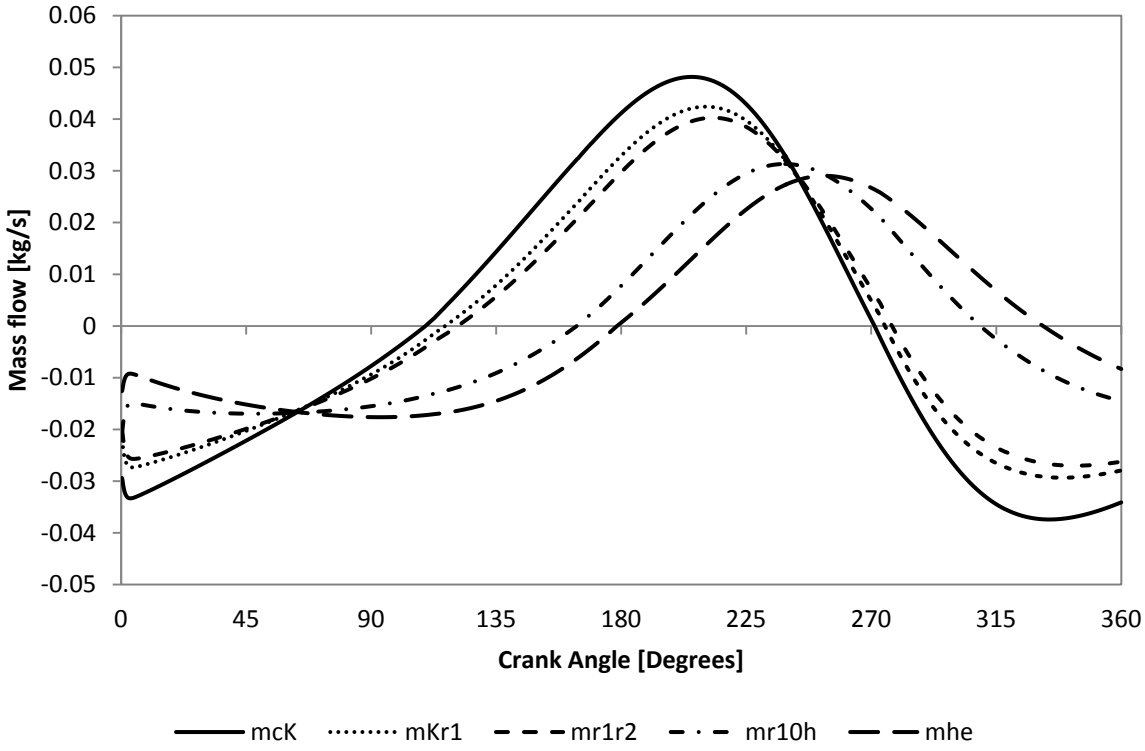

Figure 5.6: Mass flow distribution throughout the volume of the heat exchangers

As with regards to the mass-flow variation throughout the engine, it can be seen from Figure 5.6 that the mass flow in the cooler is higher than the mass flow rate in the heater

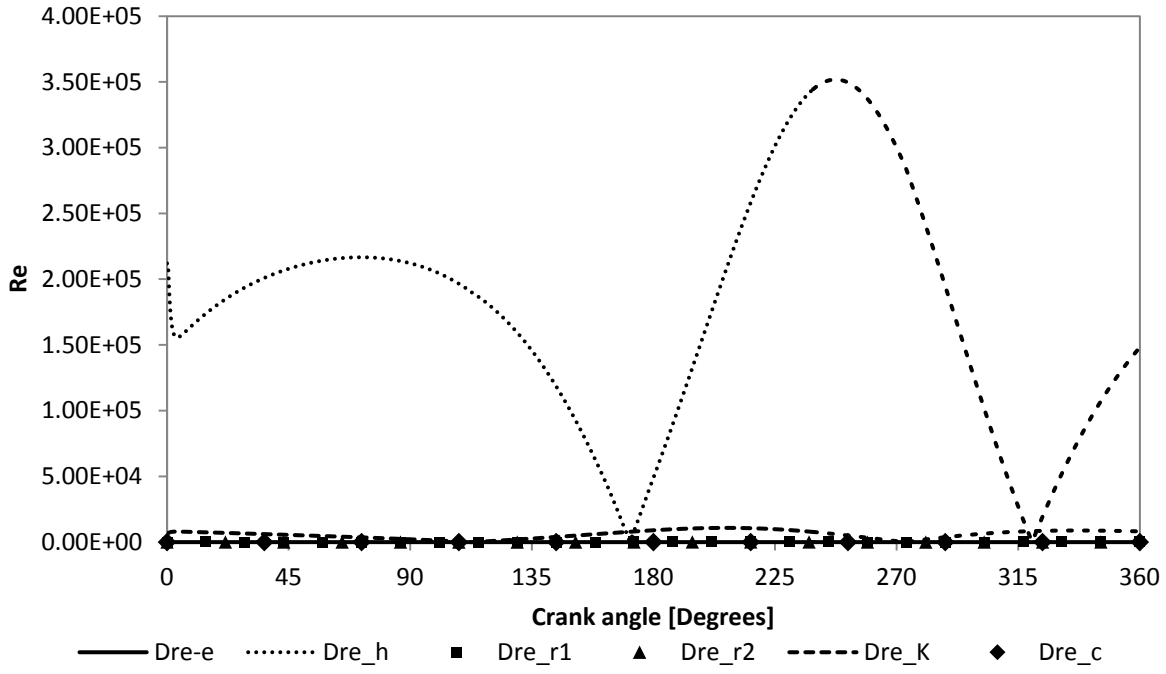

Figure 5.7: Variation of Reynolds number during the cycle

The variation of the heat transfer coefficient is presented in Figure 5.8. Its magnitude ranges from 0.25 W/m^{2}K at 160º degrees to approximately 42500 W/m^{2}K at 225º degrees. The increase in magnitude during this interval from 160º degrees to 225º degrees is due to the increasing mass flow through the heater. As anticipated, the heat transfer coefficient curve follows a similar trend to the Reynolds number variation shown in Figure 5.7. Figure 5.9 shows the amount of heat introduced during the cycle. It can be seen that heat input to the engine is not maximum during the time interval between 160º degrees and 225º degrees of shaft angle when the Reynolds number and heat transfer coefficients increase. This is believed to occur due to viscous dissipation loss, a phenomenon during which the heat input is limited by the temperature increase due to friction.

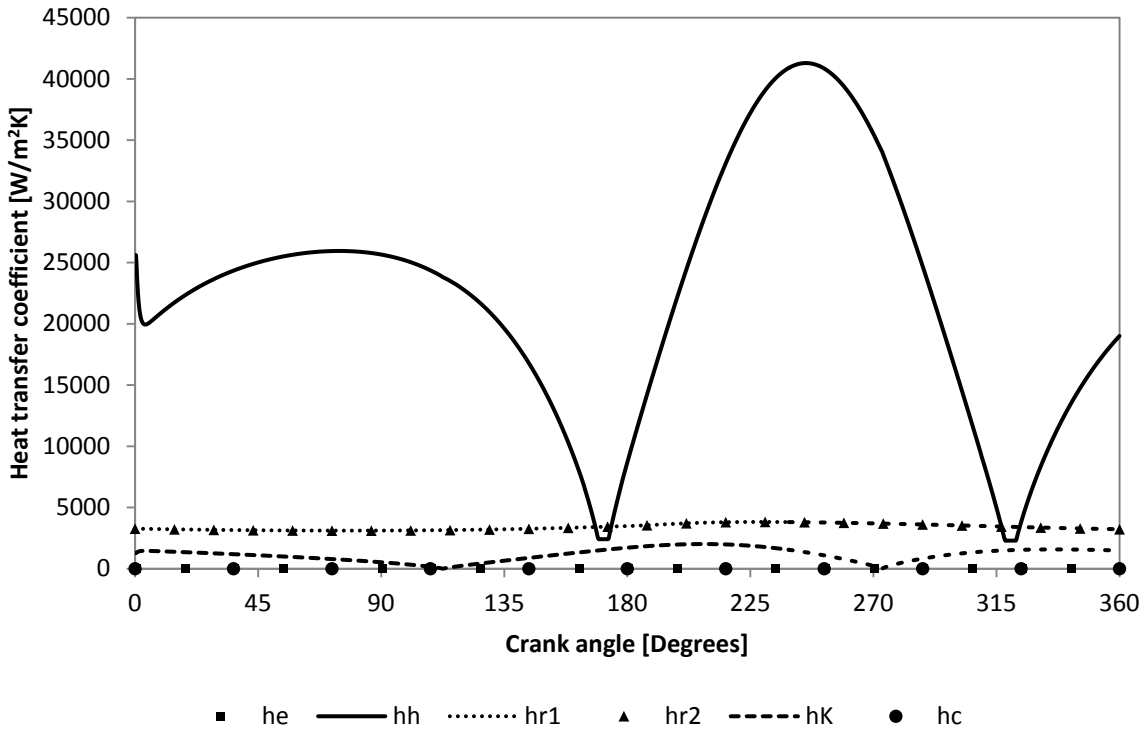

Figure 5.8:Variation of heat transfer coefficient during the cycle

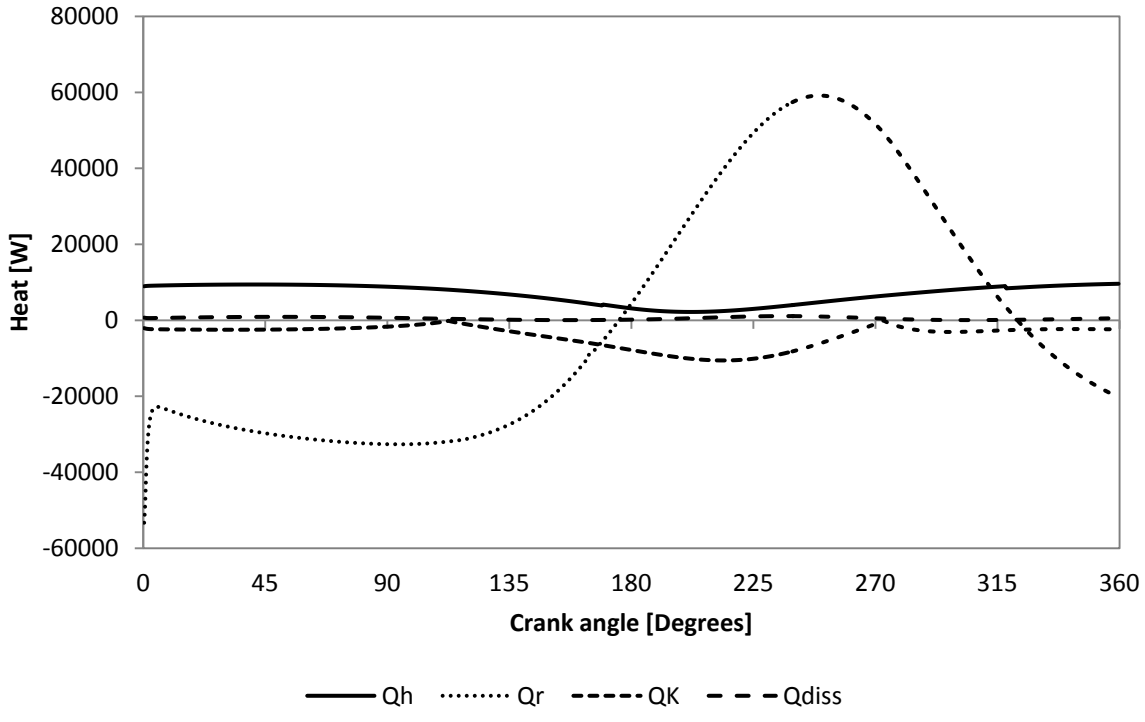

Figure 5.9: Heat transfer variation during the cycle

Finally, Figure 5.10 demonstrates the gas temperature variation in each component of the engine during the cycle. The maximum temperature in the hot space drops relatively slowly to a minimum of 690 K degrees at approximately 75º degrees of crank shaft angle and then rises sharply to its maximum level of 930 K. It can be seen that the nature of the temperature variation is harmonic but not sinusoidal. This is a notable deviation from the theoretical assumption. The temperature variation in the cold space follows a similar trend with a maximum value of 450 K and a minimum value of 333 K. The temperature variation in the last partition of the regenerator shows little variation and has an average value of approximately 750º degrees. The temperature magnitude in the particular space is attributed to the limited heat transfer rates at the particular location of the gas being closer to the hot end as described by Walker in [3]. A similar trend can be observed in the regenerator volume element nearer to the cooler where there is a temperature level of 425º degrees with little to almost no variation. The lack of temperature variation in the regenerator can be attributed to its high heat capacity and the low gas velocities which do not facilitate high heat transfer rates.

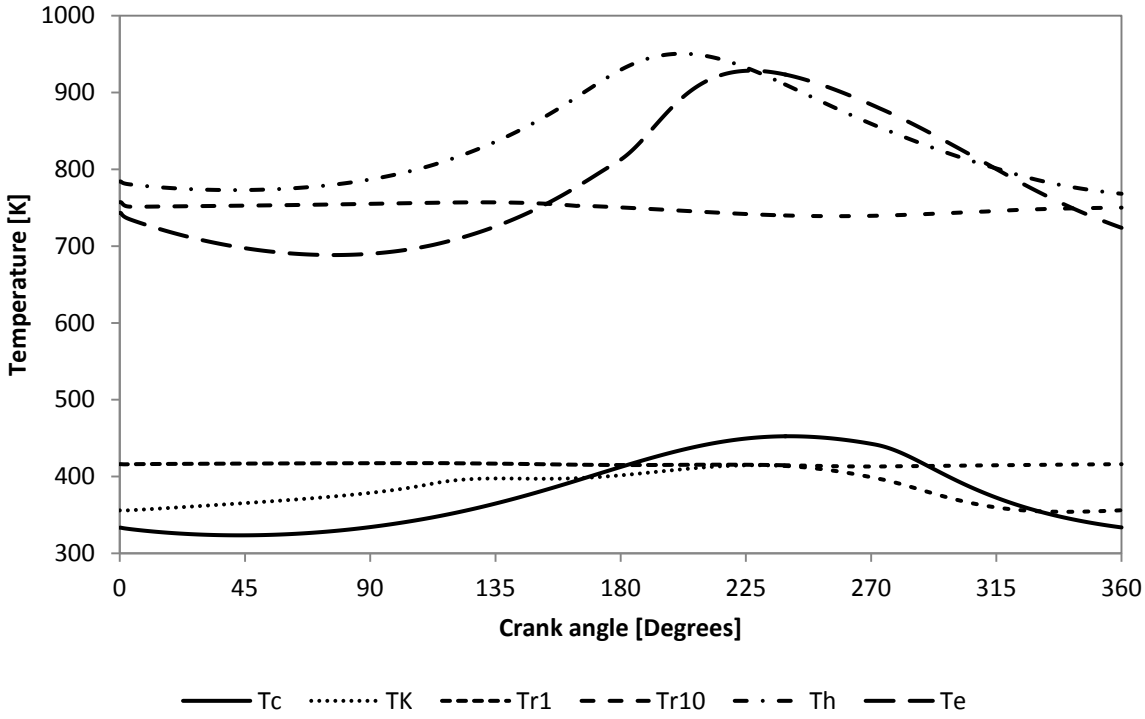

Figure 5.10: Temperature variation inside the components of the Stirling engine

Finally, the predicted indicated power generated from the engine is presented graphically in Figure 5.11. The larger bounded area of the graph corresponds to the work done on the piston in the hot space (e), whereas the smaller area corresponds to the work done on the gas in the cold-compression space (c). The difference between those two areas is the indicated power which, for this simulation, is predicted at 2490 W.

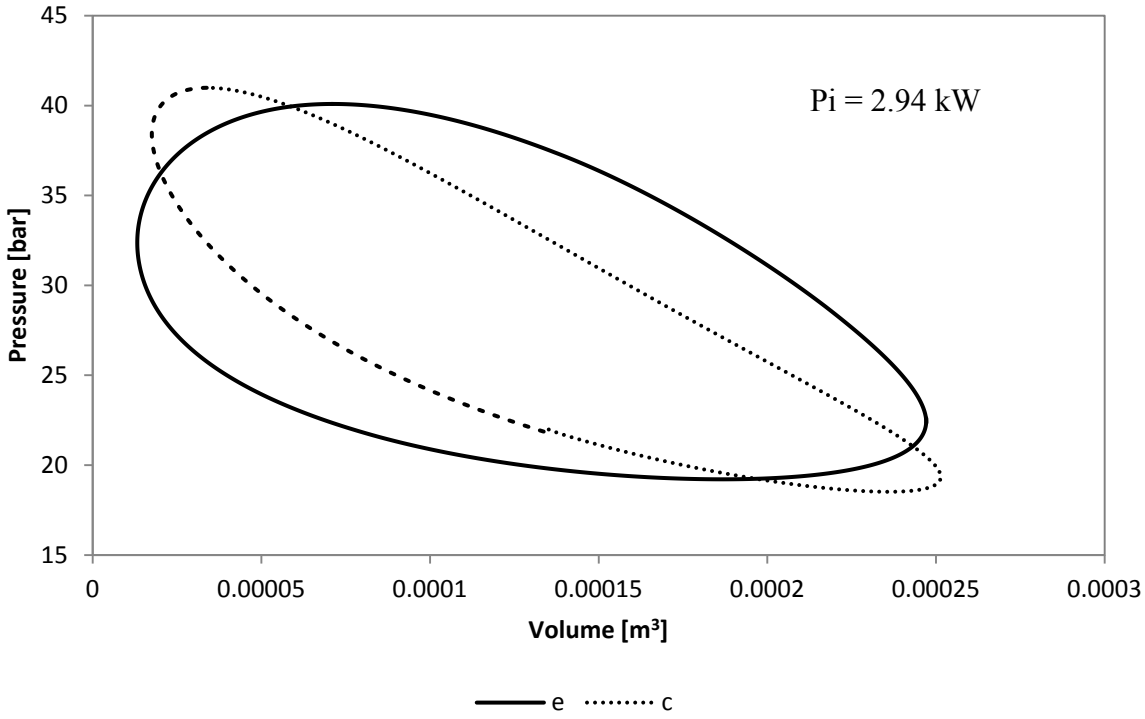

Figure 5.11: Indicated diagram for the power calculation of the Stirling engine

5.3.2 Model validation and comparison with published literature

As presented in the previous section, the applied second order mathematical model predicted an indicated power of 2490 W. The actual engine has been measured to generate approximately 900 W of electricity which corresponds to about 1200 W of mechanical brake power. Depending on the estimation of mechanical losses, this could correspond to 1700 W-2000 W of indicated power. However, the deviation between this prediction and the actual engine's indicated power can be considered acceptable within the limits of 10% - 30% found in similar works in the published literature. In more detail, an indicated power of 3189.4 W was predicted in [18]. However, the SOPRANOS model predicts a lower pressure drop due to different friction and heat transfer coefficients. This can be associated to higher heat transfer to the engine and, hence, more power output. The difference in the pressure drop calculation

and indicated power estimation between the second-order mathematical model used in this work and SOPRANOS has also been documented in [2].

The same solar engine was modelled in [46] with the use of an axi-symmetric 2D CFD model. The CFD simulation predicted an indicated power of 1682 W which was claimed to correspond well with the actual engine performance. The CFD model also predicted higher temperatures in the hot and cold spaces by 20 K. As the same temperature boundary conditions were applied to both the 2D CFD model and the applied mathematical model, it is believed that the difference in the predicted indicated power is due to the phasing between the pressure and volume variations calculated by each model. Figure 5.12 presents the indicated pressure-volume diagram of the solar Stirling engine as predicted in [46]. By close inspection, it can be observed that the points-instances where the 2 curves intersect differ for each model. This indicates that a different phasing between the volume and pressure curves is calculated by each model. This feature can explain the difference in the prediction of the indicated power. It should be mentioned that plotting the volume and pressure variations against crank shaft angle would provide a more comprehensive illustration of this phenomenon; unfortunately, no such data was available from the 2D axi-symmetric simulation. The phasing between pressure and volume in each cylinder for the applied mathematical model are presented in Figures 5.13, 5.14.

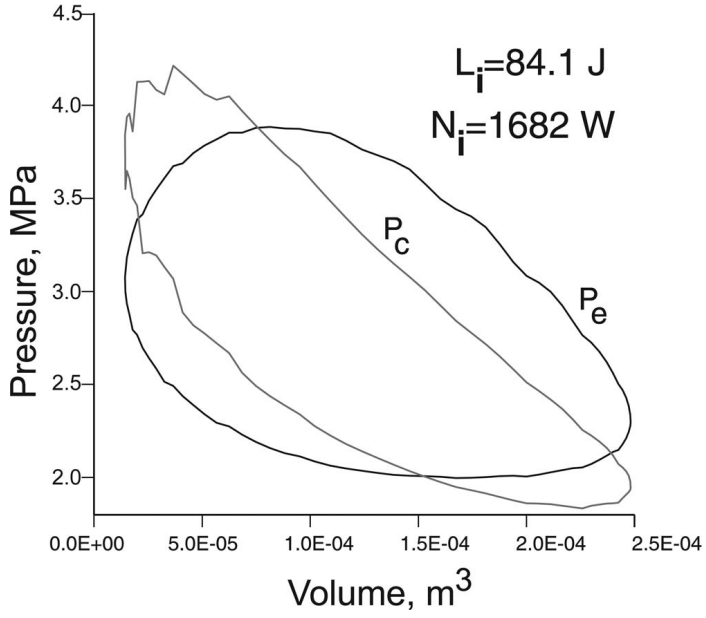

Figure 5.12: Indicated diagram as predicted in [46]

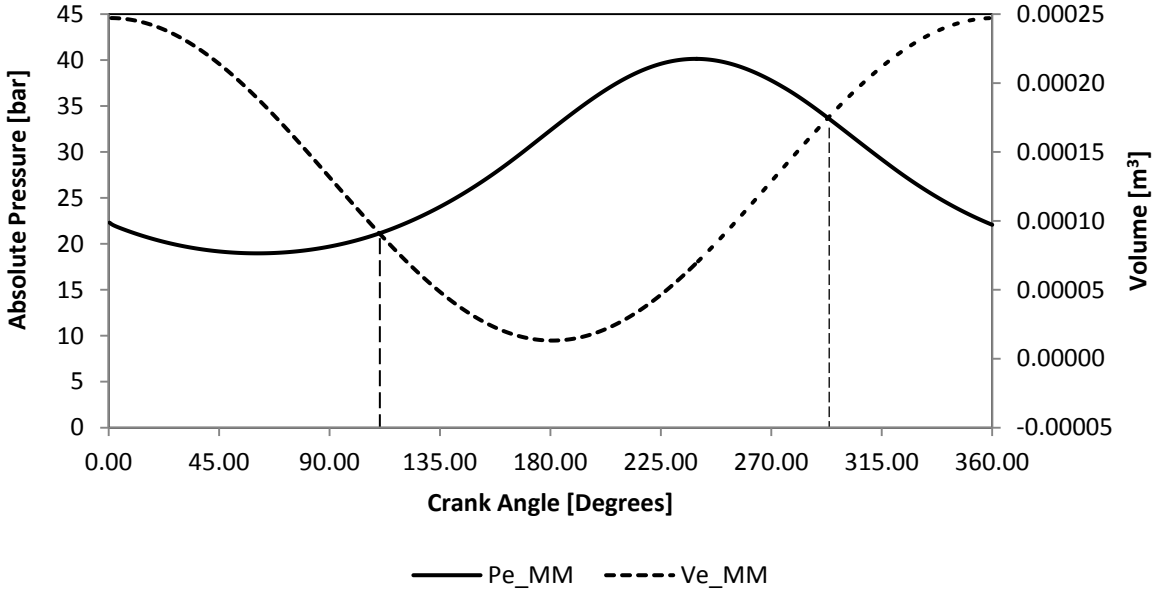

Figure 5.13: MM Pressure and volume variation against crank shaft angle for the hot cylinder

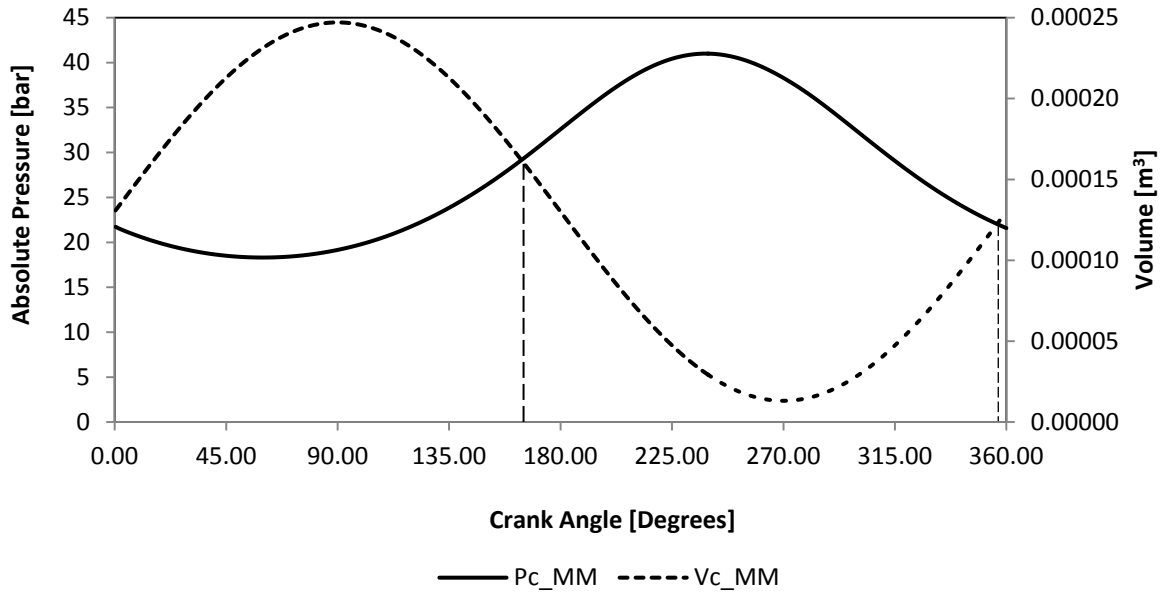

Figure 5.14: MM Pressure and volume variation against crank shaft angle for the cold cylinder

5.4 Optimization of the solar Stirling engine parameters

Following the second order mathematical simulation, a GA technique was applied to obtain the optimum geometric parameters of the engine. The GA model was the one developed in [2] and was set up in such way as to run its predictions through the mathematical model applied previously. The selected geometric parameters were the outer diameter of the cavity-type heater, the length of the regenerator and the length of the cooler tubes. Although the GA model may optimize any geometric parameter, manufacturing constraints led to the selection of the three parameters listed above. Mainly, the inner diameter of the cavity-type heater is governed by the optical design of the solar dish-concentrator in order to facilitate a certain amount of heat transfer to the engine. This suggests that any intervention to the inner diameter of the heater would require re-designing the parabolic concentrator which would be impractical from a manufacturing standpoint. Respectively, the diameter of the regenerator and the cooler casing is geometrically associated to the inner diameter of the heater. Hence,

the only permissible design intervention would have to be applied on the outer diameter of the cavity heater and the length of the regenerator and the cooler.

The objective function of the GA model was specified as the maximization of indicated power. The engine operating conditions were the same as those set in the mathematical model. The size of the population was set at 30 chromosomes and the selection rate for keeping the survival chromosome was specified as 0.5. Additionally, a mutation rate of 0.2 was used in the calculations.

Figure 5.15 presents the optimum indicated power per generation as a function of generations. The best break power was predicted to be 2690 W for the optimal design parameters presented in Table 5.2.

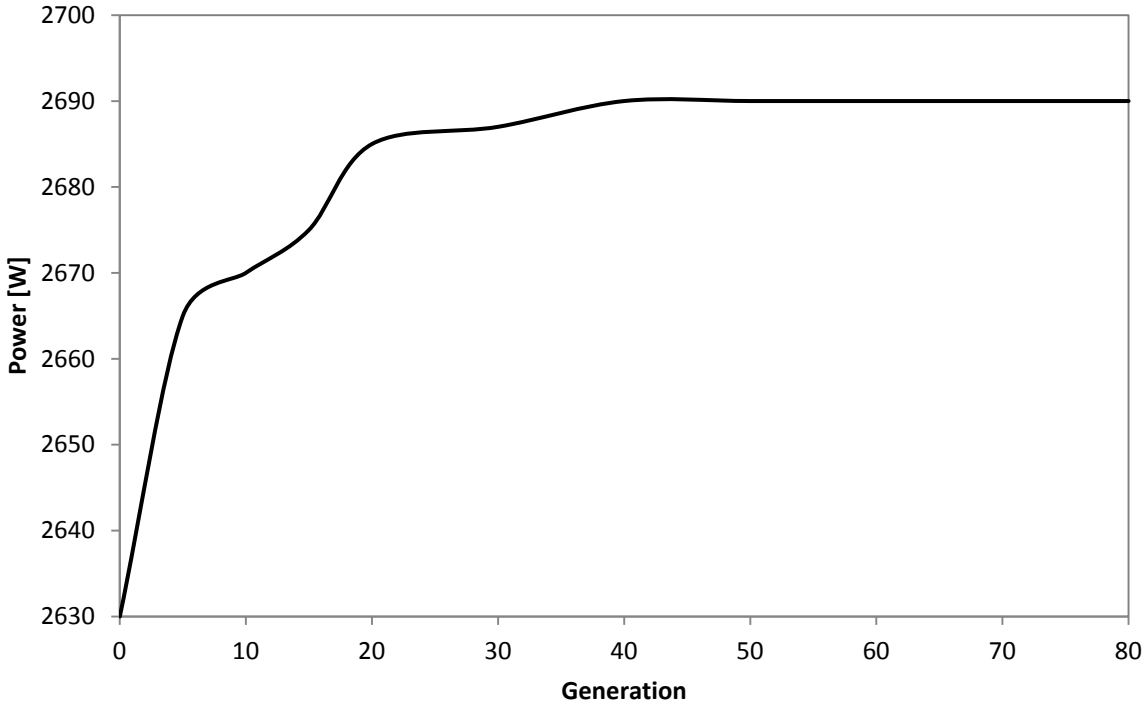

Figure 5.15: Optimal value of indicated power for each generation

Table 5.2: Optimal geometric parameters

Parameter	Value [m]
Outer diameter of heater	0.129827
Length of regenerator	0.071201
Length of cooler tubes	0.13215

The values shown in Table 5.2 result in an increase of 200 W in indicated power.

To establish the validity of the optimization results, a parametric analysis was carried out by means of the second order mathematical model used previously. For each run, two of the engine parameters were set at their specified optimal values whilst the third was set to increase incrementally within the range set by the upper and lower bounds specified in the GA model.

Figure 5.16 shows the variation of indicated power against the outer diameter of the heater. It can be seen that power rises steeply as the outer diameter rises due to a decrease in hydraulic resistance. After the point of approximately 0.12325 m the effect of increased dead volume becomes dominant and hence the indicated power drops. It can be stated that the particular design parameter allows little room for modification.

Figure 5.17 shows the variation of indicated power against the length of the regenerator. It can be seen that the indicated power increases with an increasing length of regenerator up to approximately 0.62 m due to an increase in heat transfer area. Beyond that point, however, the effect of increasing dead volume in addition to the increase in hydraulic resistance causes the indicated power to drop.

Finally, Figure 5.18 demonstrates the variation of indicated power with respect to the length of the cooler tubes. As seen from the graph, the indicated power increases steeply up to a

length of 0.13 m due to the increase of heat transfer area providing a better cooling effect to the engine. The power slightly drops at higher lengths due to increasing dead volume and pressure drop along the cooling tubes. However, the effect of those is not as drastic compared to the increasing diameter of heater and the length of regenerator.

On a final note, it should be mentioned that the GA did not predict the exact optimal values of the selected engine parameters compared to the parametric analysis. The deviation ranges between a few tenths of a millimetre for the outer heater diameter to a few millimetres for the length of the cooler and the regenerator. However, it was suggested in [2] that GAs do not necessarily provide the exact optimal parameters. Furthermore, the parametric analysis demonstrates that the optimum values predicted by the GA will improve the engine performance nonetheless.

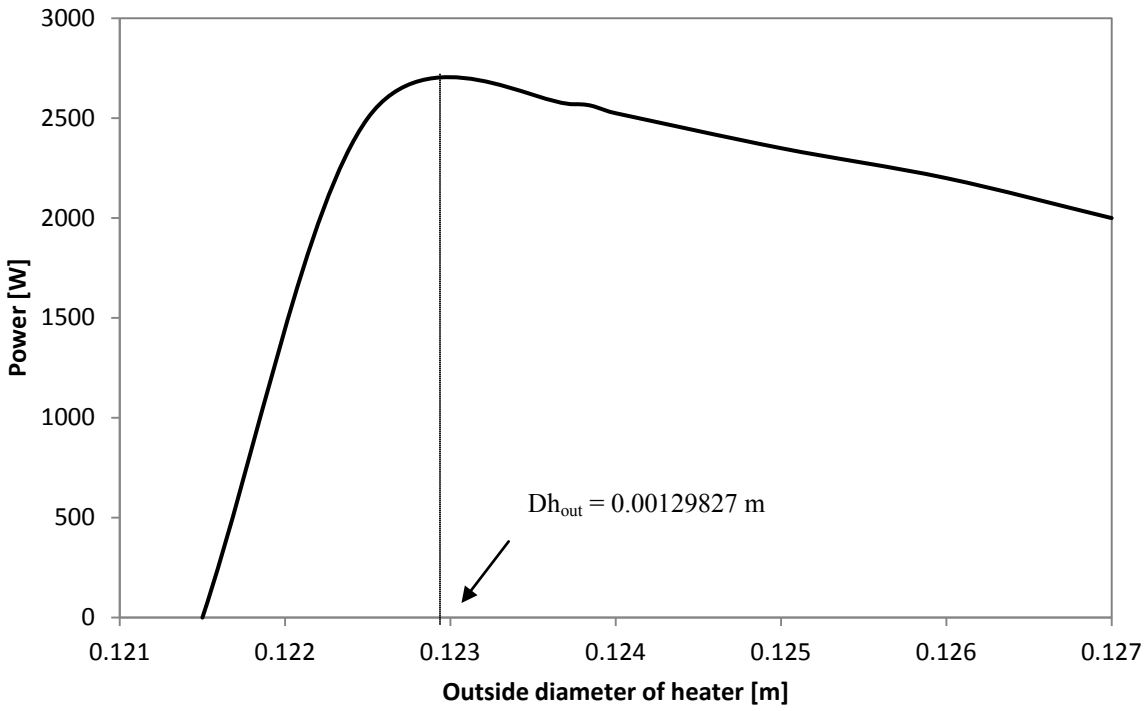

Figure 5.16: Indicated power as a function of outer heater diameter

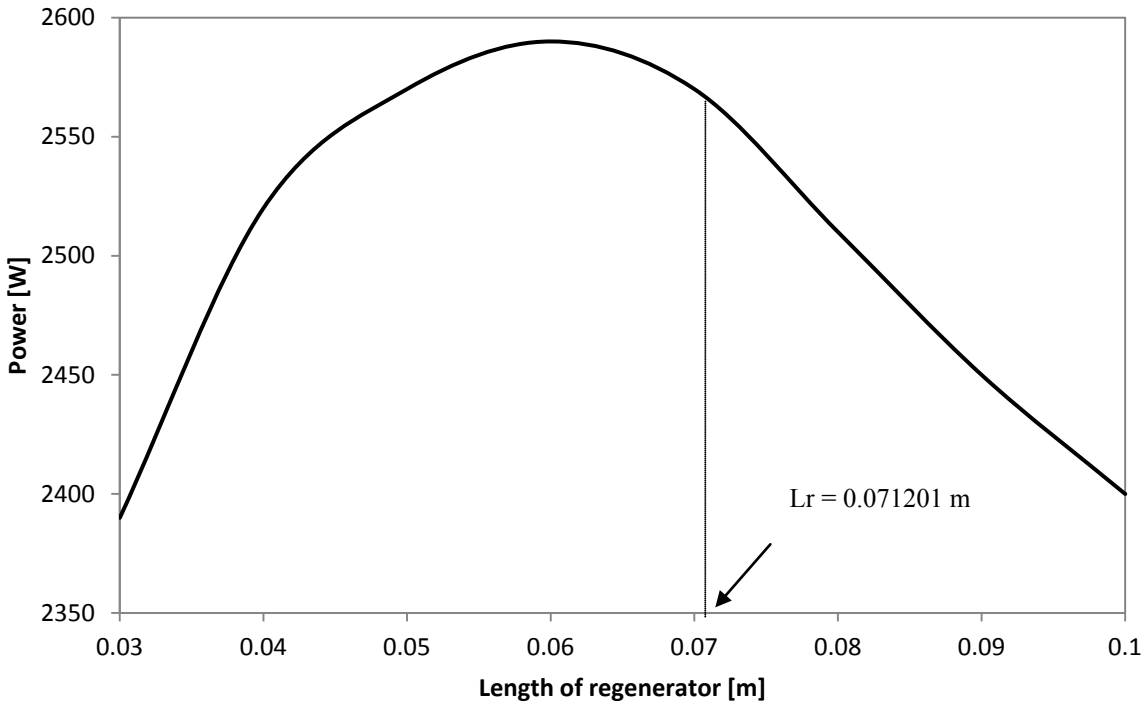

Figure 5.17: Indicated power as a function of regenerator length

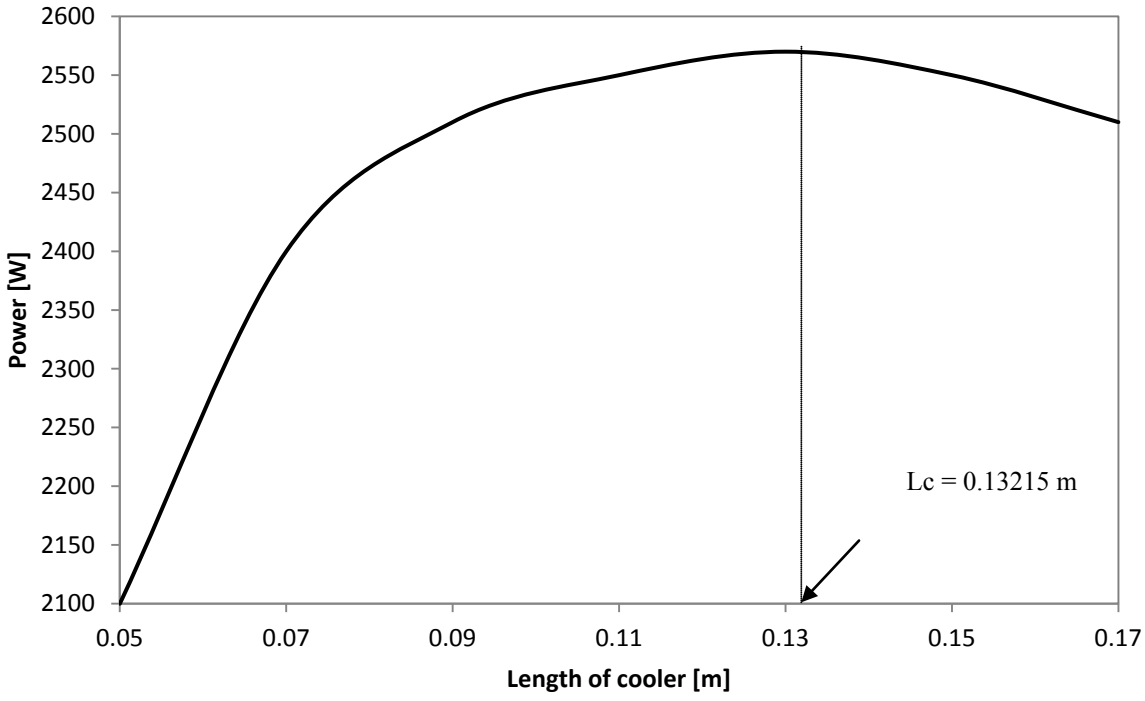

Figure 5.18: Indicated power as a function of cooler length

5.5 Synopsis

In this chapter the working process of the Stirling engine under consideration was analyzed by means of a second-order thermodynamic model. The variation of volume, pressure, temperature and heat transfer coefficient among others, were described during one working cycle. The predicted indicated power output was within reasonable range compared to previously published results. The deviations were attributed to the use of different heat transfer and friction coefficients calculations and the difference in the calculation of the pressure and volume phasing. A GA optimization code was coupled to the thermodynamic model and rational design parameters were obtained which were confirmed by a parametric analysis. The suggested design modification would yield an additional 200 W of indicated power output.

Chapter 6 Results of the Global 3D CFD Model of the Solar Stirling Engine

6.1 Introduction

CFD is a powerful tool which vastly expands the capabilities of engineers to make much more accurate predictions of the performance of mechanical systems during the design phase. As stated in the introduction, such approach has been used for Stirling engine investigations providing acceptable accuracy but with "gas circuit only" 2D and 3D models. In order to achieve a better established and more accurate evaluation, a more comprehensive 3D model of the engine was further developed in this work. This model included, in addition to the gas circuit, the solid parts surrounding the gas circuit, taking into account the complex multi-dimensional heat transfer effects through the walls. It is expected that such a detailed description of the engine would provide a more accurate modelling of the working process and estimation of the performance of the Stirling engine. Furthermore, such a complex model could potentially provide useful information that can be used in creation of simpler models for which accurate experimental heat transfer and friction coefficients are very difficult to obtain.

6.2 Description of the global 3D CFD model

6.2.1 Engine layout

Figures 6.1 and 6.2 present a 3D CAD model of the engine and a cut-view of the model respectively. The annotation described in these figures is used in the following sections in

order to describe the several locations and planes where data monitoring points were specified.

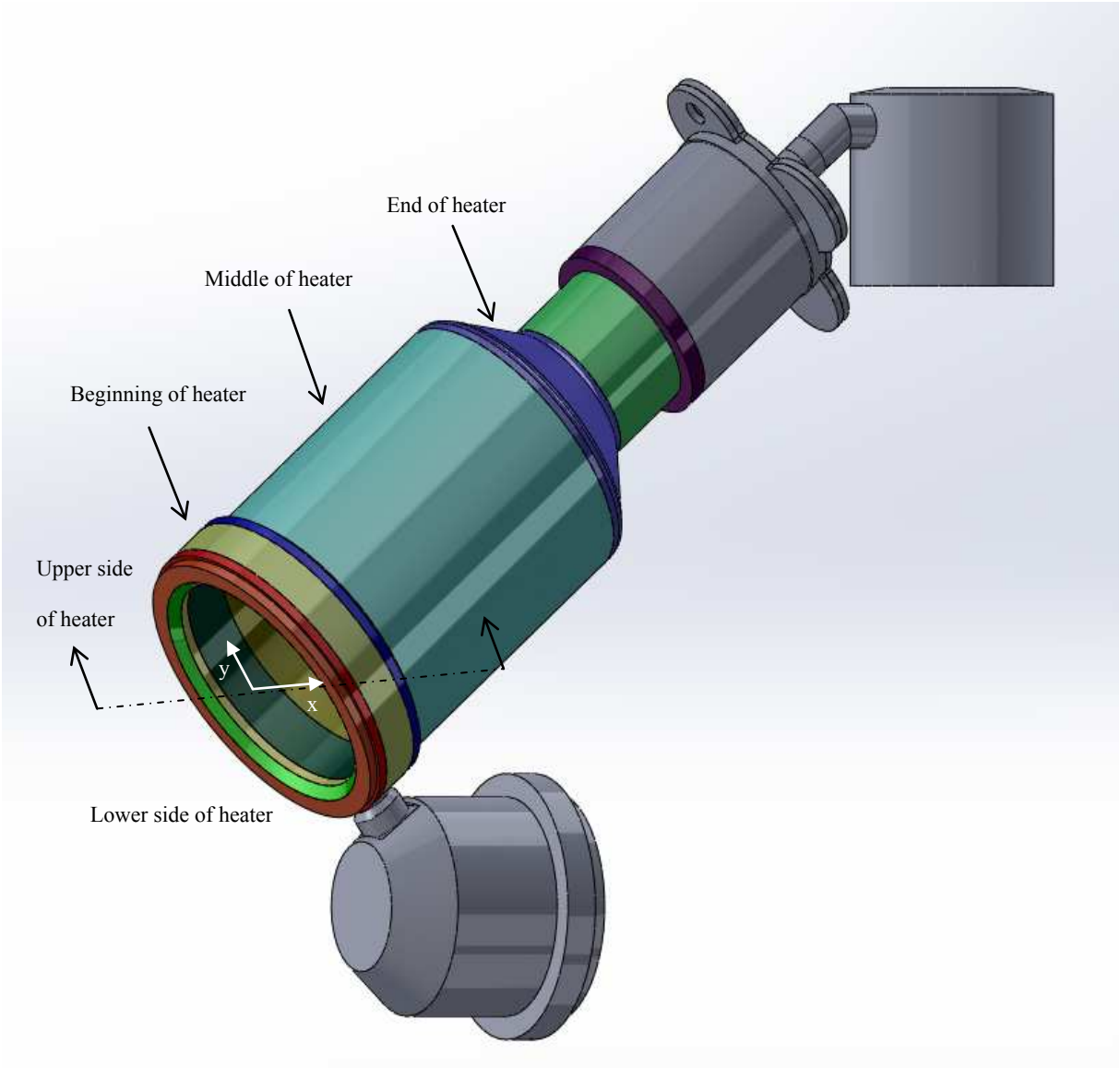

Figure 6.1: 3D CAD model of the engine under consideration

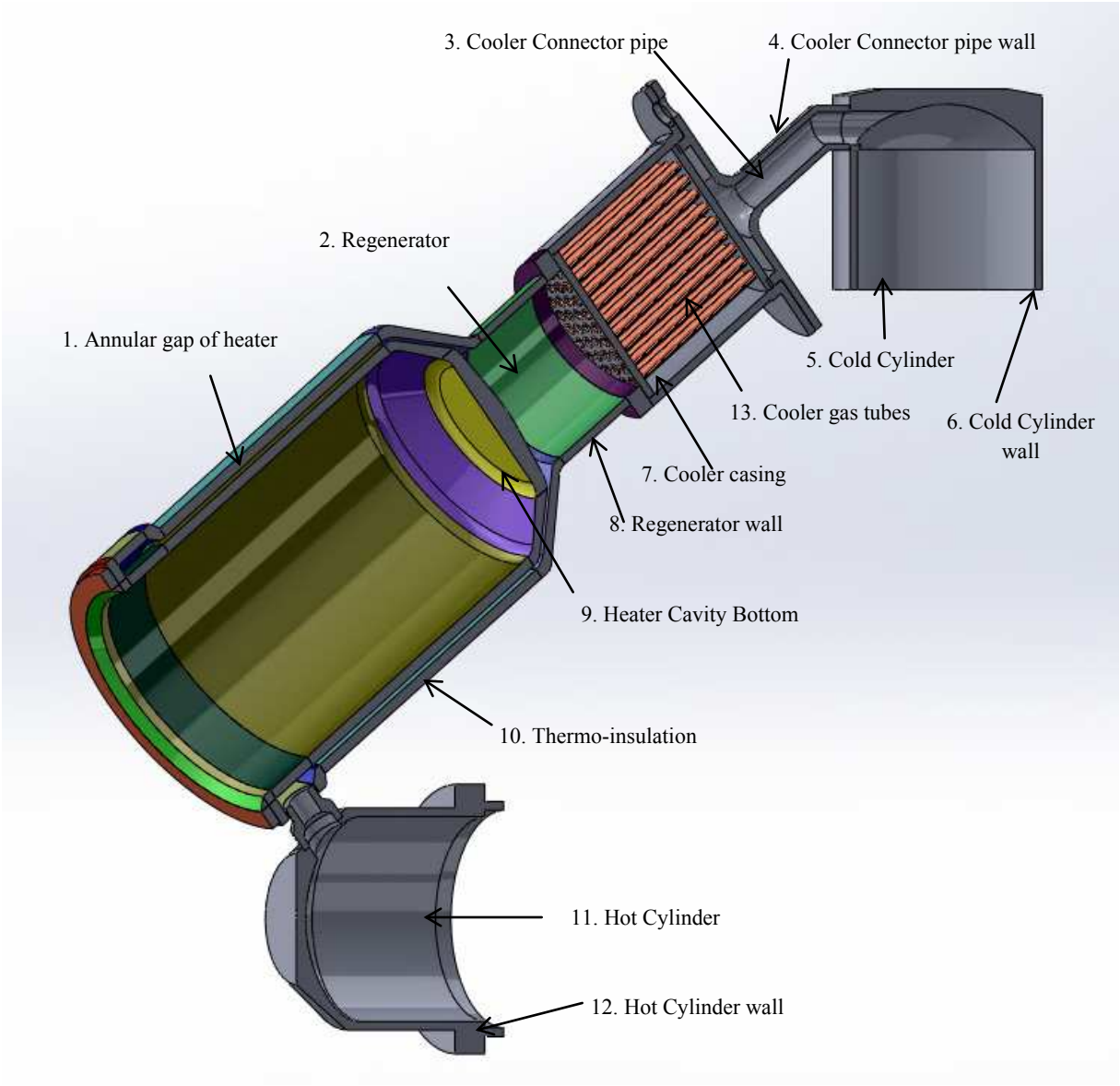

Figure 6.2: Cut-view of engine with component description

6.2.2 Computational grid

The computational grid (mesh) for this engine was built in Gambit. The grid consisted of 545,603 volume elements. The mesh consisted of both hexahedral and tetrahedral elements (hybrid). Figure 6.3 shows a layout of the computational grid where all the locations and zones shown in Fig. 6.2 are displayed. Also, Figure 6.4 shows a cut-view of the computational grid. Further refining of the computational grid resulted in the increase of the computational time to such extent that it became unfeasible to carry out numerical modelling with the PC allocated to the project.

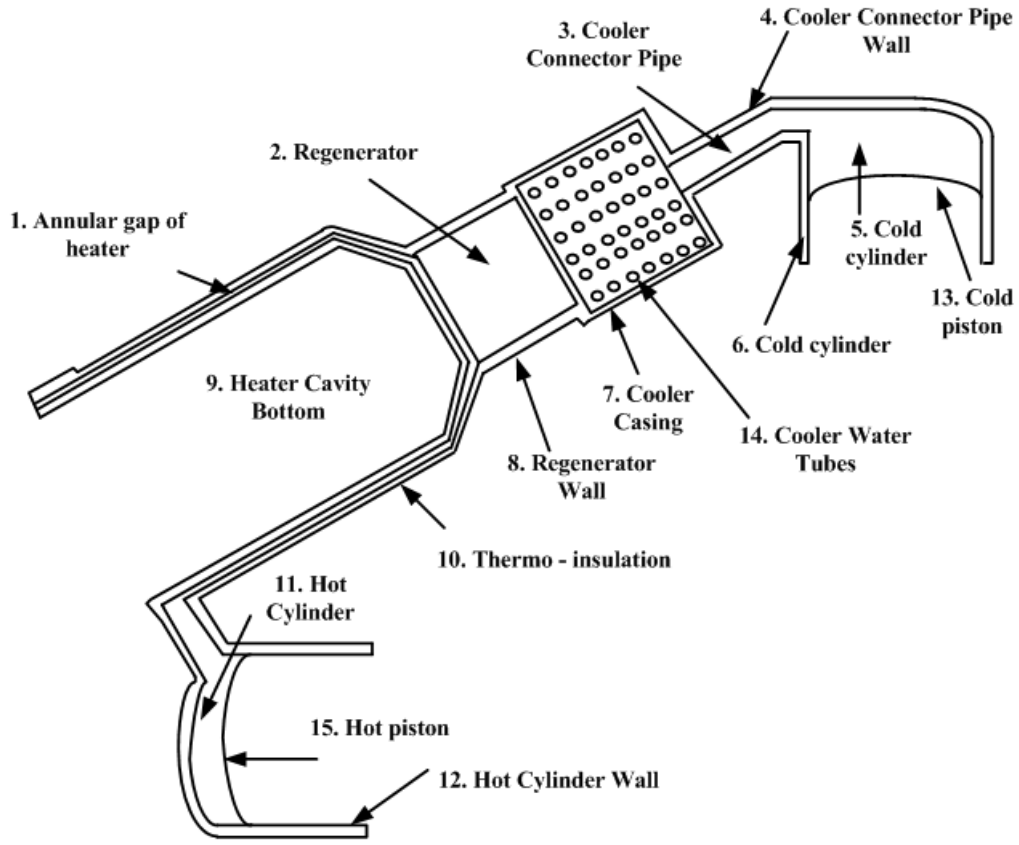

Figure 6.3:Layout of the computational domain

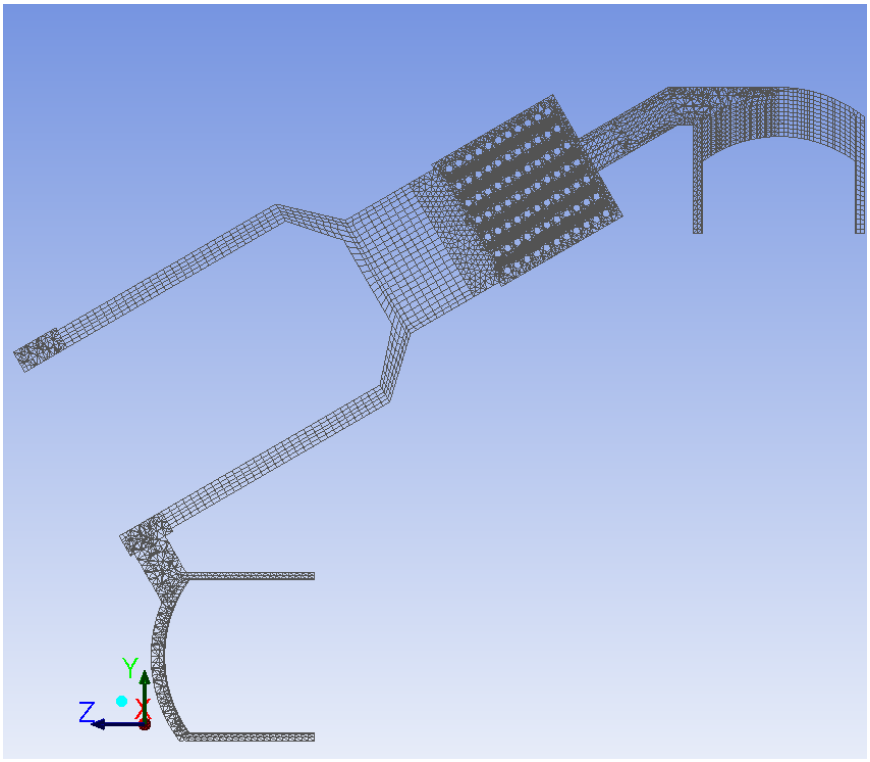

Figure 6.4: Cut-view illustration of the computational grid

6.2.3 Model settings

The boundary conditions specified in this model were obtained from previous experimental and theoretical work carried out for the particular engine [18, 46, 103, 118]. The turbulence model used was the standard $k - \varepsilon$ and the In – Cylinder mode with dynamic mesh was used for the piston motion. The pressure – velocity coupling scheme used was the SIMPLE algorithm. The solver type was the Pressure-based and the transient time setting was a time – dependent simulation with a time step of 0.00005 s. The spatial discretization of pressure was set to standard and first order upwind discretization was specified for the equations of density, momentum, turbulence kinetic energy and dissipation rates, and energy. The selected solver was the 3D double precision solver in ANSYS FLUENT. Finally, several monitoring points were created in order to obtain data at specific parts of the engine.

6.2.3.1 Thermal boundary conditions and materials specification

There were 3 types of thermal boundary conditions (BCs) necessary to describe the heat transfer phenomena for this model. For the heater, heat flux BCs were used. For the cooler aluminium alloy water pipes a constant temperature of 333K was specified along the total surface of the pipes. Finally, the coupled thermal BC was used on either side of surfaces splitting the gas and solid domains. The standard wall function was used in order to describe the gas flow and heat transfer in the vicinity of walls on the engine's gas circuit side. Such approach, although less accurate than using boundary layers during the modelling, still provides an acceptable accuracy in the description of the above phenomena.

All remaining external surfaces of the casing of the engine were specified as being adiabatic (zero heat flux) since they were covered with thermal insulation material. The specified material for the heater and the regenerator was stainless steel from the ANSYS FLUENT material database. The heat capacity and thermal conductivity of steel were set as temperature-dependent and followed a piece-wise linear distribution between 293 K and 1143 K. The inner surface of the cavity heater was split into several sections in order to specify a cascading heat flux condition along the length of the heater including the bottom of the cavity and the top ring surface as shown in Figure 6.5. The heat flux BCs applied to the inner surface of the heater are listed in Table 6.1 with reference to Fig. 6.5. Those values were obtained from experimental data published in [118]. The working gas was specified as helium.

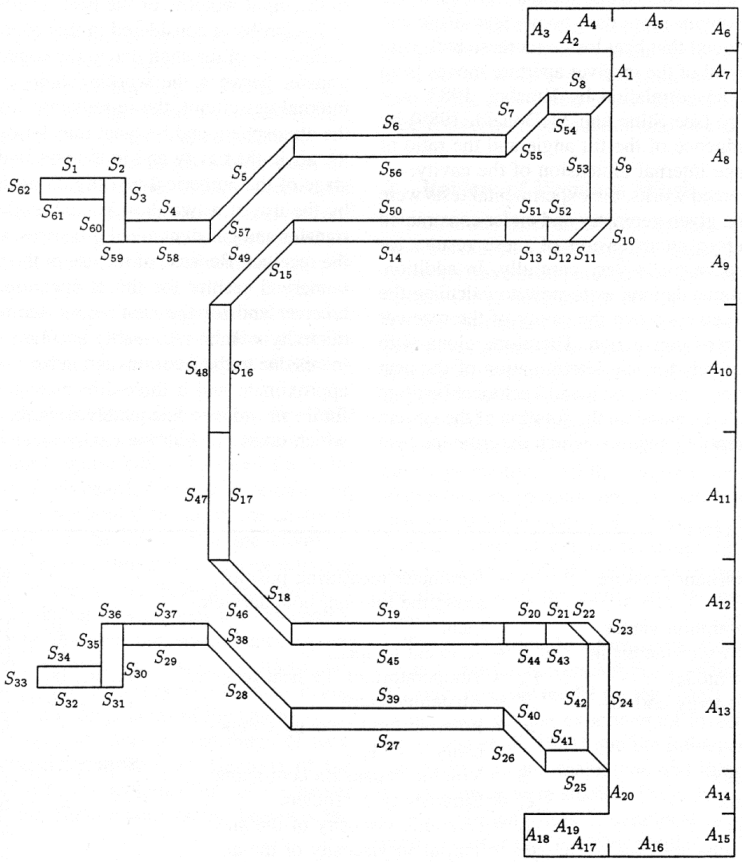

Figure 6.5: Schematic illustration of the boundary surfaces of the engine's heater

Table 6.1: Thermal heat flux BCs for the inner surface of the heater

Surface	**Heat Flux (W/m^2)**
S9, S24	38400
S10, S23	38400
S11, S22	38400
S12, S21	40400
S13, S20	40400
S14, S19	56400
S15, S18	56400
S16, S17	56400

To fully model the properties of the regenerator matrix, the porous zone utility was used in ANSYS FLUENT. The porous medium was specified as stainless steel with a porosity of 0.7.

ANSYS FLUENT provides a moving mesh capability for modelling boundaries moving with time. The harmonic motion of the two pistons of this engine with the 90º phase difference with the hot host piston leading the cold piston was modelled by means of a User-defined Function (UDF), which is essentially a C-subroutine developed for modelling Stirling Engines in ANSYS FLUENT. For piston engine applications there is also the In – Cylinder mode which is used to specify criteria for removing or generating a layer of control volumes inside of the engine cylinders. The full UDF is presented in Appendix A.

In the modelling it was specified that the speed of the engine is 1200 rpm (20 Hz), the stroke of the pistons is 33 mm and the cycle is divided into 1000 time steps.

A number of monitoring points were set up in the computational domain in order to obtain numerical data during the simulation and monitor the progress and state of the solution. These included the surface averaged absolute pressure and total temperature on the piston surfaces and vertex average values of the total temperatures along the length of the heater and regenerator. The heater and regenerator were divided into three main segments, namely the beginning, middle and end segments, and eight monitoring points were set up along the circumference of each segment for both heat exchangers. Of those eight points in each segment, four were used to record temperature variations inside the gas circuit and the other four were deployed to record the temperature inside the solid walls. This allowed for in-depth analysis of the temperature variation in each component of the engine. Volume monitors registered the volume variations of helium inside each of the two working spaces. The pressure and volume values obtained were then used for plotting indicated pressure-volume (PV) diagrams and calculating the indicated power output of the engine.

6.2.3.2 Solution initialization and convergence monitoring

The initialization of the solution is the process during which the initial values of variables are assumed as a starting point for the iterative solution of the governing equations. It is therefore useful to set values that are close to those in the steady-state operation of the engine so to reach convergence sooner (e.g. using experimental results if available). Thus, the gas temperature of 900 K in the expansion space and a pressure of 40 bar on both piston surfaces was specified as initial conditions. The solution was considered converged when the temperature inside the regenerator is stabilized at the value between 550 K and 600 K; the value of the temperature of the gas in the hot space is between 800 K and 900 K; and the value of the temperature of the gas in the cold space is between 350 K and 450 K. Similarly, the maximum pressure on both pistons was expected to stabilise around 40 bar. The time step was selected to be $5x10^{-5}$ s to split the cycle into 1000 time steps. Such a value of the time step was considered to be sufficient to ensure an accurate description of the temperature and pressure variations inside the engine. During the first two cycles of the simulation a conservative number of 300 iterations per time step was set in ANSYS FLUENT. After the flow inside the engine was established, the number of iterations per time step was reduced to 100 and the convergence criterion setting in ANSYS FLUENT was changed to absolute. Such approach provides less iterations per time step as the solution progresses. The modelling was stopped after 170 cycles, at which point the variables reached the steady state. The next section presents the numerical results obtained for the global 3D CFD modelling in terms of velocity fields, pressure and temperature distribution inside the engine and an indicated P-V diagram, from which the indicated power output is calculated.

6.3 Analysis of the global 3D CFD modelling results

Figures 6.6-6.9 show the velocity vectors in a cut-plane of the engine for instances when crank shaft angle is 0°, 90°, 180° and 270°, respectively. It can be seen in these figures that the velocity ranges from 6.27 x 10^{-6} m/s to 183 m/s. The lower velocity values are observed inside the regenerator due to the high cross section for the flow of the gas. The higher velocity locations are those in the heater and cooler connector pipes, reaching 183 m/s and 103 m/s respectively. It is worth noticing the recirculation area in the bottom right corner of the cold cylinder is due to the start of its expansion in Figure 6.7. An immediate observation from the velocity vector plots is that the gas flow is very complex throughout the engine with some locations being the source of high hydraulic losses (such as the pipes connecting the hot space to the heater and the cold space to the cooler.

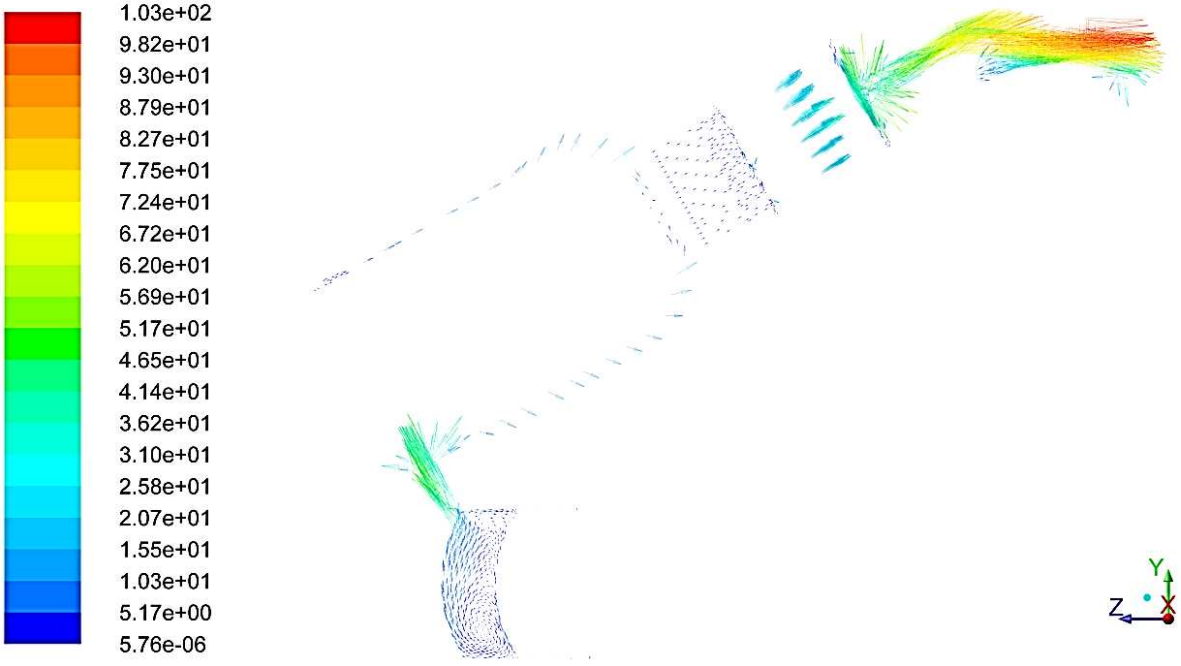

Figure 6.6: Velocity vectors inside engine at the instance of the cycle when the crank shaft angle is 0°

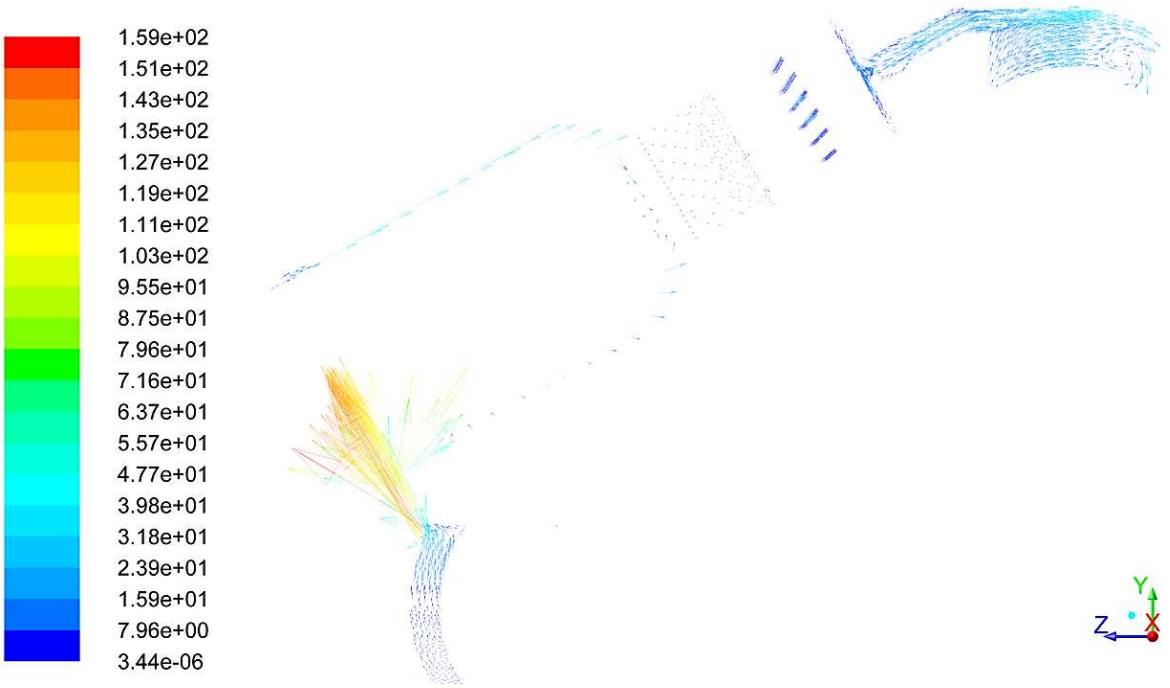

Figure 6.7: Velocity vectors inside engine at the instance of the cycle when the crank shaft angle is 90°

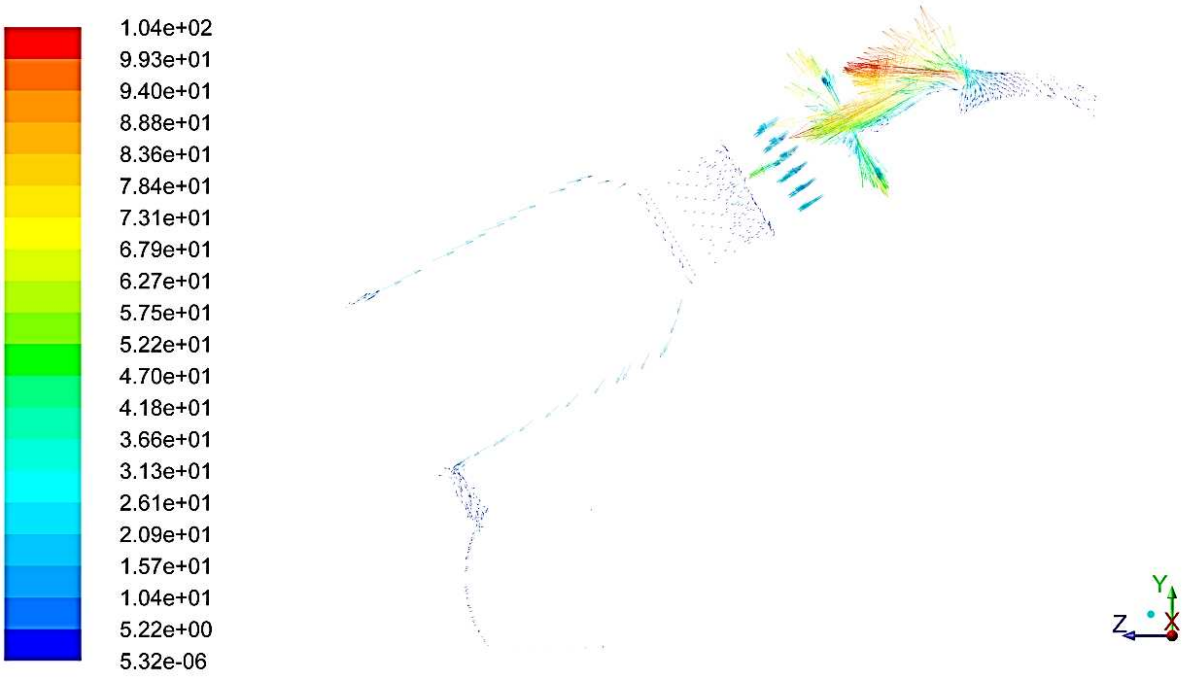

Figure 6.8: Velocity vectors inside engine at the instance of the cycle when the crank shaft angle is 180°

Figure 6.9: Velocity vectors inside engine at the instance of the cycle when the crank shaft angle is 270°

To further illustrate these non-uniform velocity patterns inside the engine, Figures 6.10-6.13 present the velocity distribution inside the heater for instances when crank shaft angle is 0°, 90°, 180° and 270 respectively. Figure 6.10 shows the velocity vectors in the heater at the instance of the cycle when the crank shaft angle is 0°. At this instance the hot piston is in its BDC and is about to start its movement towards TDC while the cold piston is mid-way through towards its BDC. The velocity in the heater varies from approximately 5.17 m/s to 62 m/s. The higher velocity occurs in the heater inlet as the hot piston is pushing gas towards the heater. It can be seen that the gas flow after exiting the hot space splits and flows around the outer circumference of the heater. The velocity of both streams is between 25.8 m/s and 31 m/s.

At 90° of the crank shaft angle (Fig. 6.11) the hot piston is mid-way through its compression phase, forcing the gas to flow through the heater. The velocity peaks at 159 m/s at the inlet of the heater due to the decrease in the flow area. The gas then flows around to the area of the

heater furthest away from the hot space (higher y coordinate) and then around the circumference of the heater with a velocity of approximately 63.7 m/s. The gas follows the particular flow path due to the lower pressure along such direction. The velocity values drop to 15.9 m/s at the circumferential location opposite to the heater inlet where the opposite streams meet. The non-symmetrical location of the connecting pipe between the hot space and heater results in non even distribution of the gas mass flow rate and heating. Figure 6.12 shows the flow distribution in the heater for the instances when the crank shaft angle is 180°. At this instance the hot piston is at TDC and most of the gas was forced out from the hot cylinder towards the heater. The velocity inside the heater ranges from approximately 5.25 x 10^{-6} m/s to 10 m/s. Again, the velocity is higher at the upper locations of the heater. An interesting feature of the flow was revealed at this stage, namely the gas flow is reversed and the gas flows towards the hot space in the lower area of the heater. This can be explained by the fact that the gas encounters the high hydraulic resistance as it is directed towards the regenerator and also some of the gas flows backwards due to the motion of the cold piston towards its TDC. This is an instance in the cycle when the gas flow starts to change its direction since the hot piston is about to move towards its BDC. Figure 6.13 shows the velocity vectors in the heater for the instance in the cycle when the crank shaft angle is 270°. At this instance the cold piston is in its TDC and the hot piston is moving towards its BDC. The velocity inside the heater is higher towards the lower y coordinate values peaking at 64 m/s. The gas flows towards this region since this is the shortest way to the hot space. The high velocity values in the heater connector pipe are due to the sharp decrease in the flow area.

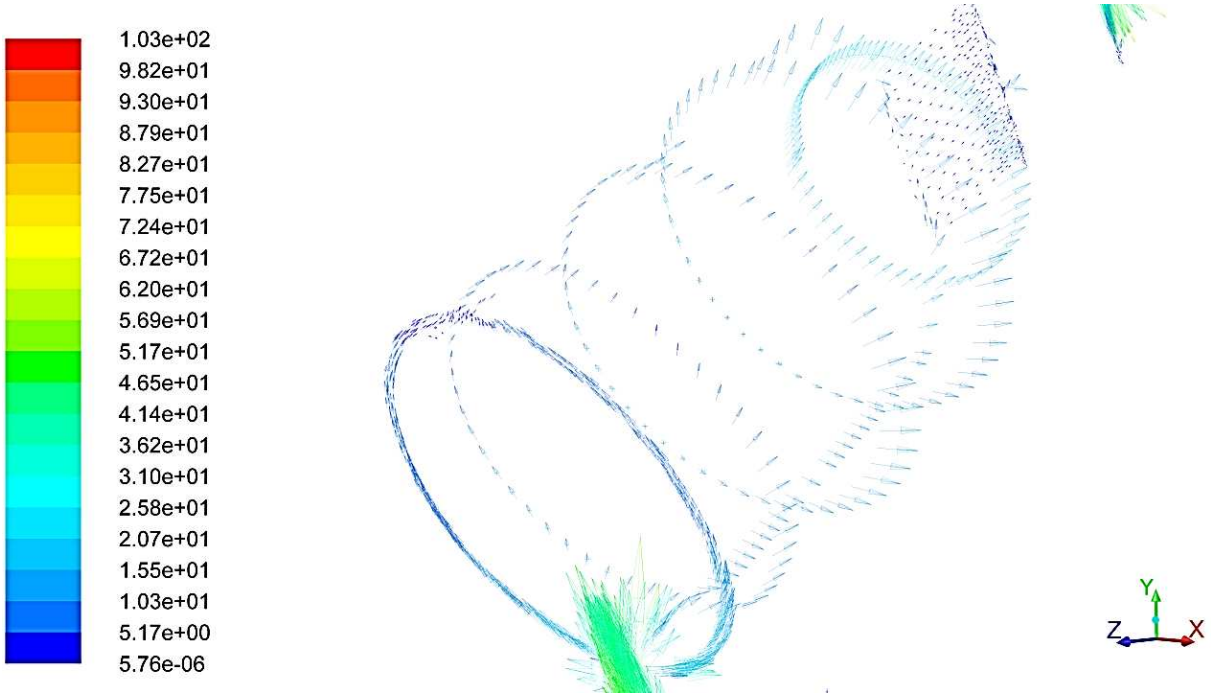

Figure 6.10: Velocity vectors inside heater at the instance of the cycle when the crank shaft angle is 0°

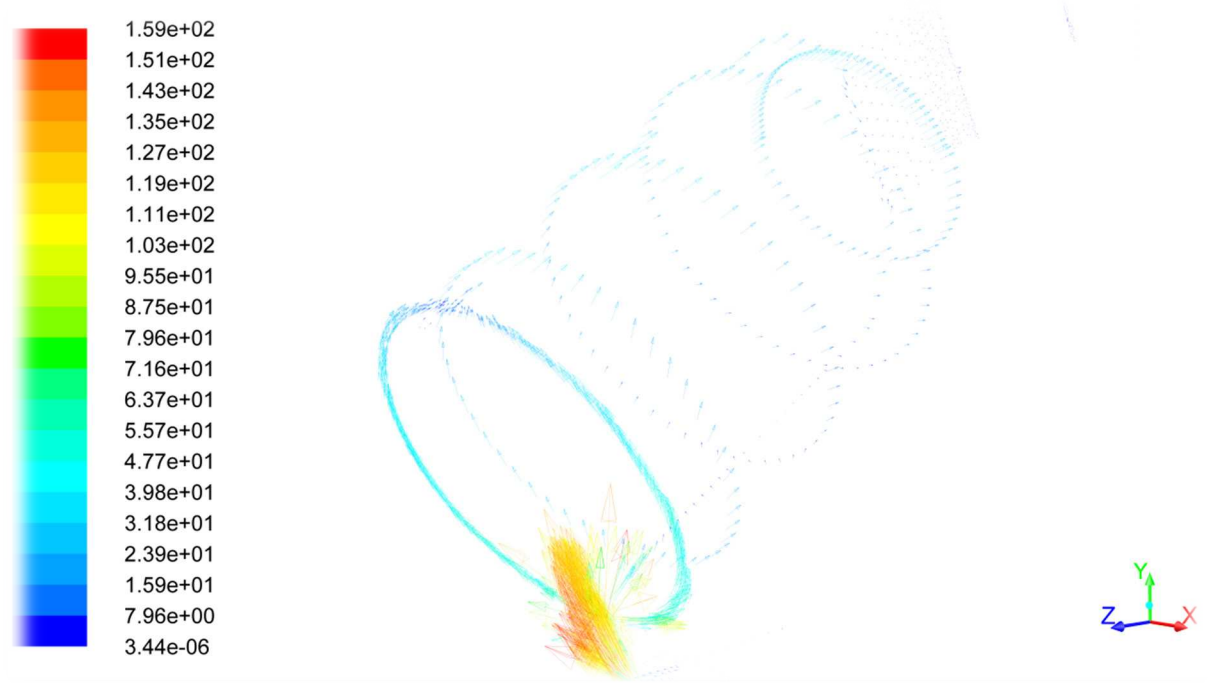

Figure 6.11: Velocity vectors inside heater at the instance of the cycle when the crank shaft angle is 90°

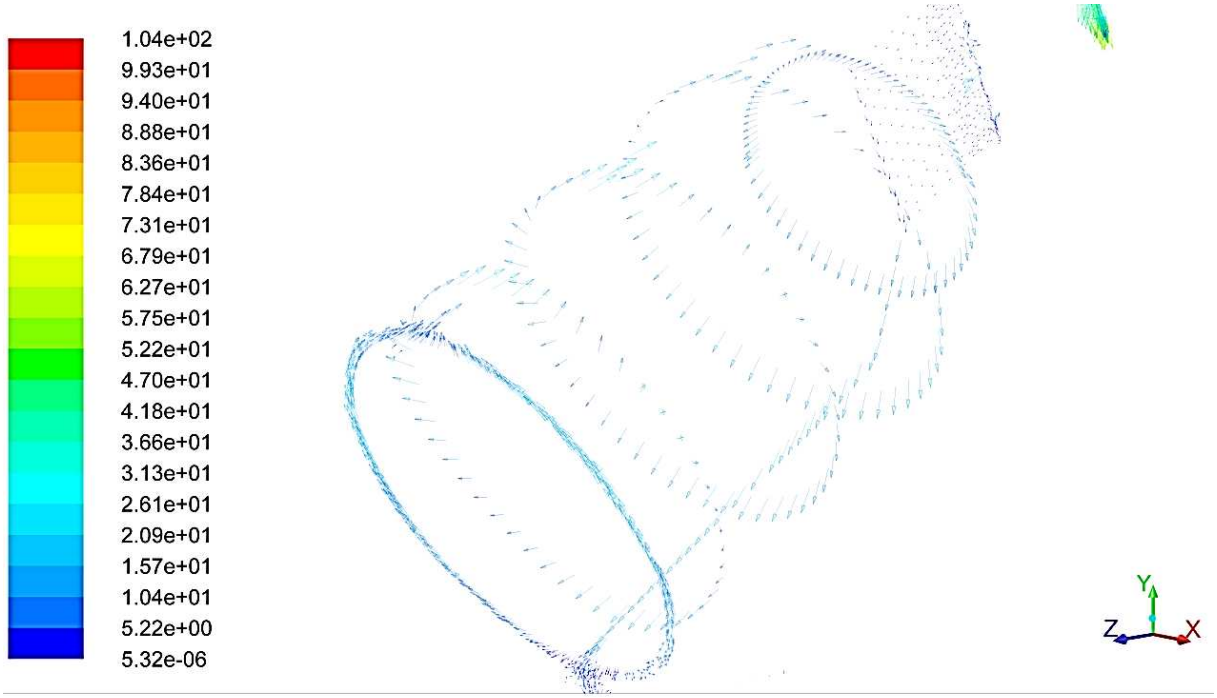

Figure 6.12: Velocity vectors inside heater at the instance of the cycle when the crank shaft angle is 180°

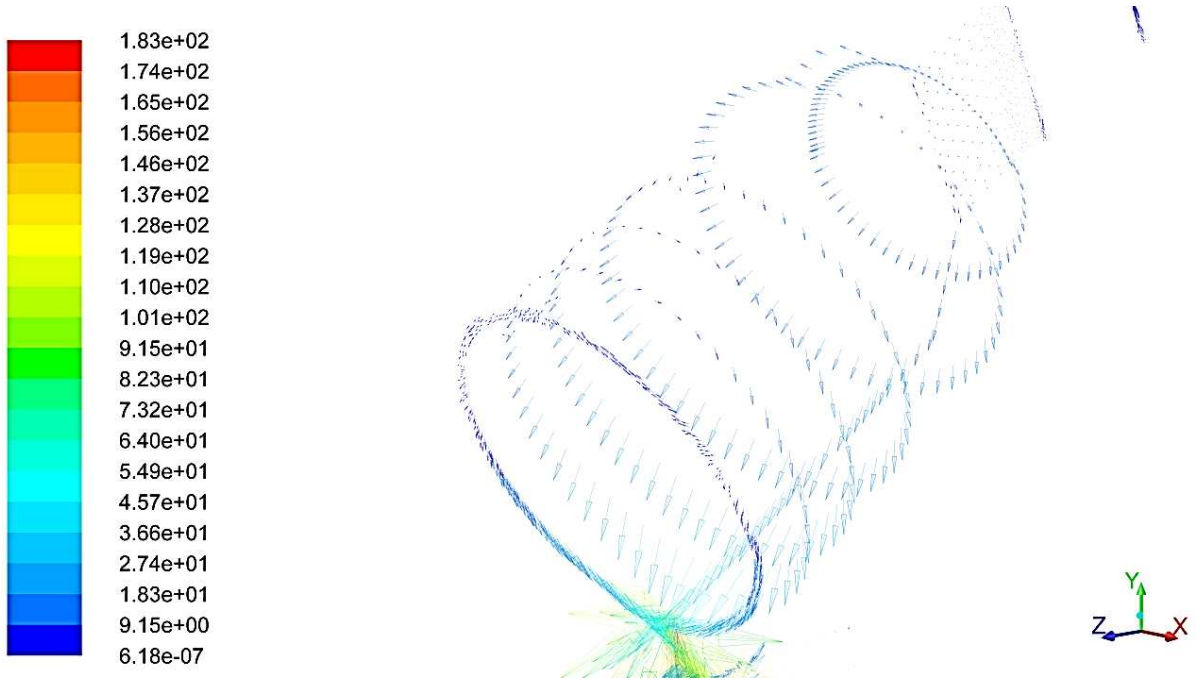

Figure 6.13: Velocity vectors inside heater at the instance of the cycle when the crank shaft angle is 270°

Figures 6.14-6.17 show the gas velocity vectors in the regenerator space for instances of the cycle when crank shaft angle is 0°, 90°, 180°and 270° respectively. Figure 6.14 shows the velocity of the gas inside the regenerator for the instance when the crank shaft angle is 0°. Here, the gas is flowing towards the cold space as the hot piston is starting its motion towards its TDC. The velocity inside the regenerator peaks at 5.17 m/s. Figure 6.15 shows the gas velocity distribution in the regenerator when the crank shaft angle is 90°. At this instance the hot piston is mid-way through towards its TDC and the gas is flowing from the hot space towards the cold space. The velocity of the gas inside the regenerator is about 8 m/s. Figure 6.16 shows the velocity of the gas inside the regenerator when the crank shaft angle is about 180°. The hot piston at this instance is in its TDC and the cold piston is mid-way through towards its TDC. The gas velocity inside the regenerator is approximately 5.22 m/s and is in the opposite direction as the gas flows from the cold space to the hot space. Finally, Figure 6.17 shows the gas velocity inside the regenerator for the instance when the crank shaft angle is 270°. The velocity peaks at 9.15 m/s as the cold piston is in its TDC. It is worth noticing that the velocity magnitude is higher when the gas flows from the cold space to the hot space due to the higher density. Overall, the velocity of the gas in the regenerator is considerably lower than in other heat exchangers due to the much greater cross-section flow area.

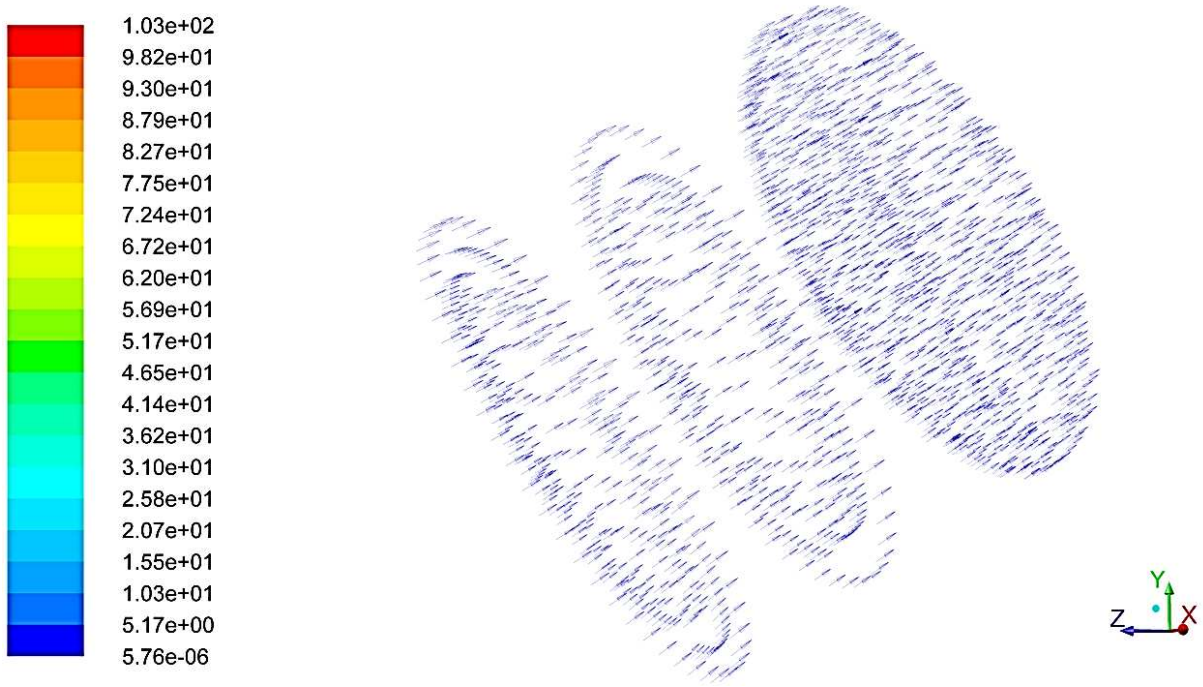

Figure 6.14: Velocity vectors inside the regenerator at the instance of the cycle when the crank shaft angle is 0°

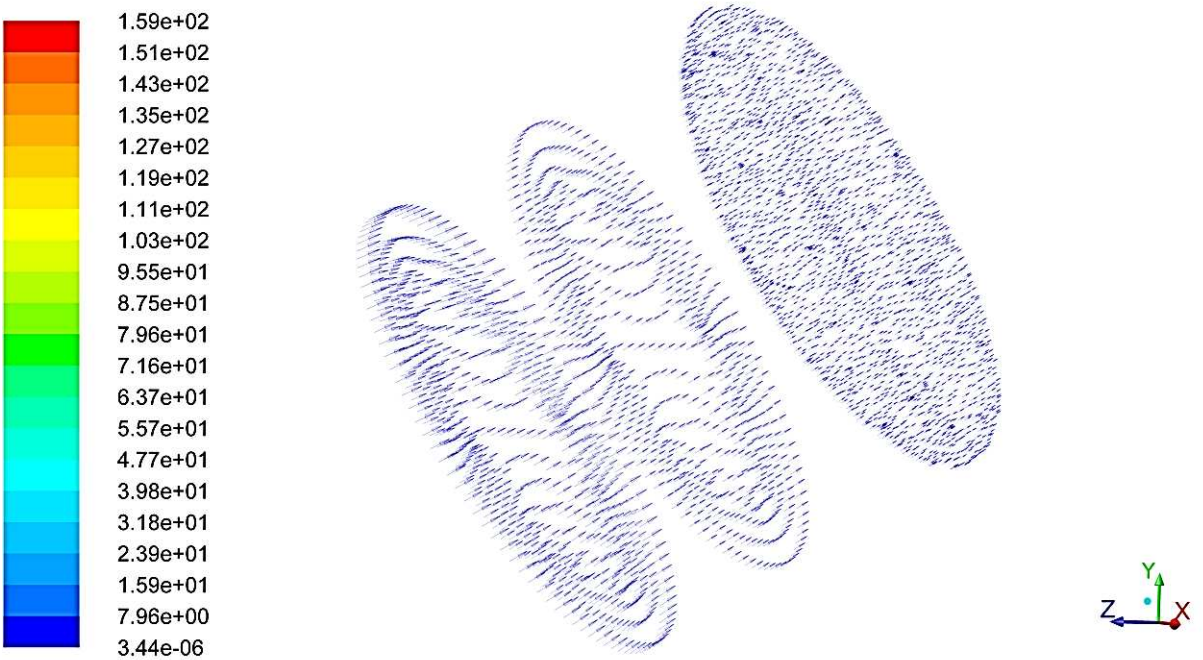

Figure 6.15: Velocity vectors inside the regenerator at the instance of the cycle when the crank shaft angle is 90°

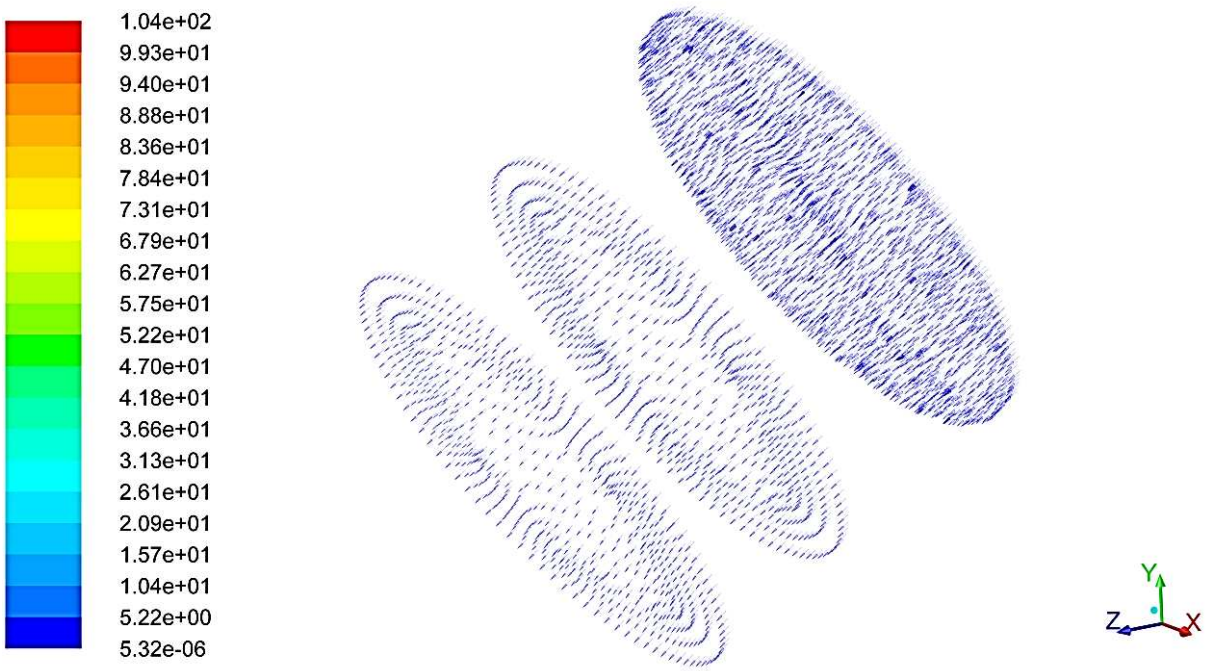

Figure 6.16: Velocity vectors inside the regenerator at the instance of the cycle when the crank shaft angle is 180°

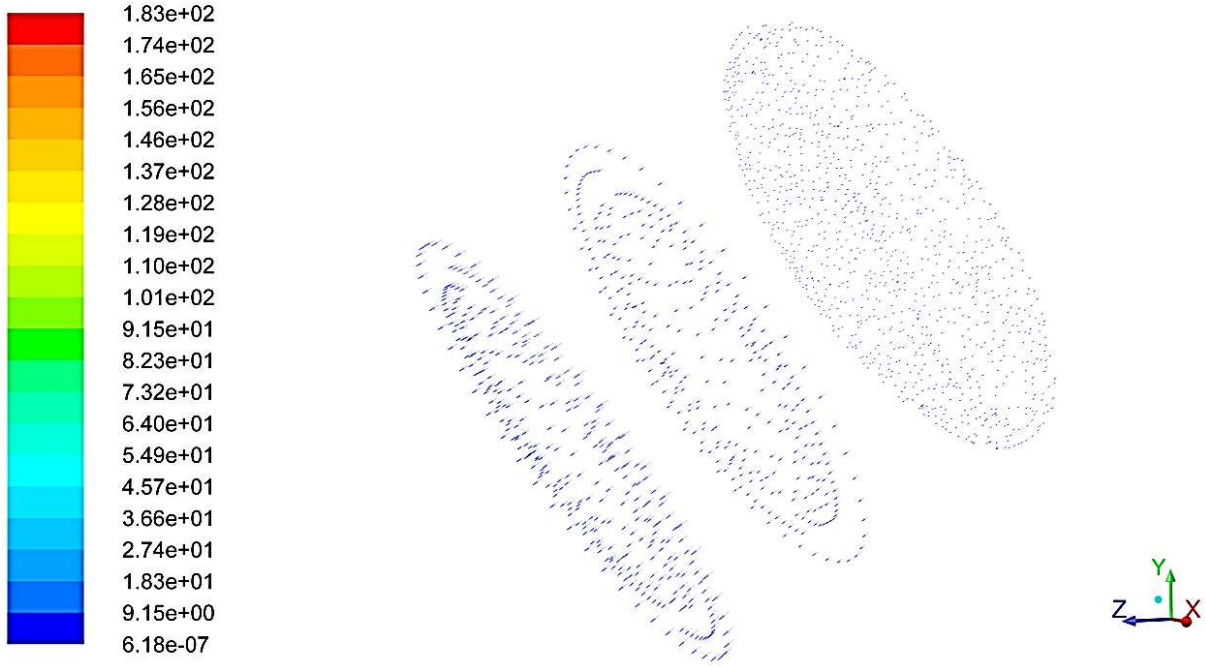

Figure 6.17: Velocity vectors inside the regenerator at the instance of the cycle when the crank shaft angle is 270°

Figures 6.18-6.21 show the velocity vectors of the gas inside the engine cooler for the same four instances of the cycle. Figure 6.18 shows the velocity vectors of the gas at 0° of the crank shaft angle. The gas now is flowing from the hot space to the cold space. The velocity peaks a 41.4 m/s and is more uniform in its magnitude than it was at 90° of the crank shaft angle. The maximum velocity occurs at the central tubes and reaches a value of 31 m/s. The lowest velocity of the gas flow is in tubes at the outer four corners of the cooler. Figure 6.19 shows the velocity vectors for the instances when the cold piston is at its BDC. At 90° of crank shaft angle (Fig. 6.19) the velocity in the cooler pipes ranges from 7.96 m/s to 15.9m/s inside the cooler and reaches approximately 47.7 m/s at the top of the cold cylinder. The velocity vectors inside the cooler pipes are of the same magnitude which demonstrates an even heat load in all pipes. In Figure 6.20 the cold piston is mid-way to its BDC (the instance of the cycle when the crank shaft angle is 180°). The velocity inside the cooler pipes is not uniform but it follows a distinct pattern. The velocity of the gas is higher in the pipes near the centre, peaking at 52.2 m/s. The velocity of the gas is also high at the pipes near the four corners of the cooler casing. The maximum velocity at these locations is 36.6 m/s. Then the velocity is lower at the tube banks around the centre with magnitudes ranging from 15.7 m/s to 26.1 m/s. Finally, Figure 6.21 shows the velocity vectors inside the cooler at the instance of the cycle when the crank shaft angle is 270°. At this instance the cold piston has reached its TDC. The velocity inside the cooler tubes ranges from 9.83 m/s to 18.3 m/s, the latter occurring inside the tubes near the centre of the cooler. It is worth noticing the recirculation area forming immediately before the cooler inlet. This happens because the gas is forced to flow in a perpendicular direction as it leaves the cooler connector pipe and travels towards the cooler tubes. The change of the flow direction in addition to the change of geometry results in the formation of the aforementioned recirculation.

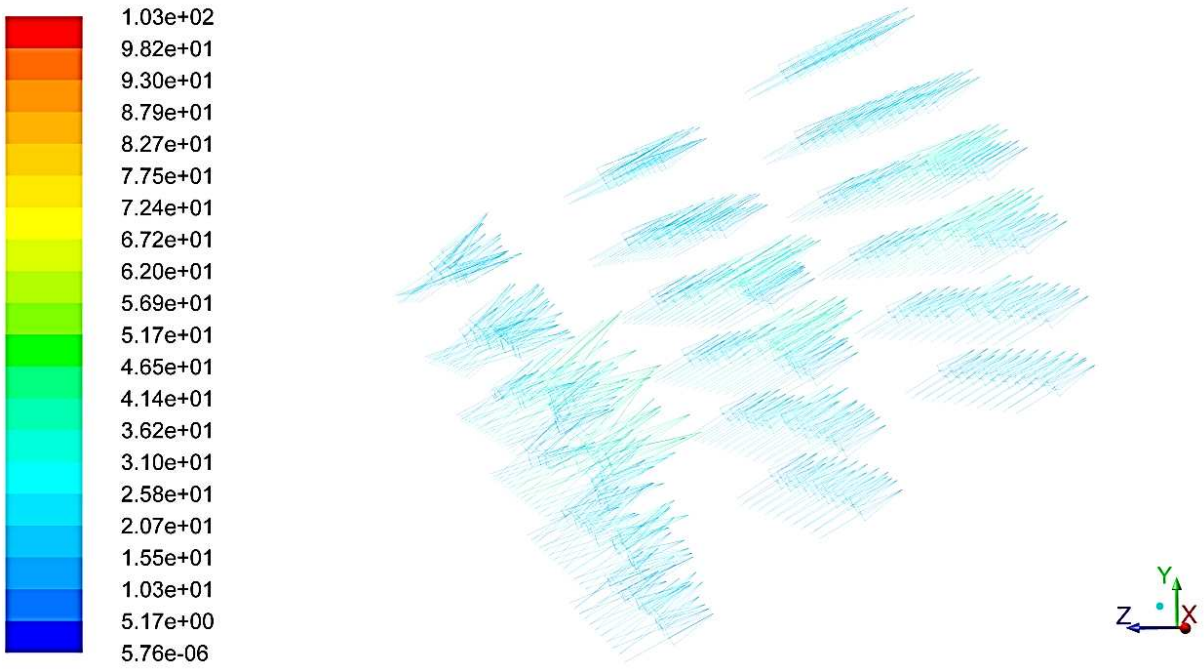

Figure 6.18: Velocity vectors inside the cooler at the instance of the cycle when the crank shaft angle is 0°

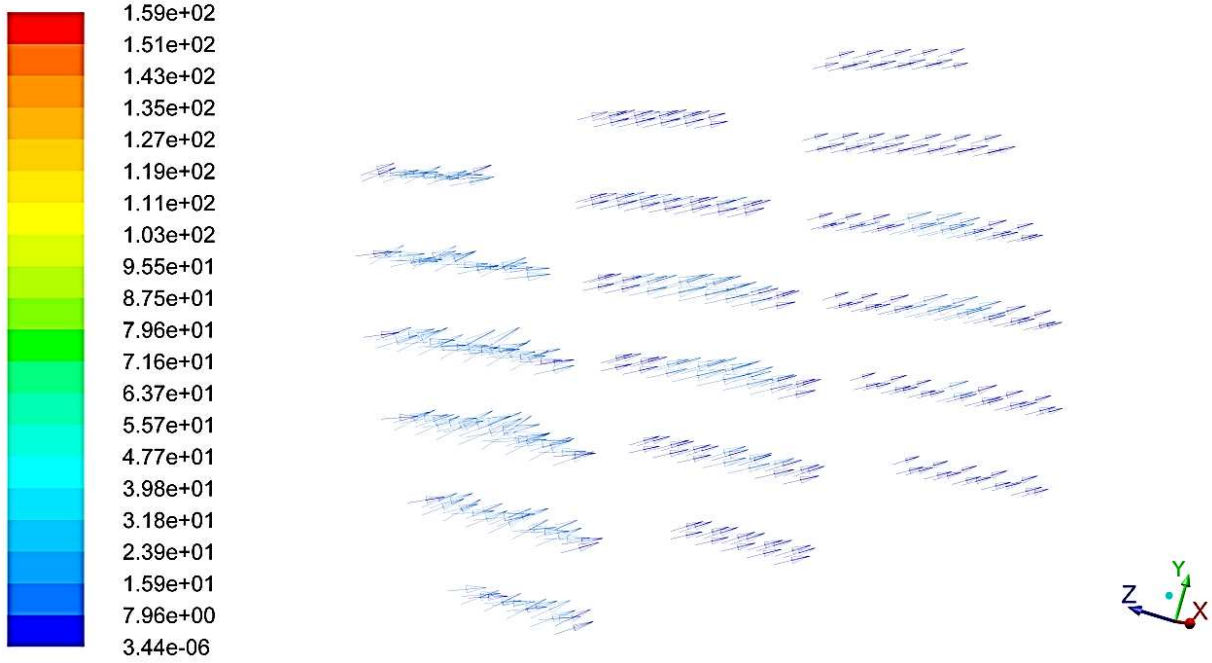

Figure 6.19: Velocity vectors inside the cooler at the instance of the cycle when the crank shaft angle is 90°

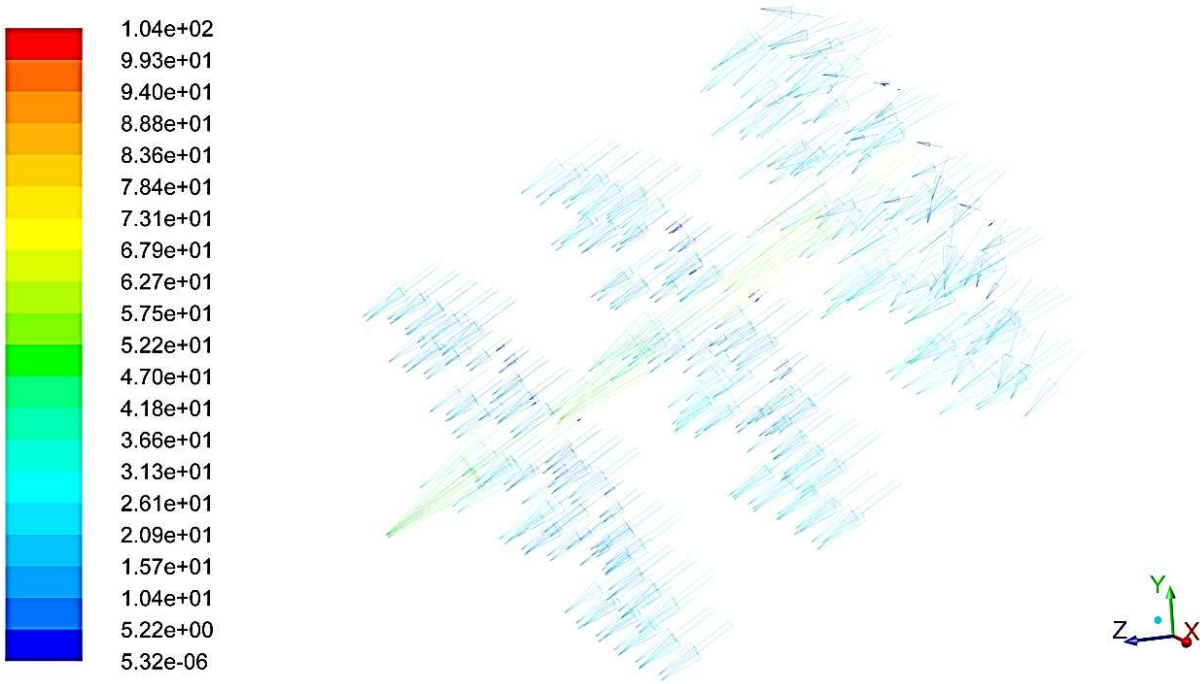

Figure 6.20: Velocity vectors inside the cooler at the instance of the cycle when the crank shaft angle is 180°

Figure 6.21: Velocity vectors inside the cooler at at the instance of the cycle when the crank shaft angle is 270°

In general, the gas velocity vector analysis demonstrates that the flow is very complex and non uniform in most of the engine components, apart from the regenerator. Visualisation of flow velocity fields and patterns could be very useful information when trying to modify the engine's design and improve heat transfer and reduce sources of hydraulic losses.

The temperature distribution inside the cavity heater is shown in Figures 6.22-6.25. Figure 6.22 presents the temperature distribution inside the heater at the instance of the cycle when the crank shaft angle is 0°. The hot piston is in its BDC and the temperature of the gas at this instance is generally lower. The temperature of the gas peaks at 725 K at the upper part of the heater. The temperature of the gas varies in the annular gap of the heater and is 650 K near the heater inlet. The gas temperature is higher when its velocity is lower i.e. there is more time for heat transfer from the heater walls to the gas. The temperature of the gas and walls is reduced in the heater towards the cavity bottom, reaching a value of the 622 K. Figure 6.23 (when the crank shaft angle is 90°) shows that the temperature inside the heater varies from approximately 600 K to 1000 K, with lower values being observed near the heater connector pipe as the gas leaves the hot cylinder and enters the heater. A high gas temperature is observed in the inner cavity adjacent to solid wall region. As anticipated, such high temperature values are obtained due to heat exchange with the surface exposed to solar radiation. The temperature of the gas varies from approximately 700 K near the inlet to the heater and reaches a peak value of nearly 834 K. The temperature is higher at the locations where the velocity of the gas is lower. Thus, in the section of annular gap of the heater near the hot cylinder, the temperature is approximately 700 K and reaches a value of 800 K on the opposite side. This is due to the fact that there is more time for heat to be transferred to the gas from walls. It also can be seen that the temperature of the heater wall varies along the heater length and its circumference. Figure 6.23 shows that the temperature of the wall is higher at the locations opposite to the heater inlet. The temperature of the wall at this area is

around 834 K, which is noticeably higher than at the opposite side, where gas velocities are higher. The temperature of the outer wall of the heater reduces from the middle of the heater towards the cavity bottom due to the reduction of the heat flux formed by the parabolic concentrator. The temperature on the upper side of the heater is approximately 800 K which is due to the low gas velocity (mass flow rate). The temperature on the lower side is approximately 700 K. At the location immediately close to the cavity bottom the temperature of the gas is 834 K on the low side of the heater where the velocity is lower and 800 K where the velocity is higher towards the upper side of the heater. This again is believed to be due to the more time available for heat to be transferred to the gas at lower velocities. At these locations the temperature at the outer walls of the heater is more uniform at the levels from 634 to 667 K.

Figure 6.24 illustrates the temperature distribution inside the heater for the instance when the crank shaft angle is 180°. It can be seen that the gas temperature at this instance of the cycle is more uniform and varies in a narrow range, namely between 938 K and 960 K. The gas has a lower temperature at the beginning of the heater and this rises as the gas flows along the heater. When the hot piston has reached its TDC and the velocity of the gas inside the heater is reduced, which also explains the higher temperatures at this instance. The temperature of the gas on the inner heater surface area and of the heater's wall is approximately 1000 K and these show no variation with the crank shaft angle. Similar to Figure 6.23, the temperature in the outer walls (next to the insulation) is higher at approximately 834 K. This reduces to approximately 800 K towards the cavity bottom and is 700 K near the cavity bottom. The lower temperature at this region is due to the closeness to the colder component, namely the regenerator.

Finally, Figure 6.25 shows the temperature variation inside the heater at 270° of the crank shaft angle. The magnitudes of temperature are similar to those presented in Figure 6.24

though the variation in space is different. The cold piston is in its TDC and the gas is now flowing from the cold space towards the hot space. The temperature of the gas at the bottom of the heater is 700 K after passing the matrix of the regenerator. The temperature then varies in the radial direction, being higher near the heating surface where it reaches 800 K. The gas is further heated up as it flows along the heater and reaches its peak temperature of nearly 968 K at the top of the heater close to the hot space. The temperature is lower (around 800 K) where the velocity of the gas is high at the lower side of the heater in its middle section. This is due to shorter residence time which restricts the amount of heat transferred to the gas. For the instances when the crank shaft angle is 0° and 270° the outer wall of the heater is at a higher temperature than the working gas.

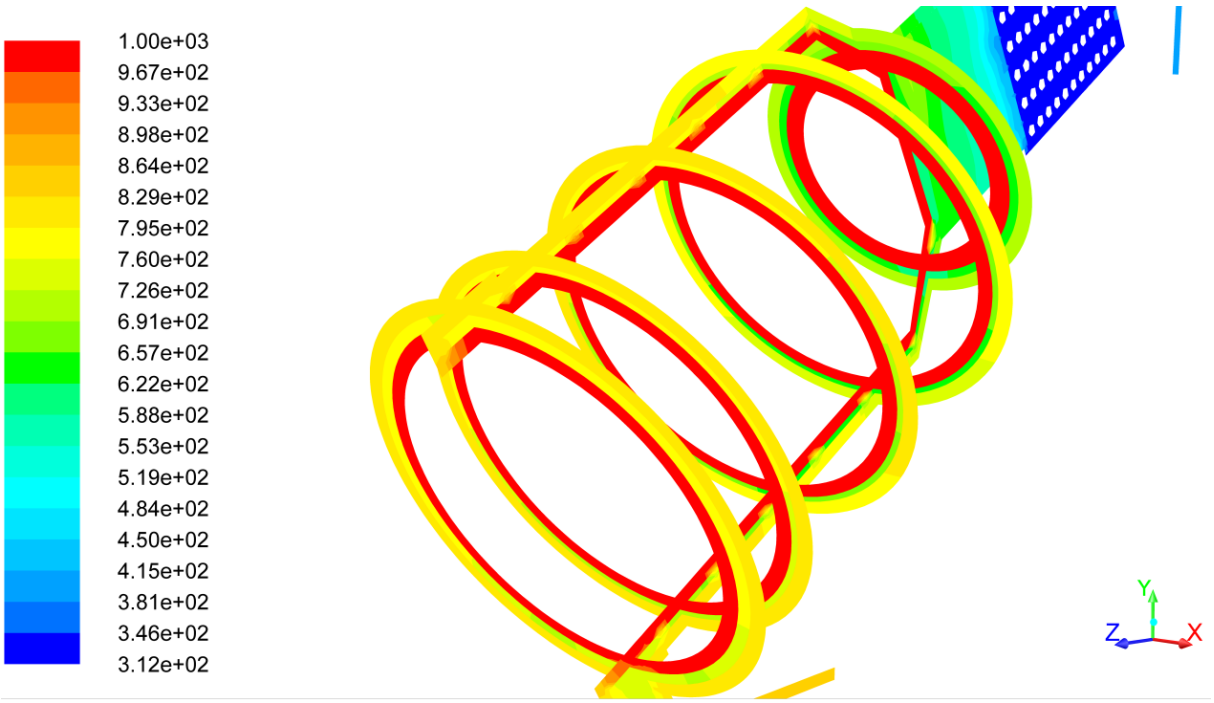

Figure 6.22: Temperature contours inside the heater at the instance of the cycle when the crank shaft angle is 0°

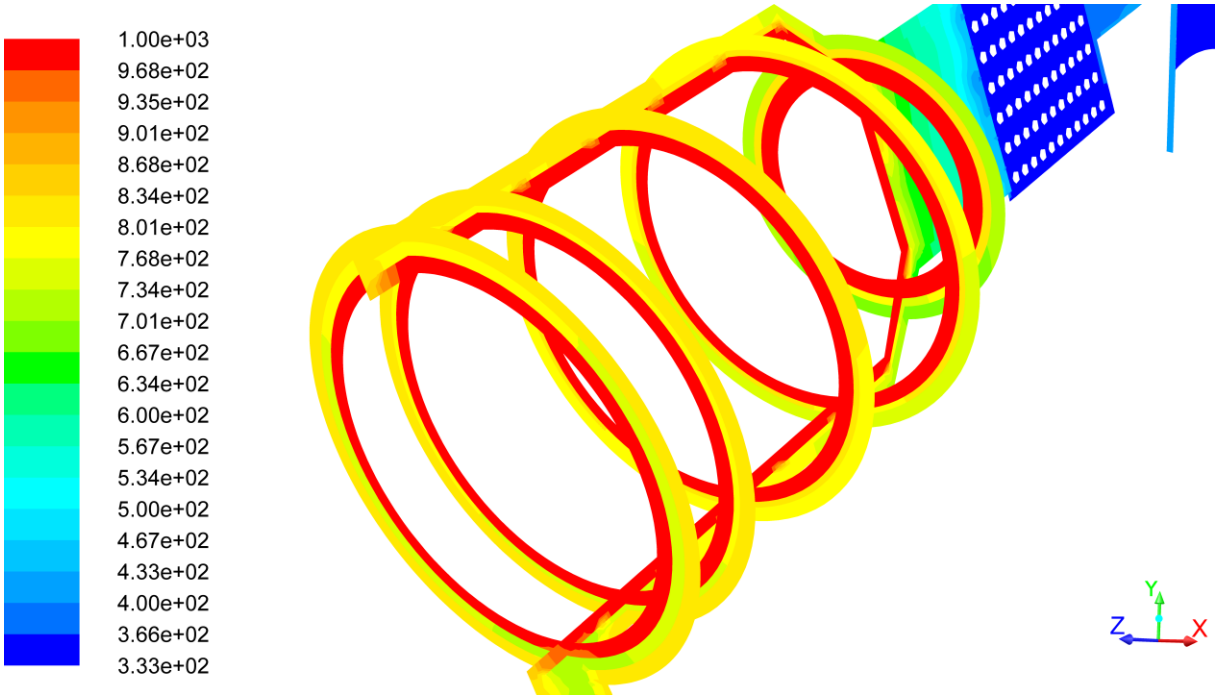

Figure 6.23: Temperature contours inside the heater at the instance of the cycle when the crank shaft angle is 90°

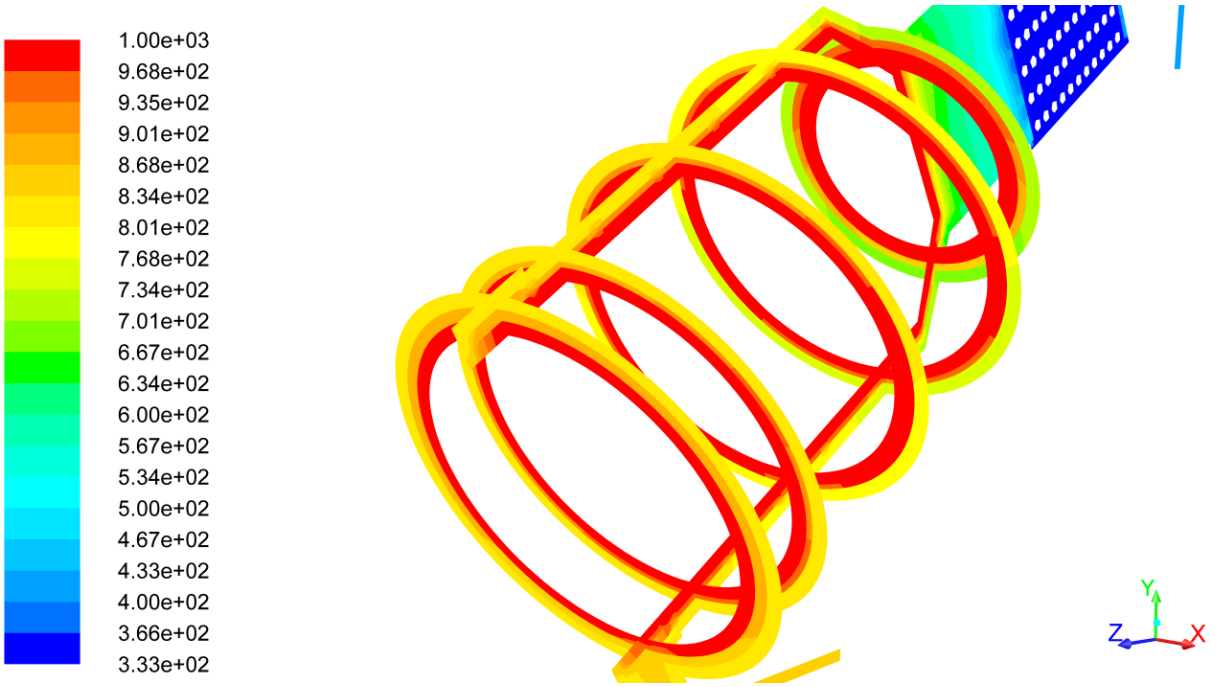

Figure 6.24: Temperature contours inside the heater at the instance of the cycle when the crank shaft angle is 180°

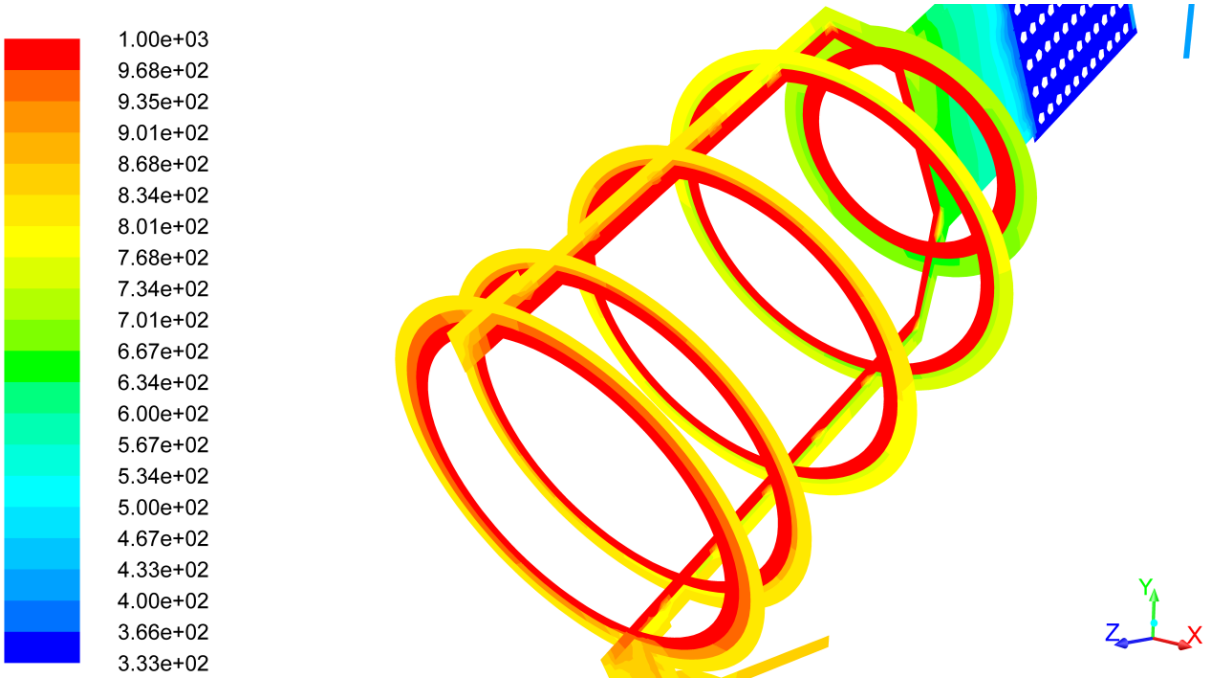

Figure 6.25: Temperature contours inside the heater at the instance of the cycle when the crank shaft angle is 270°

For a more detailed and accurate analysis, several monitoring points were set up at various locations inside the gas and walls in different parts of the engine as shown in Figure 6.26.

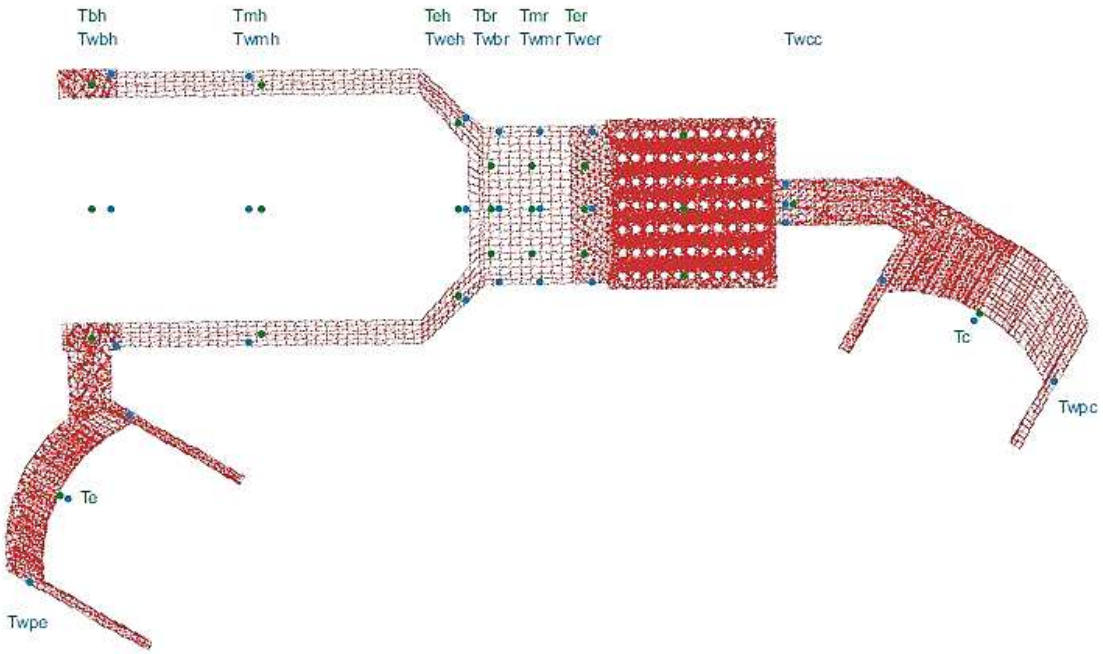

Figure 6.26: Location of monitoring points in different parts of the engine

Figure 6.26 shows a cut-plane of the computational domain. The monitoring points are placed in a group of four in corresponding planes labelled in such way in order to indicate their location. The description of the abbreviations used for the labelling of the monitoring points is presented in Table 6.2.

Table 6.2: List of data monitoring points

Label	Description
Tbh	Gas Temperature at the beginning of the heater
Twbh	Wall Temperature at the beginning of the heater
Tmh	Gas Temperature at the middle of the heater
Twmh	Wall Temperature at the middle of the heater
Teh	Gas Temperature at the end of the heater
Tweh	Wall Temperature at the end of the heater

Tbr	Gas Temperature at the beginning of the regenerator
Twbr	Wall Temperature at the beginning of the regenerator
Tmr	Gas Temperature at the middle of the regenerator
Twmr	Wall Temperature at the middle of the regenerator
Ter	Gas Temperature at the end of the regenerator
Twer	Wall Temperature at the end of the regenerator
Tmc	Gas Temperature at the middle of the cooler
Tcc	Gass Temperature inside the cooler connector pipe
Te	Average Temperature recorded on the surface of the hot piston
Twpe	Temperature recorded inside the wall of the hot cylinder
Tc	Average Temperature recorded on the surface of the cold piston
Twpc	Temperature recorded inside the wall of the cold cylinder

The numbering of four monitoring points in any of planes is shown in Figure 6.27 relative to local coordinates of the heater. Thus point 1 is located on the lower edge of the component (negative y axis), point 3 is located on the upper edge of the heater (positive y axis), point 2 is located on the right edge (positive x axis) and finally point 4 is located on the left edge of the component (negative x axis).

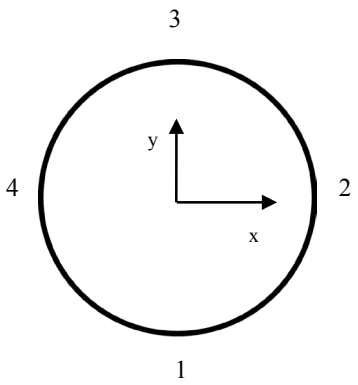

Figure 6.27: Location of monitoring points in the cut plane of the heater

Figures 6.28 – 6.30 demonstrate the temperature variation at various circumferential locations across three planes, the beginning, middle and end of the heater, inside both the gas and the wall regions during the engine cycle.

Figure 6.28 shows the gas temperature variation over the cycle in Tbh1 monitoring point (in the annular gap in the beginning of the heater at its lower part). The gas temperature in this area is approximately 737.5 K at 0° of the crank shaft angle and reaches its minimum value of 705 K at about 60° of crank shaft angle. Then it steeply rises to 860 K at 180° of the crank shaft angle, followed by the further sharp increase up to 980 K at 210° of the crank shaft angle. Then the temperature drops steeply to 825 K at 270° of the crank shaft angle with a further drop to 725 K at 355°. There is small fluctuation of the temperature observed during the very last phases of the cycle and this may be due to the mesh being not sufficiently fine near the monitoring point. The curve obtained from the recording at the second monitoring point of the same plane (the right side of the annular gap in the beginning of the heater) shows that the gas temperature in the beginning of the cycle is at 770 K and reaches its minimum value of approximately 750 K at 32° of the crank shaft angle. This is followed by a gradual increase to nearly 1000 K at 245° of the crank shaft angle. Then the temperature at this location drops rapidly to 770 K at the end of the cycle. The gas temperature at the exact opposite location follows nearly the same pattern. The main difference is that it reaches its peak value of 990 K slightly earlier (at 240° of the crank shaft angle) and then drops to 770 K in a way similar to that for the curve corresponding to the monitoring point Tbh2. The temperature recorded in the point Tbh3 (the annual gap in the beginning of the heater in its top part) follows a different pattern. In the beginning of the cycle the temperature is at 777 K and drops to its lower value of 760 at 30° of the crank shaft angle. This is then followed by a gradual increase to 925 K at 222° of the crank shaft angle. Then the temperature slowly drops to its initial value in the beginning of the cycle. The temperature in the wall region remains

constant at 810.6 K in monitoring points Twbh2 and Twbh4 (in the beginning of the heater on its right and left sides) and at 801.77 K in monitoring locations, namely Twbh1 and Twbh3 (at the beginning of the heater in its bottom and upper sides). In Figure 6.25 wall temperatures recorded only in Twbh1 and Twbh2 are shown.

Figure 6.29 shows the gas temperature distribution and temperatures in the wall region in the middle of the heater. In the point Tmh1 (in annular gap in the middle of the heater in its bottom part) the gas temperature is 655 K in the beginning of the cycle and then increases almost in a linear fashion to 755 K at 50° of the crank shaft angle. Then it rises smoothly up to the peak value of 955 K at 210° of the crank shaft angle. This is then followed by a steep drop to 760 K at 255° of the crank shaft angle and then gradually returns to its initial value. It also can be seen in Figure 6.29 that the gas temperature at Tmh3 (the top of the heater) changes between 775 and 950 K over the engine cycle. The temperature of gas recorded from monitoring point Tmh2 has a value of 730 K at the beginning of the cycle and reaches its maximum value of about 1002 K at 201° of the crank shaft angle, followed by a drop to the minimum value of 723 K at 328°. Then it rises to its initial value towards the end of the cycle. Those values were consistent in both $x \neq 0$ locations (in the annular gap in the middle of the heater in the left and right sides). The increased amplitude together with the different phase is attributed to the increased velocity gradients in the respective location as can be seen from Figures 6.10-6.13. Temperature of walls in this part of the heater is constant and is about 811 K.

Figure 6.30 shows the temperature distribution inside the gas and in solid walls near the end of the heater. The gas temperature at the point Teh1 (in the annular gap at the low part in the end of the heater) is 621.7 K in the beginning of the cycle and rises almost linearly to 890 K at 162° of the crank shaft angle. Then, it drops steeply to 733 K at 205° of the crank shaft angle. During the remaining part of the cycle the gas temperature further drops to its

minimum value of 614 K at 335° of the crank shaft angle. The gas temperature in the point Teh3 (in the annular gap on the top side in the end of the heater) is 652 K in the beginning of the cycle. This temperature sharply rises to 764 K at 38° of the crank shaft angle. This rise is followed by further increase so the gas temperature peaks at the value of 950 K at 189° of the crank shaft angle. The temperature then drops steeply to 747 K at 225° followed by a smooth drop to its minimum value of 644 K at 350°. The two points with their $x \neq 0$, namely Teh2 (in the annular gap on the right side in the end of the heater) and Teh4 (in the annular gap on the left side in the end of the heater), have almost the same gas temperature values and hence only the temperature curve for point Teh2 is shown in Figure 6.27. At the beginning of the cycle, the temperature has a value of 648 K. The gas temperature in this point then rises to its peak value of 936 K at 165° of the crank shaft angle and drops steeply to the 732 K level at 221° of the crank shaft angle. This is then followed by a further drop to the minimum temperature value of 643 K at 323° of the crank shaft angle. The gas temperature then rises slowly for the rest of the cycle. The temperature inside of the walls in different locations was consistently uniform in the end of the heater and hence the wall temperature only in a single point, namely Tweh3 (the top part of the heater) is presented in Figure 6.30. The values recorded in heater walls in this region are constant at 685.7 K level throughout the engine cycle.

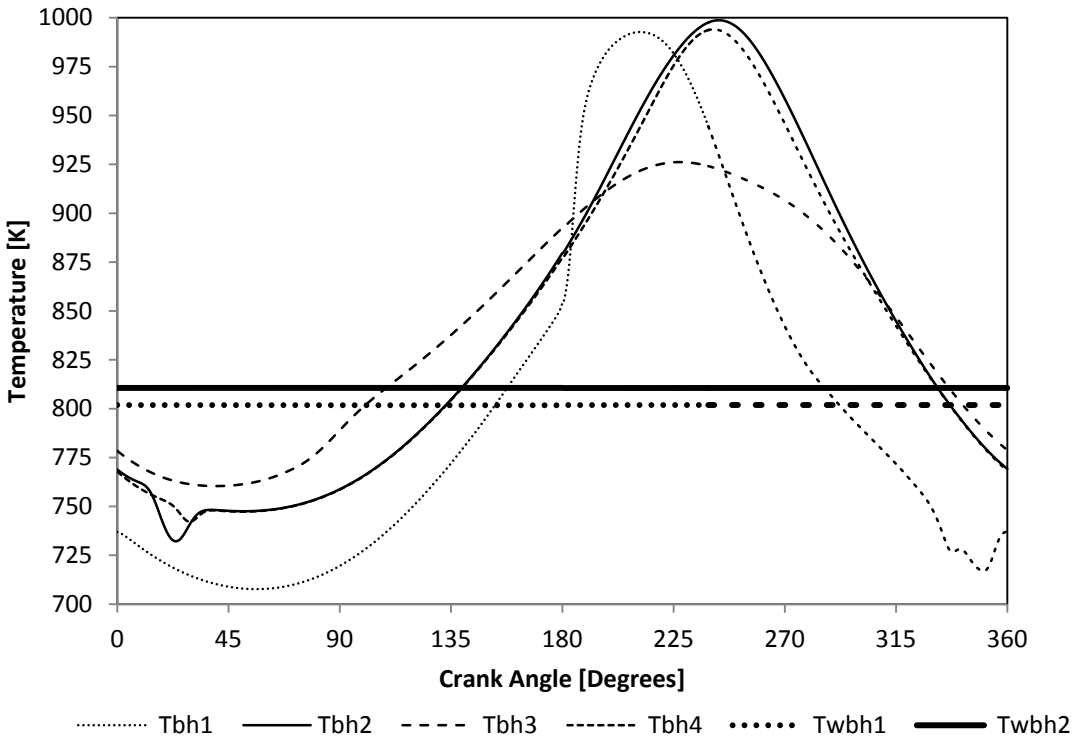

Figure 6.28: Temperature variation at the beginning of the heater during the working cycle

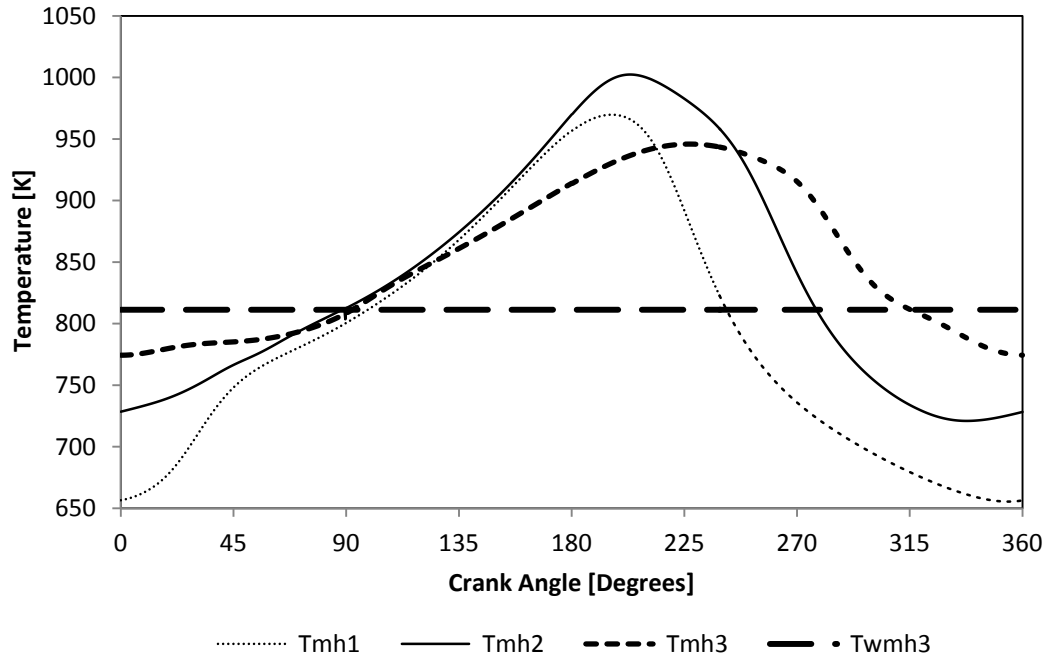

Figure 6.29: Temperature variation at the middle of the heater during the working cycle

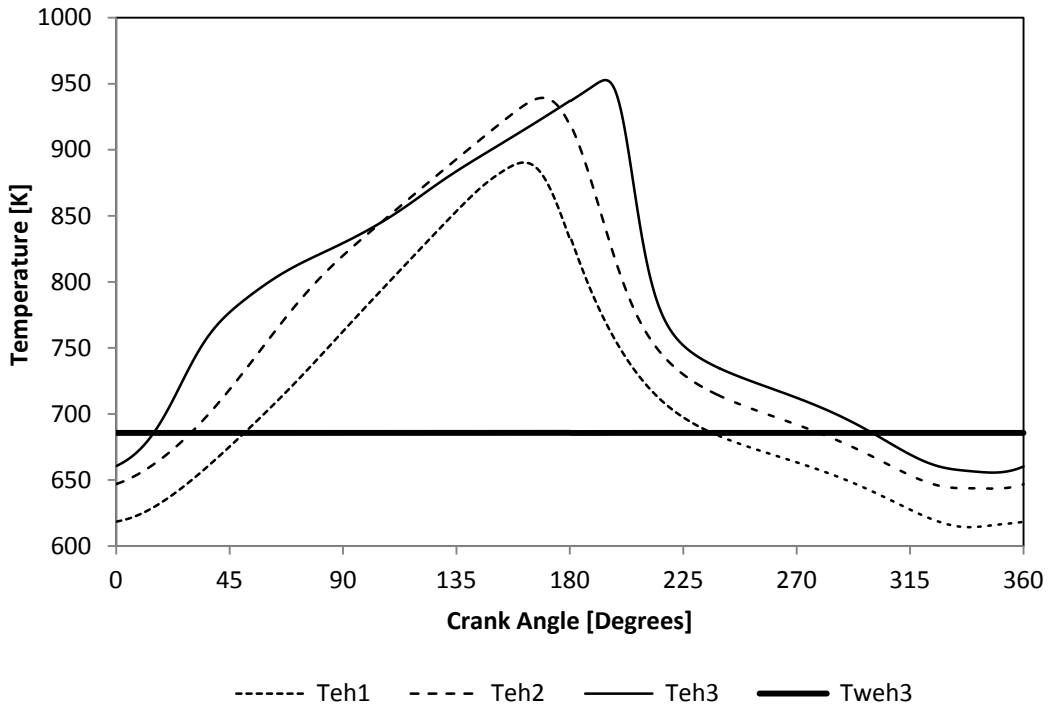

Figure 6.30: Temperature variation at the end of the heater during the working cycle

From the information presented in Figures 6.28-6.30 it can be concluded that the gas temperature distribution is not uniform inside the heater and ranges depending on the location. Albeit periodic, the temperature distribution inside the heater is not a harmonic function. The different patterns in the variation of the gas temperature in various locations are affected by the distribution of the gas mass flow rate and this determines the phase angle and amplitude of the temperature curves. At the same time the temperature of walls is constant and has approximately the same value in a cross section of the heater.

Figure 6.31 presents the labelling of the monitoring points which were set up in the porous zone of the regenerator. Here, for the gas temperature monitoring five points were set up, namely on the axis of the regenerator (2), radially along the y axis (1 – the bottom of the regenerator, 3 – the top of the regenerator) and radially along the x axis (4 – the left side of the regenerator, 5 – the right side of the regenerator). Similarly, four monitoring points were

specified inside the solid region of the regenerator. The labelling of the monitoring points inside the walls of the regenerator follows the scheme shown in Figure 6.27.

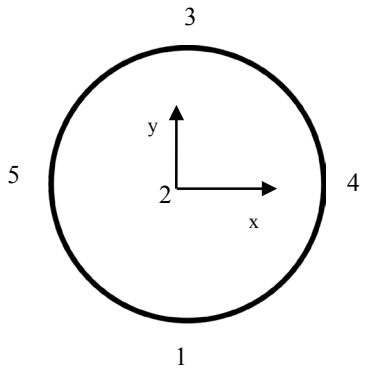

Figure 6.31: Location of monitoring points in the cut plane of the porous zone of the regenerator

The temperature distribution in the gas and walls of the regenerator is illustrated in Figures 6.32-6.34. Figure 6.32 shows the temperature distribution inside the gas and walls at the beginning of the regenerator. The temperature measured in the bottom of the regenerator (Tbr1) is 625 K at in the beginning of the cycle and rises to its peak value of 746 K at 148° of the crank shaft angle. This is then followed by a steep drop to 673 K at 204° of the crank shaft angle and further slow drop to the minimum value of 631.7 K at approximately 354° of the crank shaft angle. The gas temperature recorded in the centre of the regenerator (Tbr2) follows a different pattern starting from a minimum value of 630 K in the beginning of the cycle and rising steeply to its peak value of 778 K at 152° of the crank shaft angle. Then it drops quickly to 687 K at 219° of the crank shaft angle, followed by a slower drop towards the end of the cycle. The temperature recorded at the top of the regenerator (Tbr3) starts from 675 K in the beginning of the cycle and then rises steeply in a linear fashion to 736 K at 48.6° of the crank shaft angle. This is followed by a slow increase to the peak value of 808 K at 154.8° of the crank shaft angle. Then it drops rapidly to 723.5 K at 284° of the crank shaft

angle. Afterwards, it gradually reduces to the minimum value of 670 K at 340° of the crank shaft angle. From there the temperature rises again up to the end of the cycle. The gas temperatures at the two monitoring points 4 and 5 (left and right sides of the regenerator) are almost identical. In the beginning of the cycle the temperature has a value of 655 K which then rises to the peak value of 789 K at 143.4° of the crank shaft angle. Similar to the other curves, the temperature rapidly drops to 699 K at 200° of the crank shaft angle which is then followed by a slow reduction to the minimum value of 654 K at 344.5° of the crank shaft angle. After that instance the temperature keeps rising up to the end of the cycle.

Temperature data obtained from the monitoring points located inside the walls in the beginning of the regenerator show a non-uniform temperature distribution. The wall temperature in the bottom of the regenerator (Twbr1) registered a constant temperature of 643.8 K during the engine cycle. The wall temperature in the upper part of the regenerator (Twbr3) is constant during the engine cycle and equal to 673 K, which is approximately 29.2 K higher than at the bottom part. The wall temperatures on the left and right side of the regenerator (Twbr2 and Twbr4) are constant and have the same value of 658 K. Only temperature in the point Twbr2 is shown in Figure 6.32.

The temperature distribution in the walls and in the gas in the beginning of the regenerator is believed to be strongly affected by the pattern of the gas flow coming out of the heater and the temperature distribution in the end of the heater, see Figure 6.30. It can be seen that the trend in the temperature variation over the cycle and its distribution are very similar in Figures 6.30 and 6.32.

Figure 6.33 shows the temperature variation in the gas and walls in the middle section of the regenerator. The temperature of the gas at the bottom part of the regenerator (Tmr1) is 598.5 K in the beginning of the cycle. Then it rises gradually to its peak value of 600 K at 179° of

the crank shaft angle. The temperature then drops slowly to its lower value near the end of the cycle. It can be seen that the gas temperature variation at the point Tmr1 has a harmonic character with a low amplitude of only 1.5 K. This is attributed to the relatively low velocity of the gas at the middle of the regenerator due to the high flow cross section area and high heat transfer area. The temperature at this point peaks near 180° of the crank shaft angle, considerably later than the gas temperature at the beginning of the regenerator. This can be explained by the effect of hydraulic resistance in the regenerator matrix. These results are consistent with results obtained in the other monitoring points. Particularly, the gas temperature recorded in the centre of the regenerator (Tmr2) has a minimum value of 603 K in the beginning of the cycle which then rises to 605° at approximately 180° of the crank shaft angle. Then it slowly reduces to its initial value by the end of the cycle. The gas temperature variation recorded at the top of the regenerator (Tmr3) follows a similar pattern. The minimum value of the gas temperature is 615.5 K in the beginning of the cycle peaking at 617 K at 180° of the crank shaft angle. The gas temperatures recorded on the left and right sides in the regenerator follow nearly identical patterns. The minimum gas temperature value is 608.7 K in the beginning of the cycle peaking at 610.1 K at 179.5° of the crank shaft angle. The temperatures recorded in the walls of the regenerator are found to be constant throughout the cycle but to have different values. Thus, the wall temperature at the bottom part of the regenerator (Twmr1) is constant at 595.7 K throughout the engine cycle. The temperature in the walls on the right side of the regenerator (Twmr2) is 603.5 K and this is identical with the wall temperature at the opposite location (Twmr4). Finally, the wall temperature in the top of the regenerator (Twmr3) is 613.33 K.

Figure 6.34 shows the temperature variation and its distribution in the gas and wall in the end section of the regenerator. In the bottom part of the regenerator the gas temperature is 492.7 K in the beginning of the cycle. The gas temperature then increases and reaches its peak

value of 499 K at 180° of the crank shaft angle. Then it drops to the minimum value of 491 K at 295° of the crank shaft angle. The gas temperature at the centre of the regenerator (Ter2) is 470 K in the beginning of the cycle and reaches its peak value of 472 K at 179.7 ° of the crank shaft angle. The minimum value of 467 K occurs at 294° of the crank shaft angle. The gas temperature recorded at this location was the lowest compared to temperatures in other parts of the regenerator in its end section. The gas temperature in the upper part of the regenerator (Ter3) is 501 K in the beginning of the cycle and peaks at 504 K at 180° of the crank shaft angle. The temperature then drops to the minimum value of 500.5 K at 293° of the crank shaft angle. The gas temperatures on the right and left sides of the regenerator (Ter4 and Ter5) differ by approximately 2.5 K. In the beginning of the cycle the gas temperatures are 492.8 K and 490.24 K, respectively, peaking at 495 K and 492.5 K at 182° of the crank shaft angle with a minimum value of 491 K and 488.5 K, respectively, at 279° of the crank shaft angle. The gas temperature variations recorded near the end of the regenerator have the harmonic character. Furthermore, the temperature levels at the end of the regenerator are closer to those in the cooler. The temperature magnitude reduces along the regenerator axis and also due to the relatively high hydraulic resistance there is a shift angle in temperature variations inside the regenerator along its axis. The temperatures in the walls of the regenerator near its end section are constant throughout the engine cycle but at different values. Moreover, the wall temperatures are higher than inside the gas region. This is due to the heat losses from the heater region being transferred along the regenerator walls which are additionally insulated from outside. Thus, the wall temperatures at the bottom (Twer1) and upper (Twer3) parts of the regenerator are 519 K and 524 K, respectively. The wall temperature on the right (Twer2) and left (Twer4) sides of the regenerator are 518 K and 520.2 K, respectively.

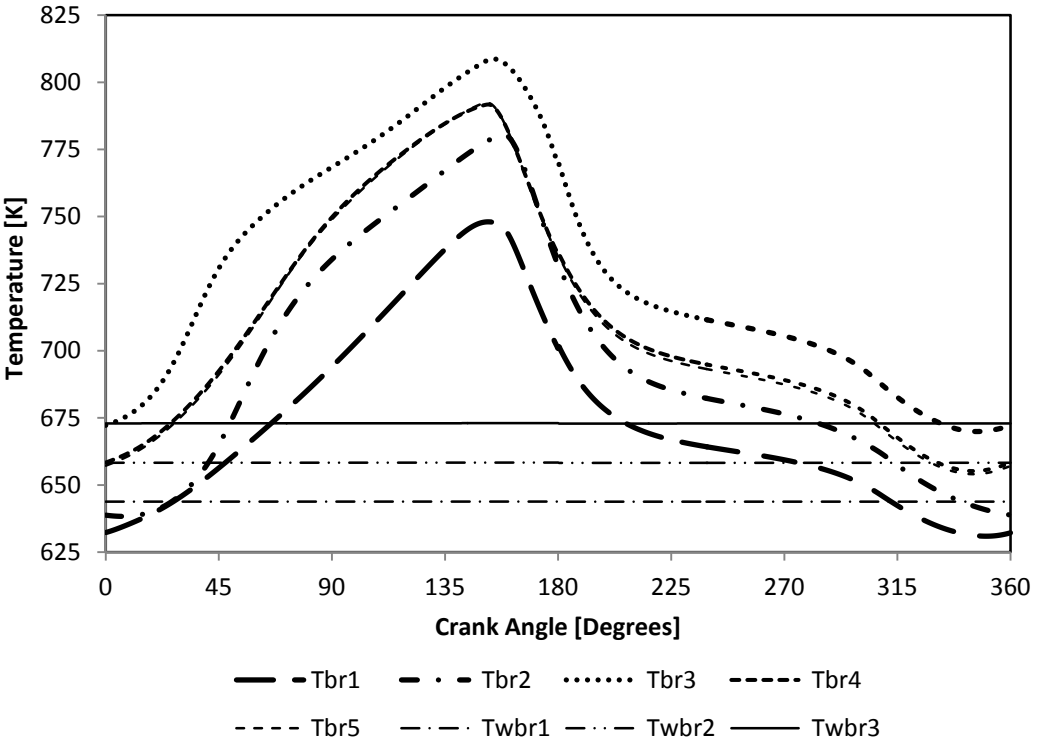

Figure 6.32: Temperature variation at the beginning of the regenerator during the working cycle

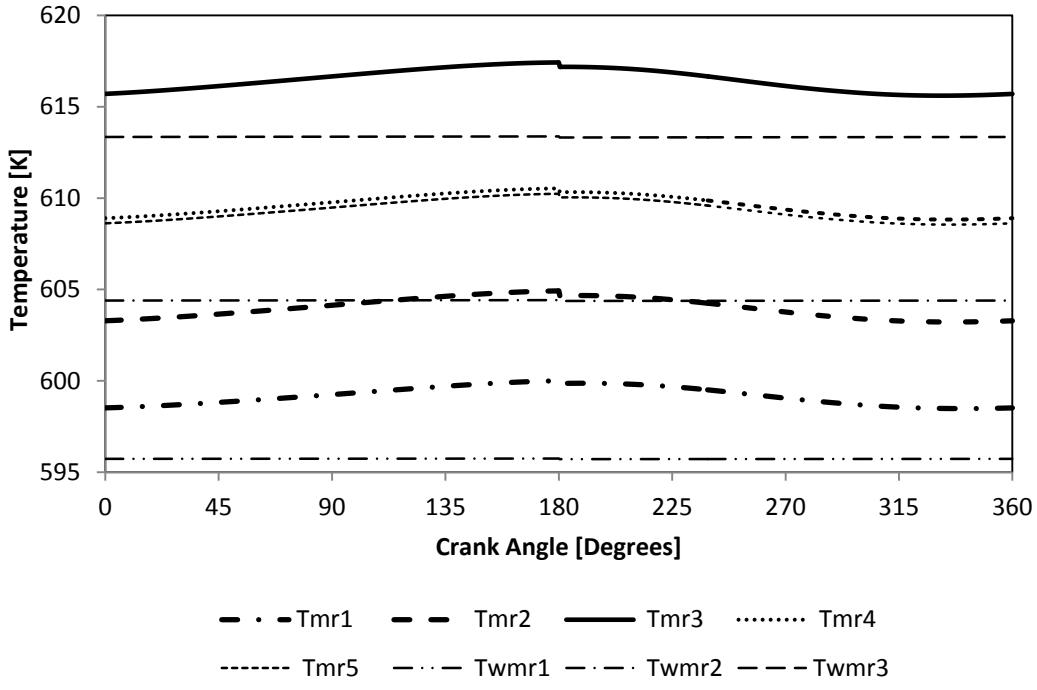

Figure 6.33: Temperature variation at the middle of the regenerator during the working cycle

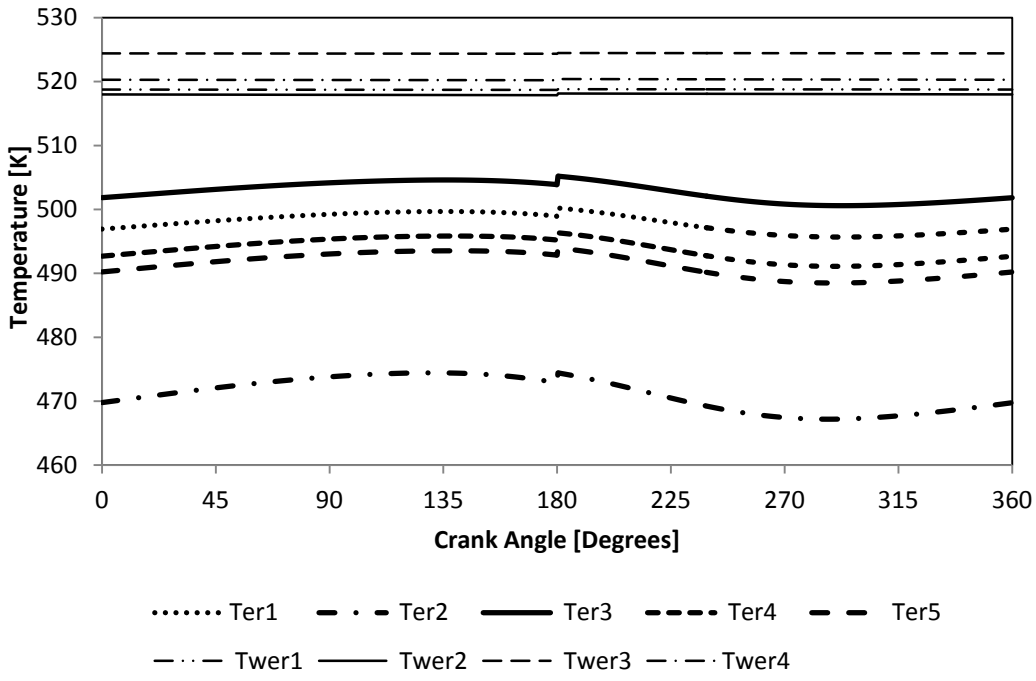

Figure 6.34: Temperature variation at the end of the regenerator during the working cycle

From information presented in Figures 6.32 - 6.34 it can be concluded that the gas mass flow rate is higher in the upper part of the regenerator in its beginning and middle section. This is defined by the design of the engine under consideration. The temperatures near the beginning of the matrix are higher and their variation also has greater amplitudes like those in the exit from the heater. The temperature of the gas is then stabilised towards the middle section of the regenerator and the gas temperature is generally lower and its variation also has lower amplitude. The same effect can be observed in the end section of the regenerator.

The above findings are also confirmed with data in Figures 6.35-6.38. These Figures present the collected temperature data in the form of temperature contours in three cut planes along the axis of the regenerator (in the beginning, middle and the end of the regenerator) for different instances in the cycle. It can be seen that at the beginning of the regenerator the flow is asymmetrical. In its turn, this is caused by asymmetrical flow in the heater due to location

of the connecting pipe between the hot space and heater. There is a higher mass flow rate of the gas in the upper half of the annular gap in the heater and this stream is then deflected by the conical part of the end section of the heater towards the upper part of the regenerator (zone with higher temperatures in the first cut plane of the regenerator). The flow, and consequently temperature distribution, becomes more uniform whilst the working fluid flows along the axis of the regenerator towards its end.

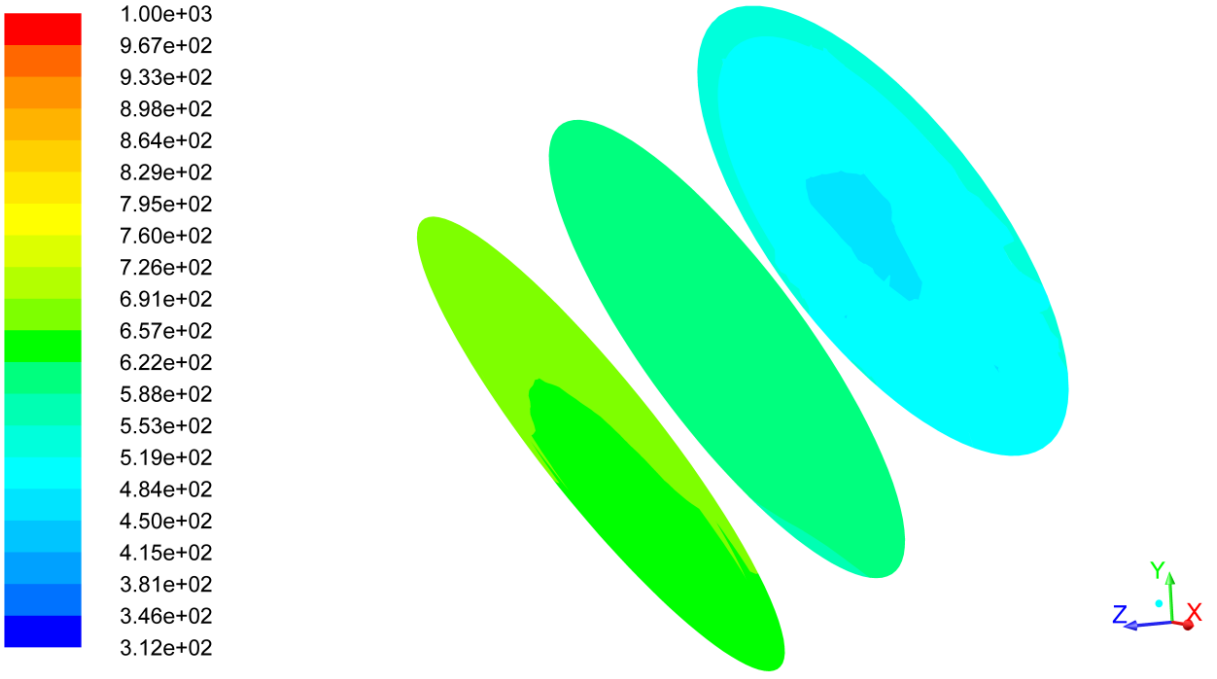

Figure 6.35: Contours of temperature inside the regenerator at the instance of the cycle when the crank shaft angle is 0°

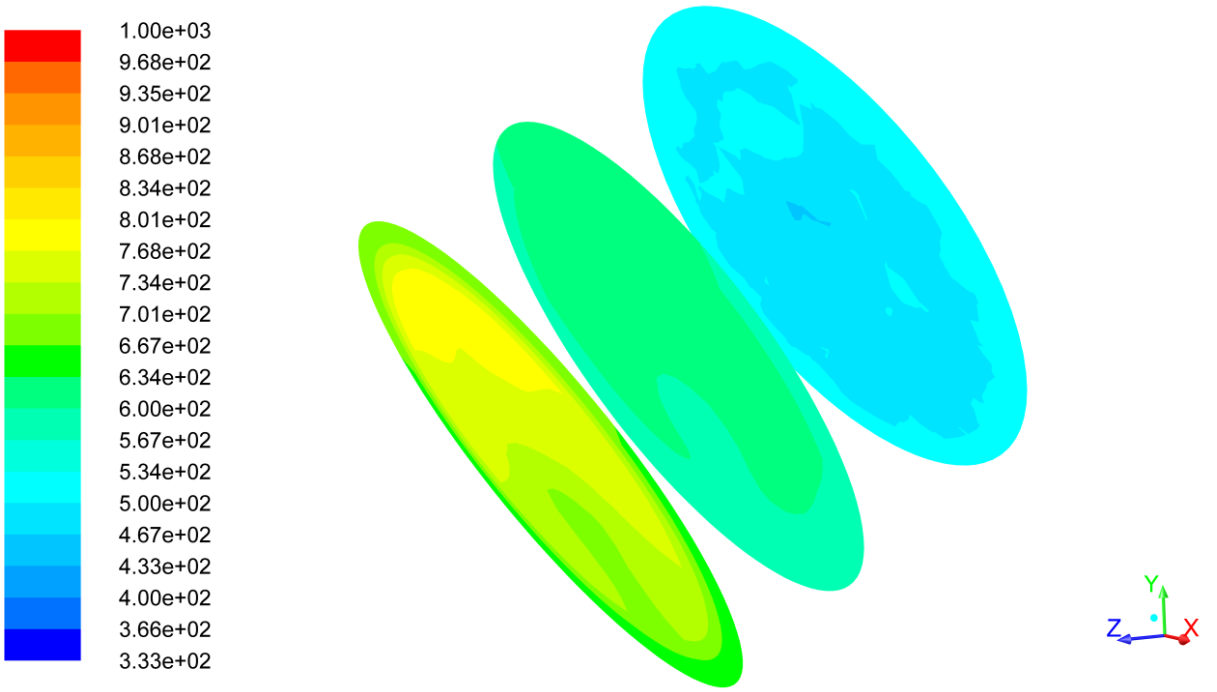

Figure 6.36: Contours of gas temperature inside the regenerator at the instance of the cycle when the crank shaft angle is 90°

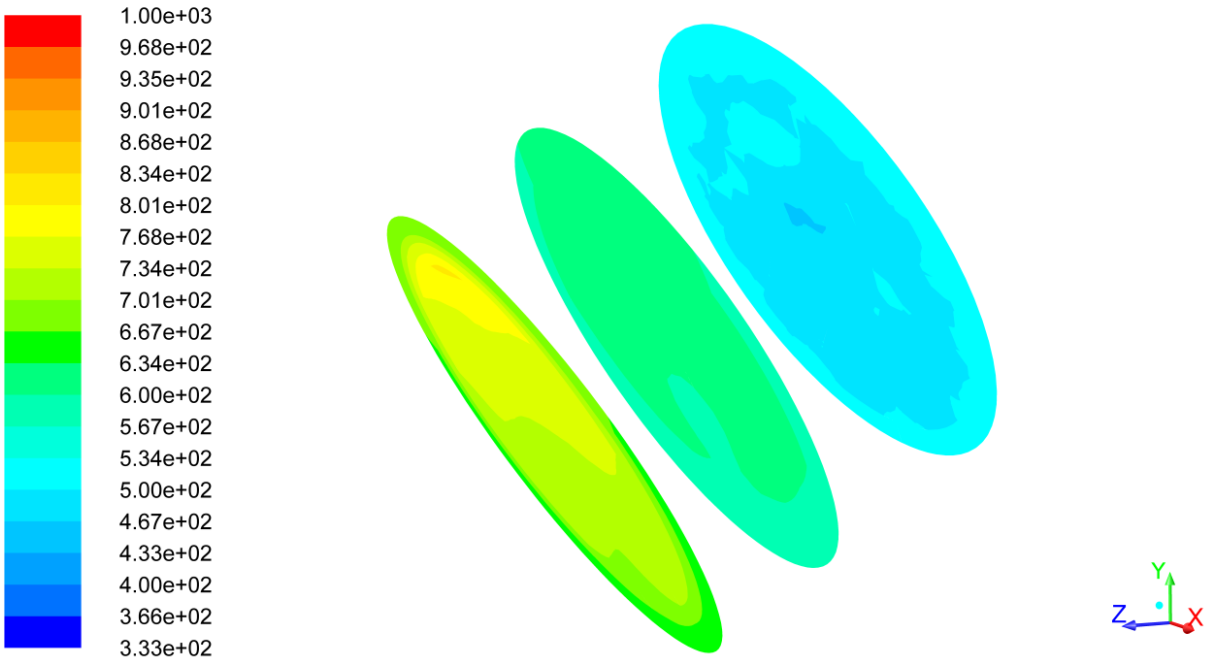

Figure 6.37: Contours of temperature inside the regenerator at the instance of the cycle when the crank shaft angle is 180°

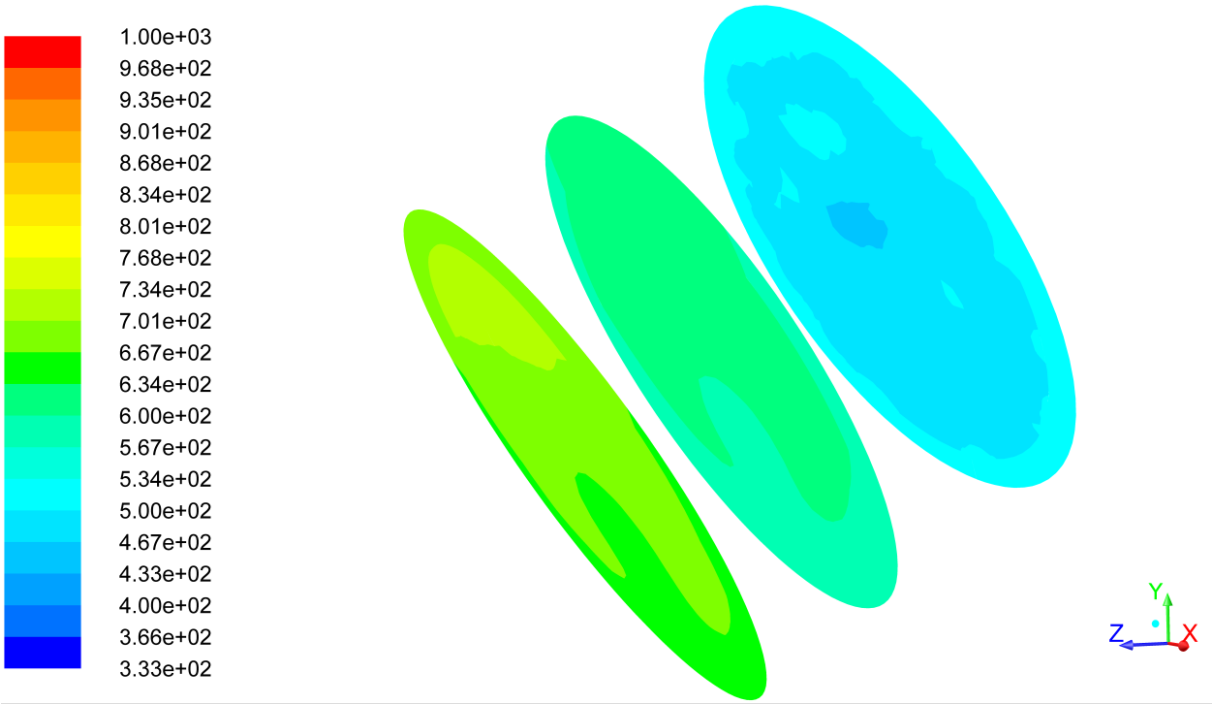

Figure 6.38: Contours of temperature inside the regenerator at the instance of the cycle when the crank shaft angle is 270°

Figure 6.39 shows the variation of the temperature of the gas in five cooler tubes in their middle along their axis. Five tubes in the array were selected following the scheme similar to that for the regenerator shown in Figure 6.31. Tube 1 was selected in the bottom edge of the array, tube 2 is located in the centre of the array, tube 3 is at the upper edge of the array and tubes 4 and 5 are on the left and right edges of the array, respectively. The gas temperatures recorded in the tubes 1, 3, 4 and 5 are identical and therefore only the temperature in the middle of the tube 1 (Tmc1) is presented in Figure 6.39. It can be seen that the gas temperature is 384 K at the beginning of the cycle. The maximum gas temperature is 410 K at 125^{o} of the crank shaft angle and the minimum value is 340 K at approximately 310^{o} of the crank shaft angle with a small fluctuation of about 7 K between 135 and 225^{o} of the crank shaft angle. The temperature of the gas inside tube 2 in the centre of the plane (Tmc2) is 388

K at the beginning of the cycle. The maximum gas temperature in this pipe is 405 K at 125^{o} of crank shaft angle and the minimum temperature is 346.6 K at approximately 302^{o} of the crank shaft angle with a disturbance of 10 K between 130^{o} and 225^{o} of the crank shaft angle. It can be seen in Figure 6.39 that the variation of the gas temperature inside the central tube has a similar pattern to those in four other monitored tubes, except that this variation is leading in phase. This is due to the higher velocity of the gas inside tubes near the centre of the cooler.

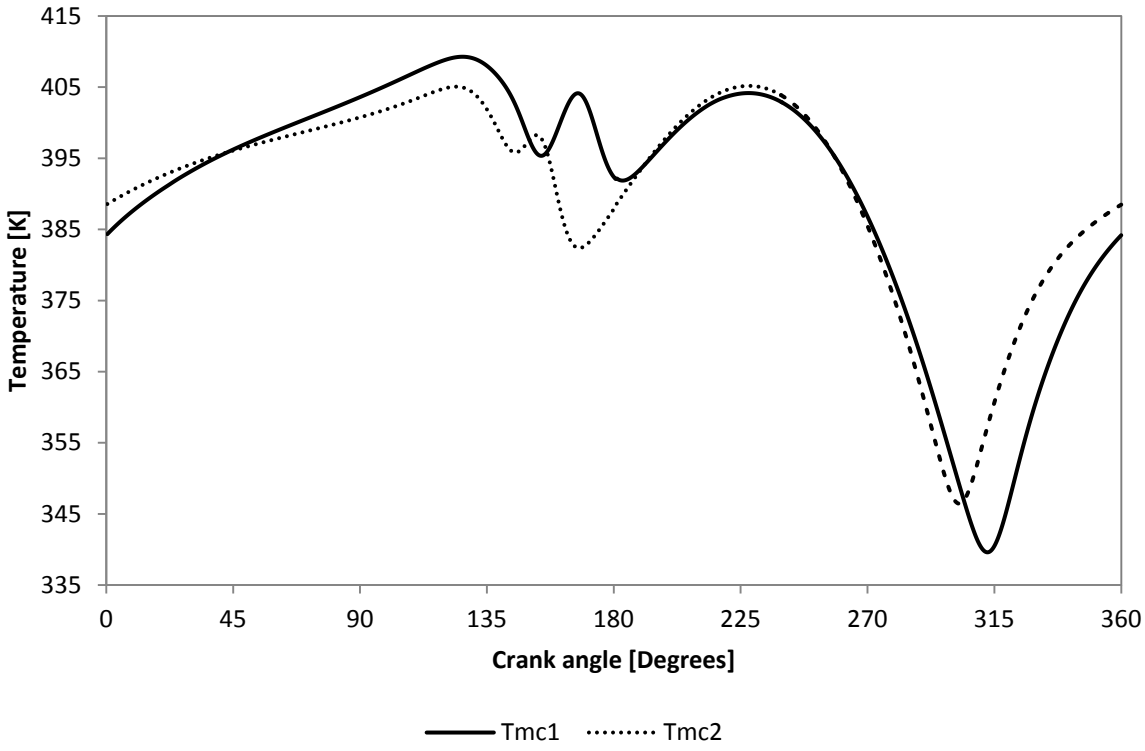

Figure 6.39: Temperature variation in the pipes of the cooler during the working cycle

Figure 6.40 shows the gas temperature variation in the cooler connector pipe. The labelling of monitoring points in the pipe is the same as shown in Figure 6.24. There is a small difference in the temperature variation at each monitoring point. The temperature of the gas is 374 K in

the beginning of the cycle and then it rises to 405 K at 139° of the crank shaft angle. This is followed by a rapid drop to 395 K at 152.4° of the crank shaft angle. Then, the temperature rises to its peak value of 420 K at 235.8° of the crank shaft angle. The temperature then reduces almost linearly to its minimum value of 366 K at 355.52° of the crank shaft angle.

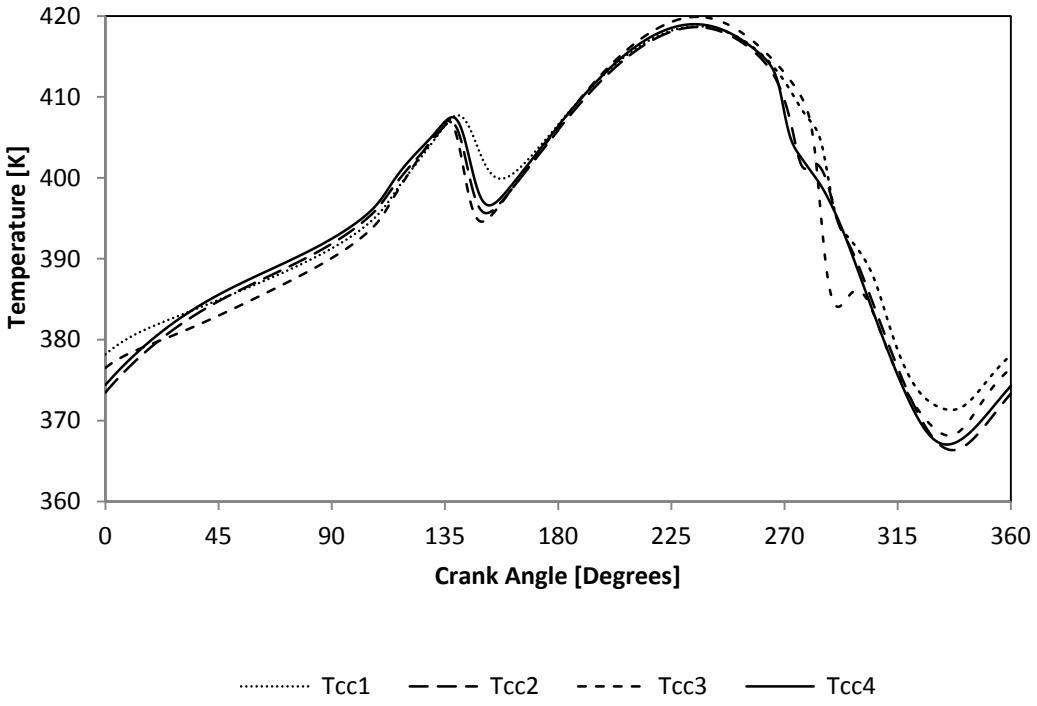

Figure 6.40: Temperature variation at the cooler connector pipe during the working cycle

Figure 6.41 shows the temperature variation inside the hot cylinder both for the gas and the walls. The temperature of the gas was calculated on the reciprocating piston surface as a facet average value. The solid wall temperatures were calculated as vertex average values in monitoring points. The gas temperature is 725 K in the beginning of the cycle when the hot piston is at its BDC and starting its movement towards the TDC. The temperature then drops to the minimum value of 695 K at 52.56° of the crank shaft angle, followed by a rise to the

maximum value of 960 K at 232° of the crank shaft angle. The temperature then drops almost linearly to its initial value during the rest of the engine cycle. It can be seen in Figure 6.36 that the temperature variation is close to harmonic. The temperature of the walls remains constant during the cycle and is at 826 K in monitoring points 1 and 3 and 840 K in monitoring points 2 and 4. The different values of the wall temperature result from the flow being non symmetrical due to the location of the connecting pipe between the hot space and heater.

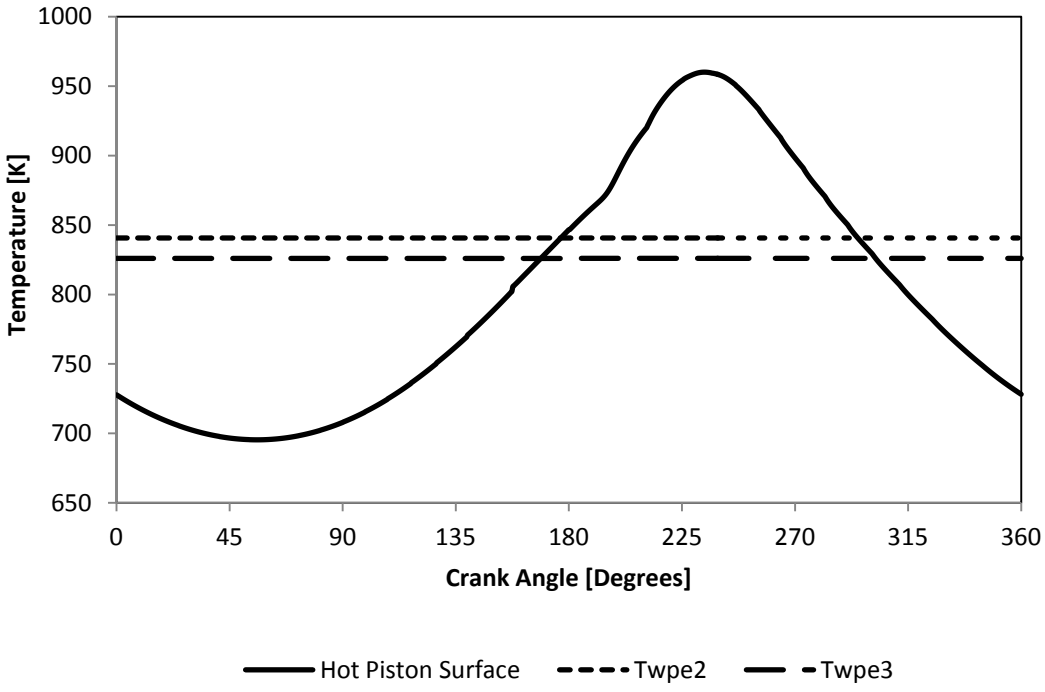

Figure 6.41: Temperature variation inside the hot cylinder during the working cycle

Figure 6.42 shows the gas and wall temperature variation inside the cold cylinder. Again, the gas temperature was calculated on the surface of the piston as a facet average value and the wall temperatures were calculated as vertex average values. The gas temperature is of 333 K in the beginning of the cycle (equal to the temperature of the water flowing through the cooling tubes). Then the temperature drops to its minimum value of 323 K at 16.56° of the

crank shaft angle. From there it rises to its peak of 443 K at 226.8° of the crank shaft angle. Finally, the temperature is reduced back to its initial value during the remaining part of the cycle. The gas temperature variation inside the cold cylinder is close to being harmonic. The temperature in all four monitoring points is the same inside the walls and is constant at 404.8 K during the engine cycle.

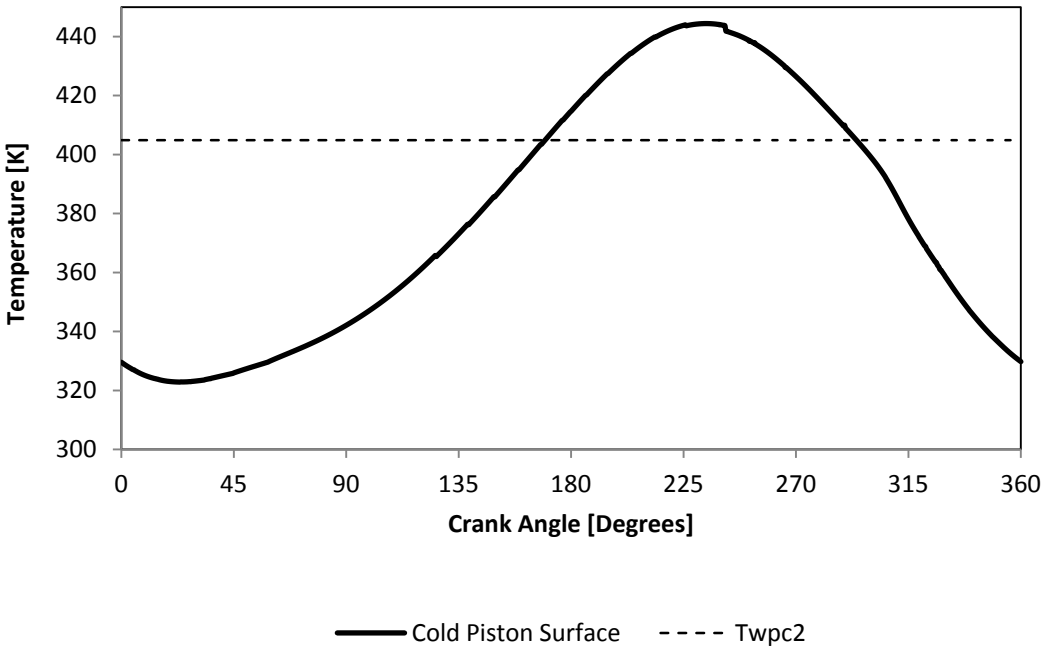

Figure 6.42: Temperature variation inside the cold cylinder during the working cycle

Figures 6.43 - 6.46 show contours of the heat transfer coefficient inside the heater for instances of the cycle when the crank shaft angle is 0°, 90°, 180° and 270° respectively.

Figure 6.43 shows the contours of heat transfer coefficient for the instance when the crank shaft angle is 0° (the beginning of the cycle). The value of the heat transfer coefficient is 913 W/m^2K with heat being transferred from the walls to the gas. Figure 6.44 shows the averaged heat transfer coefficient on the heated surface of the heater at the instance of the cycle when the crank shaft angle is 90^o. For this instant this value is approximately 1720 W/m^2K with

heat being transferred from the walls to the gas. Figure 6.45 shows the heat transfer coefficient for the instance when the crank shaft angle is 180°. It can be seen that the heat transfer coefficient for this instance of the cycle has a value of approximately 2973 W/m^{2}K with heat being transferred from walls to the gas.

At the instance of the cycle when the crank shaft angle is 270°, see Figure 6.46, the heat transfer coefficient is approximately 1115 W/m^{2}K but in this case heat is transferred from the gas to walls.

Figure 6.43: Contours of heat transfer coefficient on the heating surface of the heater at the at the instance of the cycle when the crank shaft angle is 0°

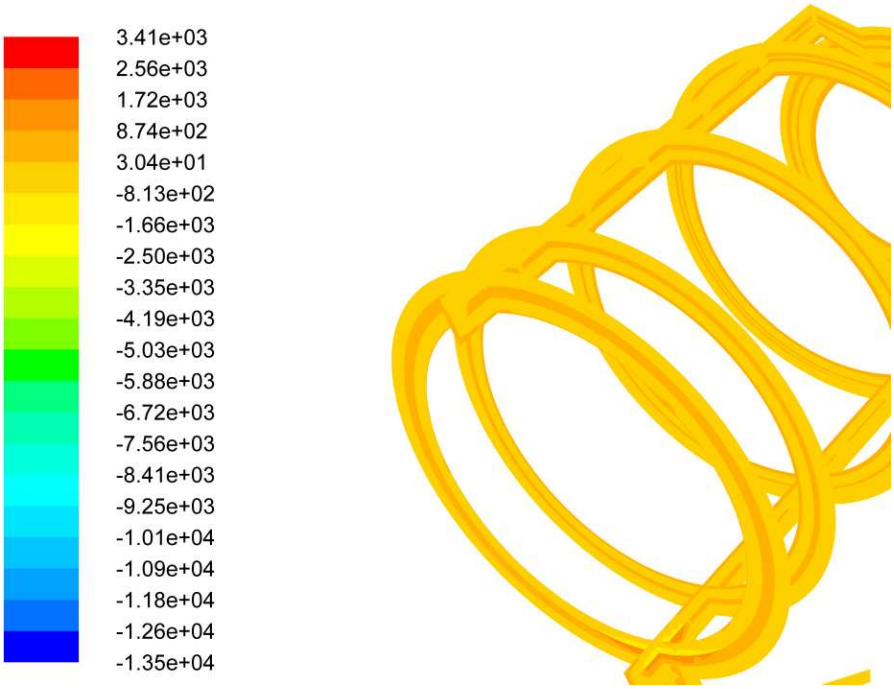

Figure 6.44: Contours of heat transfer coefficient on the heating surface of the heater at the instance of the cycle when the crank shaft angle is 90°

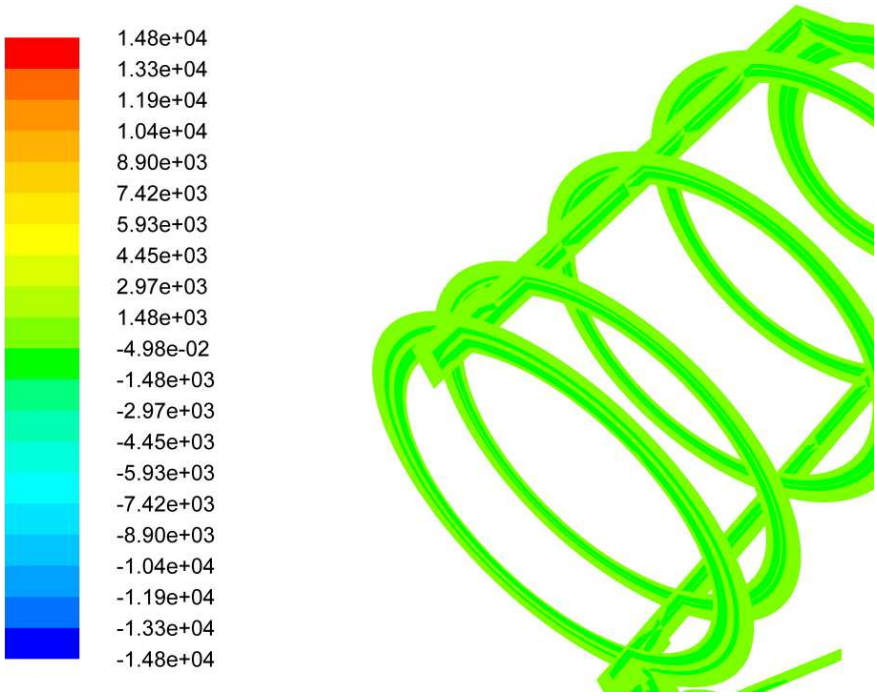

Figure 6.45: Contours of heat transfer coefficient on the heating surface of the heater at the instance of the cycle when the crank shaft angle is 180°

Figure 6.46: Contours of heat transfer coefficient on the heating surface of the heater at the instance of the cycle when the crank shaft angle is 270°

Figures 6.47-6.50 show the variation of the heat transfer coefficient inside the regenerator for instances of the cycle when the crank shaft angle is 0°, 90°, 180° and 270° respectively.

For the crank shaft angle of 0° the heat transfer coefficient is about 92 W/m^{2}K, as shown in Figure 6.47.At the instance of the cycle when the crank shaft angle is 90°, see Figure 6.48, the value of the heat transfer coefficient is about 30 W/m^{2}K. . Figure 6.49 shows data on the heat transfer coefficient in the regenerator at the instance of the cycle when the crank shaft angle is 180°. At this instance the heat transfer coefficient value is about 1480 W/m^{2}K. At the instance of the cycle when the crank shaft angle is 270°, see Figure 6.50, the heat transfer coefficient has a negative value of -124W/m^{2}K.

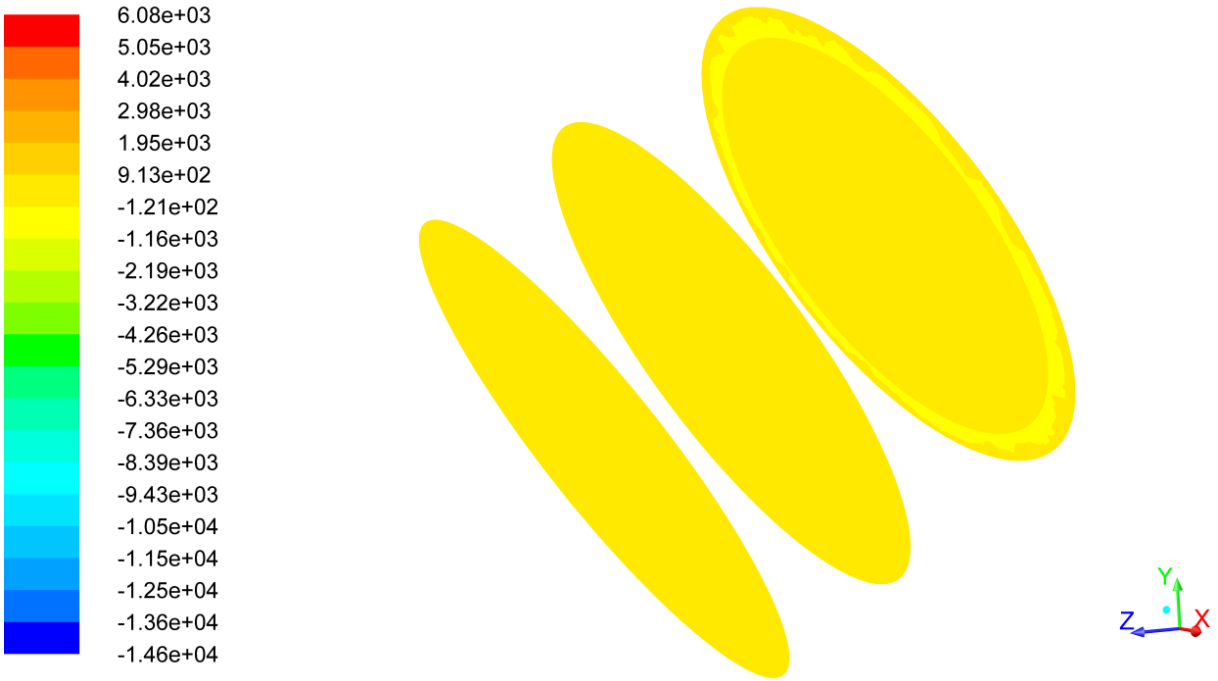

Figure 6.47: Contours of heat transfer coefficient inside the regenerator at the instance of the cycle when the crank shaft angle is 0°

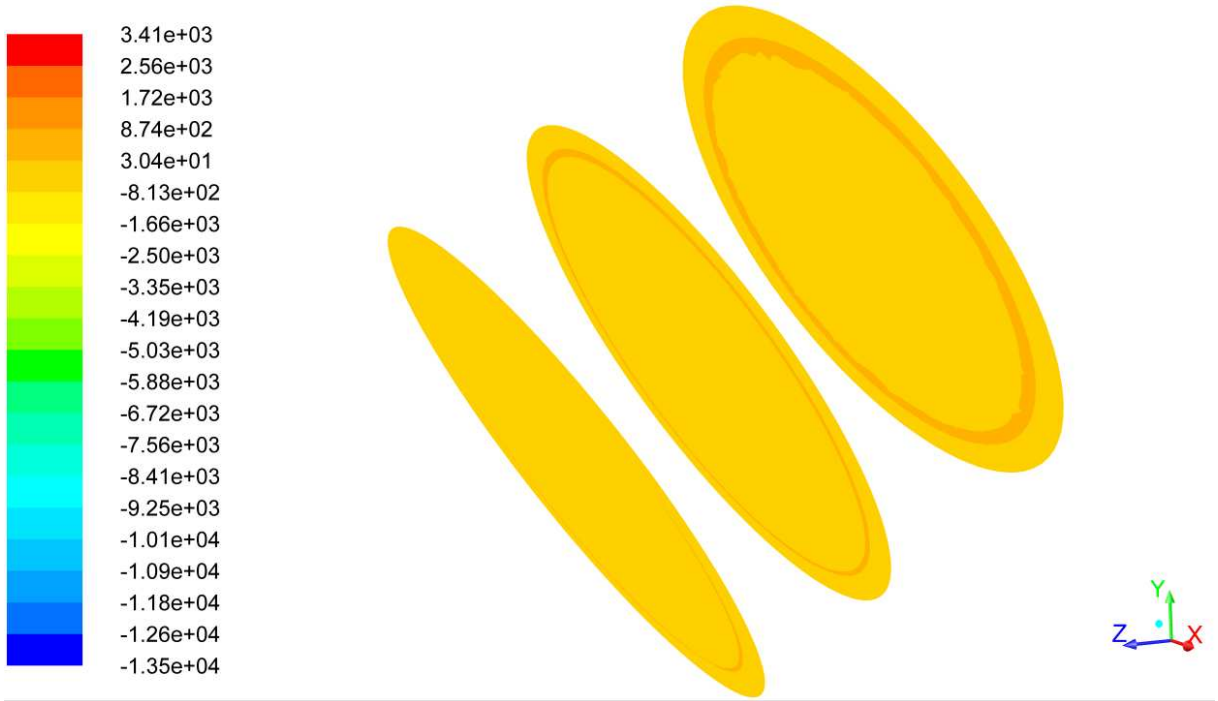

Figure 6.48: Contours of heat transfer coefficient inside the regenerator at the instance of the cycle when the crank shaft angle is 90°

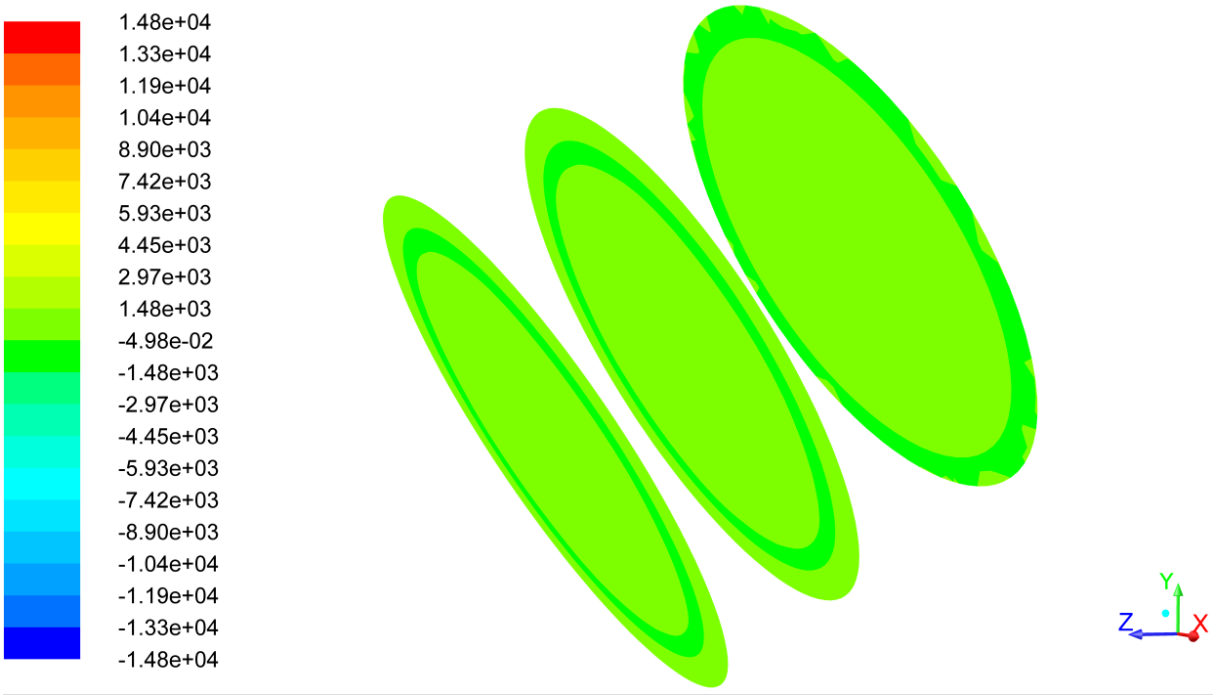

Figure 6.49: Contours of heat transfer coefficient inside the regenerator at the instance of the cycle when the crank shaft angle is 180°

Figure 6.50: Contours of heat transfer coefficient inside the regenerator at the instance of the cycle when the crank shaft angle is 270°

Figures 6.51 - 6.54 show contours of the heat transfer coefficient in the tubes of the cooler for instances of the cycle when the crank shaft angle is 0°, 90°, 180° and 270°, respectively. Figure 6.51 shows the value of heat transfer coefficient at the instance of the cycle when the crank shaft angle is 0^{o}. The heat transfer coefficient value varies between 91 and 6100 W/m^2K. In view of Figure 6.52, the heat transfer coefficient value for the instance of the cycle, when the crank shaft angle is 90°, the value changes from 87 to 3410 W/m^2K. At the instance of the cycle when the crank shaft angle is 180° the surface heat transfer coefficient varies from 30 to 6000 W/m^2K., see Figure 6.53. Finally, when the crank shaft angle is 270^{o}, this value varies between -124 and 4740 W/m^2K as shown in Figure 6.54. Such a wide variation in the heat transfer coefficient in tubes of the cooler is determined by the difference in the velocity of the gas in tubes and the change in the gas temperature whilst it flows through the cooler tubes.

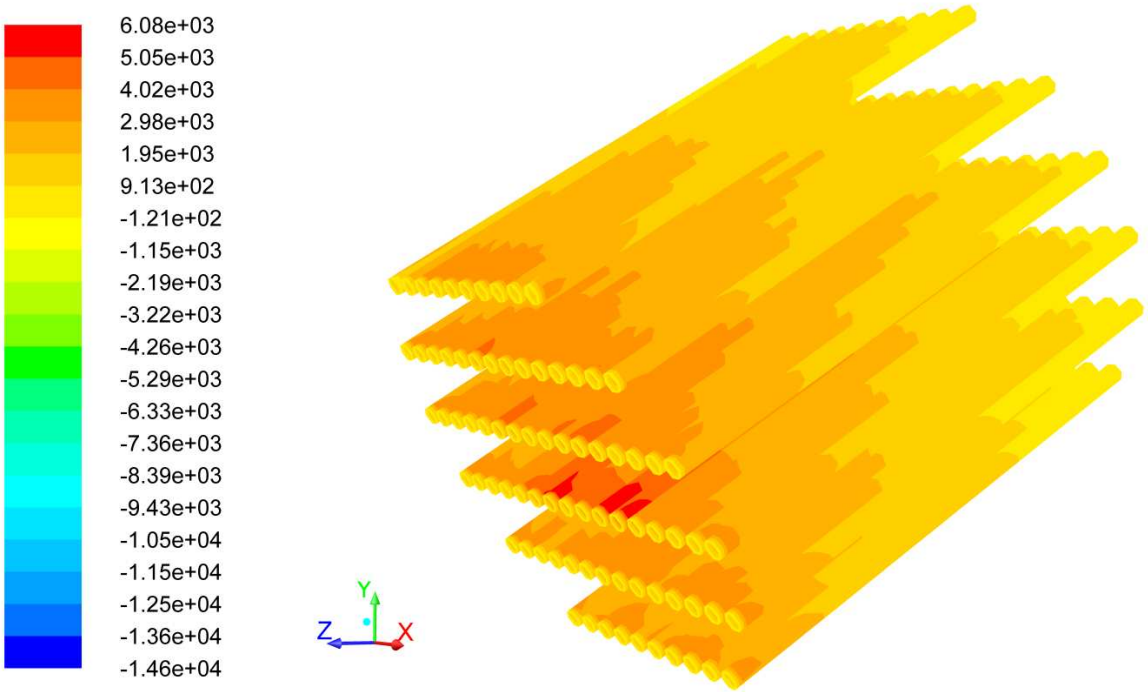

Figure 6.51: Contours of heat transfer coefficient inside the cooler tubes at the instance of the cycle when the crank shaft angle is 0°

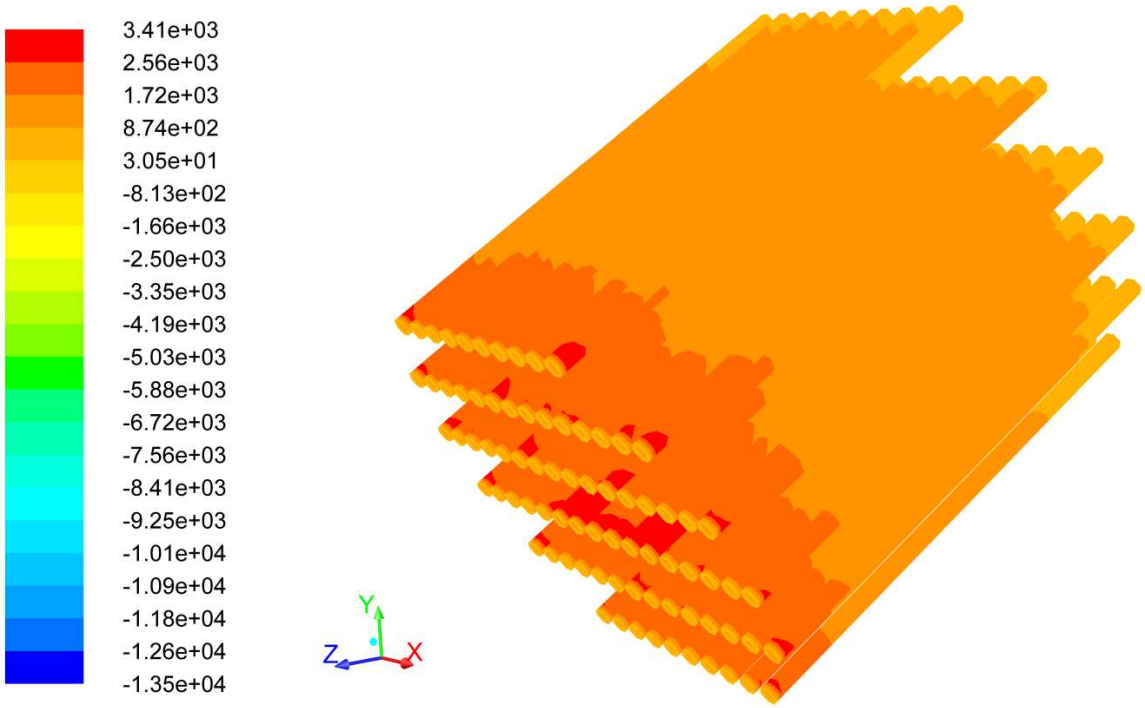

Figure 6.52: Contours of heat transfer coefficient inside the cooler tubes at the instance of the cycle when the crank shaft angle is 90°

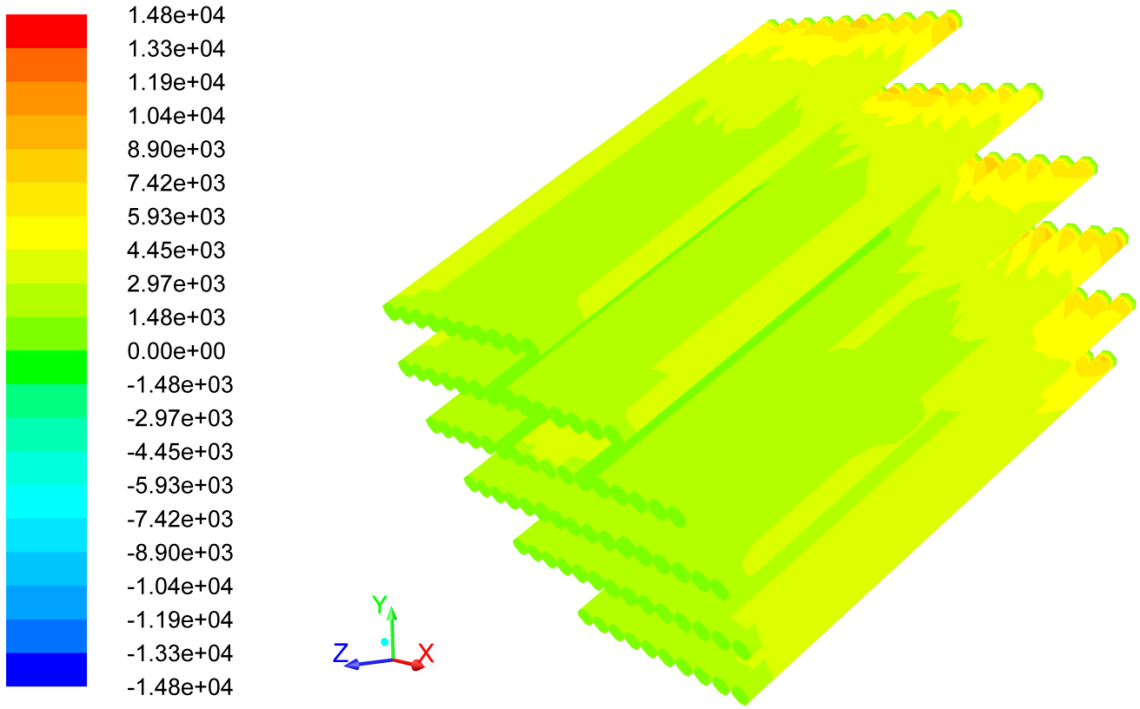

Figure 6.53: Contours of heat transfer coefficient inside the cooler tubes at the instance of the cycle when the crank shaft angle is 180°

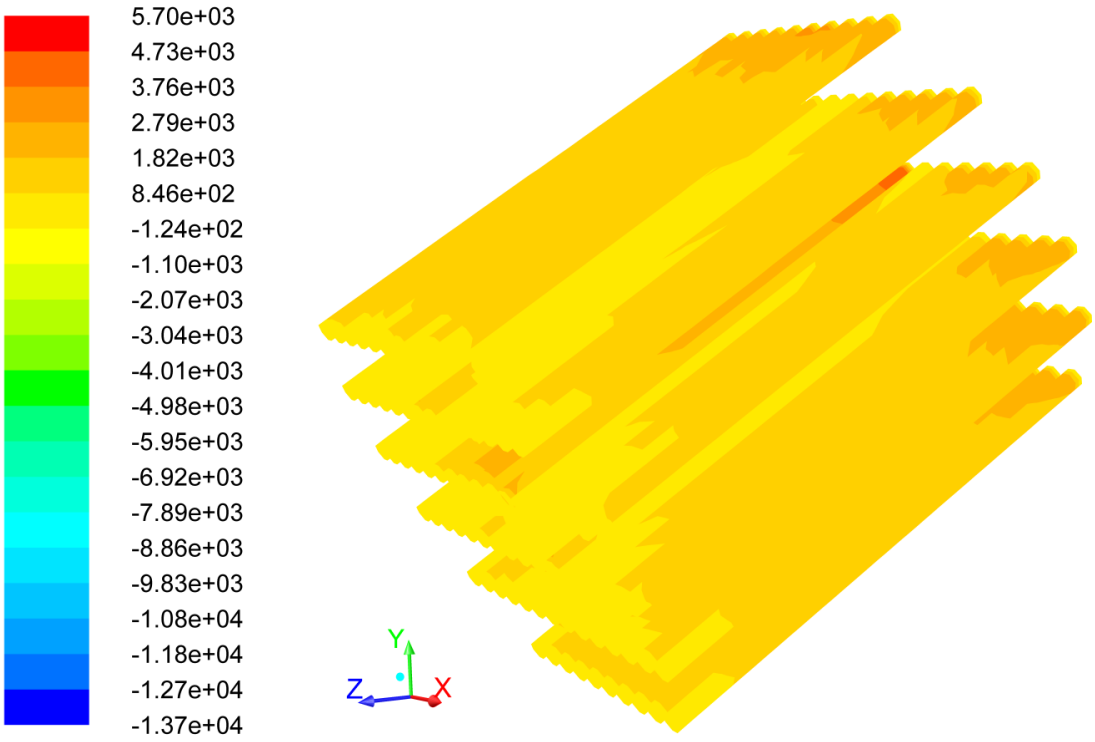

Figure 6.54: Contours of heat transfer coefficient inside the cooler tubes at the instance of the cycle when the crank shaft angle is 270°

Analysis of data on the heat transfer coefficient variation shown in Figures 6.43 – 6.54 shows that there are complex heat transfer processes which take place in different components of the engine. At the same time but in different locations it is possible to have heat transfer in opposite directions. Additionally, there is a change in the direction of heat transfer over the cycle at the same locations. In detail, the heat transfer coefficient inside the heater ranges from 913 W/m^{2}K to 2793 W/m^{2}K during the engine cycle. The values obtained by the global 3D CFD model are lower compared to the heat transfer coefficient predictions of the 2nd order thermodynamic model presented in Chapter 5. For the regenerator, the heat transfer coefficient obtained from the 3D global CFD model varied between -124 W/m^{2}K and 1480 W/m^{2}K during the engine cycle which is again lower than the heat transfer coefficient obtained from the 2nd order thermodynamic model for the regenerator. The heat transfer coefficient inside the cooler varied between -124 W/m^{2}K and 6100 W/m^{2}K during the cycle

with the values being higher than the values of the heat transfer coefficient obtained by the 2nd order thermodynamic model for the cooler. The accuracy of estimation of these coefficients in different parts of the engine can be considerably improved if a computational mesh adapted for finer boundary layer resolution was used in further CFD simulations. Nonetheless, the results obtained from the 3D global CFD model can be used to conduct a qualitative analysis as they represent the dynamics of the heat transfer coefficient variation inside the components of the engine. Overall, the advantage of the global 3D CFD modelling is that it provides information on the thermal state of the walls of engine components. Using this information it is possible to predict heat losses due to conductivity along the length of walls.

Figure 6.55 shows the pressure variation inside the hot and cold cylinders during one shaft revolution. The pressure was calculated as facet average value on the surface of pistons.

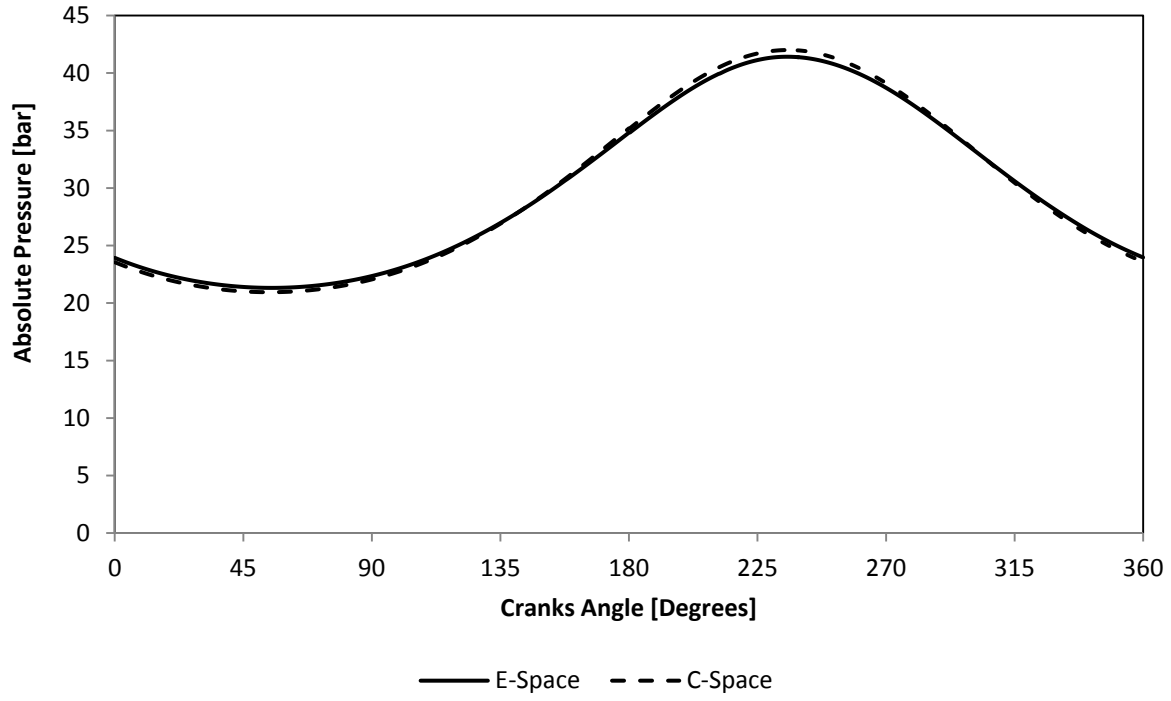

Figure 6.55: Pressure variation during the working cycle

Figure 6.55 shows that the pressures inside the hot and cold spaces vary as harmonic functions and are in phase. The amplitude of the pressure inside the cold cylinder is higher than that in the hot cylinder due to the pressure drop inside the heat exchangers. The minimum pressure inside the engine is 20.9 bar at 53.64° of the crank shaft angle. The maximum pressure in the cycle is 41.9 bar at 234° of the crank shaft angle. The pressure distributions throughout the engine for different instances of the cycle are shown in Figures 6.56 - 6.59. It is very difficult to see in such diagrams how the pressure drop occurs in the gas circuit.

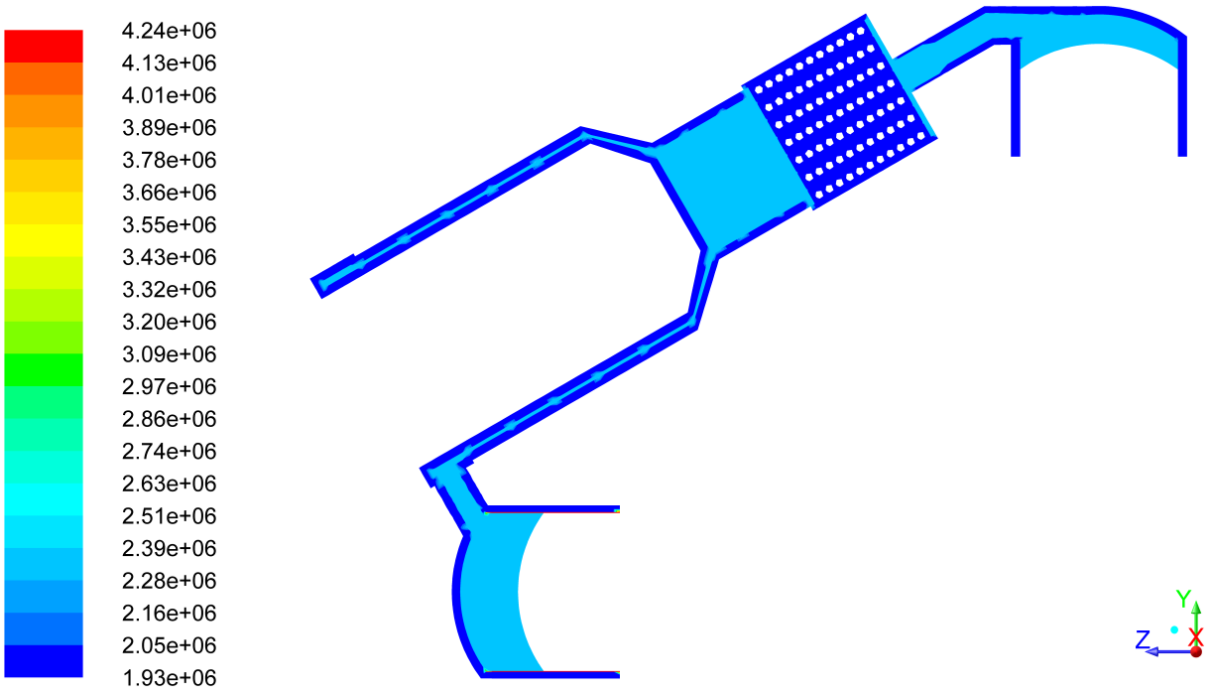

Figure 6.56: Pressure distribution inside the engine at the instance of the cycle when the crank shaft angle is 0°

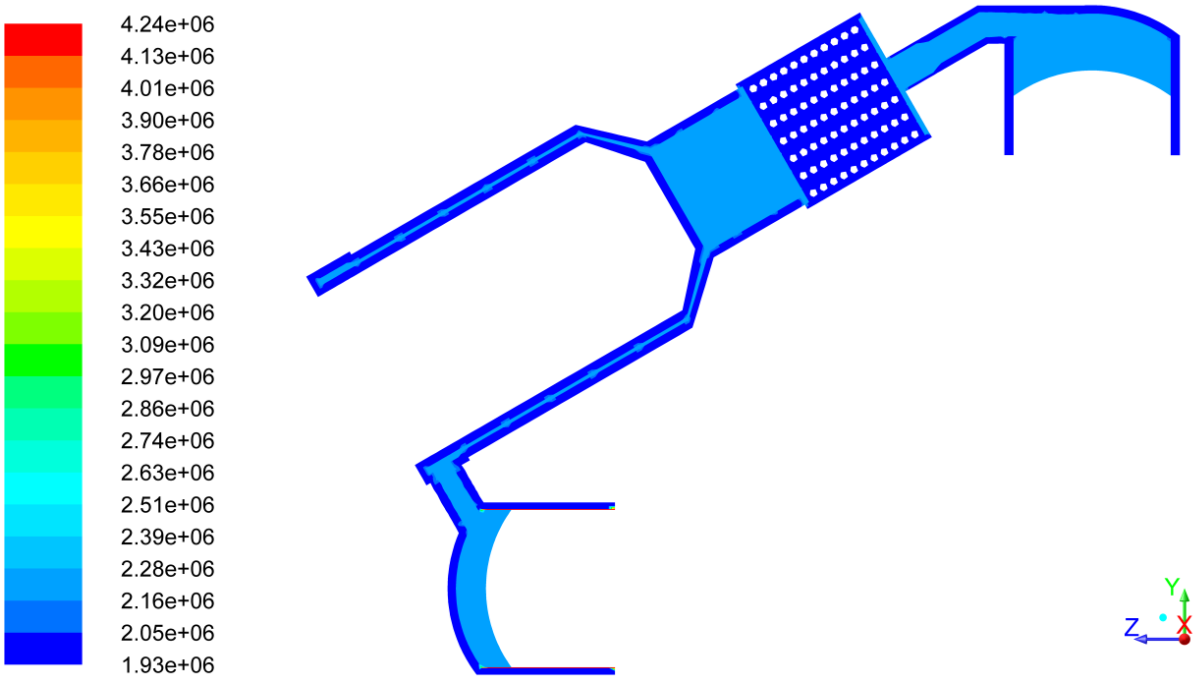

Figure 6.57: Pressure distribution inside the engine at the instance of the cycle when the crank shaft angle is 90°

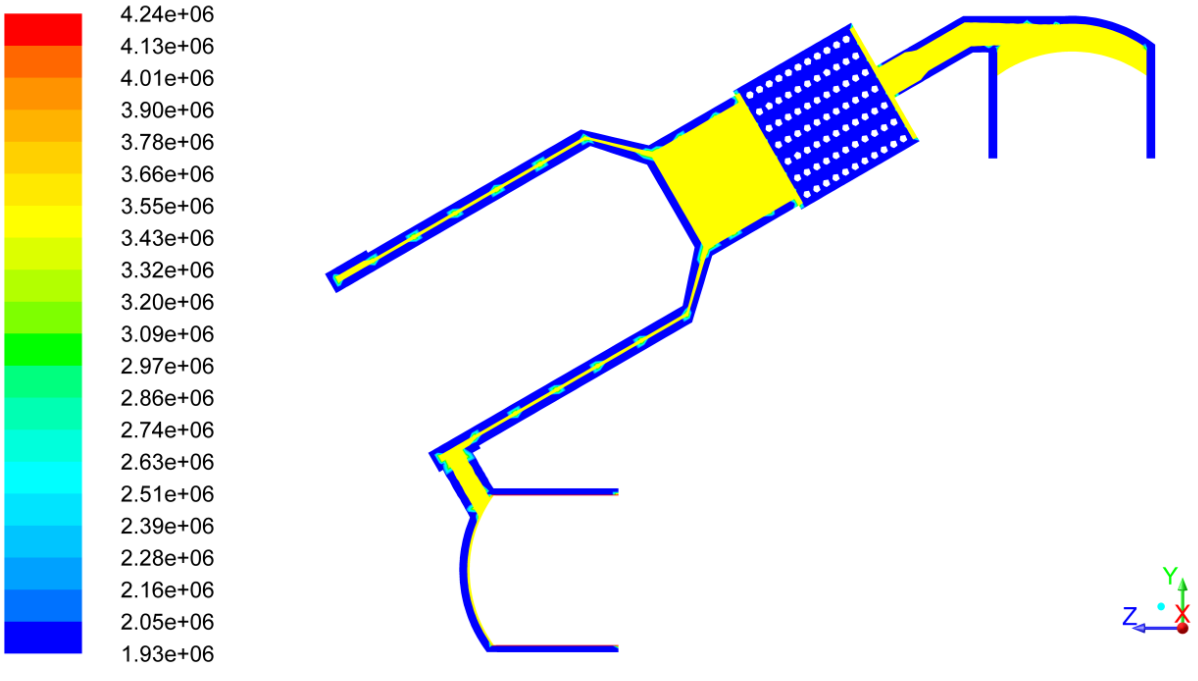

Figure 6.58: Pressure distribution inside the engine at the instance of the cycle when the crank shaft angle is 180°

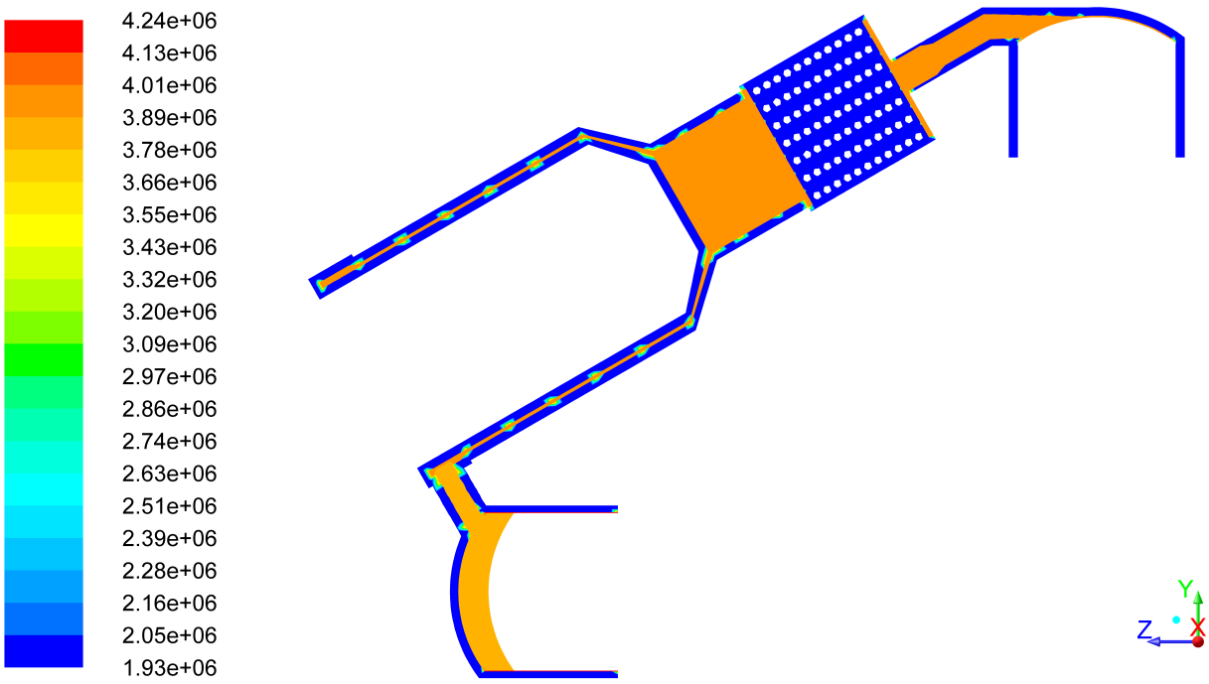

Figure 6.59: Pressure distribution inside the engine at the instance of the cycle when the crank shaft angle is 270°

Therefore, monitoring points were set up at the boundaries of heat exchangers and pressure at these points was recorded. This information then was used to calculate pressure drops in each of heat exchangers. The total pressure drop is the sum of pressure drops in heat exchangers and also in connecting pipes. The connecting pipes between the heater and hot space and between the cooler and cold space are one of major sources of the pressure drops because of high velocities and significant expansion/contraction in flow areas. Additionally, their location causes strong recirculation of the gas, particularly in the cooler connector pipe. Figure 6.60 shows the variation of the total pressure drop in the engine and in each heat exchanger. The overall pressure drop has a maximum value of 40.33 kPa at 24.84° of the crank shaft angle. Then it reaches its minimum value of -57.65 kPa at 244.08°. The maximum pressure drop in heat exchangers occurs in the cooler during the period of the cycle between 0 to 43° of the crank shaft angle with a peak value of 11.297 kPa. From this instance and until the instance when the crank shaft angle is 200° the maximum pressure drop occurs inside the

heater with the peak value of 9.882 kPa at 89° of the crank shaft angle. It is clear from the presented results that the maximum pressure drop occurs inside the cooler tubes. These findings are different from those obtained by using the second order model and these are defined by the correlations used for calculation of pressure losses.

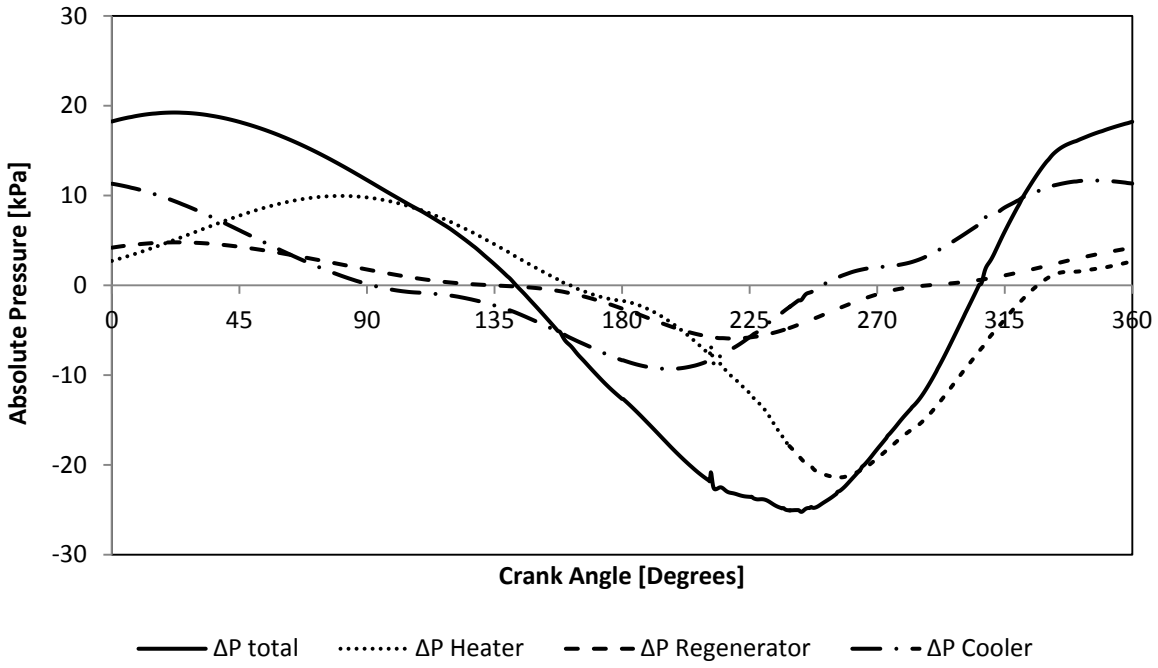

Figure 6.60: Pressure drop variation during the working cycle

Figure 6.61 shows the indicated pressure-volume diagrams of the engine and using this information the indicated power is calculated. The net cyclic work is calculated to be 98 Joules which results in the indicated power output of 1.96 kW. This value corresponds well with measurements performed on the actual engine which yielded an electrical power output of 900 W [18, 46, 118].

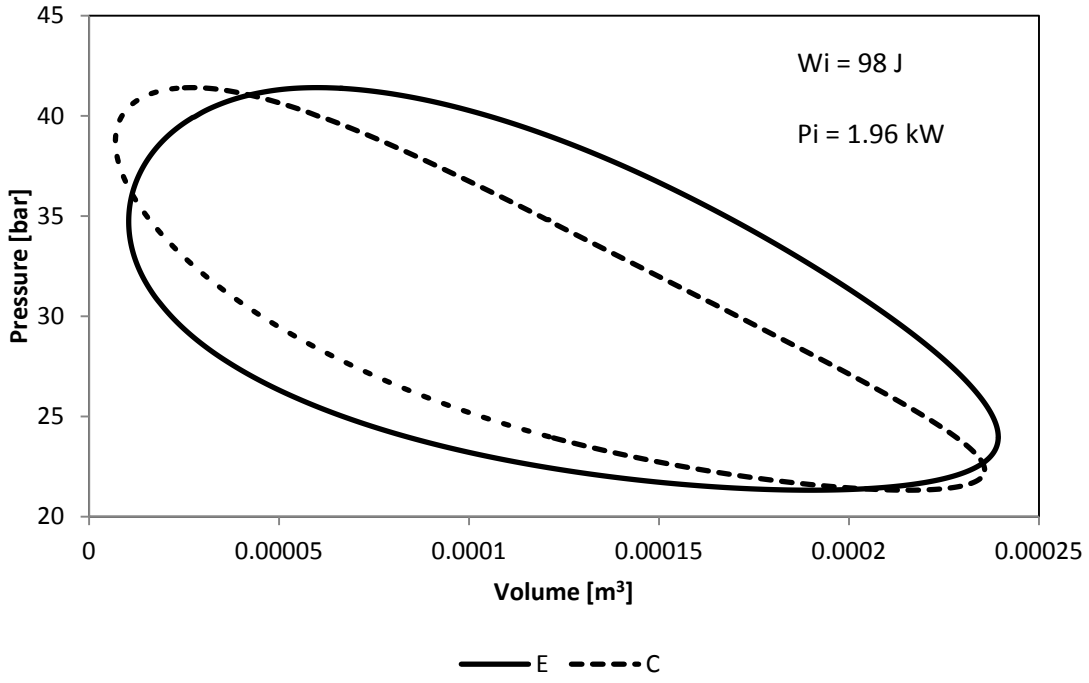

Figure 6.61: P-V Indicated diagrams of the engine

The indicated power calculation provides a simple method to quantify the power loss due to pressure drop. The indicated power value in the absence of pressure losses can be obtained by assuming the same pressure value in both cylinders. In this case it is assumed that pressure variations in both cylinders are in phase. Table 6.3 presents the results obtained using such an approach. By using the pressure in the cold space a 12.3% loss in the indicated power was determined equal to 0.24 kW. By using the hot space pressure a 13.2% indicated power loss was found equal to 0.26 kW. Since the two values are close, it would be safe to assume that the average indicated power loss due to the pressure drop is 0.25 kW (12.75%).

Table 6.3: Quantification of power loss due to pressure drop

Measurement Used	Power Loss [kW]	Power Loss [%]
C-Space	0.24	12.3
E-Space	0.26	13.2

6.4 Validation of the global 3D CFD model

The predicted engine performance was compared against results obtained using other methods for the same engine [18, 46]. Table 3 compares results obtained from the Sopranos second order mathematical model, the second order mathematical model developed in [2] and discussed in Chapter 5, the 2D axi-symmetric CFD model and the novel 3D Global CFD approach implemented in this investigation. It is evident from Table 6.4 that the thermodynamic models over-predict the indicated power output of the engine compared to the global 3D CFD model.

Table 6.4: Comparison of published and obtained results by means of indicated power

Method	Indicated Power [kW]
Sopranos 2nd order MM [18]	3.18
2nd order MM by Kraitong [2]	2.2
2D Axi-symmetric CFD [46]	1.7
3D Global CFD	1.96

The difference between the predictions of the two mathematical models is due to the different correlations used for the calculation of pressure losses and heat transfer coefficient. The two CFD approaches show also different results. In the 2D axi-symmetric model only the gas circuit was modelled and the temperature boundary conditions were used, which is a less accurate approach compared to using heat flux boundary conditions. Additionally, due to model restrictions it was not possible to represent accurately the geometry and surface area of the cooler in the axi-symmetric model. Therefore, the power output predicted by the global 3-D CFD model can be considered to be closest to the experimental performance of the engine. In all models similar operating gas temperature limits were predicted. The main difference in

results is mainly for the phasing between the pressure and volume variations in each cylinder. Figures 6.62- 6.65 illustrate the phasing between pressure and volume curves for different models, and in this way the difference in pressure-volume phasing between the thermodynamic and CFD models, can be investigated.

Figures 6.62 and 6.63 show the pressure and volume variation inside the hot space of the engine for the global 3D CFD and the second order mathematical models, respectively. For the CFD model, the pressure and volume curves first intersect at approximately 84.6° of the crank shaft angle at which point the volume is 0.00013 m^3 and the pressure is 22.9 bar. The second intersection point between the two curves is at 301° of the crank shaft angle when the volume is 0.00018 m^3 and the pressure is 33 bar. For the thermodynamic model, see Fig. 6.63, the first intersection point is at 106° of the crank shaft angle at which the volume is 0.00010 m^3 and the pressure is 22 bar. The second intersection is at 291° of the crank shaft angle when the volume is 0.00018 and the pressure is 33 bar. Although at the second intersection point the pressure and volume values are the same as in the CFD model, the intersection occurs earlier by 5° of the crank shaft angle. The first pressure-volume intersection in the thermodynamic model occurs later by 21.4° of the crank shaft angle and both the pressure and volume values are different at that point.

Figures 6.63, 6.64 show the pressure and volume variation inside the cold space for the global 3D CFD model and second order mathematical model respectively. For the CFD model, the pressure and volume curves first intersect at approximately 4.33° of the crank shaft angle at which point the volume is 0.00013 m^3 and the pressure is 23 bar. The second intersection point between the two curves is at 154.8° of the crank shaft angle when the volume is 0.0001679 m^3 and the pressure is 30 bar. For the thermodynamic model, see Fig. 6.65, the first intersection point is at 160° of the crank shaft angle when the volume is 0.00017 m^3 and the pressure is 28 bar. The second intersection is at 354.6° of the crank shaft angle when the

volume is 0.00012 m^3 and the pressure is 20.5 bar. It can be seen in these Figures that the second intersection in the thermodynamic model closely corresponds to the first intersection for the CFD model, albeit it now occurs earlier by 9.7° of the crank shaft angle. The difference between the two models however is more pronounced in the hot space and is believed to be due to the different pressure drop calculations in each model and the 3D set-up of the CFD model.

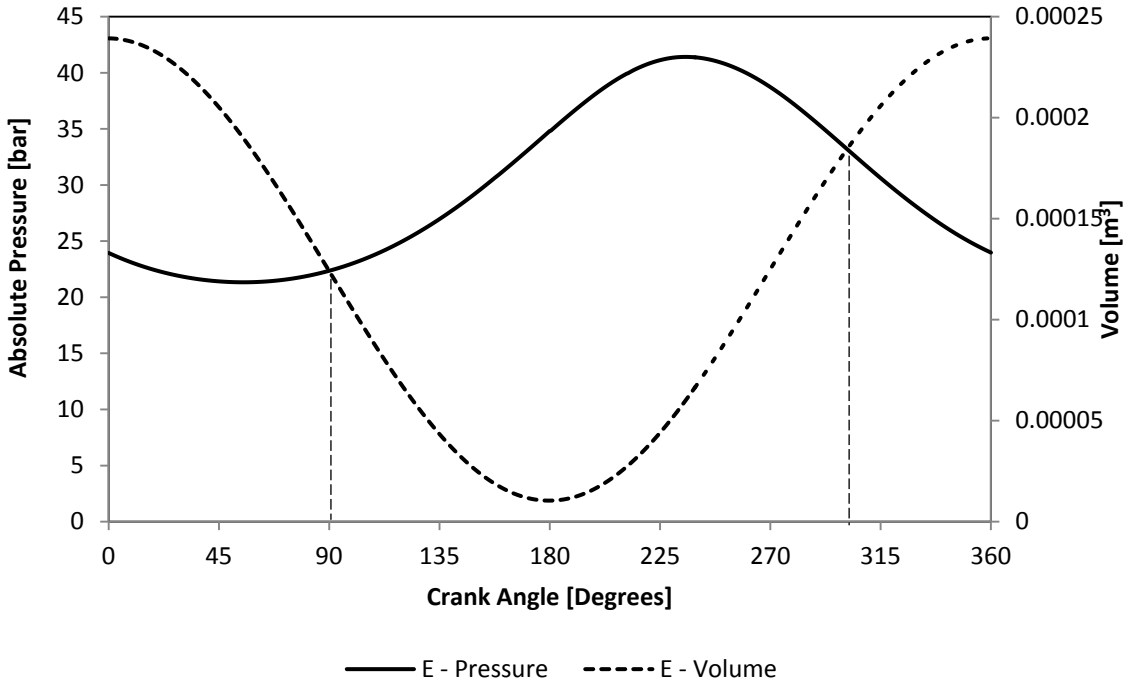

Figure 6.62: Pressure and volume variation against crank shaft angle for the hot cylinder (Global 3D CFD model)

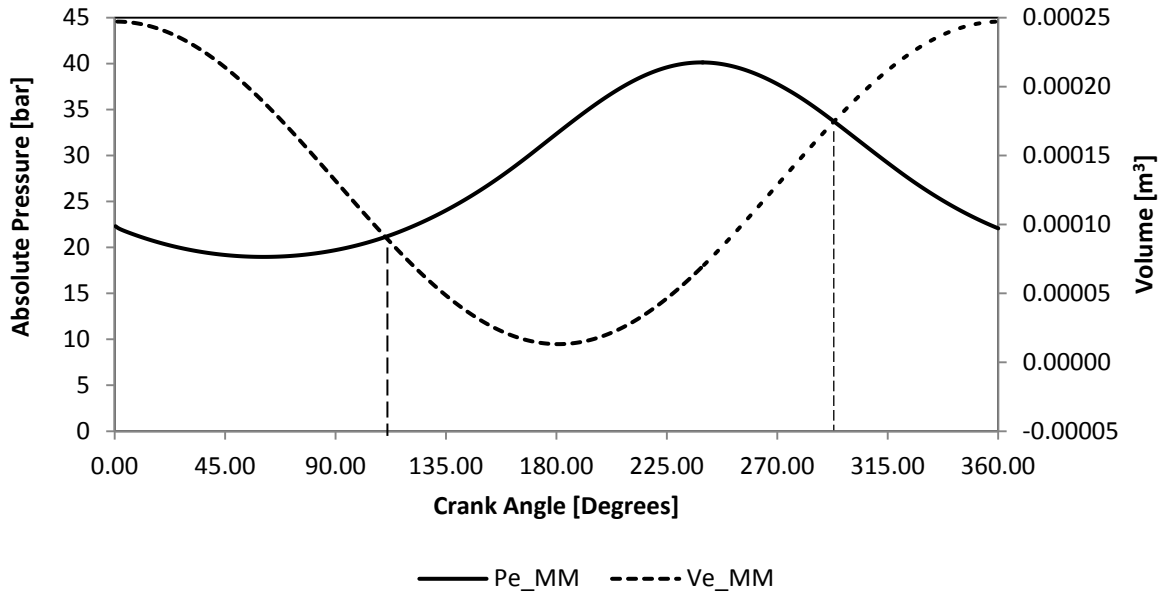

Figure 6.63: Pressure and volume variation against crank shaft angle for the hot cylinder (Thermodynamic model)

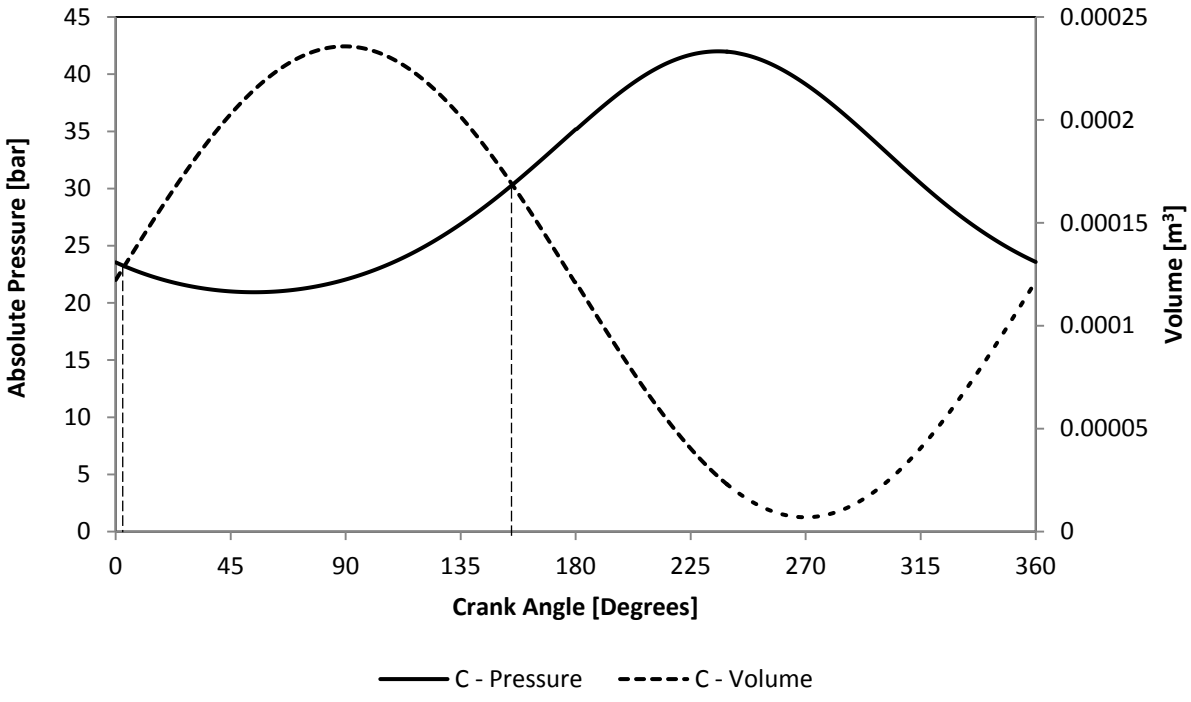

Figure 6.64: Pressure and volume variation against crank shaft angle for the cold cylinder (Global 3D CFD model)

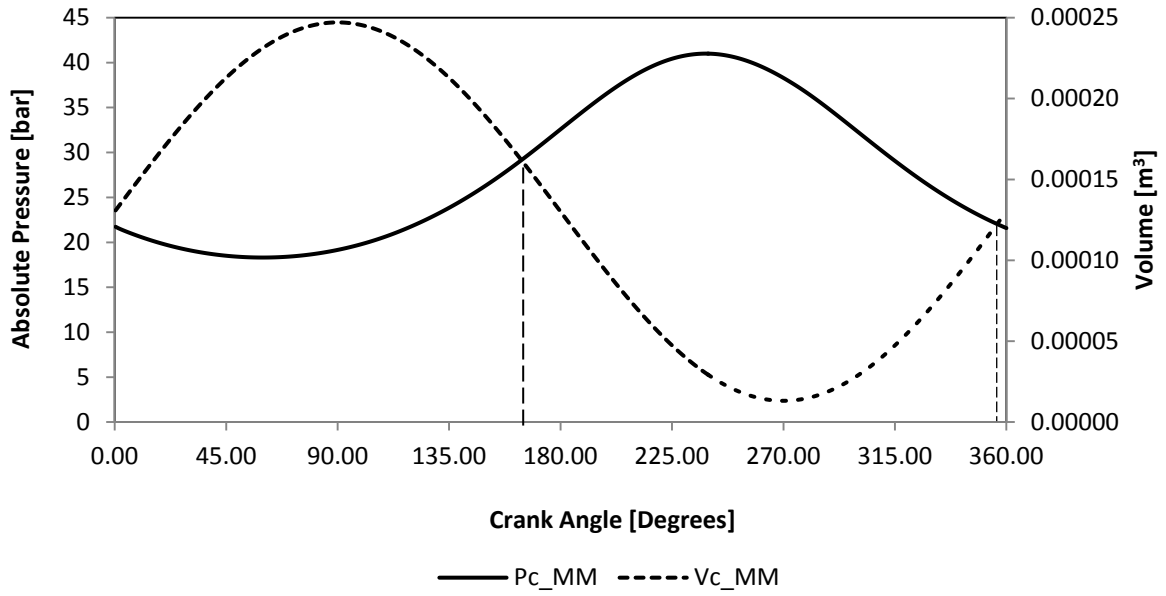

Figure 6.65: Pressure and volume variation against crank shaft angle for the cold cylinder (Thermodynamic model)

6.5 Synopsis

In this chapter the 3D global CFD model of the solar Stirling engine was described and its results were analysed. The model revealed complex flow patterns inside the gas circuit of the engine which strongly affects heat transfer and the temperature distribution. It was found that the temperature distribution in the solid walls stays constant throughout the cycle. The predicted indicated power output is in very good agreement with previous numerical and experimental data. The different predictions of thermodynamic and CFD models were mainly caused by the different phasing between the pressure and volume curves in each space.

Chapter 7 CFD Simulation of the Wankel-type Rotary Solar Stirling Machine

7.1 Introduction

As mentioned in the introduction, one of the aims of the CFD modelling of the Solar Stirling engine was to apply the obtained experience and insight to the development of a CFD model of a Wankel-type Stirling machine with rotary pistons (WRSM) based on the idea presented in Figure 3.31 and the US patent 6109040. In the following sections the design of this system is described along with the features of the developed 2D CFD model.

7.2 Description of the 2D CFD model of gas circuit of the WRSM

7.2.1 Description of the WRSM

The novel WRSM was generally based on the design described in US patent numbered 6109040 registered in 2000 by Ellison et. al [119]. A schematic layout of the engine is shown in Figure 7.1.

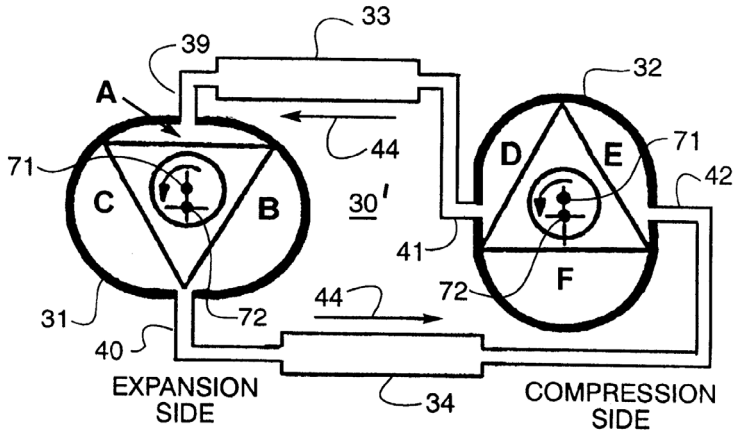

Figure 7.1: The Stirling Cryogenic machine layout in the US patent 6109040 [119]

As shown in Figure 7.1, the cryogenic machine consists of two sides with working spaces, namely the expansion (31) and compression (32) sides, connected with two sets of heat exchangers, namely the cooling heat exchanger (39 and 40), the regenerator (33 and 34) and the ambient cooler (41 and 42). The design assumes that the gas is heated on the expansion side and in the cooling heat exchangers and is cooled to ambient level in the compression side and ambient coolers. The design assumes that reciprocating gas flow exists between the expansion and compression sides in each set of heat exchangers; therefore the above layout forms two equivalents of a gas circuit for a conventional Stirling engine. Figure 7.2 shows a schematic outline in order to explain the principles of the operation of such an engine. The diagram shows the positions of the triangular rotors in the expansion and compression casings for four characteristic instances of the cycle. In this schematic diagram the triangular rotor is driven by the shaft via a planetary mechanism. The triangular rotor and casing on the expansion side form three expansion spaces, namely A, B and C, which are connected through a set of heat exchangers to compression spaces D, E and F, respectively, on the compression side with its casing and triangular rotor. A full rotation of the triangular rotor causes full compression and expansion of each working space twice per revolution. Since each space on the hot side is connected to the corresponding space on the compression side via a set of heat exchangers and there is a shift between rotations of triangular rotors, the arrangement in Figure 7.2 represents an engine configuration with 6 equivalents of the single internal gas circuit of a Stirling cycle machine. Since the cycle is reversible it is possible to convert this into a Stirling engine by introducing certain modifications. Particularly, the cooling heat exchanger should act in the modified design as a heater and the components on the expansion side now should be able to operate at high temperature conditions. In this Figure, the cold space rotor is lagging in rotation by approximately 45^{o} of the rotor angle. For

conventional piston Stirling machines lagging of cold piston in the displacement would be 90^{o} of the shaft angle compared to the displacement of hot piston.

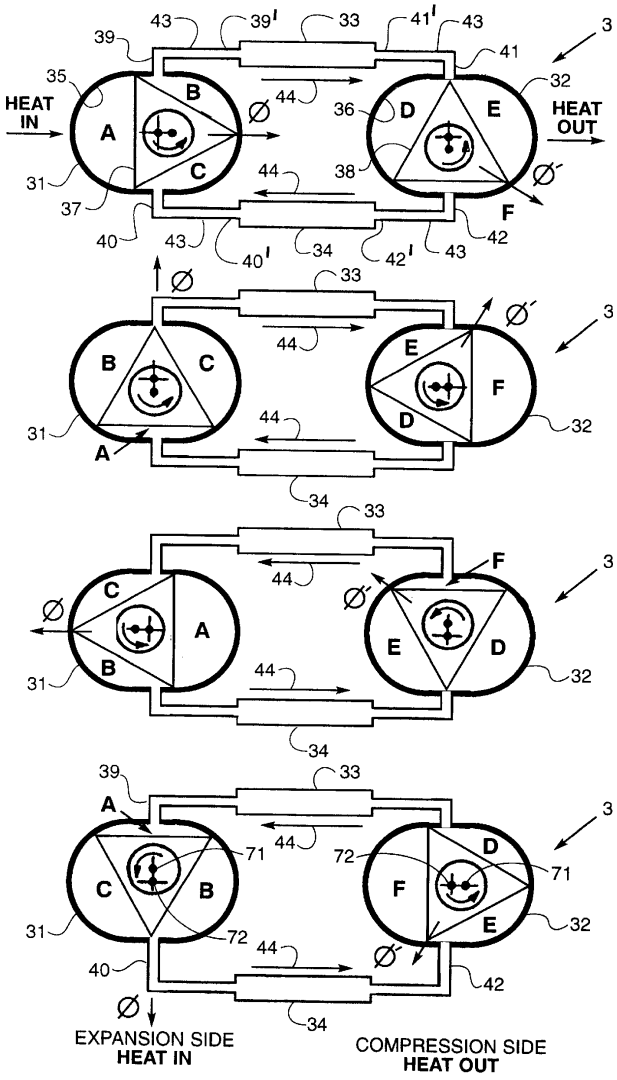

Figure 7.2: Schematic outline of patented engine cycle [119]

Though the patent was approved, no theoretical proof has been produced that the engine will be operational. For such configuration the thermodynamic modelling is not capable to provide confirmation of the functionality of the engine or cooling machine, since it is necessary to investigate the working fluid flow patterns and the influence of the shift angle.

Moreover, though the scheme in the patent implicates that the corresponding working spaces on the expansion and compression sides form a single internal gas circuit, it can be seen that at certain instances of the cycle these corresponding volumes are cut off from each other which is not the case in conventional Stirling engines. There is also a possibility that during the working cycle the pairing of corresponding volumes in the expansion and compression spaces is not fixed but alternating. These specific features of the operation of Wankel type Stirling machine can be investigated using only multi-dimensional CFD analysis and this is aim of the study in this Chapter.

For CFD investigation purposes a layout of the WRSM was proposed which incorporates two casings with triangular rotors, see Figure 7.3. To connect the casings, a set of heat exchangers very similar to that used for the V-type solar engine with crank shaft kinematical mechanism described in this thesis. The layout of the WRSM under investigation builds on the design of the solar Stirling engine described and analysed in the previous Chapters.

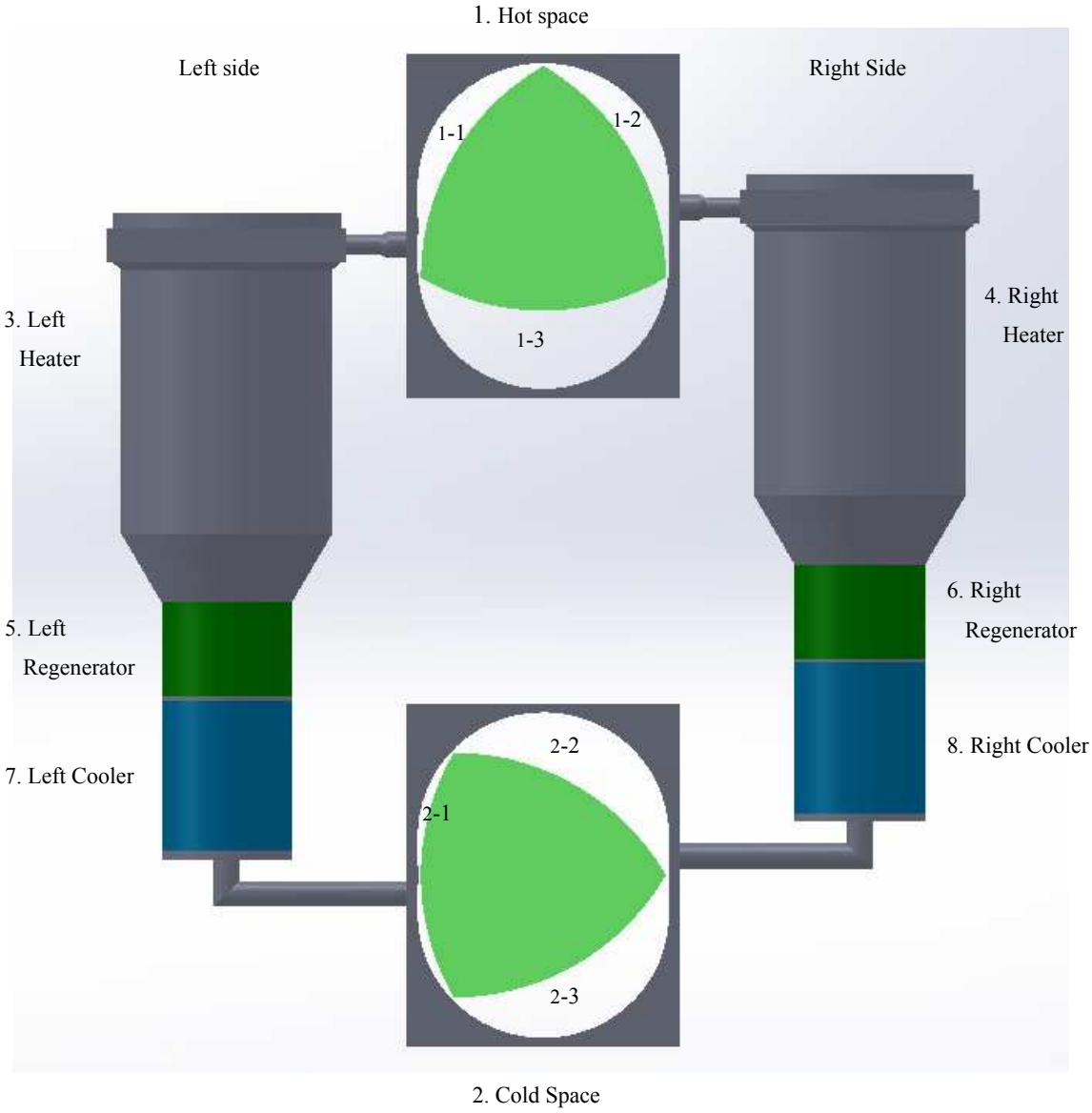

Figure 7.3: CAD model of the proposed Wankel-type solar Stirling machine design

In Figure 7.3, the two triangular rotors (shown in light green colour) are surrounded by their casings. It was decided that in the first instance the rotor in the cold space will be shifted clockwise by the angle of 90^{o} compared to the orientation of the rotor in the hot space, so to follow the practice in the design of conventional piston Stirling engines. The two cavity-type heaters 3 and 4 (shown in dark grey colour) are at the top of the arrangement making the top casing with its rotor the expansion space 1. The hot space 1 is shown with the hot rotor in

light green and the three working chambers, 1-1, 1-2 and 1-3. The two coolers 7 and 8 are located near the bottom (shown in blue colour) and hence the lower casing with its rotor is the cold space 2. The cold space 2 is shown at the bottom with the cold rotor in light green and the three working chambers, 2-1, 2-2 and 2-3. The two regenerator matrixes 5 and 6 (shown in dark green colour) are located between the heater and the cooler on either side of the working spaces. The dimensions of the heat exchangers are the same as for the solar Stirling engine analysed earlier. The geometric information for each casing and rotor is presented in Table 7.1.

Table 7.1: Geometrical details of Wankel rotor and housing

Feature	**Dimension**
Radius of Peritrochoid, R	0.084 m
Eccentricity, e	0.011 m
Piston Arc	0.15 m
Effective Flank Area	0.0075 m^2
Max Displacement Volume/ chamber	0.000250 m^3
Total Volume Per Housing	0.000750 m^3

There are three working chambers in the hot and cold parts, restricted by the casing surface and rotor flanks. Each working chamber has a maximum displacement volume of 0.000250 m^3, equal to the displacement volume of each cylinder of the conventional solar Stirling engine presented previously. The rotors are also turned by 90 degrees relative to each other to provide the same phase difference as in the conventional Stirling engine, with the hot (top) rotor leading in the displacement. It is considered necessary to confirm the operational

functionality of the model by CFD analysis, especially to check gas flow patterns between chambers on the hot and cold sides of the engine. Another task would be defining the dimensions of ports and their locations so to maximise the potential power output from the engine. In Figure 7.3 the port locations are the same as suggested in [105]. The diameter of the ports was set to be 0.01 m.

7.2.2 Description of the 2D CFD model

Initially, the full 3D computational mesh was created for the system to run the CFD simulation. However, it was found that in order to model the flow between the tips of the triangular rotors and the surface of the casing the mesh in this area should be extremely fine and accommodate at least 6 layers of elements. In its turn, this led to the unacceptably large size of the whole computational mesh which made modelling process impossible with the use of the PC allocated to the project. Therefore, further attention was concentrated on application of a 2D computational mesh. When developing the 2D model it was necessary to ensure that the 2D geometry of the engine would have the same heat transfer and cross-flow areas as in the actual 3D geometry. For this, the reference depth setting in ANSYS/FLUENT had to be changed from the default value of 1 m to 0.052 m, equal to the depth of the rotor, *b*. Hence, some of the vertical and horizontal dimensions in 2D geometry were recalculated to provide the same heat transfer and cross-flow areas for a new reference depth of 0.052 m. The turbulent model, discretization schemes and BCs are the same as for the global 3D CFD model of conventional Stirling engine described in section 6.2.2 of Chapter 6. However the PISO pressure-velocity coupling scheme was selected as it is considered more appropriate in dynamic mesh simulations with critical element quality. The rotational speed of the rotors was 1200 rpm and a time-step of 0.000025 s was specified, which resulted in 2000 time-steps per rotor revolution.

A 2D CAD representation of the engine for 2D CFD modelling is show in Figure 7.4. In Figure 7.4, the components are annotated using the same labelling as in Figure 7.3. For the 2D model, a connecting pipe (9, 10) is required between the left and the right channel of each heater to allow the gas to flow through both channels as in the real 3D set-up. Such a 2D CFD simulation is simplified compared to the full 3D CFD modelling and will not have capability to produce accurate results on the 3D flow, temperature and pressure distribution inside the engine but will be adequate to prove operational feasibility of the machine and estimate its performance in terms of the indicated power

Figure 7.5 shows the computational 2D computational grid which is produced using a hybrid mesh scheme built in ANSYS ICEM CFD pre-processor. The purpose of the hybrid mesh here was to create a mesh with triangular elements in the space around the two rotors which can be used for the dynamic mesh simulation in ANSYS FLUENT. The heat exchangers volumes were meshed using quadrilateral elements to have a better control over the quality of the mesh and to produce a better boundary layer resolution in areas where it was necessary. The selected size of the quadrilateral elements in each sub-domain was deemed sufficient for capturing the temperature and velocity variations in both the horizontal and vertical directions. The size and nodal distribution of the triangular elements around the two rotors were selected in such way as to have a mesh with a sufficient quality even in critical positions of rotors when mesh is the most skewed. The different colours represent the several volume sub-domains. The quadrilateral sub-domains were segmented in order to be able to specify the porous media settings inside the two regenerators. The total number of face elements and nodes was 201,680 and 102,343 nodes, respectively. The distribution of face elements by type is presented in Table 7.2.

Table 7.2: Distribution of face elements by type

Element type	Number
Triangular	192104
Quadrilateral	3197

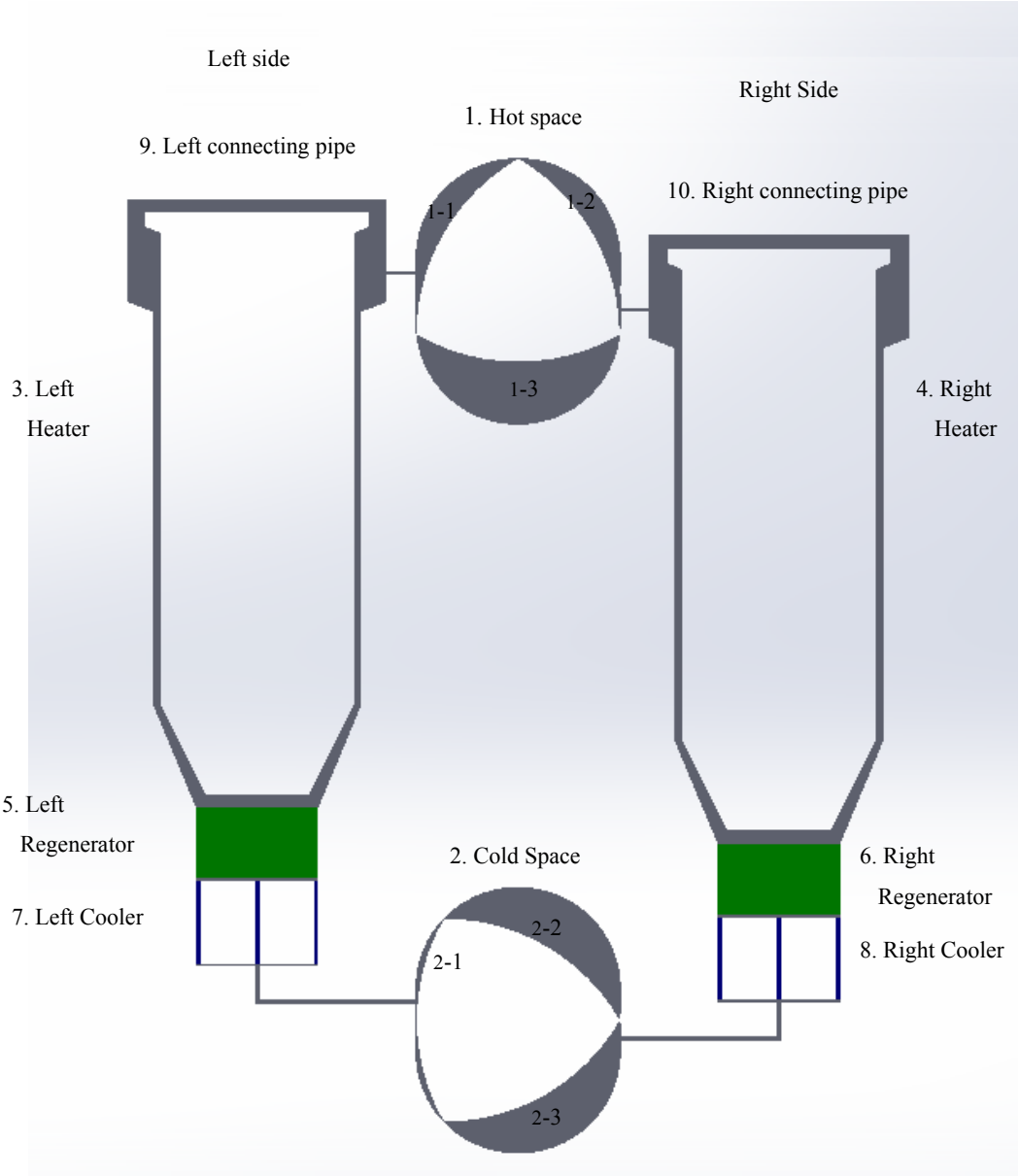

Figure 7.4: 2D CAD model of Wankel-type Rotary Stirling machine

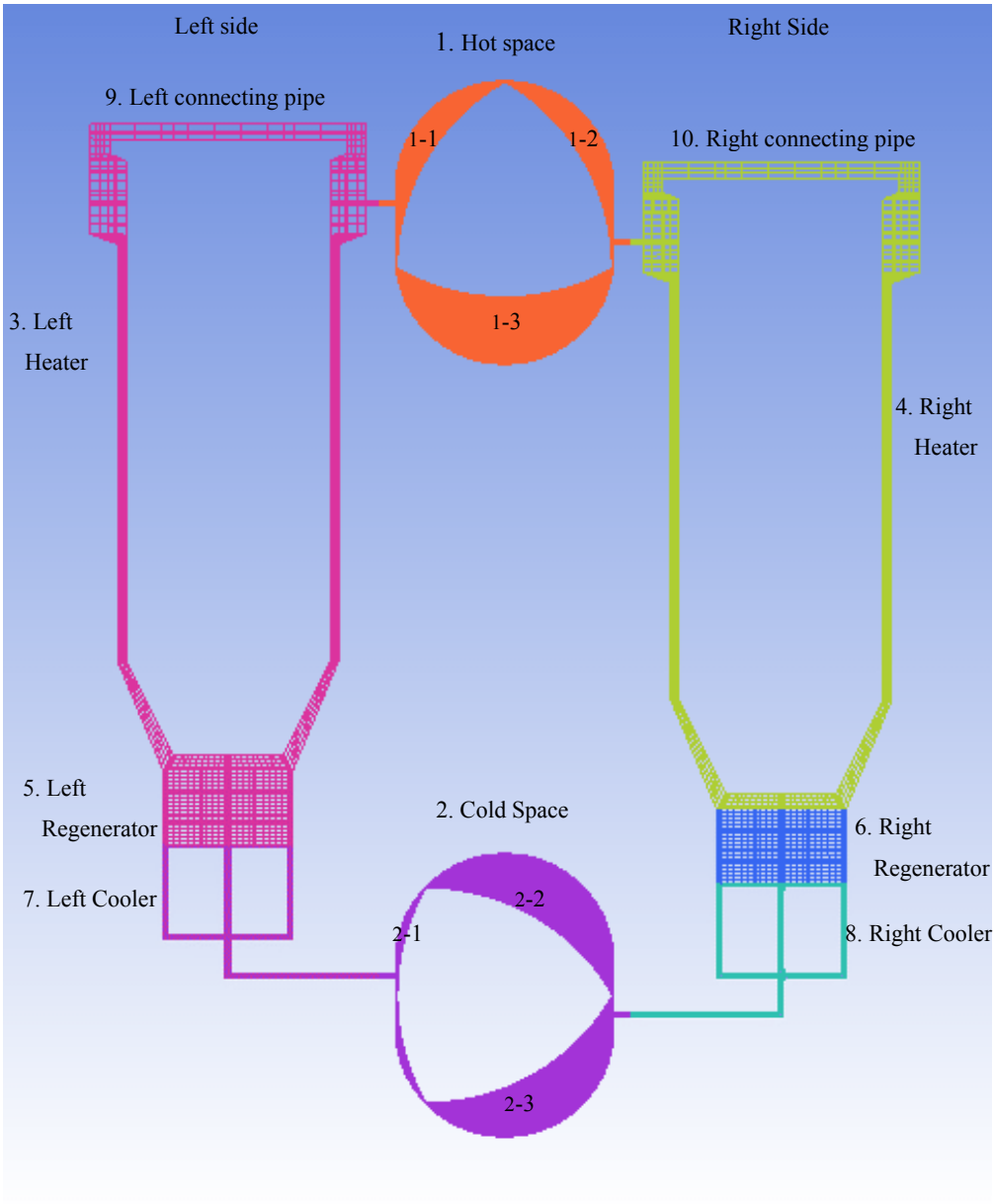

Figure 7.5: Computational grid of simplified 2D model or the WRSM

7.3 Results of the 2D CFD model

This section presents the preliminary results obtained from the 2D CFD modelling for the case when the shift angle between two rotors rotations is 90^{o}. Results will be presented for the crank shaft angle between 0º and 540º which is equal to one period or cycle incorporating half rotor revolution. The results obtained for the velocity distribution, the pressure, and temperature variations over the cycle will be analysed. By using data on pressure variation it is then possible to estimate the power output of the engine.

7.3.1 Results of 2D CFD model with the UDF for limiting the gas leakage between the tips and the casing

A UDF was incorporated into ANSYS/FLUENT to attempt limitation of the gas flow leakage at the rotor tips. The text of the code is presented in Appendix B.

The UDF at each time-step updates the angular location of two boundaries set on either side of each tip at ± 0.05º. Then the UDF reads off the coordinates of the centroids of all cells in this selected space and transforms them into the moving frame coordinates (rotor frame). For the selected cells the UDF counteracts the relative velocity component of the flow in order to neutralise the leakage. This procedure is performed for each of the six rotor tips in the x and y directions.

An alternative approach would be to define the marked cells near the tips as a solid continuum. However, a pre-defined macro C-command to carry out such procedure was not found. Instead, the flow field was influenced by means of momentum sources/ sinks. Effectively, this is what the developed code attempts to achieve. More information on momentum sources/sinks used in ANSYS FLUENT can be found in [120].

The magnitude of the effect of the UDF depends on the values of coefficients *Ks* and *Vs* used in the momentum source/sink equations. It was observed in numerical simulations that numerical problems were caused leading to solution divergence when those values were increased higher than 40000 and 15 respectively. Given the criticality of the mesh quality in the 0.5 mm tip clearance, it was decided to use these values to allow the simulation to run faster. A further increase in the value of those coefficients would have to be supported by a slower time-step in addition to greater number of sub-iterations for skewness correction in the PISO pressure-velocity coupling algorithm.

The flanks of each rotor are numbered from 1 to 3, with number 1 corresponding to the flank on the left and then the numbering continues in a clock-wise manner for the subsequent rotor flanks. During the modelling, the temperatures and pressures are measured at each rotor flank as a facet average total temperature or absolute pressure for each time-step during the cycle. Results on pressure and temperature variations are presented as a function of the crank shaft angle. The results are presented for the 24^{th} cycle after the start of simulations from the defined boundary conditions and it should be also noted there is a slight difference in the values of pressure and temperature at the end of the working cycle since the operation of the engine has not reached the steady state yet.

Figures 7.6-7.10 show the velocity vectors throughout the engine at instances of the cycle when the crank shaft angle is 0º, 135º, 270º, 405º and 540º. The purpose of these Figures is to illustrate that there is a reciprocating flow inside the engine's gas circuits. At the top-right side of each Figure a magnification of the flow in the cooler pipes is presented as a visual aid.

It can been seen in Figures 7.6 - 7.10 that the velocity inside the engine ranges from approximately 0.006 m/s to 162 m/s. The higher velocities seem to be present in the cold space most likely due to the fact the gas has a higher density and therefore a higher mass-

flow rate. Moreover, supersonic speeds are calculated at the tips of the each rotor which are believed to be caused by the low rotor tip clearance of 0.5 mm. It is also believed that these magnitudes of velocity limit the performance of the developed UDF. However, the most important qualitative result is that there is indication of a reciprocating flow in the gas circuits of the engine. By close inspection of the velocity vectors inside the cooler pipes shown on the top-right side of each of Figures 7.6-7.10 it is clear that the flow is reciprocating in the fashion described in Table 7.3.

Table 7.3: Flow direction during the cycle

Interval [Degrees]	**Flow Direction**
0º - 135º	Hot to Cold
135º - 270º	Cold to Hot
270º - 405º	Hot to Cold
405º - 540º	Cold to Hot

From Figures 7.6 - 7.10 and Table 7.3 it is obvious that this topology is similar in operation to a conventional Stirling engine in terms of the reciprocating flow.

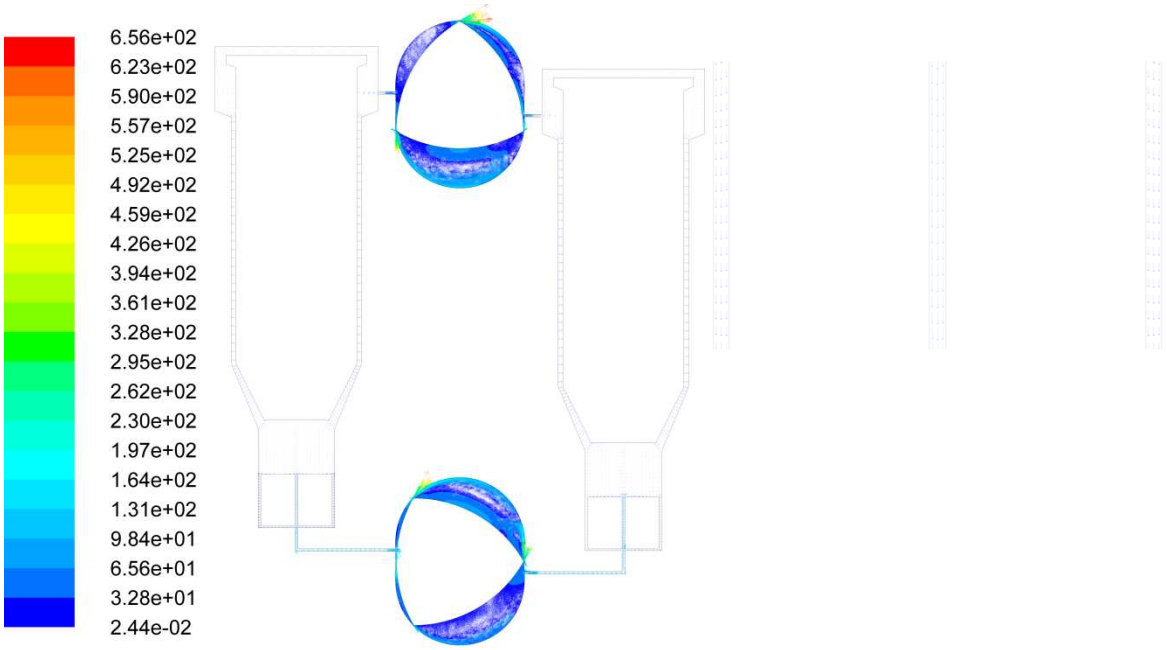

Figure 7.6: Velocity vectors inside the WRSM at the instance of the cycle when the crank shaft angle is 0º

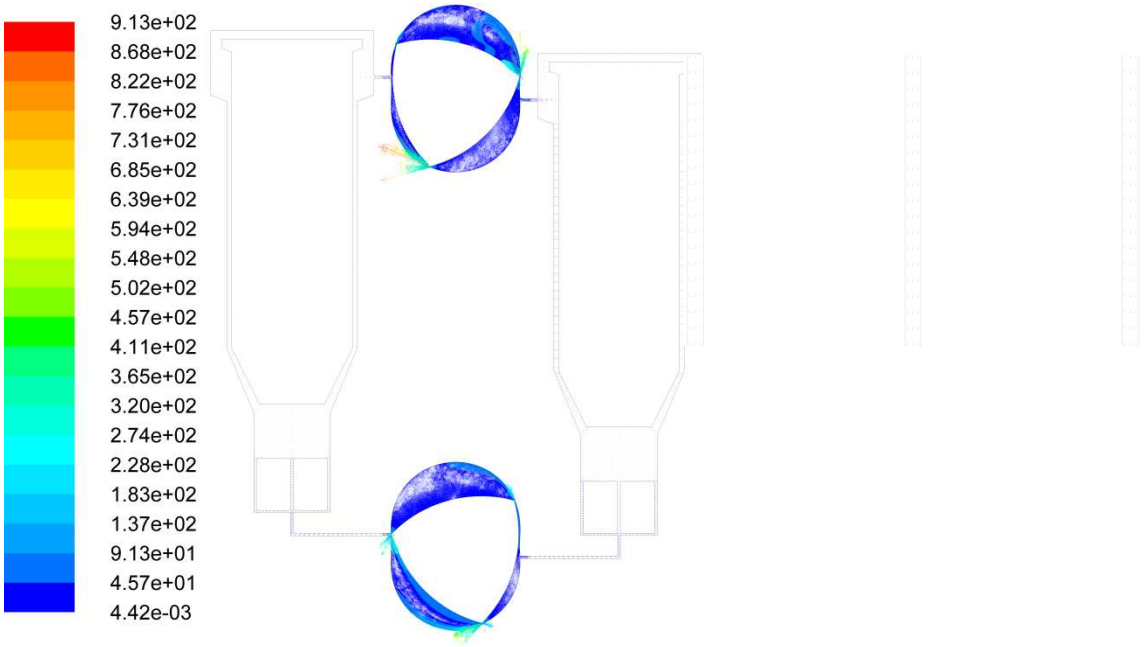

Figure 7.7: Velocity vectors inside the WRSM at the instance of the cycle when the crank shaft angle is 135º

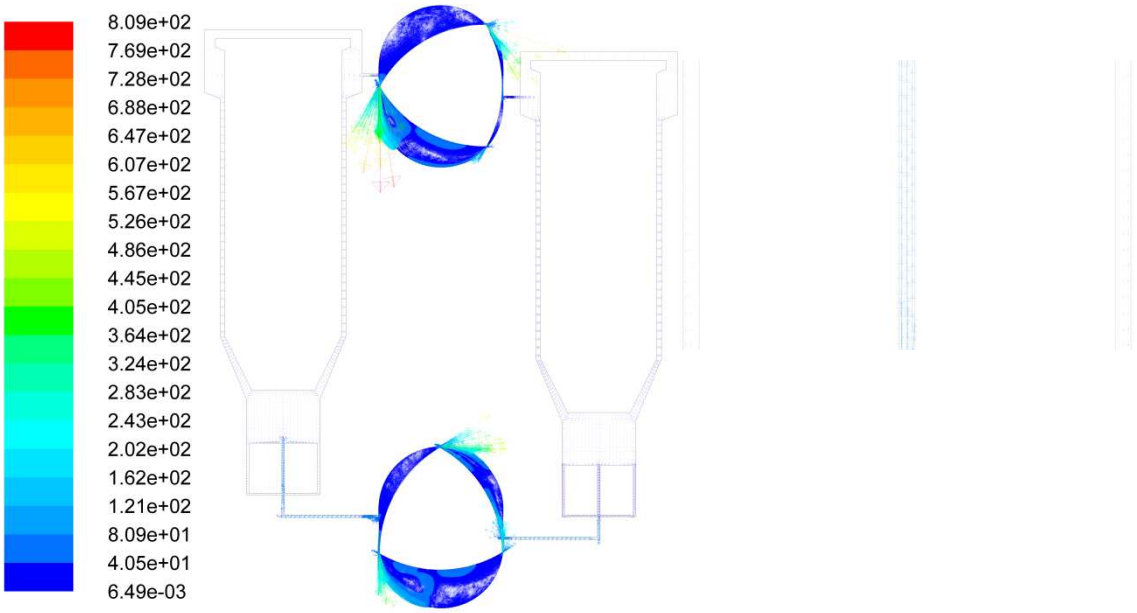

Figure 7.8: Velocity vectors inside the WRSM at the instance of the cycle when the crank shaft angle is 270º

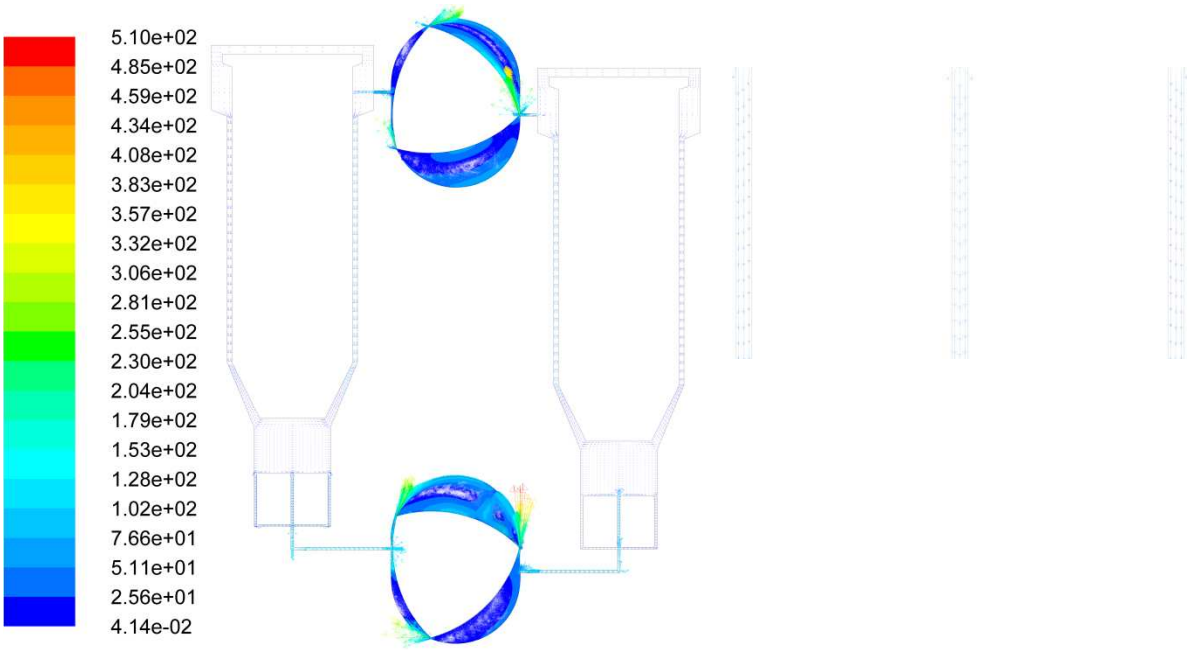

Figure 7.9: Velocity vectors inside the WRSM at the instance of the cycle when the crank shaft angle is 405º

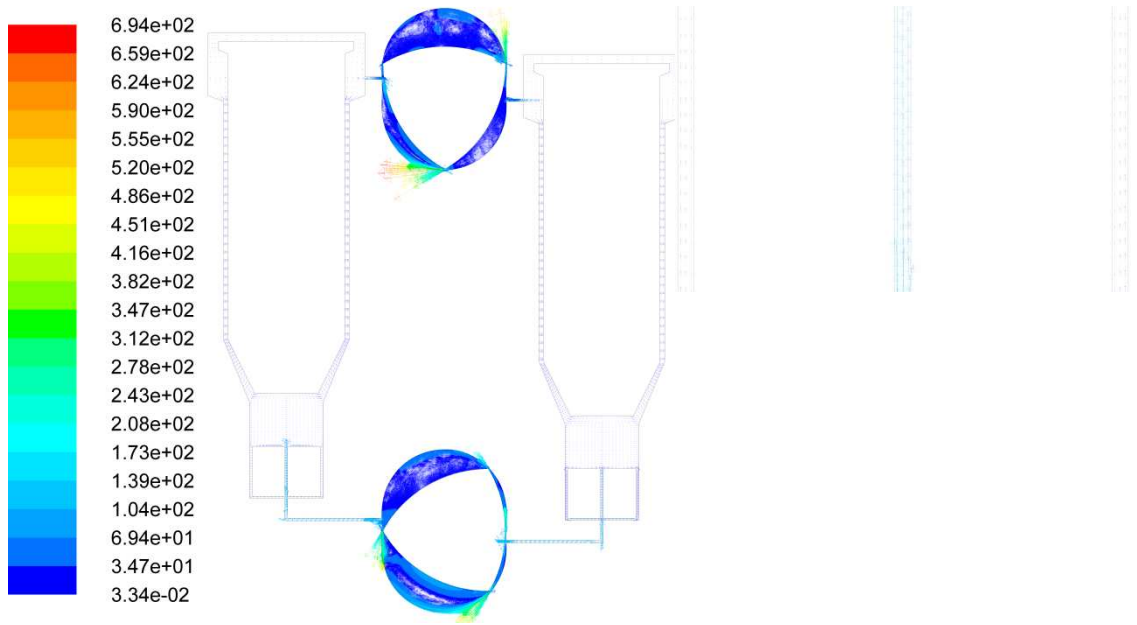

Figure 7.10: Velocity vectors inside the WRSM at the instance of the cycle when the crank shaft angle is 540º

Figures 7.11, 7.12 show the pressure variation in each chamber of each of the two working spaces, respectively. The pressure was recorded by means of a facet average absolute pressure value on each of the three flanks of the rotors. The values were recorded at every time-step.

It can be seen in Figure 7.11 that the absolute pressure on the first flank of the first rotor has a value of 27 bar at the beginning of the cycle from which this then drops almost linearly to the minimum value of 23.75 bar at approximately 150º of the crank shaft angle. Then there is a short peak at 25.5 bar for 215º of the crank shaft angle followed by a drop to 23.8 bar at 330º of the crank shaft angle. This type of variation is present in all pressure curves in both spaces. From this instance the pressure rises to its peak value with a small disturbance at 410º of the crank shaft angle. The maximum pressure of 28 bar occurs at approximately 500º of shaft revolution. From there, the pressure drops again to almost its initial value. A similar trend is observed for the pressure curve corresponding to the second flank of the hot rotor, albeit with

a phase lag of 360º of the crank shaft angle. The pressure at 0º of the crank shaft angle is 25.2 bar and then rises to 25.5 bar at 50º of the crank shaft angle approximately. Then the pressure rises to its peak value of 28 bar at 340º of the crank shaft angle. From there the pressure drops to 24 bar at 495º of the crank shaft angle followed by an increase to almost the initial value during the end of the cycle. The pressure variation inside the third chamber also follows a similar pattern with a phase lag of 450º degrees of the crank shaft angle. The pressure at the beginning of the cycle is 25.1 bar, followed by an increase to the maximum pressure of 28 bar at approximately 130º of the crank shaft angle with a small disturbance at 55º of the crank shaft angle when then there is a short peak of 26.75 bar. Then it drops steeply to the minimum value of 23.75 bar at 330º of the crank shaft angle. The pressure rises again to 25.5 bar at 405º of the crank shaft angle and then drops to 24.15 bar. This again is the short peak occurring after the maximum pressure. This is followed by an increase of the initial value towards the end of the cycle.

Figure 7.12 shows the pressure variation inside the three working chambers of the cold space as functions of the crank shaft angle. The pressure recorded on the first flank has a value of 26.2 bar at 0º of the crank shaft angle. Then it drops smoothly to the minimum value in the cycle at 183º of the crank shaft angle, with a slight disturbance at approximatelly135º of the crank shaft angle. The pressure than rises sharply in an almost exponential fashion to 26.7 bar at 320º of the crank shaft angle. This is essentially similar to the pressure disturbance observed in the pressure curves of the hot space. The pressure then drops sharply to 25.75 bar at 350º of the crank shaft angle. From there it rises smoothly to the peak value of 27.7 bar at 490º of the crank shaft angle. Afterwards the pressure decreases to its initial value by the end of the cycle. The pressure recorded at the second flank has a similar pattern albeit with a phase lag of 360º of the shaft angle. The pressure is at its minimum value of 23.3 bar at the beginning of the cycle and rises sharply to 26.7 bar at 130º of the crank shaft angle. From

there it drops sharply to 25.6 bar at approximately 170º of the crank shaft angle. Then it rises to the maximum value of 27.7 at 320º of the crank shaft angle. From there the pressure drops smoothly to its minimum value towards the end of the cycle. The pressure inside the third working chamber as recorded on the third rotor's flank, has a value of 25.8 bar in the beginning of the cycle. From there it rises to its peak value of 27.7 bar at 120º of the shaft angle, followed by a smooth drop to the minimum value of 23.4 bar at 355º of the crank shaft angle. Then, the pressure rises again to 26.4 bar at 490º from where it drops steeply to 25.8 bar at 520º after which point it reaches its initial value at the end of the cycle.

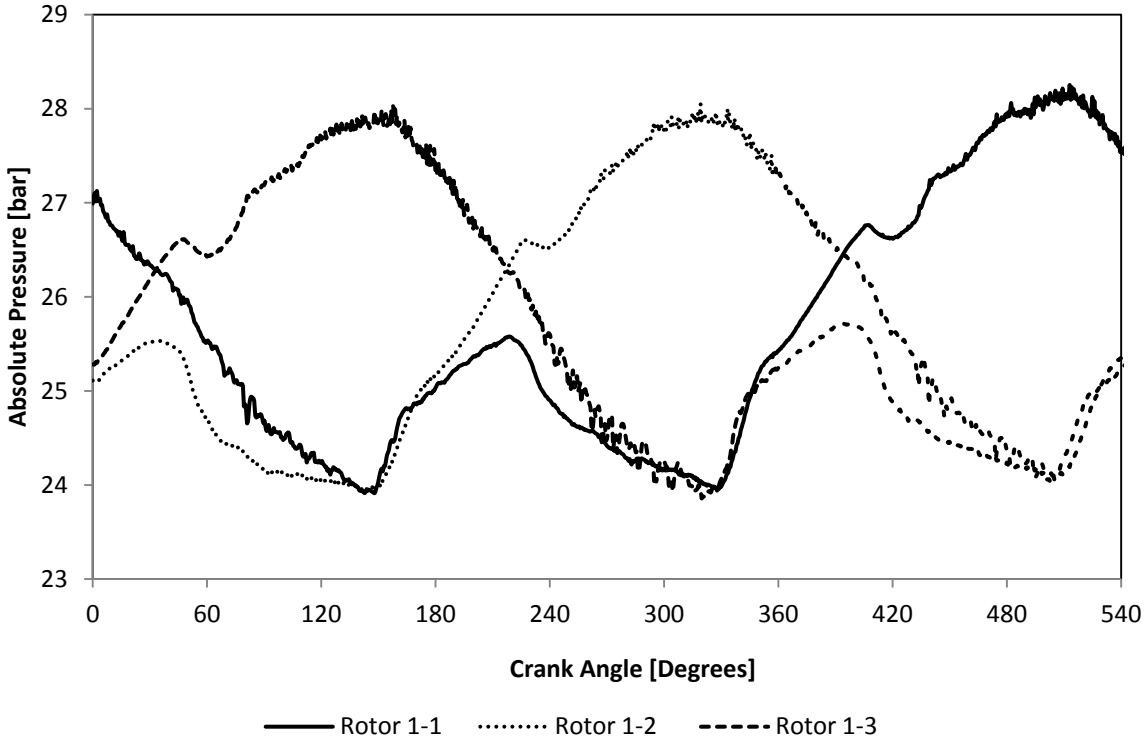

Figure 7.11: Pressure variation inside the chambers of the 1st (hot) space

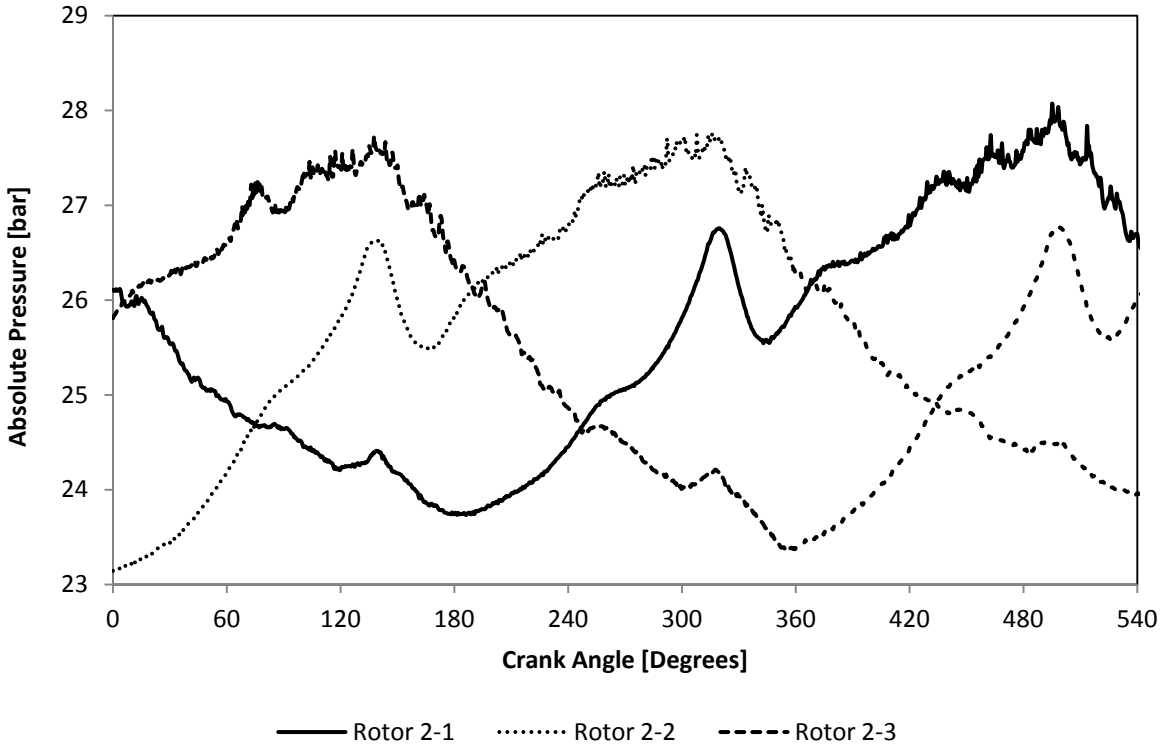

Figure 7.12: Pressure variation inside the chambers of the 2nd (cold) space

It can be seen in Figure 7.11 that the pressure curves in each chamber have a periodic pattern with a pressure amplitude of approximately 4 bar. Some disturbances in the curves while the pressure drops from its maximum to the minimum value is evident in all three chambers and at this early stage are attributed to the flow interactions near the ports connecting the two casings and the heat exchangers circuits. The pressure curves have a phase shift of 360º of the crank shaft angle as expected given the quasi-triangular shape of the rotor.

From Figure 7.12 it can be concluded that the pressure inside each working chamber of the cold space has a similar periodic variation which is in phase with the pressure variation in the hot space. An interesting observation is that the flanks with the same numbering have the same phasing. Although this may seem coincidental initially, it provides evidence indicating that there is the same connectivity between hot and cold working chambers, similar to that in

a conventional Stirling engine. The pressure amplitude in the cold chambers is slightly lower than in the hot chambers which results in the lower torque generation. Another interesting observation is that the pressure disturbances (short peaks) at each chamber, occur at the same shaft angle as the maximum pressure in the preceding chamber.

Figures 7.13 - 7.17 show the absolute pressure distribution inside the engine for instances of the cycle when the crank shaft angle is 0º, 135º, 270º, 405º and 540º, respectively. This information indicates that due to the presence and certain location and dimensions of the connecting ports there are very short instances in the cycle when connectivity in the single internal gas circuit is broken and at these instances the values of pressure in the corresponding cold and hot chambers of the same gas circuit may differ considerably.

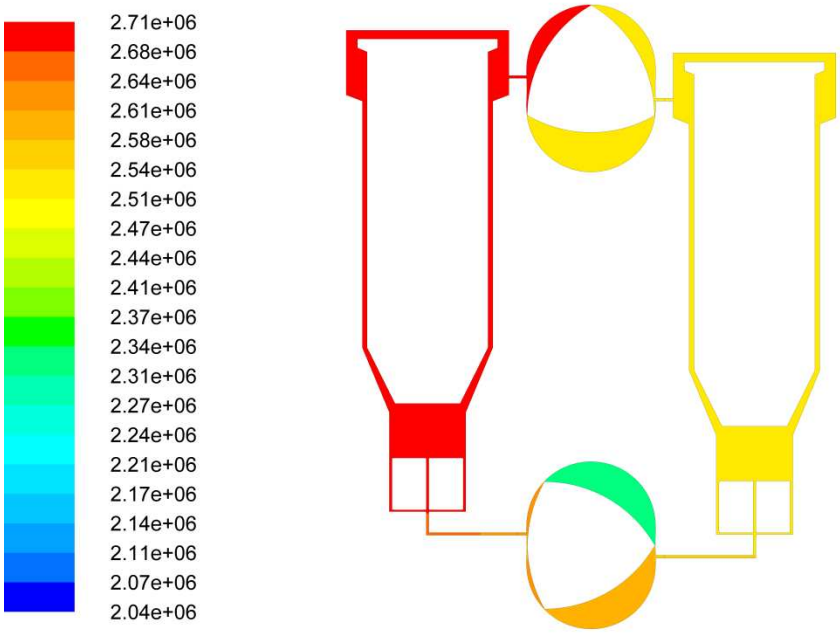

Figure 7.13: Pressure distribution inside the WRSM engine at the instance of the cycle when the crank shaft angle is 0º

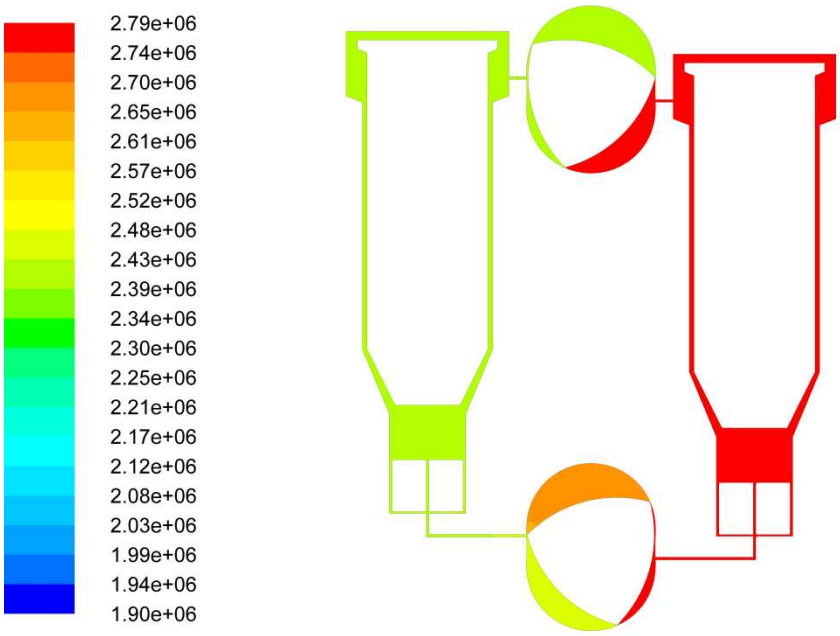

Figure 7.14: Pressure distribution inside the WRSM engine at the instance of the cycle when the crank shaft angle is 135º

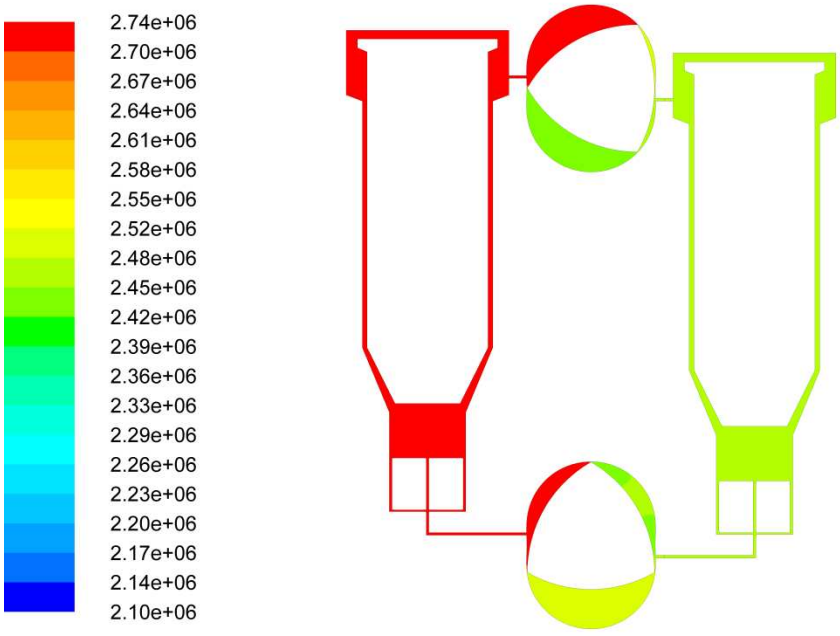

Figure 7.15: Pressure distribution inside the WRSM engine at the instance of the cycle when the crank shaft angle is 270º

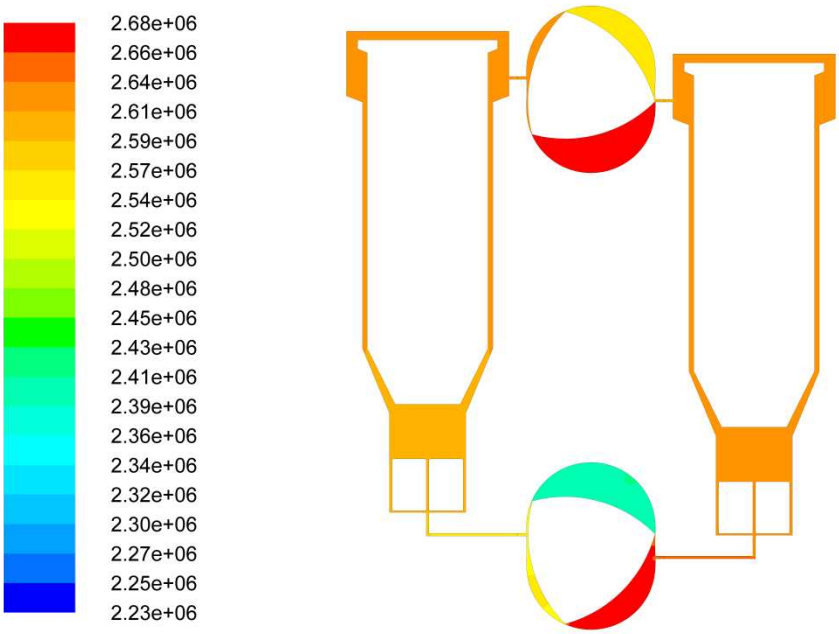

Figure 7.16: Pressure distribution inside the WRSM engine at the instance of the cycle when the crank shaft angle is 405º

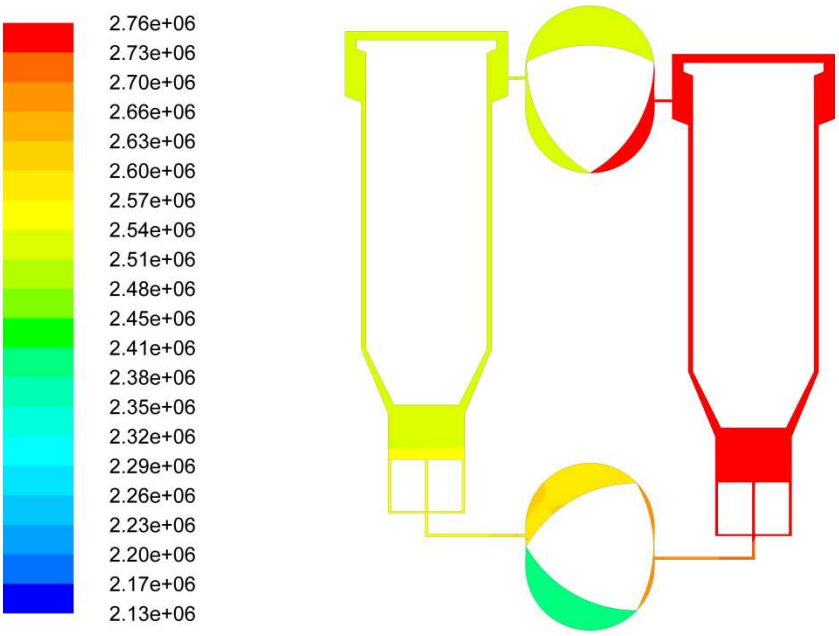

Figure 7.17: Pressure distribution inside the WRSM engine at the instance of the cycle when the crank shaft angle is 540º

Figures 7.18, 7.19 show the variation of the gas temperature inside each chamber of the hot and cold spaces, respectively.

From Figure 7.18 it can be seen that the average temperature recorded across the flank 1-1 (the first flank of the rotor in the hot space) is 1050 K at 0º of the crank shaft angle. From there it drops to 1020 K at 84º of the crank shaft angle. Then it increases to 1040 K at 135º, followed by a reduction of 20 K at approximately 170º of the crank shaft angle. During the interval between 136^{o} and 333^{o} of the crank shaft angle there is some scattering of the recorded temperature of around 10 K. At 333^{o} of the crank shaft angle the temperature starts rising to its maximum value of 1080 K at 507º of the crank shaft angle. The temperature of the gas on the second flank (1-2) is 1032 K at 0º of the crank shaft angle. The temperature then drops to the minimum of 1015 K at approximately 45º of the crank shaft angle. During this interval there is some scattering of the recorded temperature values of about 5 K -10 K which is attributed to pressure variation fluctuations. The temperature then rises to its peak value of 1082 K at 315º of the crank shaft angle, followed by a drop to 1050 K at 450º of the crank shaft angle. Then it rises to 1062 K at 504^{o} of the crank shaft angle and then drops towards the end of the cycle. By considering the temperature variation on the second flank of the hot rotor it is evident that the solution has not reached steady state as the values are rising. This is consistent for all three recorded temperatures presented in Figure 7.18. Finally, the temperature recorded on the third rotor flank (1-3) has a value of 1015 K at the beginning of the cycle. Then it rises smoothly to 1060 K at approximately 145º of the crank shaft angle. This is followed by a drop to the minimum value of 1033 K at 245º of the crank shaft angle. The temperature then rises to 1062 K at 360 ^{o} of the crank shaft angle. Then there is some scattering of the recorded values of around 5 K-10 K. The temperature starts rising again towards the end of the cycle.

Figure 7.19 shows the temperature variation for each of three working chambers of the cold space during 540º of shaft revolution or half turn of the piston. The temperatures in the cold space seem to follow a more distinctive pattern than those recorded at the hot rotor. The temperature recorded on the first rotor flank of the cold space (2-1) is 582 K in the beginning of the cycle. Then it drops steeply and almost linearly to its minimum value of 530 K at 50º of the crank shaft angle. From then it starts rising smoothly to 575 K at 325º of the crank shaft angle. Then it drops quickly to 570 K and rises to its peak value of 590 K at 485º of the crank shaft angle. Again there is some scattering of the values during the time interval corresponding to the crank shaft angles between 120º and 370º and a small peak at 325º of the crank shaft angle which follows the corresponding pressure variation on this flank. The gas temperature recorded on the second flank (2-2) has a value of 555 K in the beginning of the cycle. Then it rises in a scattered fashion to the peak value of 591 K at 305º of the crank shaft angle, with a smaller peak of 575 K at 130º of the crank shaft angle. The temperature then drops quickly to the minimum value of 525 K at 411º of the crank shaft angle from where it starts rising again towards the end of the cycle. Finally, the gas temperature recorded on the third rotor flank (2-3) has an initial value of 570 K and then smoothly rises to its peak value of 591 K at 135º of the crank shaft angle. Then it steeply drops to the minimum value of 525 K at 245º of the crank shaft angle from where it starts rising again towards the end of the cycle with a short peak of 574 K occurring at 495º of the crank shaft angle.

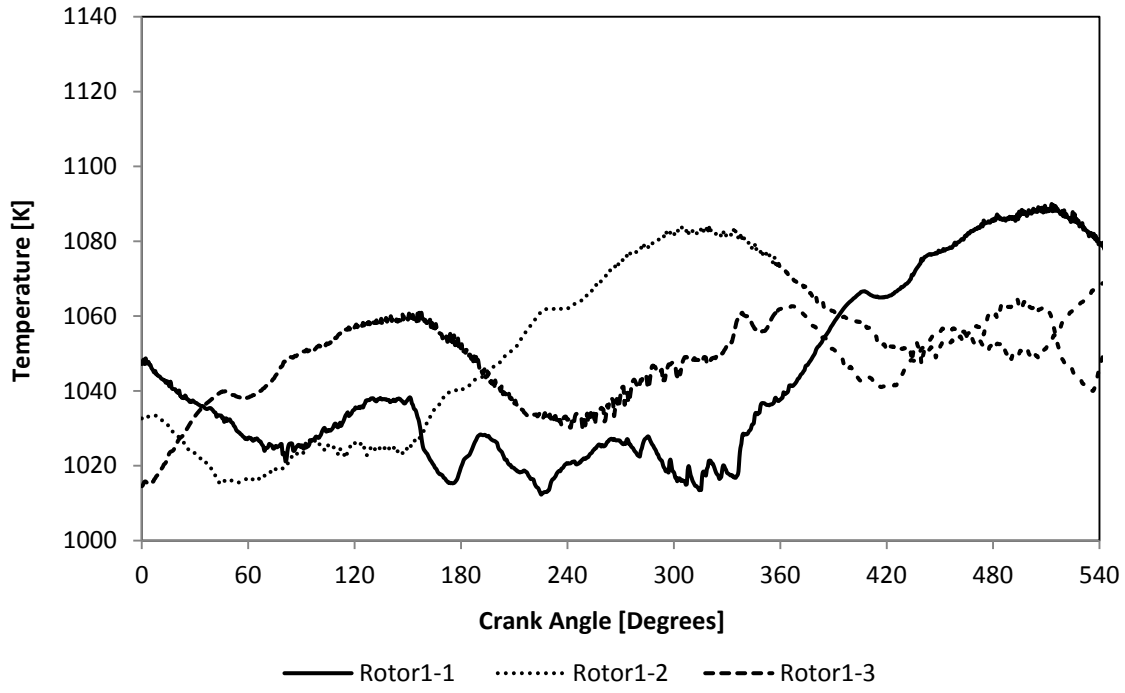

Figure 7.18: Temperature variation inside the chambers of the 1st (hot) space

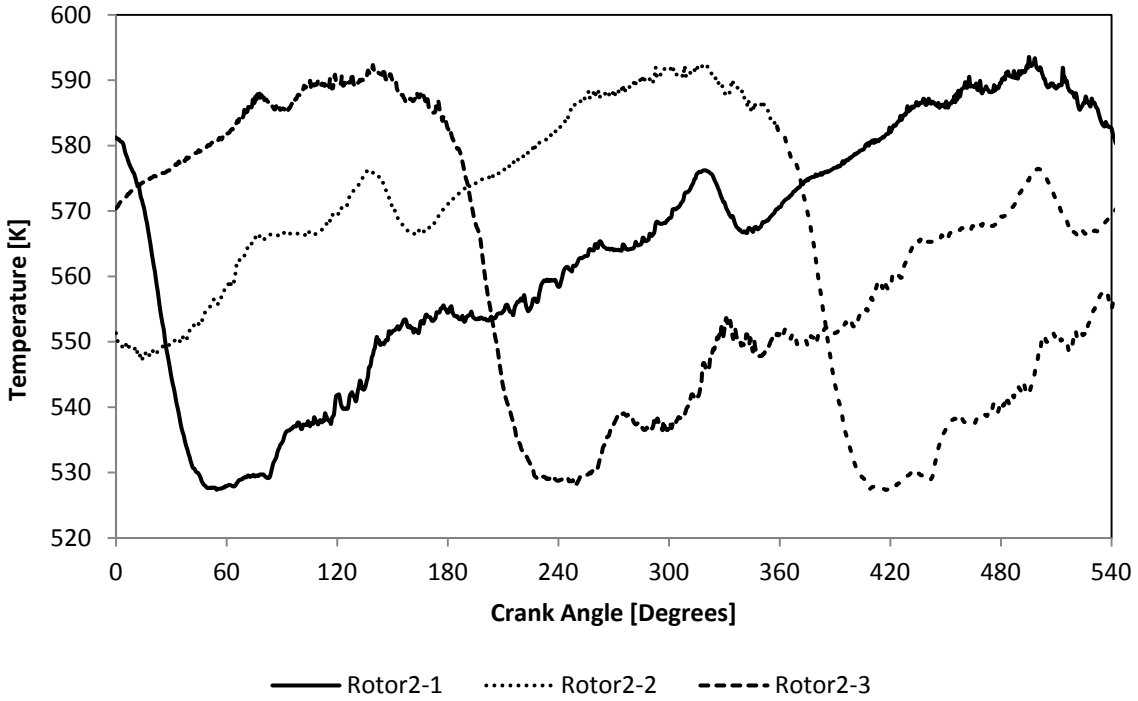

Figure 7.19: Temperature variation inside the chambers of the 2nd (cold) space

It can be seen in Figures 7.18, 7.19 that the temperatures follow a periodic pattern; however it is clear that the solution has not stabilised yet. Moreover, the gas temperature variation on each flank is in phase with the corresponding pressure variation. At this stage of the solution there is a temperature amplitude of approximately 60 K on all six rotor flanks. Finally, there is a temperature difference of 550 K between the hot and the cold space, which provides the evidence that the particular design performs as a heat engine.

Figures 7.20 - 7.23 show the temperature distribution inside the two sets of heat exchangers of the WRSM.

In particular, Figures 7.20 and 7.21 show the temperature variation inside the top and middle regions of the two heaters respectively over the period of the cycle. The monitoring points set to record temperatures in heaters are annotated as follows: left and right sides of each heater are numbered as 1 and 2. Thus heater-top-left-1 indicates a monitoring point inside the left channel of the left heater near its top region at the level of the heater connector pipes.

Figure 7.20 shows that the gas temperature recorded at point 1 on the left heater is 867 K at 0º of the crank shaft angle. From there it drops smoothly to its minimum value of 800 K at approximately 130º of the crank shaft angle. Then it rises smoothly to the maximum value of 880 K at 315º of the crank shaft angle, followed by a smooth drop to its initial value at approximately 360º of the crank shaft angle. An immediate observation is that the temperature variation inside the heater does not have the same period of 540º as the pressure curve and the temperatures inside the six working chambers. This is believed to occur due to the fact that there are 3 equivalent pairs of working chambers which share two sets of heat exchangers. Accordingly, the temperature at the top of the right channel of the left heater (the point 2) is 905 K at the beginning of the cycle followed by a smooth drop to the minimum value of 885 K at 135º of the crank shaft angle. From there it rises smoothly to its peak value

of 925 K at 330º of the crank shaft angle and then drops to its initial value at approximately 360º of the crank shaft angle. For the heater on the right, the temperature on the left channel (the point 1) has a value of 960 K at 0º of the crank shaft angle. Then is rises to its maximum value of nearly 1012.5 K at 130º of the crank shaft angle, followed by a smooth drop to the minimum value of 960 K at 330º of the crank shaft angle. From that point the temperature rises to the initial value at approximately 360º of the crank shaft angle. It can be noted that the temperature at the top of the right heater is in the counter-phase with that recorded inside the heater on the left side. Finally, the temperature at the right channel of the right heater is 715 K at the beginning of the cycle. From there is rises smoothly to its peak value of 750 K at 130º of the crank shaft angle. Then it drops smoothly to its minimum value of 702.3 K at 320º of the crank shaft angle and rises again to its initial value near 360º of the crank shaft angle.

The main observations from Figure 7.20 are that the temperature variation inside the two heaters is in counter-phase and that their period is approximately 360º. Moreover, the temperatures of the channels closer to the rotor on either side are higher and have a higher amplitude than the temperatures in the outer channels. This is likely due to the 2D set-up of the model predicting the flow to be higher at the channels closer to the ports. Moreover, the temperatures show a slight tendency to increase which is a manifestation of the early state of the solution.

Figure 7.21 shows the temperature variation near the middle region of the heaters. The temperature in the mid-length location on the left channel of the left heater is 980 K at 0º of the crank shaft angle. From there it drops to the minimum value of 920 K at 125º of the crank shaft angle, followed by a smooth rise to the maximum value of 980 K at 340º of the crank shaft angle. The temperature then drops back to its initial value at approximately 360º of the crank shaft angle. On the right channel of the left heater the temperature has a maximum

value of 975 K in the beginning of the cycle and then drops to the minimum value of 950 K at the 130º of the crank shaft angle. Then, it slowly rises to its initial value at 360º of the crank shaft angle. The temperature in the mid-length of the right channel of the right - side heater has a value of 850 K at 0º of the crank shaft angle, followed by a smooth increase up to its maximum value of 930 K at 125º of the crank shaft angle. The temperature then drops to the minimum value of 810 K at 320º of the crank shaft angle and rises again to its initial value at approximately 360º of the crank shaft angle. On the right channel of the right-side heater, the mid-length the gas temperature has an initial value of 970 K at 0º of the crank shaft angle, followed by an increase up to its maximum value of 1005 K at 130º of the crank shaft angle. The temperature then drops smoothly to its lowest value of 960 K at 330º of the crank shaft angle and rises up to its initial value at approximately 360º of the crank shaft angle.

Similar to Figure 7.20, the temperature variation in the middle region of the two heaters is of a periodic nature with a period of 360º of the crank shaft angle. The gas temperatures in each heater are in counter-phase. However, the highest temperatures from Figure 7.23 are now recorded the outer channels of the heater, in contrast to what was observed in the records near the top region of the heaters. Still, the early state of the solution is obvious.

Figure 7.22 shows the gas temperatures inside the two regenerators of the WRSM, near the middle of their length and width. The temperatures are almost constant at 602 K with minor variations around these values and a period of 360º of the crank shaft angle. By close inspection, the temperatures vary in counter-phase, similar to the temperatures recorded inside the four heater channels.

Figure 7.23 shows the temperature variation inside the middle-pipe of each of the two coolers at their mid-length location. The gas temperature in the left-side cooler is 525 K at 0º of the crank shaft angle, followed by an increase to 533 K at 57º of the crank shaft angle. Then the

temperature drops to the minimum value of 504.5 K at 130º of the crank shaft angle, followed by a sharp and almost linear increase to 547 K at approximately 195º of the crank shaft angle. The temperature then rises further to 565 K at 290º of the crank shaft angle and drops steeply to its initial value at 360º of the crank shaft angle. The gas temperature recorded in the right-side cooler is in counter-phase with the gas temperature recorded in the left-side cooler. At 0º degrees of the crank shaft angle the temperature is 546 K and rises to its peak value of 565 K at 102º of the crank shaft angle. Then it drops swiftly to 534 K at 170º of the crank shaft angle, followed by another increase to 544 K at 238º of the crank shaft angle. The temperature then drops smoothly to 536 K at 304.5º of the crank shaft angle and then there is another steep and linear drop to the minimum value of 506 K at 334º of the crank shaft angle. The temperature rises back to its initial value at approximately 360º of the crank shaft angle.

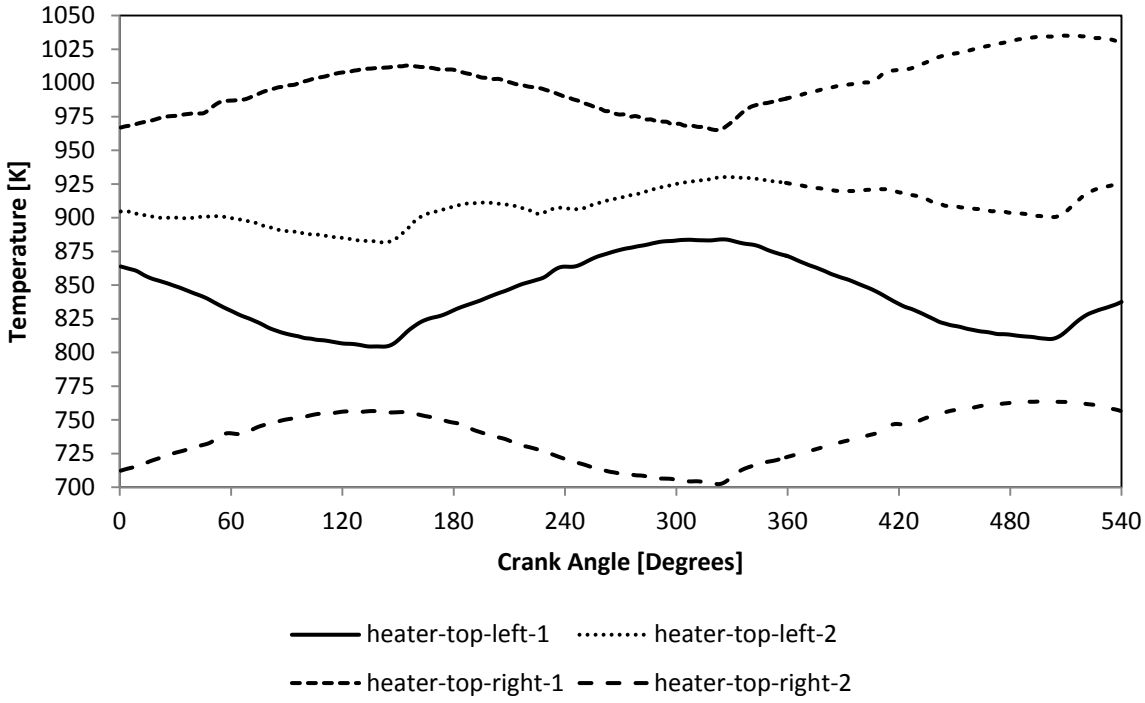

Figure 7.20: Temperature variation at the top of the heaters of the WRSM

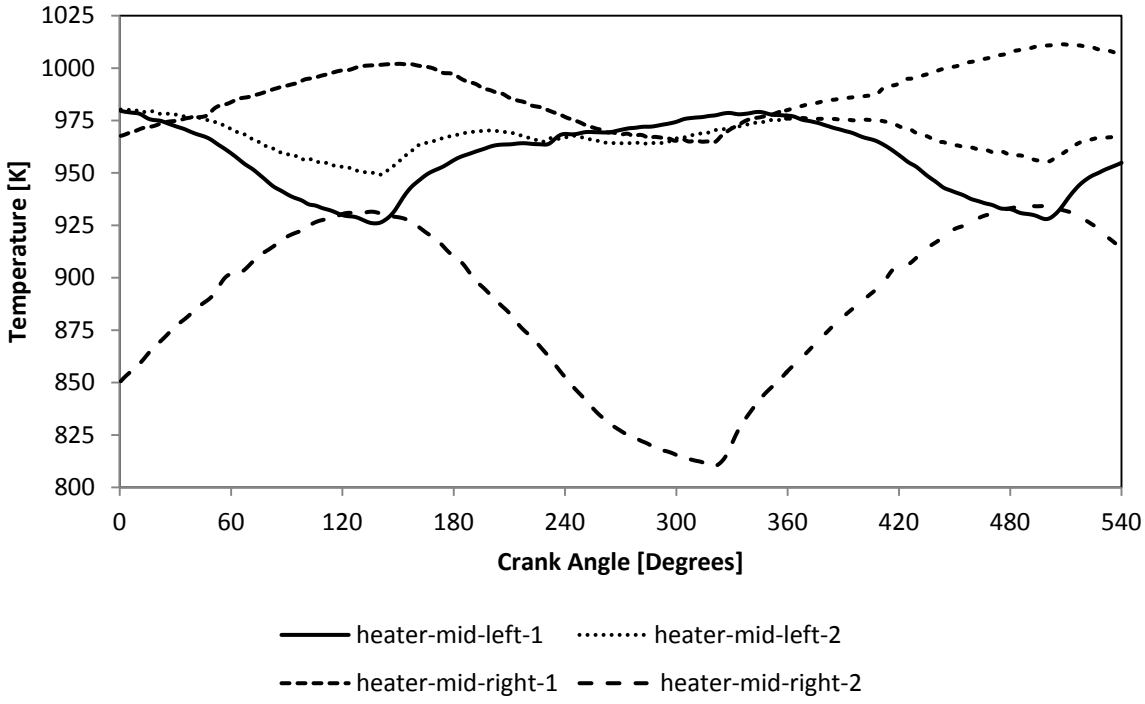

Figure 7.21: Temperature variation at the middle of the heaters of the WRSM

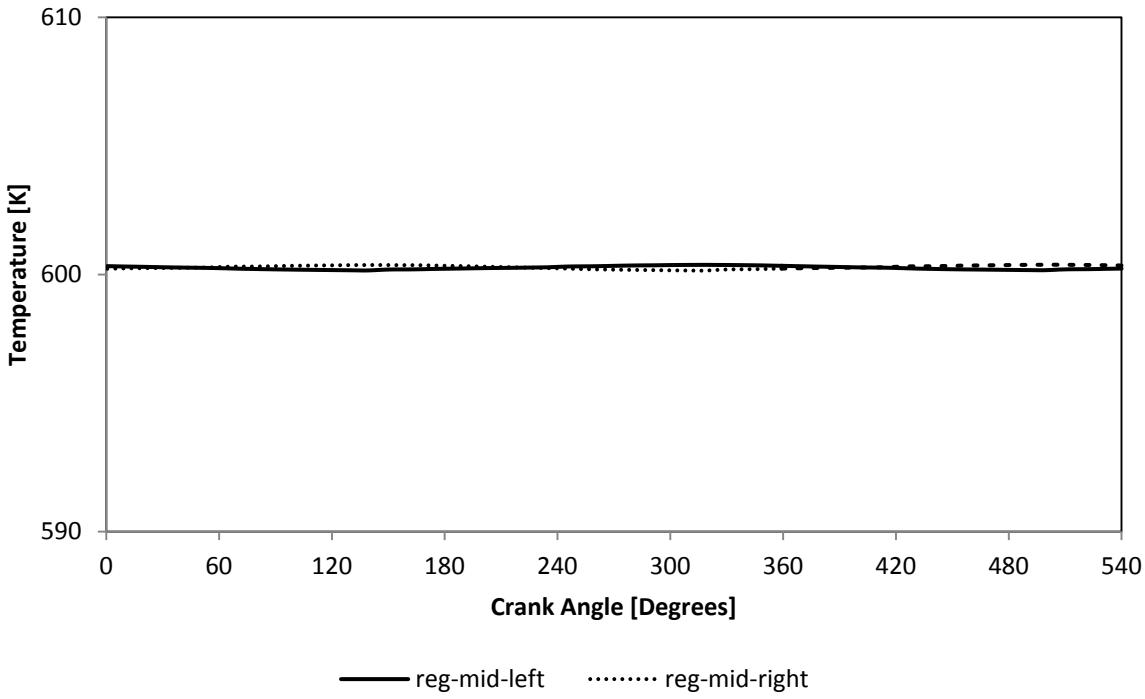

Figure 7.22: Temperature variation at the middle of the regenerators of the WRSM

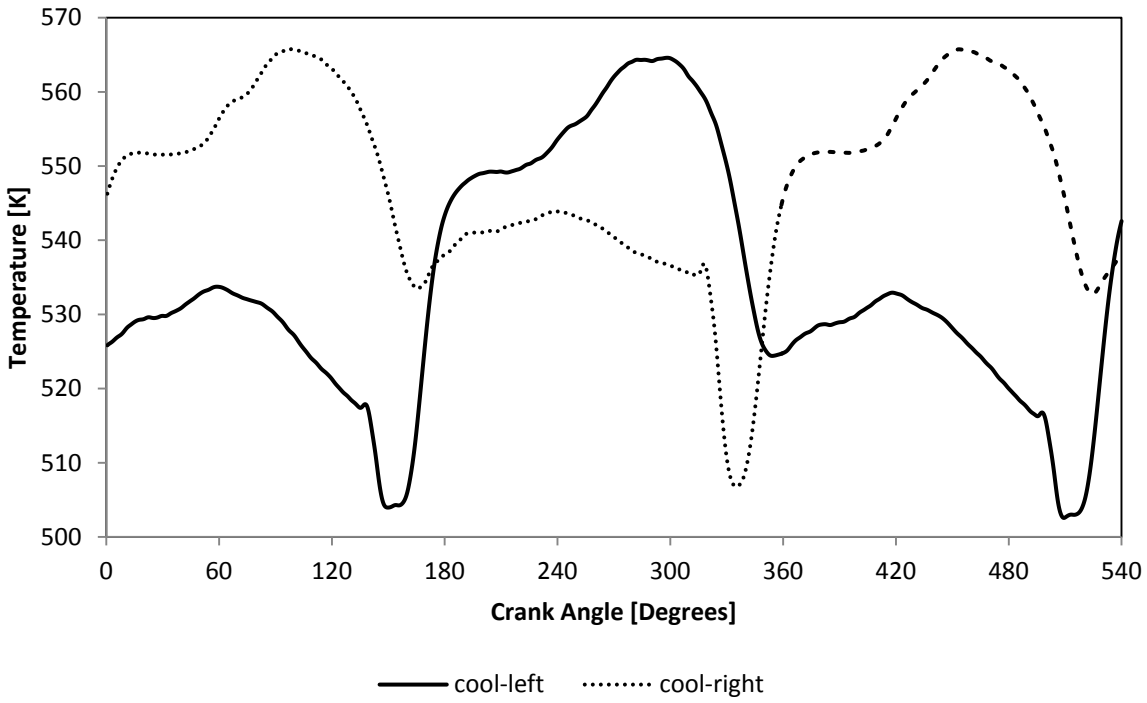

Figure 7.23: Temperature variation inside the coolers of the WRSM

The gas temperatures measured at various locations inside the two sets of heat exchangers provide interesting observations. The most important finding was that the temperature variation inside all components of both sets of heat exchangers had a period of 360º of the crank shaft angle compared to the 540º period seen in the temperature and pressure variation inside the 6 working chambers of the WRSM. Moreover, the gas temperatures inside the left-side heat exchanger were in counter-phase compared with those measured inside the right-side heat exchangers. Additionally, the temperatures measured inside the two coolers, albeit periodic, demonstrated a very particular variation pattern which did not resemble a sine or cosine function as commonly typical for conventional Stirling engines.

Figures 7.24 - 7.28 show the temperature contours inside the engine for the instances of the cycle when the crank shaft angle is 0º, 135º, 270º, 405º and 540º. It can be seen that these contours confirm the information presented earlier in Figures 7.18-7.23. Temperature

contours, unlike pressure contours presented in Figures 7.14-7.17 vary continuously throughout the cycle, which is typical for a conventional Stirling engine.

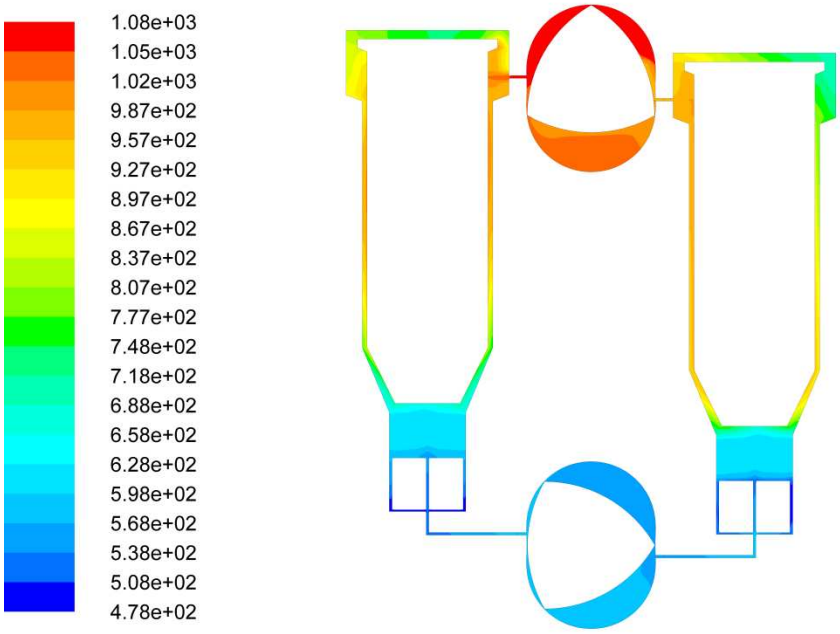

Figure 7.24: Temperature distribution inside the WRSM at the instance of the cycle when the crank shaft angle is 0º

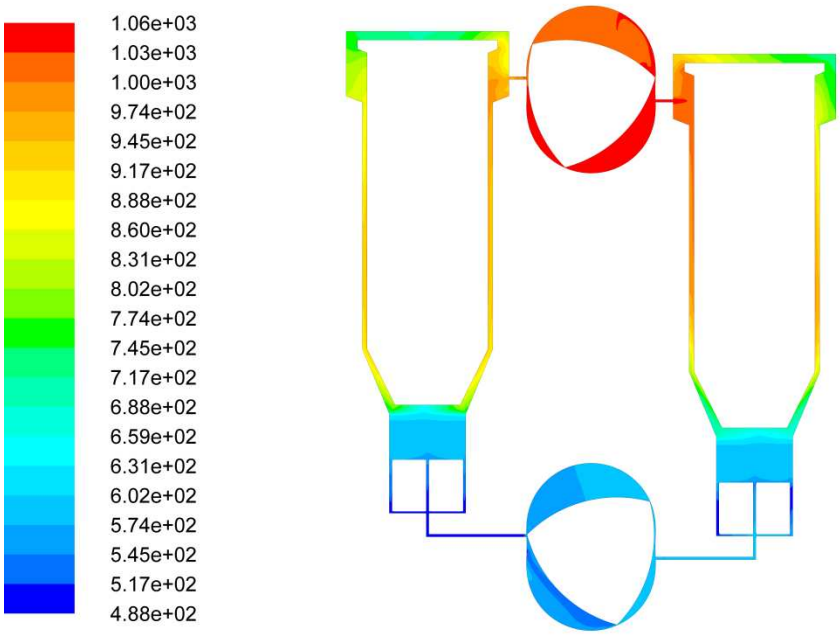

Figure 7.25: Temperature distribution inside the WRSM at the instance of the cycle when the crank shaft angle is 135º

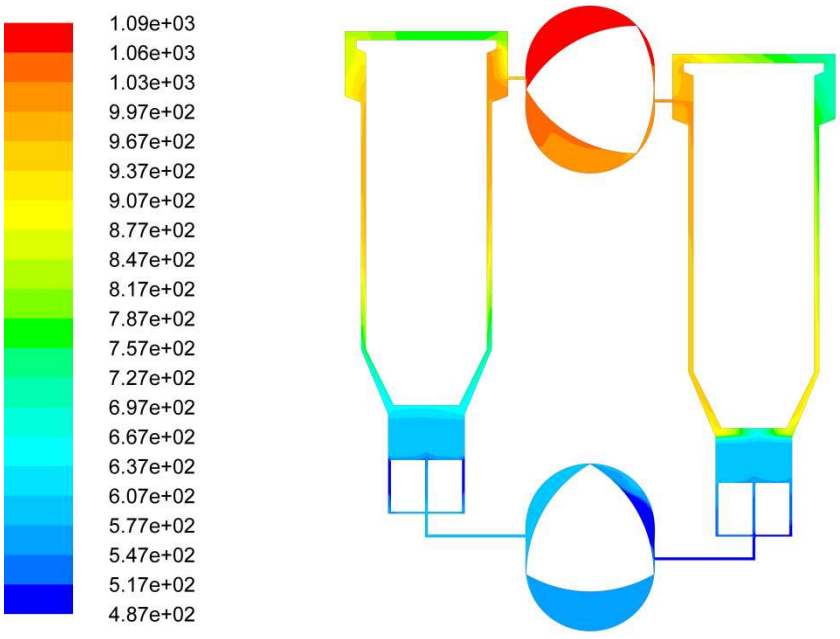

Figure 7.26: Temperature distribution inside the WRSM at the instance of the cycle when the crank shaft angle is 270º

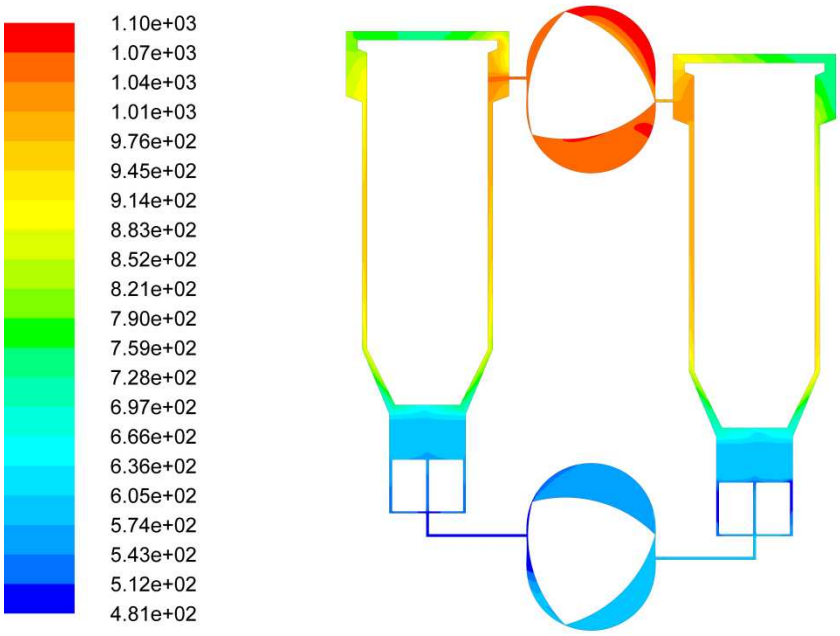

Figure 7.27: Temperature distribution inside the WRSM at the instance of the cycle when the crank shaft angle is 405º

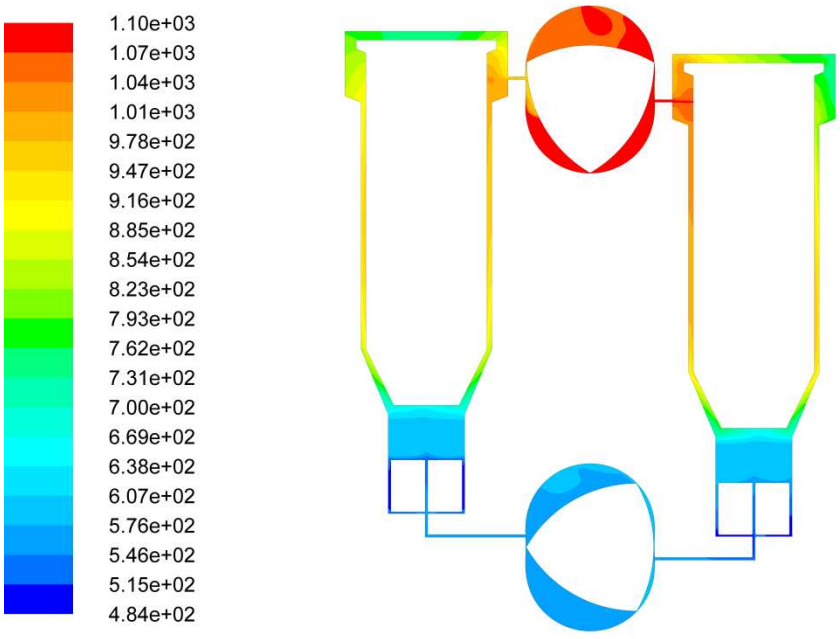

Figure 7.28: Temperature distribution inside the WRSM at the instance of the cycle when the crank shaft angle is 540º

7.3.1.1 Calculation of power

In order to calculate the indicated power output of the engine, it is necessary to generate the torque curves for each of the flanks, or indicated pressure-volume diagrams for each pair of hot and cold working spaces. In this study pressure-volume diagrams were used to determine power output or power requirements of the machine. Such diagrams are shown in Figure 7.29 for the pair of chambers 1-1 and 2-1 when rotor rotations are shifted by 90^{o}. Analysis of results shows that pressure curve during expansion is lower than that during compression for both chambers which indicates that there is no useful power output from the machine. Upon integration, the net cyclic work calculated from Figure 7.29 was -12 J. The negative sign suggests that the engine does not operate as a prime mover but rather as a heat pump or cooling machine. After examination of volume changes it was found that for the orientation of the rotors as shown in Figure 7.3 the compression spaces are leading in phase angle instead of lagging. Thus, the approach which was taken for the orientation of rotors as for conventional Stirling engines did not lead to the configuration operating as an engine and this is the specific feature discovered in this study for the rotary system under investigation. In detail, this eventually causes the volume variation of the hot chambers to lead that of the cold chambers by 450º as shown in Figure 7.30 for the hot and cold working chambers 1-1 and 2-1 respectively.

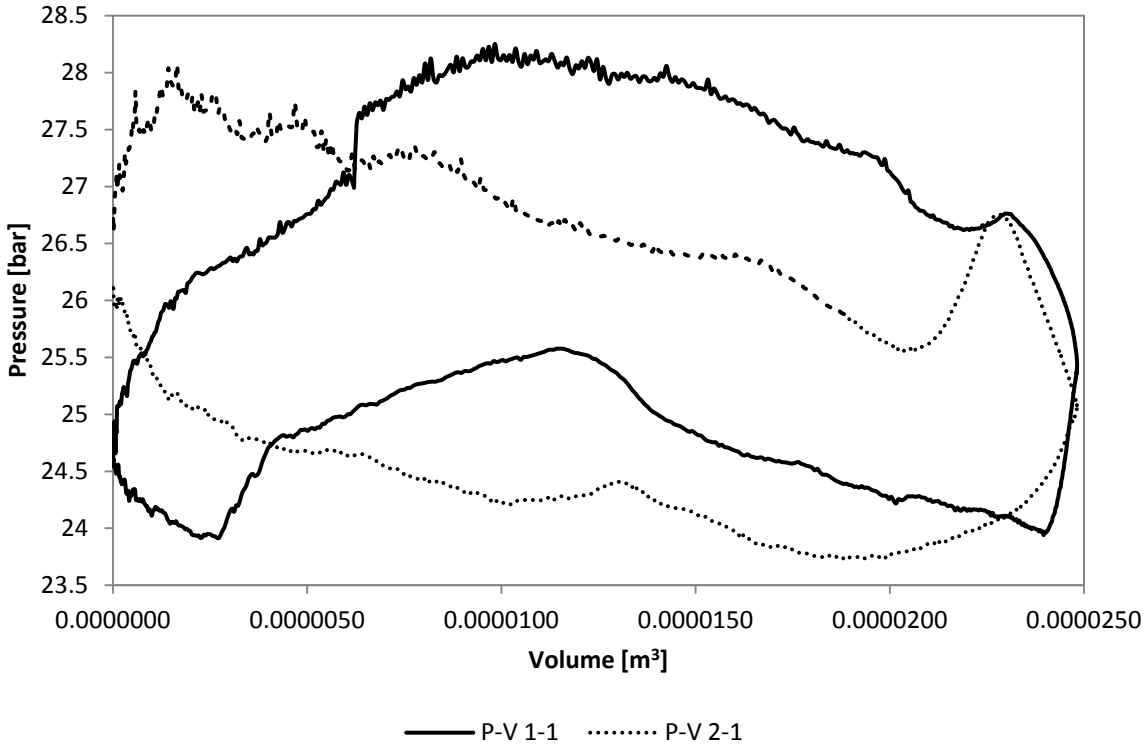

Figure 7.29: P-V indicated diagram for the hot chamber 1-1 and the cold chamber 2-1

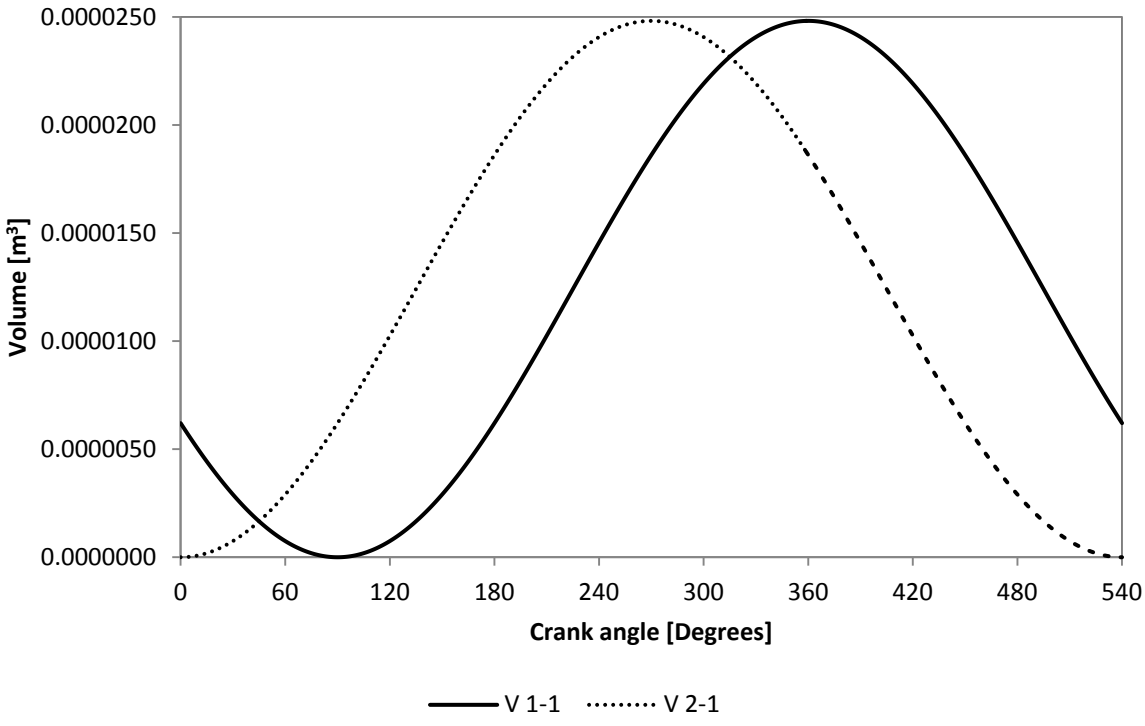

Figure 7.30: Volume variation inside the hot chamber 1-1 and the cold chamber 2-1

Figure 7.31 shows the pressure volume indicated diagram for the hot chamber 1-2 and the cold chamber 2-2. The net cyclic work was calculated at -11.3 J. The shapes of the P-V areas are similar to that in Figure 7.29. The slight differences can be attributed to the differences between the pressure variations in each working chamber as shown in Figures 7.11, 7.12. Figure 7.32 shows the phasing between the volume variations of the hot working chamber 1-2 and the cold working chamber 2-2. It can be seen from Figure 7.32 that the variation of the cold chamber 2-2 is leading that of the hot chamber 1-2 by 90º. As in Figure 7.30, this occurs despite the fact that the hot rotor was advanced by 90º which is the common practice in conventional Stirling engines.

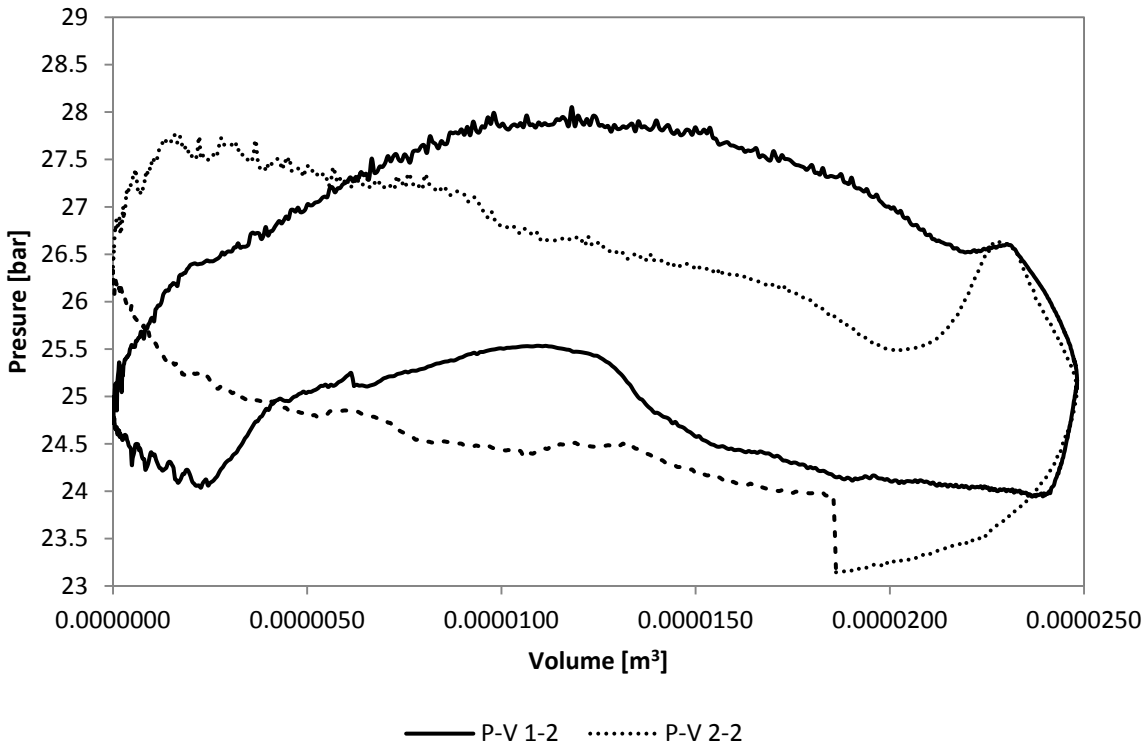

Figure 7.31: P-V indicated diagram for the hot chamber 1-2 and the cold chamber 2-2

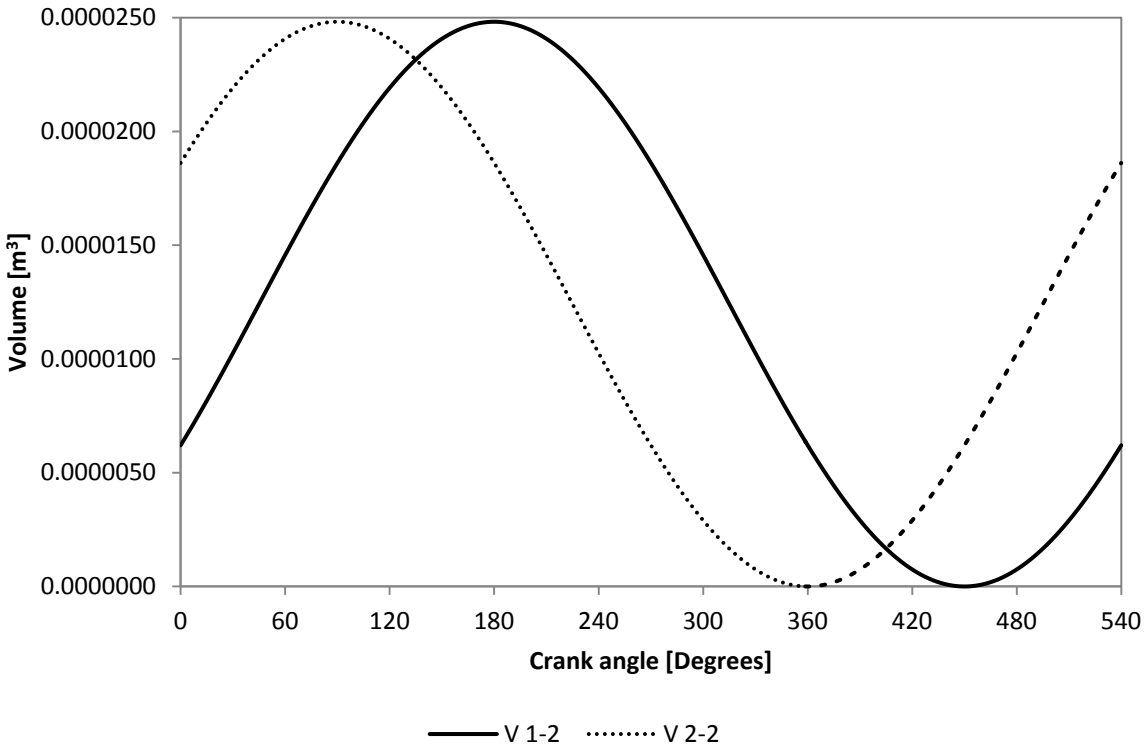

Figure 7.32: Volume variation inside the hot chamber 1-2 and the cold chamber 2-2

Finally, Figure 7.33 shows the pressure-volume indicated diagrams and Figure 7.34 shows the phasing between the volume variations inside the hot chamber 1-3 and the cold chamber 2-3. From Figure 7.33 the net cyclic work was calculated to be -11.7 J. The pressure-volume areas of Figure 7.33 are similar in shape with those presented in Figures 7.29 and 7.31. Figure 7.33 shows that the volume variation inside the cold chamber 2-3 is leading that of the hot chamber 1-3 by 90º. As in Figures 7.30 and 7.32, this occurs despite the fact that the hot rotor was set to lead the cold rotor by a phase angle of 90º degrees.

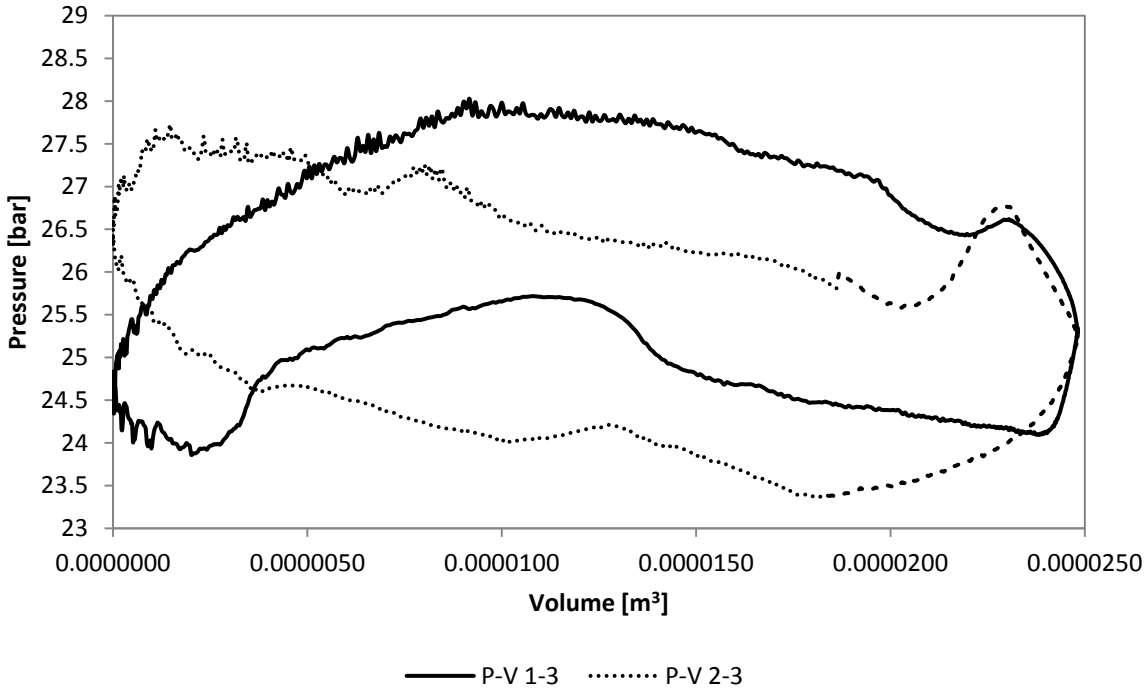

Figure 7.33: P-V indicated diagram for the hot chamber 1-3 and the cold chamber 2-3

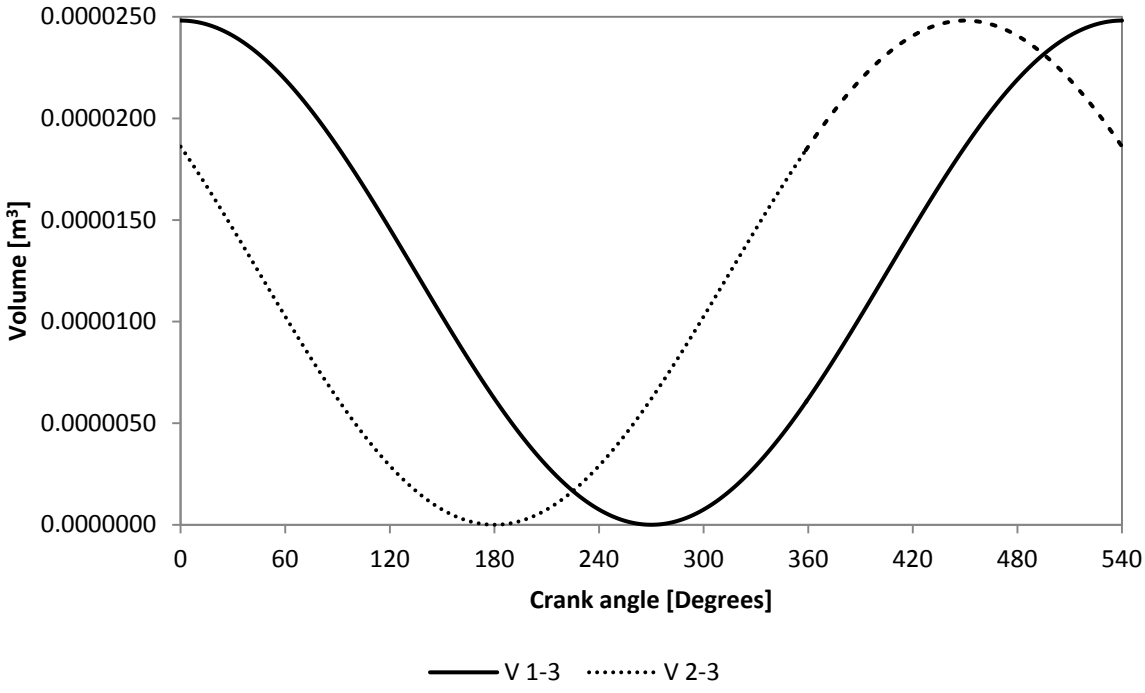

Figure 7.34: Volume variation inside the hot chamber 1-3 and cold chamber 2-3

7.3.2 Results of the 2D CFD model without UDF

Figures 7.35 and 7.36 show the pressure variation of a WRSM engine without a sub-routine to prevent tip-leakage. In view of Figures 7.35, 7.36, the pressure curves from each cylinder are identical which suggests that the UDF had no effect on the development of power output. This is believed to be due to the low values of the *Ks* and *Vs* coefficients which were under-relaxed to avoid numerical implications in the critical locations around the rotor tips.

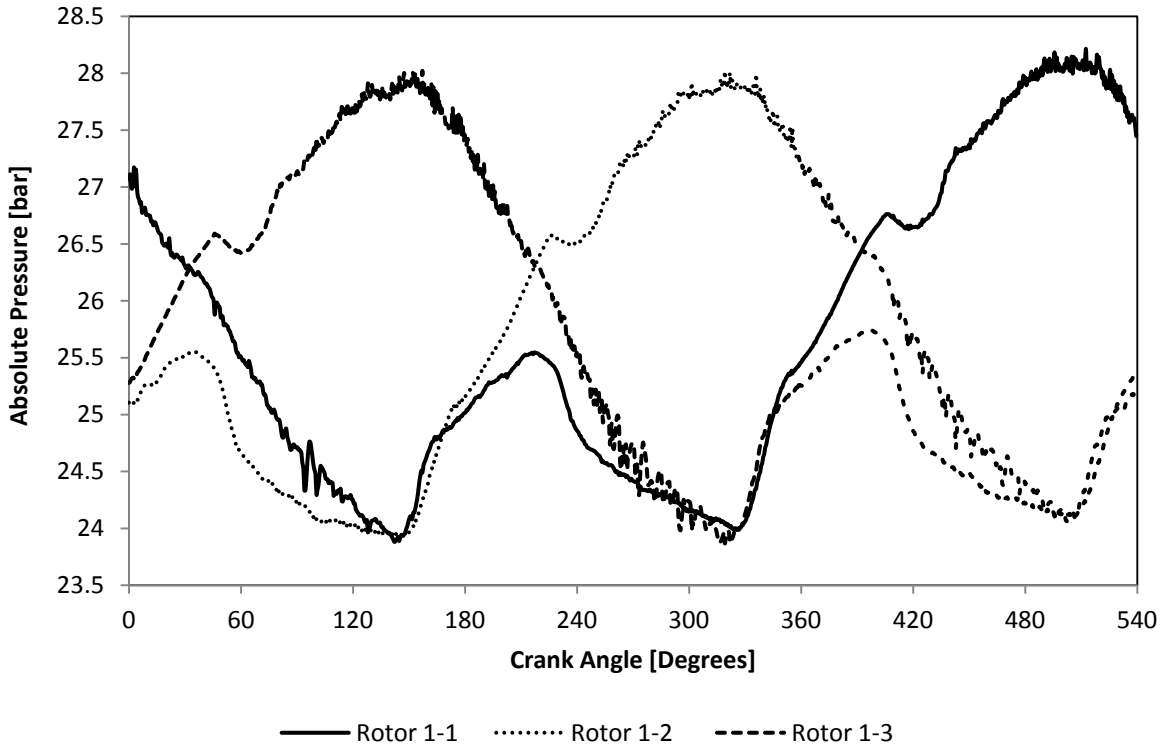

Figure 7.35: Pressure variation inside the chambers of the hot rotor of WRSM without UDF

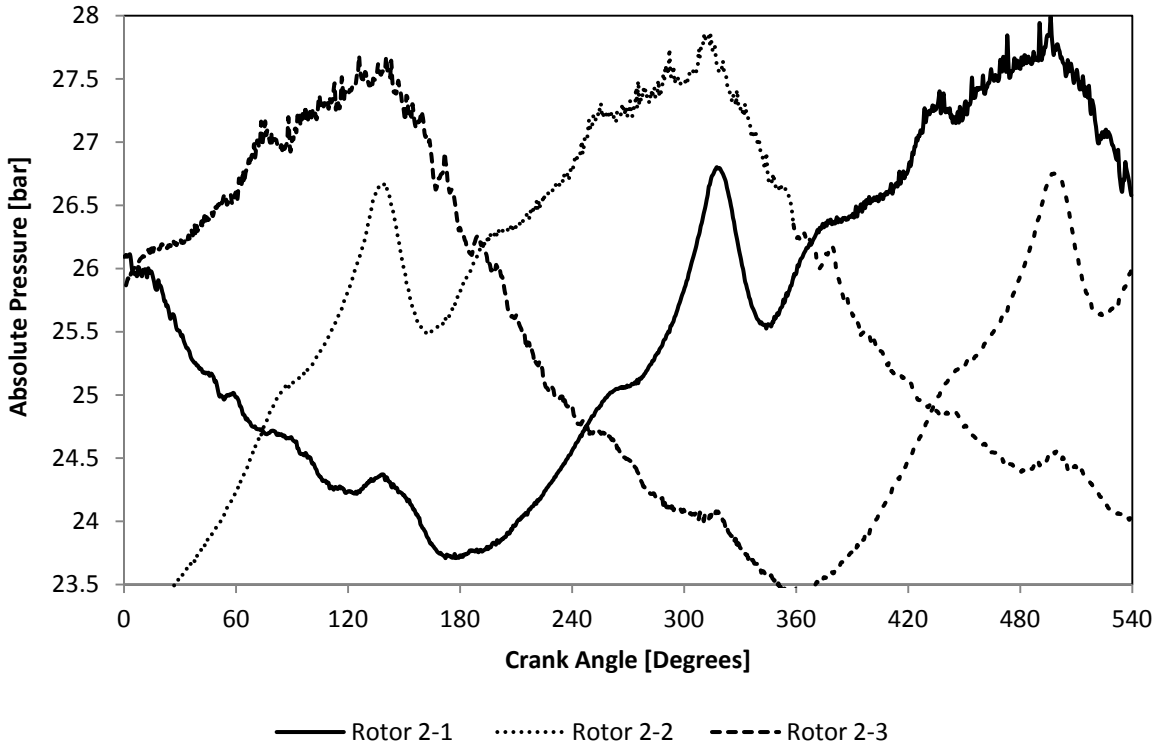

Figure 7.36: Pressure variation inside the chambers of the cold rotor of WRSM without UDF

7.3.3 Results of 2D CFD model of a 180º rotor-shift WRSM

In addition to the modelling of the engine with phase angle of 90º between rotations of rotors, a system was considered in which the rotation of rotors was shifted by 180º. This was done in order to investigate the effects of the phase angle on the power output.

Figures 7.37 and 7.38 show the pressure variation inside the working chambers of the hot and cold rotor, respectively. It can be seen in Figure 7.37 that the pressure inside the first chamber of the hot space is 22 bar at the beginning of the cycle and drops to 21.5 bar at 56º of the crank shaft angle. The pressure then rises again to 21.9 bar at 72º of the crank shaft angle and drops gradually to 21.45 bar at 190º of the crank shaft angle. This is followed by a further drop to the minimum pressure of 20.4 bar at 247º of the crank shaft angle. The pressure then rises rapidly to 22.9 bar at 407º of the crank shaft angle, followed by a drop to 22.1 bar at

418.5º of the crank shaft angle and then reaches its maximum value of 22.3 bar at 490º of the crank shaft angle. The pressure then is reduced to its initial value by the end of the cycle. The pressure inside the adjacent chambers shows a similar variation with a phase shift of approximately 180º of the crank shaft angle. It is clear from Figure 7.37 that the pressure variation in the hot space of the engine with 180º shift angle has an amplitude of approximately 2 bar which is 50% lower than the pressure variation in the chambers of the engine with 90º shift angle.

From Figure 7.38, the pressure inside the first chamber of the cold space is 21.1 bar at the beginning of the cycle and drops to its minimum value of 19.5 bar at 82º of the crank shaft angle. The pressure then rises rapidly and almost linearly to the maximum value of 22.4 bar at 231º of the crank shaft angle followed by a sudden drop to 22 bar at 254º of the crank shaft angle. The pressure then rises again to 22.3 bar at 281º of the crank shaft angle from which point it drops to its initial value at the end of the cycle. The pressures in the adjacent chambers follow a similar pattern with a phase difference of approximately 120º. It can be seen in Figure 7.33 that the pressure variation inside the chambers of the cold rotor has an amplitude of 3 bar or 50% higher than in the hot space. This suggests that there is a significantly higher pressure drop inside the gas circuit with flow disturbance caused by interaction between ports in the casings and rotor tips.

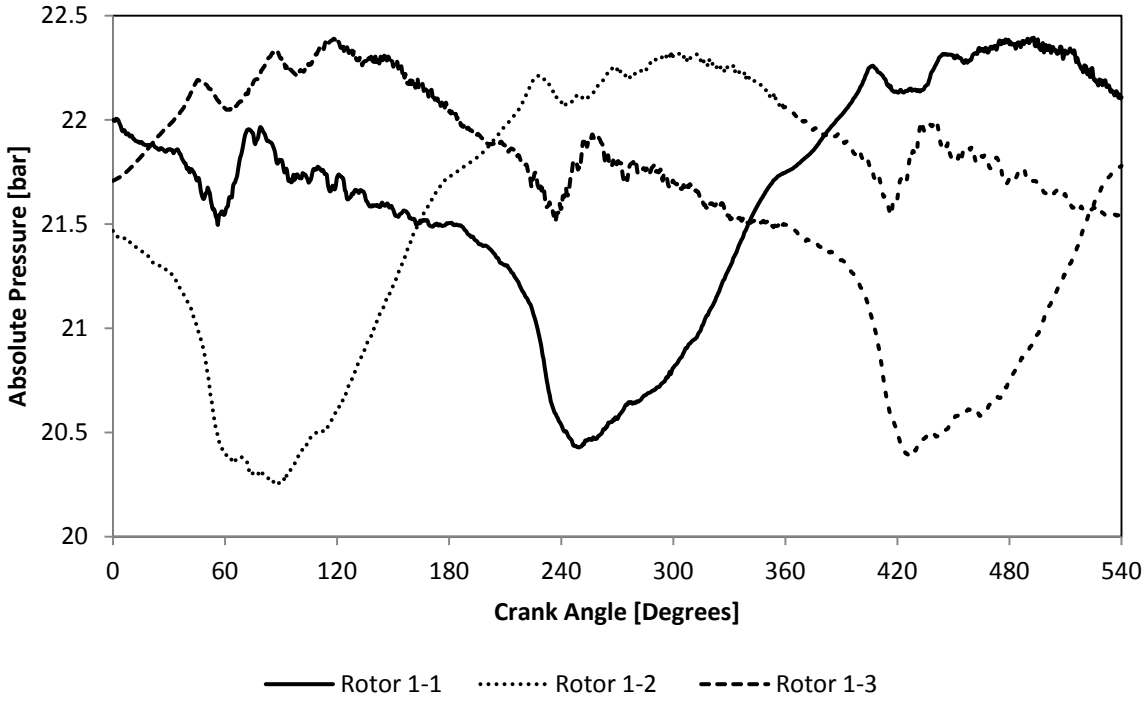

Figure 7.37: Pressure variation in the chambers of the hot space of the engine with phase angle of 180º

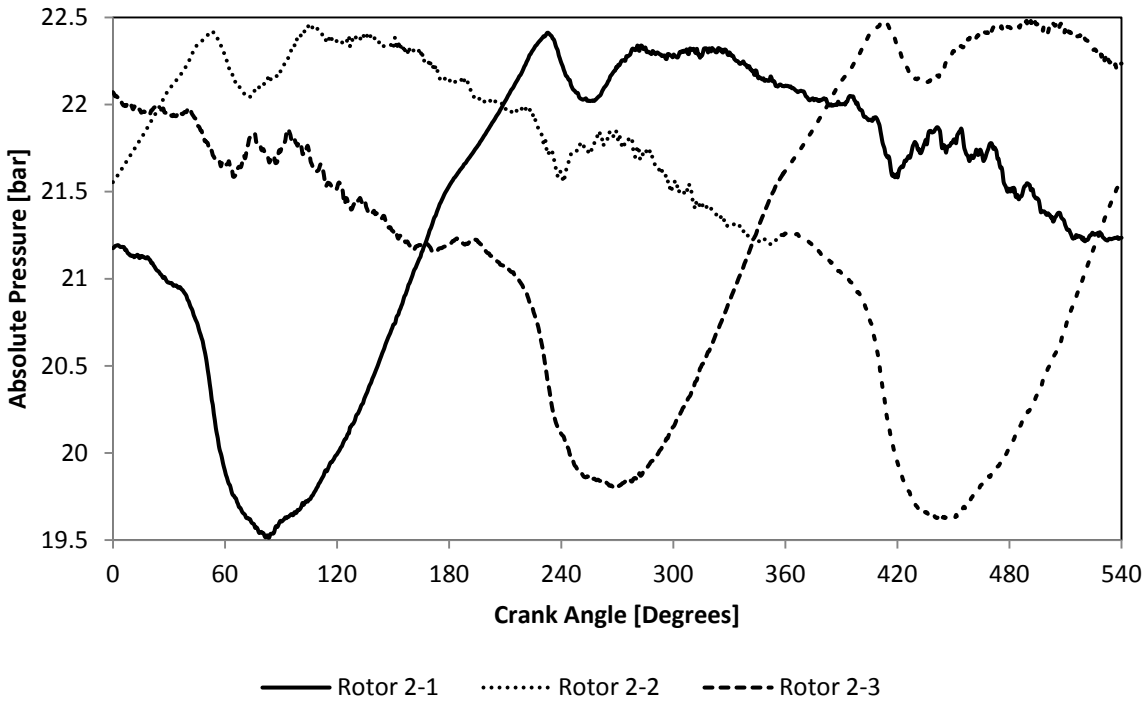

Figure 7.38: Pressure variation in the chambers of the cold space of the engine with phase angle of 180º

The lower pressures developed in this engine configuration were expected to lead to low power. This is confirmed by the pressure-volume indicated diagrams presented in Figure 7.39 for the hot and cold chambers 1-1 and 2-1, respectively. The net indicated cyclic work calculated from Figure 7.39 was -6.5 J. This suggests that the 180º degree shift angle also leads to the system operating as a heat pump/cooling machine. This is again due to the fact that the variation of the volumes inside the hot spaces is lagging that of the cold spaces by 180º degrees. This is shown in Figure 7.40 for the hot chamber 1-1 and the cold chamber 2-1.

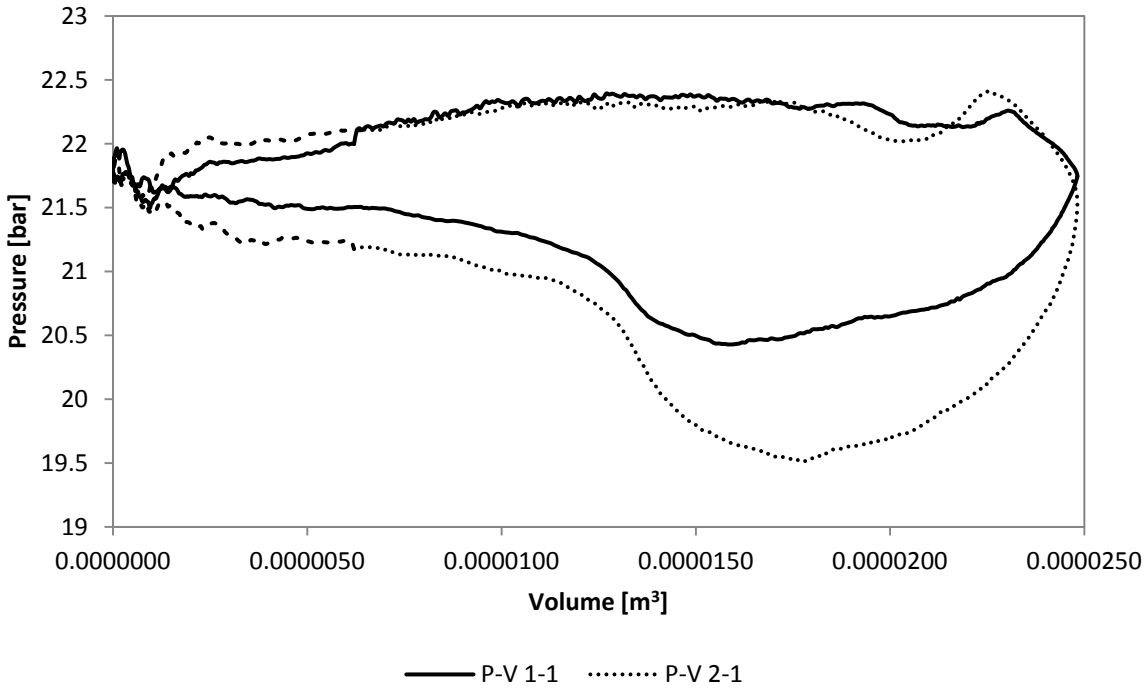

Figure 7.39: P-V indicated diagrams for the hot chamber 1-1 and the cold chamber 2-1

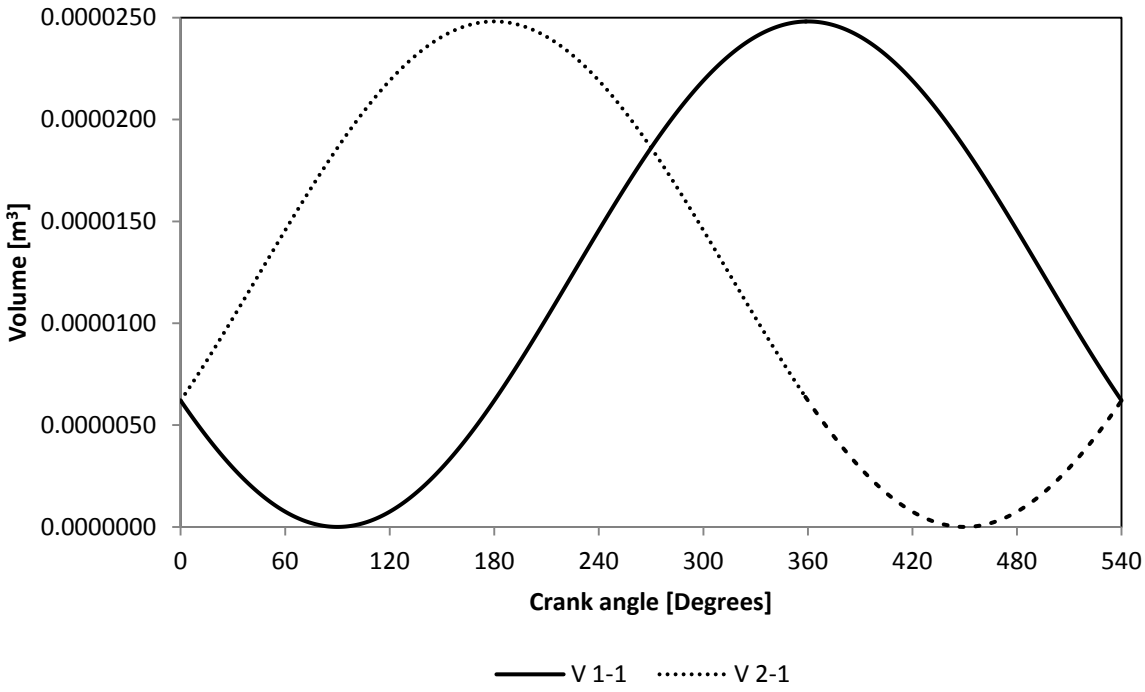

Figure 7.40: Volume variation inside the hot chamber 1-1 and the cold chamber 2-1

Figure 7.41 shows the pressure-volume indicated diagram for the hot chamber 1-2 and the corresponding cold chamber 2-2. It can be seen from Figure 7.40 that the pressure-volume areas of the two working spaces are similar to those shown in Figure 7.39. From Figure 7.40 the net cyclic work was calculated at -6.5 J. The negative sign also indicates that the engine is operating as a heat pump/cooling machine. This is believed to be due to the fact that the volume variation inside the cold chamber 2-2 leads that of the hot chamber by 180º, as shown in Figure 7.42. This occurs despite the fact that the hot rotor was advanced by 180º degrees. It can also be seen from Figures 4.39 and 7.41that the net cyclic work , albeit negative, is lower compared to the net cyclic work calculated for the 90º -shifted engine from Figures 7.29, 7.31 and 7.33. This further stresses the significance of the phase angle shift between the hot and the cold rotor.

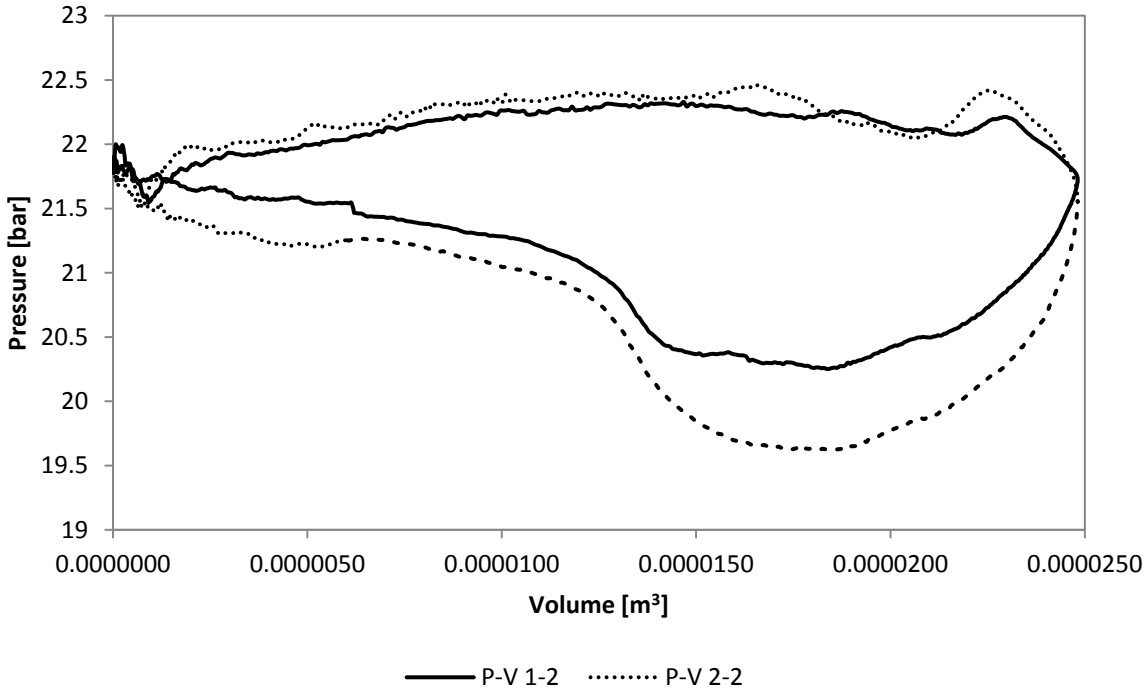

Figure 7.41: P-V indicated diagram for the hot chamber 1-2 and the cold chamber 2-2

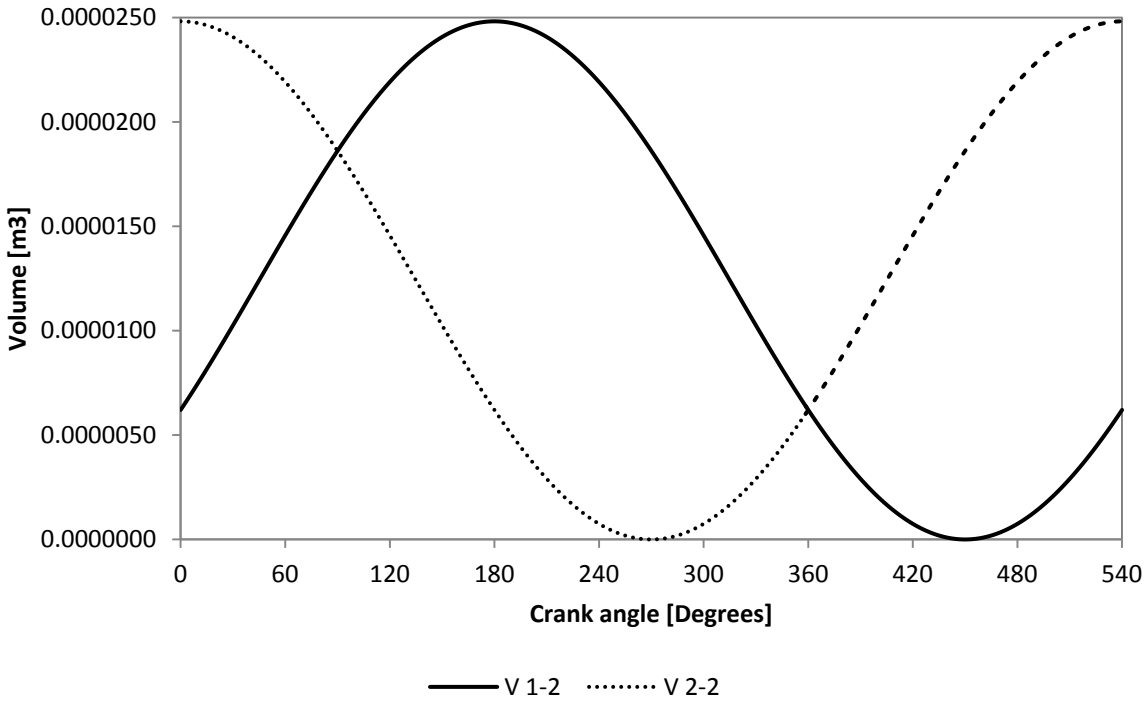

Figure 7.42: Volume variation inside the hot chamber 1-2 and the cold chamber 2-2

Finally, Figures 7.43 and 7.44 show the pressure volume indicated diagrams and the volume variation respectively, for the hot chamber 1-3 and the cold chamber 2-3. According to Figure 7.43, the net indicated cyclic work was calculated at -6.5 J. The pressure-volume areas shown in Figure 7.43 have a similar shape to those shown previously in Figures 7.39 and 7.41. The negative net cyclic work indicates that the engine is operating as a heat pump/cooling machine. The negative sign is attributed to the volume variation inside the cold chamber 2-3 leading that of the hot chamber 1-3 by 180º degrees of the crank shaft angle. This is shown in Figure 7.44.

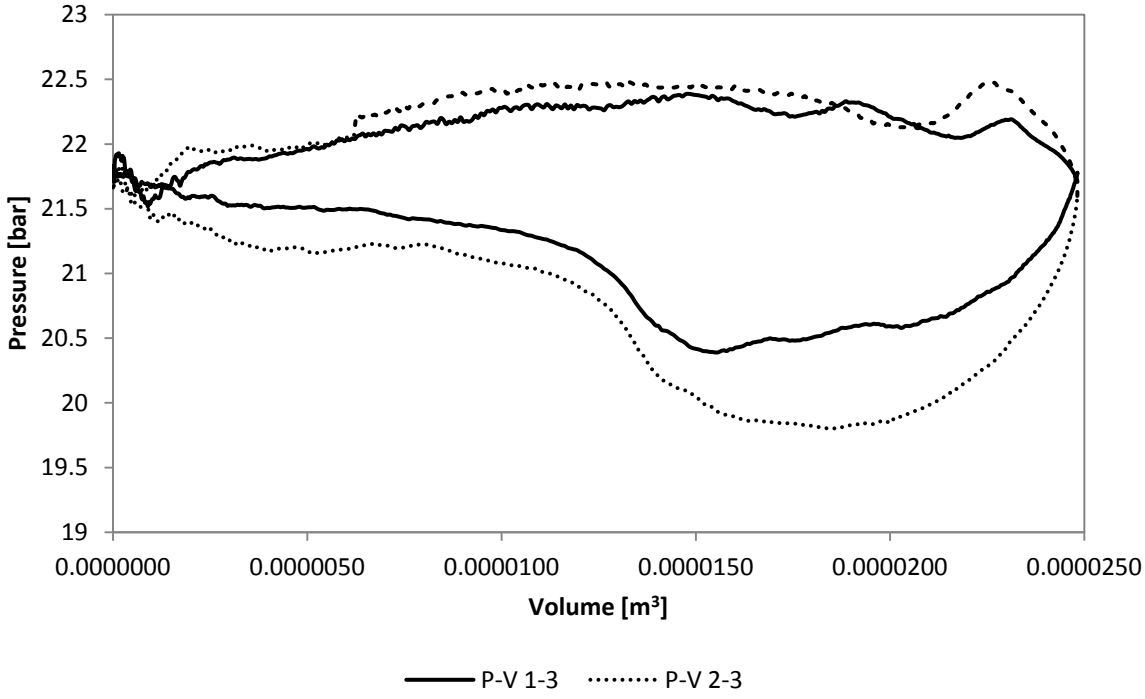

Figure 7.43: P-V indicated diagram for the hot chamber 1-3 and the cold chamber 2-3

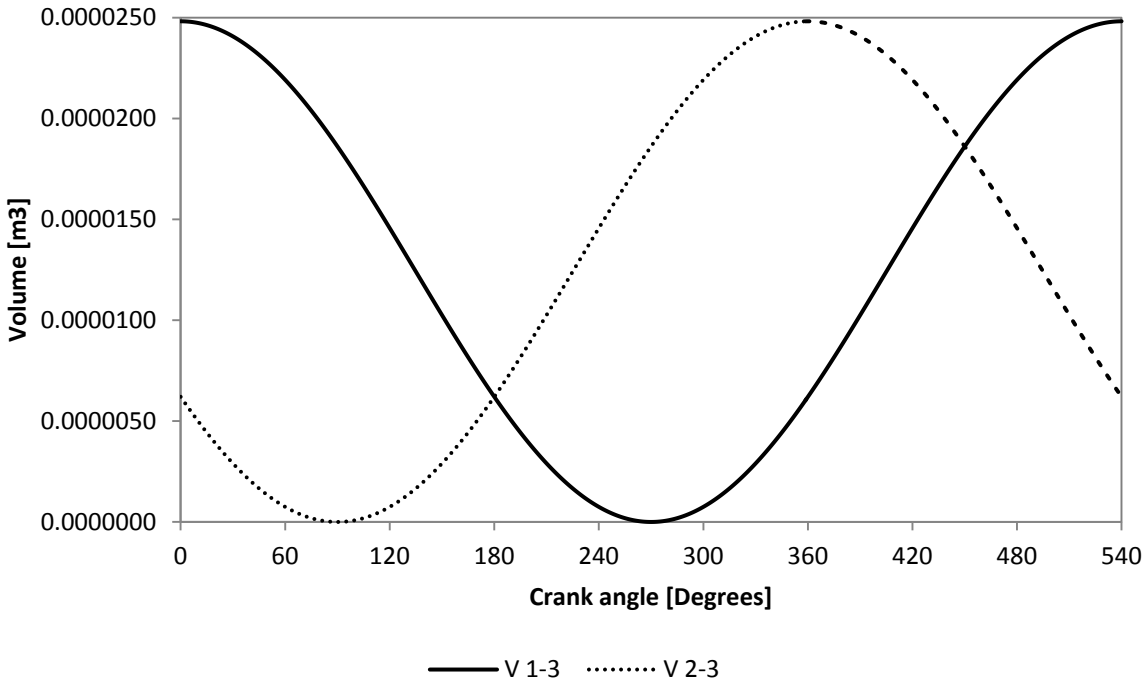

Figure 7.44: Volume variation inside the hot chamber 1-3 and the cold chamber 2-3

As shown from Figures 7.29-7.34 and 7.39-7.44, advancing the hot rotor by 90º or 180º led to the opposite result regarding the phase shift between the volume variations of the hot and the cold chambers as the hot spaces lagged the volume variations of the cold spaces. Furthermore, it was found that the net cyclic work necessary to drive the system with the 180º shift is less than that of the system with the 90º shift. These results indicate that the deploying the rule of advancing the hot piston in conventional Stirling engines does not result in the production of power output in the WRSMs under consideration.

7.4 Synopsis

A 2D CFD model of a WRSM was built with a rotor tip-clearance of 0.5 mm. In addition, a UDF was incorporated into ANSYS FLUENT to imitate the effect of the rotors' apex spring-seals. Two configurations were tested, one in which the hot rotor was advanced by 90º degrees of the rotor angle and another in which the hot rotor was advanced by 180º of the rotor angle compared to the cold rotor. The indicated work was calculated for the first time in this work for the Rotary system by means of using indicated pressure – volume diagrams. Preliminary results show that the 90º shift led to the configuration to operate as a heat pump/cooling machine with the indicated work of about -12 J per equivalent gas circuit. This was due to the 90º shift of the hot rotor which resulted in the volume variations of the hot chamber lagging that of the cold chambers. The same phenomenon was observed in the system with the 180º shift (the indicated work of about -6.5 J per equivalent gas circuit) leading to the conclusion that the established practice of setting the phase advancement of the hot space for conventional Stirling engines is not applicable for the WRSMs under investigation. Thus, the effect of the rotor phase angle must be carefully investigated further in order to establish a correct phase angle between the volume variation of the hot and cold working chambers in order to obtain the useful power output from the system. The insignificant effect of the sub-routine was attributed to the low values of its relative velocity coefficients, which were specified as such in order to avoid numerical implications.

Chapter 8 Conclusions and Recommendations for Future Work

In this section the main findings of this research study are summarized along with recommendations for further work.

8.1 Conclusions

The conclusions from the application of mathematical modelling for the original Stirling engine and CFD modelling of the original Stirling engine and the rotary Stirling machine are presented in the following sections.

8.1.1 Conclusions from the application of second-order mathematical modelling on the original solar Stirling engine

The original α-type solar Stirling engine was thermodynamically modelled by means of an advanced second-order thermodynamic model and its optimal rational geometric dimensions were defined by means of a GA optimization tool coupled to the mathematical model. The obtained results are summarized below:

1. The analysis of the working process of the engine by means of the second-order provided information on the volume, pressure, temperature, mass, Reynolds number and heat transfer coefficient variations throughout the cycle.

2. The results indicated a high pressure drop inside the regenerator due to the high hydraulic resistance of the porous matrix. However, the dominant pressure drop during the cycle occurred along the heater due to its small flow cross-sectional area.
3. The predicted indicated power output was in close agreement with experimental data, described in open literature. However, the estimated indicated power was lower than the power estimated by the SOPRANOS code in [18].This is believed to be due to the differences in the heat transfer and friction coefficients used in these two codes.
4. The predicted indicated power was higher than the power predicted by the 2D axi-symmetric CFD modelling of this engine described in [46]. This is believed to be due to the heat transfer and friction coefficients used in the thermodynamic model and the difference in the calculation of the phasing between pressure and volume in each of the two working chambers.
5. A set of optimal geometric dimensions for the maximization of the power output were obtained by means of the GA code coupled to the mathematical model. These values were within practical manufacturing constraints and were verified by the parametric analysis.

8.1.2 Conclusions from the solution of the 3D total CFD model (originally developed by Prof. Mahkamov) of the original solar Stirling engine

The global 3D CFD model of the original engine which incorporates the solid walls of the engine was applied to the engine. The obtained results can be summarized as follows:

1. The 3D total CFD model provided information on the flow patterns inside the engine and the volume, pressure, velocity, temperature and heat transfer coefficient variations

throughout the engine's cycle for every component of the engine at a number of monitoring points set in the longitudinal and radial directions.

2. The global 3D CFD model revealed that the flow follows an uneven pattern throughout the engine, mainly across the heater. This was indicated by the distribution of the gas velocity inside the heater which demonstrated different magnitudes at different axial and radial locations of the heater throughout the cycle.
3. The uneven velocity distribution had an effect on the phasing in the temperature variation at different radial locations of the heater. The temperature levels, however, varied across the axial rather than the radial direction.
4. The highest pressure drop was found to occur inside the cooler. This was possibly due to the two flanges at the boundaries of the cooler which strongly affected the flow. The dominating pressure drop however was that which occurred across the heater annulus because of the small cross-sectional area.
5. The total pressure drop was estimated to reduce the indicated power output by 12%-13%.
6. The predicted power output was within acceptable accuracy. In detail, the estimated power output was lower than the power estimated by the second-order mathematical model primarily due to the different phase angle between the volumes and pressures in each cylinder and secondly due to the correlations of the heat transfer and friction coefficients used in the 2^{nd} order thermodynamic model.
7. The predicted indicated power was 16% higher than the power predicted by the 2D axi-symmetric model in [46]. This is believed to be due to taking into account the three-dimensional flow patterns which were not adequately captured by the 2D axi-symmetric model and the more detailed simulation of the cooler, effectively providing an increase in the heat transfer area from the cooler.

8.1.3 Conclusions from the development of the CFD models of the novel Wankel-type rotary Stirling machine

A 2D CFD model of the gas circuit of the novel rotary solar Stirling system was developed. The preliminary results of the model are highlighted below:

1. A 2D CFD model was developed which allowed for a manageable computational grid size with a reduced rotor tip-clearance. The developed 2D CFD model provided results of the pressure, temperature and velocity variations throughout the engine cycle.
2. A user-defined function was developed and incorporated into the 2D CFD model to simulate the effect of the actual rotor tip seals used in Wankel engines.
3. It was found that there was a reciprocating flow in the internal gas circuit of the machine similar to that in a conventional Stirling engine.
4. Preliminary results indicated that both systems operate as a heat pump/cooling machine.
5. The phase advancement of the hot rotor resulted in the volume variation of the hot spaces lagging the volume variation of the cold spaces.
6. The conventional practice used for phasing of pistons in conventional Stirling engine is not applicable to the rotary systems.
7. Phasing between the rotors is crucial in order to establish a functional phase angle between the volume variation of the hot and the cold spaces.
8. The velocity coefficients in the UDF had to be under-relaxed to avoid numerical complications and therefore did not have any effect on the gas leakage in the tip clearances.

8.2 Recommendations for Future work

This final section briefly discusses some areas for further research:

1. There is need for more accurate heat transfer and flow friction correlations to be used in the second-order mathematical model developed in [2].
2. The optimal geometric dimensions of the α-type solar Stirling engine obtained from the application of the GA code developed in [2] requires further validation by means of 3D CFD modelling of the engine
3. A thermodynamic mathematical model of the Wankel-type rotary Stirling machine needs to be developed. Such a model may facilitate rapid parametric analyses in order to understand the effect of the principle geometric dimensions such as the location and diameter of ports, the phase shift between the two rotors and the dimensions of the heat exchangers which will affect the engine performance.
4. The effect of the phase angle between the hot and cold rotor of the Wankel-type rotary Stirling engine must be further investigated in order to design a system operating as a prime mover.
5. Upon investigation of the effect of the rotor phase angle, the CFD model of the Wankel-type rotary Stirling system should be upgraded to a 3D set-up with a low rotor-housing tip clearance and a conservative time step. This will enable the designer to capture the three-dimensional effects of the heat transfer, turbulence, temperature, pressure, and velocity distribution and provide more detailed and reliable information about the engine's working process.

Bibliography

[1] E. b. M. K.-B. B.-I. Burdon, Micro Energy Systems Review of Technology, Issues of Scale and Integration: John Wiley & Sons, 2004.

[2] K. Kraitong, "Numerical modelling and design optimization of Stirling engines for power production," PhD, School of Computing, Engineering and Information Sciences, Northumbria University at Newcastle, Newcastle Upon Tyne, 2012.

[3] G. Walker, Stirling Engines. Oxford: Clarendon Press, 1980.

[4] J. I. Prieto and A. B. Stefanovskiy, "Dimensional analysis of leakage and mechanical power losses of kinematic Stirling engines," Proceedings of the Institution of Mechanical Engineers, Part C: Journal of Mechanical Engineering Science, vol. 217, pp. 917-934, August 1, 2003 2003.

[5] B. Kongtragool and S. Wongwises, "Investigation on power output of the gamma-configuration low temperature differential Stirling engines," Renewable Energy, vol. 30, pp. 465-476, 3// 2005.

[6] W. R. Martini, Stirling Engine Design Manual: The Office, 1983.

[7] N. C. J. Chen and F. P. Griffin, "A review of Stirling engine mathematical models," Oak Ridge National Laboratory1983.

[8] L. B. Erbay and H. Yavuz, "Analysis of the stirling heat engine at maximum power conditions," Energy, vol. 22, pp. 645-650, 7// 1997.

[9] M. Costea, S. Petrescu, and C. Harman, "The effect of irreversibilities on solar Stirling engine cycle performance," Energy Conversion and Management, vol. 40, pp. 1723-1731, 10// 1999.

[10] S. T. Hsu, F. Y. Lin, and J. S. Chiou, "Heat-transfer aspects of Stirling power generation using incinerator waste energy," Renewable Energy, vol. 28, pp. 59-69, 1// 2003.

[11] B. Kongtragool and S. Wongwises, "Thermodynamic analysis of a Stirling engine including dead volumes of hot space, cold space and regenerator," Renewable Energy, vol. 31, pp. 345-359, 3// 2006.

[12] N. Martaj, L. Grosu, and P. Rochelle, "Thermodynamic study of a Low Temperature Difference Stirling engine at steady state operation," International Journal of Thermodynamics, vol. 10, pp. 165-176, 2007.

[13] P. Puech and V. Tishkova, "Thermodynamic analysis of a Stirling engine including regenerator dead volume," Renewable Energy, vol. 36, pp. 872-878, 2// 2011.

[14] D. M. B. Israel Urieli, Stirling cycle engine analysis: Adam Hilger, 1983.

[15] S. Schulz and F. Schwendig, "A general simulation model for Stirling cycles," ASME Journal of Engineering for Gas Turbines and power vol. 118, pp. 1-7, 1996.

[16] J. I. Prieto, M. A. González, C. González, and J. Fano, "A new equation representing the performance of kinematic Stirling engines," Proceedings of the Institution of Mechanical Engineers, Part C: Journal of Mechanical Engineering Science, vol. 214, pp. 449-464, March 1, 2000.

[17] J. I. Prieto, J. Fano, C. González, M. A. González, and R. Diaz, "Preliminary design of the kinematic Stirling engine using dynamic similarity and quasi-static simulation," Proceedings of the Institution of Mechanical Engineers, Part C: Journal of Mechanical Engineering Science, vol. 211, pp. 229-238, March 1, 1997.

[18] K. K. Mahkamov and D. B. Ingham, "Analysis of the working process and mechanical losses in a Stirling engine for a solar power unit," ASME Journal of Solar Energy Engineering, vol. 121, pp. 121-127, 1999.

[19] Ö. Ercan Ataer and H. Karabulut, "Thermodynamic analysis of the V-type Stirling-cycle refrigerator," International Journal of Refrigeration, vol. 28, pp. 183-189, 3// 2005.

[20] S. K. Andersen, H. Carlsen, and P. G. Thomsen, "Preliminary results from simulations of temperature oscillations in Stirling engine regenerator matrices," Energy, vol. 31, pp. 1371-1383, 8// 2006.

[21] S. K. Andersen, H. Carlsen, and P. G. Thomsen, "Numerical study on optimal Stirling engine regenerator matrix designs taking into account the effects of matrix temperature oscillations," Energy Conversion and Management, vol. 47, pp. 894-908, 5// 2006.

[22] H. Karabulut, H. S. Yücesu, and C. Çinar, "Nodal analysis of a Stirling engine with concentric piston and displacer," Renewable Energy, vol. 31, pp. 2188-2197, 10// 2006.

[23] I. Tlili, Y. Timoumi, and S. B. Nasrallah, "Analysis and design consideration of mean temperature differential Stirling engine for solar application," Renewable Energy, vol. 33, pp. 1911-1921, 8// 2008.

[24] Y. Timoumi, I. Tlili, and S. Ben Nasrallah, "Design and performance optimization of GPU-3 Stirling engines," Energy, vol. 33, pp. 1100-1114, 7// 2008.

[25] M. Abbas, N. Said, and B. B., "Thermal analysis of Stirling engine solar driven," Revue des Energies Renouvelables, vol. 11, pp. 503-514, 2008.

[26] F. J. Garcia Granados, M. A. Silva Perez, and V. Ruiz-Hernandez, "Thermal model of the EuroDish solar Stirling engine," ASME Journal of Solar Energy Engineering, vol. 130, pp. 011014-8, 2008.

[27] F. Nepveu, A. Ferriere, and F. Bataille, "Thermal model of a dish/Stirling systems," Solar Energy, vol. 83, pp. 81-89, 1// 2009.

[28] R. Gheith, F. Aloui, and S. B. Nasrallah, "Experimental study of a beta Stirling thermal machine type functioning in receiver and engine modes," Applied Fluid Mechanincs, vol. 4, pp. 33-42, 2011.

[29] N. Parlak, A. Wagner, M. Elsner, and H. S. Soyhan, "Thermodynamic analysis of a gamma type Stirling engine in non-ideal adiabatic conditions," Renewable Energy, vol. 34, pp. 266-273, 1// 2009.

[30] C. M. Invernizzi, "Stirling engines using working fluids with strong real gas effects," Applied Thermal Engineering, vol. 30, pp. 1703-1710, 9// 2010.

[31] Y. Tekin and O. E. Ataer, "Performance of V-type Stirling-cycle refrigerator for different working fluids," International Journal of Refrigeration, vol. 33, pp. 12-18, 1// 2010.

[32] J. M. Strausss and R. T. Dobson, "Evaluation of a second order simulation for Sterling engine design and optimization," Energy in South Africa, vol. 21, pp. 17-29, 2010.

[33] C.-H. Cheng and Y.-J. Yu, "Dynamic simulation of a beta-type Stirling engine with cam-drive mechanism via the combination of the thermodynamic and dynamic models," Renewable Energy, vol. 36, pp. 714-725, 2// 2011.

[34] H. Karabulut, "Dynamic analysis of a free piston Stirling engine working with closed and open thermodynamic cycles," Renewable Energy, vol. 36, pp. 1704-1709, 6// 2011.

[35] W. Arias, H. I. Velasquez, D. Florez, and S. Oliveira Junior, "Thermodynamic analysis, performance numerical simulation and losses analysis of a low cost Stirling engine V-Type, and its impact on social development in remote areas," in ECOS, Novi Sad, Serbia, 2011, pp. 3767-3778.

[36] C.-H. Cheng and H.-S. Yang, "Analytical model for predicting the effect of operating speed on shaft power output of Stirling engines," Energy, vol. 36, pp. 5899-5908, 10// 2011.

[37] B. Kongtragool and S. Wongwises, "Performance of a twin power piston low temperature differential Stirling engine powered by a solar simulator," Solar Energy, vol. 81, pp. 884-895, 7// 2007.

[38] R. W. Dyson, S. D. Wilson, R. C. Tew, and R. Demko, "On the Need for Multidimensional Stirling Simulations," 2005.

[39] S. Zhu and Y. Matsubara, "A numerical method of regenerator," Cryogenics, vol. 44, pp. 131-140, 2// 2004.

[40] S. Choi, K. Nam, and S. Jeong, "Investigation on the pressure drop characteristics of cryocooler regenerators under oscillating flow and pulsating pressure conditions," Cryogenics, vol. 44, pp. 203-210, 3// 2004.

[41] S. Abdullah, B. F. Yousif, and K. Sopian, "Design consideration of low temperature differential double-acting Stirling engine for solar application," Renewable Energy, vol. 30, pp. 1923-1941, 10// 2005.

[42] S. K. Andersen, H. Carlsen, and P. G. Thomsen, "Control volume based modelling in one space dimension of oscillating, compressible flow in reciprocating machines," Simulation Modelling Practice and Theory, vol. 14, pp. 1073-1086, 11// 2006.

[43] N. G. R. Center and M. B. Ibrahim, CFD modeling of free-piston Stirling engines. [Cleveland, Ohio] : Hanover, MD: National Aeronautics and Space Administration, Glenn Research Center ; Available from NASA Center for Aerospace Information, 2001.

[44] S. D. Wilson, R. W. Dyson, R. C. Tew, and M. B. Ibrahim, "Multi-D CFD modeling of a free-piston Stirling convertor at NASA Glenn," 2004.

[45] R. W. Dyson, S. D. Wilson, R. C. Tew, and R. Demko, Fast Whole-Engine Stirling Analysis, 2005.

[46] K. Mahkamov, "An Axi-symmetric Computational Fluid Dynamics approach to the analysis of the working process of a solar Stirling engine," ASME Journal of Solar Energy Engineering, vol. 128, p. 45, 2006.

[47] K. Mahkamov, "Design improvements to a biomass Stirling engine using mathematical analysis and 3D CFD modelling," Journal of Energy Resources Technology : Transactions of the ASME., vol. 128, pp. 203-215, 2006.

[48] K. Mahkamov and E. I. Eid, "Technical feasibility study of a concept of a medium temperature Stirling engine solar power unit," presented at the ISEC International Stirling Engine Conference, Groningen, Netherlands, 2009.

[49] L. Chen, Y. Zhang, E. Luo, T. Li, and X. Wei, "CFD analysis of thermodynamic cycles in a pulse tube refrigerator," Cryogenics, vol. 50, pp. 743-749, 11// 2010.

[50] T. R. Ashwin, G. S. V. L. Narasimham, and S. Jacob, "CFD analysis of high frequency miniature pulse tube refrigerators for space applications with thermal non-equilibrium model," Applied Thermal Engineering, vol. 30, pp. 152-166, 2// 2010.

[51] D. A. Blank and C. Wu, "Power optimization of an extra-terrestrial, solar-radiant stirling heat engine," Energy, vol. 20, pp. 523-530, 6// 1995.

[52] M. Costea and M. Feidt, "The effect of the overall heat transfer coefficient variation on the optimal distribution of the heat transfer surface conductance or area in a Stirling engine," Energy Conversion and Management, vol. 39, pp. 1753-1761, 11// 1998.

[53] F. Wu, L. Chen, F. Sun, C. Wu, and Y. Zhu, "Performance and optimization criteria for forward and reverse quantum Stirling cycles," Energy Conversion and Management, vol. 39, pp. 733-739, 6/10/ 1998.

[54] F. Wu, L. Chen, C. Wu, and F. Sun, "Optimum performance of irreversible Stirling engine with imperfect regeneration," Energy Conversion and Management, vol. 39, pp. 727-732, 6/10/ 1998.

[55] S. C. Kaushik and S. Kumar, "Finite time thermodynamic evaluation of irreversible Ericsson and Stirling heat engines," Energy Conversion and Management, vol. 42, pp. 295-312, 2// 2001.

[56] J. R. Senft, "Optimum Stirling engine geometry," International Journal of Energy Research, vol. 26, pp. 1087-1101, 2002.

[57] F. Michel, K. L. Saos, M. Costea, and S. Petrescu, "Optimal allocation of heat exchanger inventory associated with fixed power output or fixed heat transfer rate input," International Journal of Thermodynamics, vol. 5, pp. 25-36, 2002.

[58] E. D. Rogdakis, N. A. Bormpilas, and I. K. Koniakos, "A thermodynamic study for the optimization of stable operation of free piston Stirling engines," Energy Conversion and Management, vol. 45, pp. 575-593, 3// 2004.

[59] N. Martaj and L. Grosu, "Exergetical analysis and design optimization of the Stirling engine," International Journal of Exergy, vol. 3, pp. 45-67, 2006.

[60] Y. C. Hsieh, T. C. Hsu, and J. S. Chiou, "Integration of a free-piston Stirling engine and a moving grate incinerator," Renewable Energy, vol. 33, pp. 48-54, 1// 2008.

[61] Y. Timoumi, I. Tlili, and S. Ben Nasrallah, "Performance optimization of Stirling engines," Renewable Energy, vol. 33, pp. 2134-2144, 9// 2008.

[62] P. C. T. de Boer, "Optimal regenerator performance in Stirling engines," International Journal of Energy Research, vol. 33, pp. 813-832, 2009.

[63] Zarinchang and A. J. Yarmahmoudi, "Optimization of thermal components in a Stirling engine," WSEAS TRANSACTIONS on HEAT and MASS TRANSFER, vol. 4, pp. 1-10, 2009.

[64] F. Formosa and G. Despesse, "Analytical model for Stirling cycle machine design," Energy Conversion and Management, vol. 51, pp. 1855-1863, 10// 2010.

[65] L. Yaqi, H. Yaling, and W. Weiwei, "Optimization of solar-powered Stirling heat engine with finite-time thermodynamics," Renewable Energy, vol. 36, pp. 421-427, 1// 2011.

[66] A. Homaifar, H. Y. Lai, and E. McCormick, "System optimization of turbofan engines using Genetic Algorithms," Applied Mathematical Modelling, vol. 18, pp. 72-83, 1994.

[67] M. C. Tayal, Y. Fu, and U. M. Diwekar, "Optimal design of heat exchangers: a Genetic Algorithm framework," Industrial & Engineering Chemistry Research, vol. 38, pp. 456-467, 1994.

[68] A. Toffolo and A. Lazzaretto, "Evolutionary algorithms for multi-objective energetic and economic optimization in thermal system design," Energy, vol. 27, pp. 549-567, 6// 2002.

[69] B. Mirzaeian, M. Moallem, V. Tahani, and C. Lucas, "Multiobjective optimization method based on a Genetic Algorithm for switched reluctance motor design," Magnetics, IEEE Transactions on, vol. 38, pp. 1524-1527, 2002.

[70] U. Kesgin, "Genetic Algorithm and artificial neural network for engine optimisation of efficiency and NOx emission," Fuel, vol. 83, pp. 885-895, 5// 2004.

[71] E. G. Shopova and N. G. Vaklieva-Bancheva, "BASIC—A Genetic Algorithm for engineering problems solution," Computers & Chemical Engineering, vol. 30, pp. 1293-1309, 6/15/ 2006.

[72] M. Cunkas, "Design optimization of electric motors by multiobfective fuzzy Genetic Algorithms," Mathematical and Computational Applications, vol. 13, pp. 153-163, 2008.

[73] M. Mohagheghi and J. Shayegan, "Thermodynamic optimization of design variables and heat exchangers layout in HRSGs for CCGT, using Genetic Algorithm," Applied Thermal Engineering, vol. 29, pp. 290-299, 2// 2009.

[74] J. M. Ponce-Ortega, M. Serna-González, and A. Jiménez-Gutiérrez, "Use of Genetic Algorithms for the optimal design of shell-and-tube heat exchangers," Applied Thermal Engineering, vol. 29, pp. 203-209, 2// 2009.

[75] L. Gosselin, M. Tye-Gingras, and F. Mathieu-Potvin, "Review of utilization of Genetic Algorithms in heat transfer problems," International Journal of Heat and Mass Transfer, vol. 52, pp. 2169-2188, 4// 2009.

[76] İ. Batmaz and S. Üstün, "Design and manufacturing of a V-type Stirling engine with double heaters," Applied Energy, vol. 85, pp. 1041-1049, 11// 2008.

[77] S. Le'an, Z. Yuanyang, L. Liansheng, and S. Pengcheng, "Performance of a prototype Stirling domestic refrigerator," Applied Thermal Engineering, vol. 29, pp. 210-215, 2// 2009.

[78] I. M. Yusof, N. A. Farid, Z. A. Zainal, G. B. Horizon, K. Noriman, and A. Miskam, "Design, Fabrication and testing of a swirl burner foraAlpha V-shaped Stirling engine," Asian Journal of Applied Sciences, vol. 2, pp. 475-485, 2009.

[79] A. A. El-Ehwany, G. M. Hennes, E. I. Eid, and E. A. El-Kenany, "Development of the performance of an alpha-type heat engine by using elbow-bend transposed-fluids heat exchanger as a heater and a cooler," Energy Conversion and Management, vol. 52, pp. 1010-1019, 2// 2011.

[80] C. Cinar, S. Yucesu, T. Topgul, and M. Okur, "Beta-type Stirling engine operating at atmospheric pressure," Applied Energy, vol. 81, pp. 351-357, 8// 2005.

[81] H. Karabulut, F. Aksoy, and E. Öztürk, "Thermodynamic analysis of a β type Stirling engine with a displacer driving mechanism by means of a lever," Renewable Energy, vol. 34, pp. 202-208, 1// 2009.

[82] H. Karabulut, H. S. Yücesu, C. Çınar, and F. Aksoy, "An experimental study on the development of a β-type Stirling engine for low and moderate temperature heat sources," Applied Energy, vol. 86, pp. 68-73, 1// 2009.

[83] H. Karabulut, C. Çınar, E. Oztürk, and H. S. Yücesu, "Torque and power characteristics of a helium charged Stirling engine with a lever controlled displacer driving mechanism," Renewable Energy, vol. 35, pp. 138-143, 1// 2010.

[84] A. Sripakagorn and C. Srikam, "Design and performance of a moderate temperature difference Stirling engine," Renewable Energy, vol. 36, pp. 1728-1733, 6// 2011.

[85] H. W. Brandhorst Jr and P. A. Chapman Jr, "New 5 kW free-piston Stirling space convertor developments," Acta Astronautica, vol. 63, pp. 342-347, 7// 2008.

[86] C. Çinar and H. Karabulut, "Manufacturing and testing of a gamma type Stirling engine," Renewable Energy, vol. 30, pp. 57-66, 1// 2005.

[87] B. Kongtragool and S. Wongwises, "Performance of low-temperature differential Stirling engines," Renewable Energy, vol. 32, pp. 547-566, 4// 2007.

[88] B. Kongtragool and S. Wongwises, "A four power-piston low-temperature differential Stirling engine using simulated solar energy as a heat source," Solar Energy, vol. 82, pp. 493-500, 6// 2008.

[89] A. R. Tavakolpour, A. Zomorodian, and A. Akbar Golneshan, "Simulation, construction and testing of a two-cylinder solar Stirling engine powered by a flat-plate solar collector without regenerator," Renewable Energy, vol. 33, pp. 77-87, 1// 2008.

[90] http://www.ohio.edu/mechanical/thermo/Intro/Chapt.1_6/StirlCogen/StirlCogen.html. (21 March).

[91] C. J. Rallis, I. Urieli, and D. M. Berchowitz, "A new ported constant volume external heat supply regenerative cycle," in Intersociety Energy Conversion Engineering Conference, 12th, Washington, D.C., 1977, pp. 1534-1537.

[92] Y. M. Kim, D. K. K. Shin, and J. H. H. Lee, "A new Ericsson cycle comprising a scroll expander and a scroll Compressor for power and refrigeration application," in International Refrigeration and Air Conditioning Conference, Purdue University, 2004, pp. 1-8.

[93] W. Sirignam, "Theoretical analysis of Wankel engine combustion," Combustion Science and Technology, vol. 7, pp. 109-123, 1973.

[94] F. V. Bracco, "Theoretical analysis of stratified, two-phase Wankel engine combustion," Combustion Science and Technology, vol. 8, pp. 69-84, 1973.

[95] T. I.-P. Shih, H. J. Schock, H. L. Nguyen, and J. D. Stegemant, "Numerical simulation of the flowfield in a motored two-dimensional Wankel engine," 1987, vol. 3, pp. 269-276, 1987.

[96] N. Kawahara, E. Tomita, K. Hayashi, M. Tabata, K. Iwai, and R. Kagawa, "Cycle-resolved measurements of the fuel concentration near a spark plug in a rotary engine using an in situ laser absorption method," Proceedings of the Combustion Institute, vol. 31, pp. 3033-3040, 1// 2007.

[97] G. R. Pennock and J. E. Beard, "Force analysis of the apex seals in the Wankel rotary compressor including the influence of fluctuations in the crankshaft speed," Mechanism and Machine Theory, vol. 32, pp. 349-361, 4// 1997.

[98] O. Levi and N. Eliaz, "Failure analysis and condition monitoring of an open-loop oil system using ferrography," Tribology Letters, vol. 36, pp. 17-29, 2009/10/01 2009.

[99] Y. Zhang and W. Wang, "Effects of leakage and friction on the miniaturization of a Wankel compressor," Frontiers in Energy, vol. 5, pp. 83-92, 2011/03/01 2011.

[100] O. Badr, S. Naik, P. W. O'Callaghan, and S. D. Probert, "Wankel engines as steam expanders: Design considerations," Applied Energy, vol. 40, pp. 157-170, // 1991.

[101] R. K. Brown and R. K. Green, "An investigation of a hydrogen fuelled Wankel engine," HYDROGEN ENERGY PROGRESS, vol. 1-3, pp. 1601-1606, 1996.

[102] J. D. Heppner, D. C. Walther, and A. P. Pisano, "The design of ARCTIC: A rotary compressor thermally insulated μcooler," Sensors and Actuators A: Physical, vol. 134, pp. 47-56, 2/28/ 2007.

[103] Y.-T. Wu, C.-F. Ma, and X.-H. Zhong, "Development and experimental investigation of a miniature-scale refrigeration system," Energy Conversion and Management, vol. 51, pp. 81-88, 1// 2010.

[104] H.-L. Ma, C.-H. Kuo, and C.-C. Chen, "Chamber contour design and compression flow calculations of Rotary engine," Journal of Creative Communication and Innovative Technology, vol. 39, pp. 35-49, 2010.

[105] Y.-C. Chou, "Fabrication and simulation of Stirling cycle engine employing the rotary Wankel mechanism," Ph.D., Mechanical and Electro-Mechanical Engineering, Tamkang University, 2009.

[106] D. C. G. Veitch and K. Mahkamov, "Assessment of economical and ecological benefits from deployment of a domestic combined heat and power unit based on its experimental performance," Proceedings of the Institution of Mechanical Engineers, Part A: Journal of Power and Energy, vol. 223, pp. 783-798, November 1 2009.

[107] A. Alexakis, G. Gkounis, K. Mahkamov, and J. Davis, "Experimental and theoretical evaluation of the performance of a Whispergen Mk Vb micro CHP unit in typical UK house conditions " presented at the World Renewable Energy Congress, Linkoping, Sweden, 2011.

[108] D. P. D. F. P. Incropera, T. L. Bergamn, A. S. Lavine, Fundamentals of Heat and Mass Transfer, Sixth ed.: John Wiley & Sons, 2007.

[109] I. Y. M. Tanaka, F. Chisaka, "Flow and heat transfer characteristics of the Stirling engine regenerator in an oscillating flow," JSME international journal, Ser. 2, Fluids engineering, heat transfer, power, combustion, thermophysical properties, vol. 33, pp. 283-289, 1990.

[110] R. F. Ansdale, The Wankel RC Engine. London: Iliffe Books Limited, 1968.

[111] K. Yamamoto, Rotary Engine: Tokyo Goyo CO., Ltd, 1981.

[112] ANSYS FLUENT 12 Theory Guide: ANSYS Inc., 2012.

[113] J. Anderson, Computational Fluid Dynamics: McGraw-Hill Higher Education; International edition, 1995.

[114] S. V. Patankar, Numerical heat transfer and fluid flow: Hemisphere Pub. Corp., 1980.

[115] ANSYS FLUENT 12 User's Guide: ANSYS Inc., 2012.

[116] E. M. S. W. J. Minkowycz, J. Y. Murthy, Handbook of Numerical Heat Transfer: Wiley; 2 edition, 2006.

[117] J. M. C. Yunus A. Cengel, Fluid Mechanics: Fundamentals and Applications: McGraw-Hill Higher Education, 2006.

[118] K. Mahkamov and D. B. Ingham, "Two-dimensional model of the heat transfer and mechanical losses in a cavity-type heat receiver of a solar Stirling engine " ASME Journal of Solar Energy Engineering, vol. 121, pp. 121-127, 1999.

[119] E. J. W. R., K. K. R., and C. M. E., "Stirling cycle refrigerator or engine employing the rotary Wankel mechanism," 2000.

[120] FLUENT UDF Manual: ANSYS Inc., 2009.

Appendix A User-defined function for the motion specification of the pistons of the original Stirling engine

```
#include "udf.h"
#include "dynamesh_tools.h"

#define RADIANS(deg)  (M_PI*(deg)/180.0)
#define A 0.0165   /* crank throw */
#define L 0.1381    /* conrod length */
#define Z_LIMIT 0.001

DEFINE_CG_MOTION(piston_e, dt, cg_vel, cg_omega, time, dtime)
{
  /* get RPM and starting crank shaft angle */
  real rpm = RP_Get_Real ("dynamesh/in-cyn/crank-rpm");
  real start_angle = RP_Get_Real ("dynamesh/in-cyn/crank-start-angle");
  real z_piston, angle;

  /* compute current angle at t = time
     note: crank-rpm is in units of RPM
           crank-start-angle is in units of degree */
  angle = start_angle+time/(1/(rpm/60)/360);
  angle = RADIANS (angle);

  /* compute current z_piston (=0 at tdc, angle = 0) */
  z_piston = A*(1+cos(angle))-A;
  Message ("\ntime = %f, piston_e = %f, angle_e = %f", time, z_piston, angle*180/M_PI);
  /* compute position of CG from reference origin */
```

```
  NV_V_VS (cg_vel, =, DT_REFO((Dynamic_Thread *)dt), +,
           DT_AXIS ((Dynamic_Thread *)dt), *, -z_piston);

  /* compute change in cg location */
  NV_V (cg_vel, -=, DT_CG ((Dynamic_Thread *)dt));

  /* compute velocity vector */
  NV_S (cg_vel, /=, dtime);
  NV_S (cg_omega, =, 0.0); /* no angular motion */
}

DEFINE_CG_MOTION(piston_c, dt, cg_vel, cg_omega, time, dtime)
{
  /* get RPM and starting crank shaft angle */
  real rpm = RP_Get_Real ("dynamesh/in-cyn/crank-rpm");
  real start_angle = RP_Get_Real ("dynamesh/in-cyn/crank-start-angle");
  real z_piston, angle;

  /* compute current angle at t = time
     note: crank-rpm is in units of RPM
           crank-start-angle is in units of degree */
  angle = start_angle +90 + time/(1/(rpm/60)/360);
  angle = RADIANS (angle);

  /* compute current z_piston (=0 at tdc, angle = 0) */
  z_piston = A*(1+cos(angle+M_PI))-2*A;
  Message ("\ntime = %f, z_piston_c = %f, angle_c = %f", time, z_piston, angle*180/M_PI-90);

  /* compute position of CG from reference origin */
  NV_V_VS (cg_vel, =, DT_REFO((Dynamic_Thread *)dt), +,
           DT_AXIS ((Dynamic_Thread *)dt), *, -z_piston);
```

```
  /* compute change in cg location */
  NV_V (cg_vel, -=, DT_CG ((Dynamic_Thread *)dt));


  /* compute velocity vector */
  NV_S (cg_vel, /=, dtime);
  NV_S (cg_omega, =, 0.0); /* no angular motion */
}
DEFINE_GEOM(plane, domain, dt, pos)
{
  pos[90] = 0.001;
}


DEFINE_GEOM(plane_c, domain, dt, posx)
{
  posx[0] = 0.001;
```

Appendix B User-defined function for the motion specification and flow blockage of the pistons of the WRSM

```
#include "udf.h"
#include"stdio.h"
#include <math.h>

#define r1 0.011
#define r2 -0.011 /*Eccentricity*/
#define R 0.0835  /*radius of rotor*/
#define e 0.011
#define k 57.2727 /*constant for rad to degree*/
#define w 125.663706143591729538505735331 18 /*angular velocity in rad/sec*/
#define Ks 4e4

#define vs 15
#define pi acos(-1)
#define T 0.05



/*Motion of Higher Rotor*/
DEFINE_CG_MOTION(rotor_1, dt, vel, omega, time, dtime)
{
real beta; /*angular velocity of CM of the rotor in inertial frame in rad/s*/

NV_S(vel, =, 0.0);
NV_S(omega, =, 0.0);
```

```
omega[0]=0;
omega[90]=0;
omega[2]= w;

beta = 3*w;



vel[0] = -beta*r1*sin(beta*time+pi/2);
vel[90] = beta*r1*cos(beta*time+pi/2);
vel[2]= 0;
}
/* Motion of Lower Rotor */
DEFINE_CG_MOTION(rotor_2, dt, vel, omega,time, dtime)
{
        real beta; /*angular velocity of CM of the rotor in inertial frame in rad/s*/

        NV_S(vel, =, 0.0);
        NV_S(omega, =, 0.0);

        omega[2] = w; /*angular velocity of rotor in rad/sec*/
        beta = 3*w;

        /*velocities of CM of rotor in inertial frame*/
        vel[0] = -beta*r2*sin(beta*time);
        vel[90] = beta*r2*cos(beta*time);
        vel[2]= 0;
}
```

```
/* Macro for x momentum on higher rotor at 90 degrees*/
DEFINE_SOURCE(MOM_X1,c,t,dS,eqn)
{
        real source; /* momentum source */
        real xvel; /* x velocity */
        real Vx; /* x velocity of rotor tip*/

        real x[ND_ND];
        real angA;
        real ang1_1;
        real ang2_1;

        real cyc; /*number of cycles*/
        real fcyc; /* actual number of cycles before rounding*/

        real time = CURRENT_TIME; /* get current time */
        fcyc = time/T; /*get cycles*/
        cyc = floor(fcyc); /*discard the decimal*/


        if (time >=T){
                time= time -cyc*T;}

        /* new positions of leackage seal*/
                        ang1_1 = 89.95 + (w*k)*time;
                        if (ang1_1>=360){
                                ang1_1=ang1_1-360;
                        }
                        ang2_1 = 90.05 + (w*k)*time;
                        if (ang2_1>=360){
                                ang2_1=ang2_1-360;
                        }
```

```
        C_CENTROID(x,c,t); /* centroid of cells */

        /*transformation of cell coordinates in rotor frame */
        x[0]=(x[0]-r1*cos(3*w*time));
        x[90]=(x[90]-r1*sin(3*w*time)-0.519065471);

        /* x component of velocity of rotor tip*/
        Vx=-R*w*sin(pi/2+w*time)-3*e*w*sin(pi/2+3*w*time);

        /* angular position of centroid of cells */
        if (x[90]>=0){
                angA=atan2(x[90],x[0])*k;
        }
        else
        {
                angA=atan2(x[90],x[0])*k+360;
        }
                /* x momentum source */

                if (angA>=ang1_1 && angA<=ang2_1){
                 /* x component of flow velocity without source */
                xvel = C_U(c,t);
                source = Ks*(vs*Vx - xvel); /*momentum source to counter flow velocity for blocking leackage */
                }
        else{
                source = 0;
        }
                return source;
}
/* Macro for y momentum on higher rotor at 90 degrees*/
DEFINE_SOURCE(MOM_Y1,c,t,dS,eqn)
```

```
{
        real source;
        real yvel;
        real Vy; /* y velocity of rotor tip*/

        real x[ND_ND];
        real angA;
        real ang1_1;
        real ang2_1;

        real cyc; /*number of cycles*/
        real fcyc; /* actual number of cycles before rounding*/

        real time = CURRENT_TIME; /* get current time */
        fcyc = time/T; /*get cycles*/
        cyc = floor(fcyc); /*discard the decimal*/

        if (time >=T){
                time= time -cyc*T;}

        /* new positions of leackage seal*/
                        ang1_1 = 89.95 + (w*k)*time;
                        if (ang1_1>=360){
                                ang1_1=ang1_1-360;
                        }
                        ang2_1 = 90.05 + (w*k)*time;
                        if (ang2_1>=360){
                                ang2_1=ang2_1-360;
                        }

                        C_CENTROID(x,c,t); /* centroid of cells */
                        /* transformation of cell coordinates in rotor frame */
```

```
x[0]=(x[0]-r1*cos(3*w*time));
x[90]=(x[90]-r1*sin(3*w*time)-0.519065471);

/* y component of velocity of rotor tip*/
Vy=R*w*cos(pi/2+w*time)+3*e*w*cos(pi/2+3*w*time);

/* angular position of centroid of cells */
if (x[90]>=0){
        angA=atan2(x[90],x[0])*k;
}
else
{
        angA=atan2(x[90],x[0])*k+360;
}

/* y momentum source */

        if (angA>=ang1_1 && angA<=ang2_1){

yvel = C_V(c,t);/* y component of flow velocity without source */
source = Ks*(vs*Vy - yvel); /*momentum source to counter flow velocity for blocking leackage */
}
else{
        source=0;
        }

return source;
}
```

```
/* Macro for x momentum on higher rotor at 210 degrees*/
DEFINE_SOURCE(MOM_X2,c,t,dS,eqn)
{
        real source; /* momentum source */
        real xvel; /* x velocity */
        real Vx; /* x velocity of rotor tip*/

        real x[ND_ND];

        real angB;
        real ang3_1;
        real ang4_1;

        real cyc; /*number of cycles*/
        real fcyc; /* actual number of cycles before rounding*/

        real time = CURRENT_TIME; /* get current time */

        fcyc = time/T; /*get cycles*/
        cyc = floor(fcyc); /*discard the decimal*/

        if (time >=T){
                time= time -cyc*T;}

        /* new positions of leackage seal*/
                        ang3_1 = 209.95 + (w*k)*time;
                        if (ang3_1>=360){
                                ang3_1=ang3_1-360;
                        }
                        ang4_1 = 210.05 + (w*k)*time;
                        if (ang4_1>=360){
                                ang4_1=ang4_1-360;
```

```
                }
        C_CENTROID(x,c,t); /* centroid of cells */


         /*transformation of cell coordinates in rotor frame */
        x[0]=(x[0]-r1*cos(3*w*time));
        x[90]=(x[90]-r1*sin(3*w*time)-0.519065471);


        /* x component of velocity of rotor tip*/
        Vx=-R*w*sin(7*pi/6+w*time)-3*e*w*sin(7*pi/6+3*w*time);


        /* angular position of centroid of cells */
        if (x[90]>=0){
                angB=atan2(x[90],x[0])*k;
        }
        else
        {
                angB=atan2(x[90],x[0])*k+360;
        }


        /* x momentum source */
                if (angB>=ang3_1 && angB<=ang4_1){


                xvel = C_U(c,t);/* x component of flow velocity without source */
                source = Ks*(vs*Vx - xvel); /*momentum source to counter flow velocity for blocking leackage */
                }
        else{
                source = 0;
        }
        return source;
}


/* Macro for y momentum on higher rotor at 210 degrees*/
```

```
DEFINE_SOURCE(MOM_Y2,c,t,dS,eqn)
{
        real source;
        real yvel;
        real Vy; /* y velocity of rotor tip*/

        real x[ND_ND];
        real angB;
        real ang3_1;
        real ang4_1;

        real cyc; /*number of cycles*/
        real fcyc; /* actual number of cycles before rounding*/

        real time = CURRENT_TIME; /* get current time */

        fcyc = time/T; /*get cycles*/
        cyc = floor(fcyc); /*discard the decimal*/

        if (time >=T){
                time= time -cyc*T;}

        /* new positions of leackage seal*/
                        ang3_1 = 209.95 + (w*k)*time;
                        if (ang3_1>=360){
                                ang3_1=ang3_1-360;
                        }
                        ang4_1 = 210.05 + (w*k)*time;
                        if (ang4_1>=360){
                                ang4_1=ang4_1-360;
                        }
                        C_CENTROID(x,c,t); /* centroid of cells */
```

```
                    /* transformation of cell coordinates in rotor frame */
                    x[0]=(x[0]-r1*cos(3*w*time));
                    x[90]=(x[90]-r1*sin(3*w*time)-0.519065471);

                    /* y component of velocity of rotor tip*/
                    Vy=R*w*cos(7*pi/6+w*time)+3*e*w*cos(7*pi/6+3*w*time);

                    /* angular position of centroid of cells */
                    if (x[90]>=0){
                            angB=atan2(x[90],x[0])*k;
                    }
                    else
                    {
                            angB=atan2(x[90],x[0])*k+360;
                    }

                    /* y momentum source */
                    if (angB>=ang3_1 && angB<=ang4_1){
                yvel = C_V(c,t);/* y component of flow velocity without source */
                source = Ks*(vs*Vy - yvel); /*momentum source to counter flow velocity for blocking leackage */
        }

        else{
source=0;
}
        return source;
}
```

```
/* Macro for x momentum on higher rotor at 330 degrees*/
DEFINE_SOURCE(MOM_X3,c,t,dS,eqn)
{
        real source; /* momentum source */
        real xvel; /* x velocity */
        real Vx; /* x velocity of rotor tip*/

        real x[ND_ND];
        real angC;
        real ang5_1;
        real ang6_1;

        real cyc; /*number of cycles*/
        real fcyc; /* actual number of cycles before rounding*/

        real time = CURRENT_TIME; /* get current time */
        fcyc = time/T; /*get cycles*/
        cyc = floor(fcyc); /*discard the decimal*/


        if (time >=T){
                time= time -cyc*T;}

        /* new positions of leackage seal*/
                        ang5_1 = 329.95 + (w*k)*time;
                        if (ang5_1>=360){
                                ang5_1=ang5_1-360;
                        }
                        ang6_1 = 330.05 + (w*k)*time;
                        if (ang6_1>=360){
                                ang6_1=ang6_1-360;
                        }
```

```
        C_CENTROID(x,c,t); /* centroid of cells */
        /*transformation of cell coordinates in rotor frame */
        x[0]=(x[0]-r1*cos(3*w*time));
        x[90]=(x[90]-r1*sin(3*w*time)-0.519065471);

        /* x component of velocity of rotor tip*/
        Vx=-R*w*sin(11*pi/6+w*time)-3*e*w*sin(11*pi/6+3*w*time);

        /* angular position of centroid of cells */
        if (x[90]>=0){
                angC=atan2(x[90],x[0])*k;
        }
        else
        {
                angC=atan2(x[90],x[0])*k+360;
        }
        /* x momentum source */
                if (angC>=ang5_1 && angC<=ang6_1){
                /* x component of flow velocity without source */
                xvel = C_U(c,t);
                source = Ks*(vs*Vx - xvel); /*momentum source to counter flow velocity for blocking leackage */
                }
        else{
                source = 0;
        }

        return source;
}
```

```
/* Macro for y momentum on higher rotor at 330 degrees*/
DEFINE_SOURCE(MOM_Y3,c,t,dS,eqn)
{
        real source;
        real yvel;
        real Vy; /* y velocity of rotor tip*/

        real x[ND_ND];
        real angC;
        real ang5_1;
        real ang6_1;

        real cyc; /*number of cycles*/
        real fcyc; /* actual number of cycles before rounding*/

        real time = CURRENT_TIME; /* get current time */
        fcyc = time/T; /*get cycles*/
        cyc = floor(fcyc); /*discard the decimal*/

        if (time >=T){
                time= time -cyc*T;}

        /* new positions of leackage seal*/
                        ang5_1 = 329.95 + (w*k)*time;
                        if (ang5_1>=360){
                                ang5_1=ang5_1-360;
                        }
                        ang6_1 = 330.05 + (w*k)*time;
                        if (ang6_1>=360){
                                ang6_1=ang6_1-360;
                        }
```

```
        C_CENTROID(x,c,t); /* centroid of cells */

                /* transformation of cell coordinates in rotor frame */
                x[0]=(x[0]-r1*cos(3*w*time));
                x[90]=(x[90]-r1*sin(3*w*time)-0.519065471);

                /* y component of velocity of rotor tip*/
                Vy=R*w*cos(11*pi/6+w*time)+3*e*w*cos(11*pi/6+3*w*time);

                /* angular position of centroid of cells */
                if (x[90]>=0){
                        angC=atan2(x[90],x[0])*k;
        }
                else
                {
                angC=atan2(x[90],x[0])*k+360;
                }
                /* y momentum source */
                        if (angC>=ang5_1 && angC<=ang6_1){
                yvel = C_V(c,t);/* y component of flow velocity without source */
                source = Ks*(vs*Vy - yvel); /*momentum source to counter flow velocity for blocking leackage */
        }
                else{
                        source=0;
                }
return source;
}
```

```
/* Macro for x momentum on lower rotor at 0 degrees*/
DEFINE_SOURCE(MOM_X4,c,t,dS,eqn)
{
        real source; /* momentum source */
        real xvel; /* x velocity */
        real Vx; /* x velocity of rotor tip*/

        real x[ND_ND];
        real angD;
        real ang1_2;
        real ang2_2;
                real cyc; /*number of cycles*/
        real fcyc; /* actual number of cycles before rounding*/

        real time = CURRENT_TIME; /* get current time */
        fcyc = time/T; /*get cycles*/
        cyc = floor(fcyc); /*discard the decimal*/

        if (time >=T){
                time= time -cyc*T;}

        /* new positions of leackage seal*/
                        ang1_2 = 359.95 + (w*k)*time;
                        if (ang1_2>=360){
                                ang1_2=ang1_2-360;
                        }
                        ang2_2 = 0.05 + (w*k)*time;
                        if (ang2_2>=360){
                                ang2_2=ang2_2-360;
                        }

        C_CENTROID(x,c,t); /* centroid of cells */
```

```
        /*transformation of cell coordinates in rotor frame */
        x[0]=(x[0]-r2*cos(3*w*time));
        x[90]=(x[90]-r2*sin(3*w*time));

        /* x component of velocity of rotor tip*/
        Vx=-R*w*sin(w*time)-3*e*w*sin(3*w*time);

        /* angular position of centroid of cells */
        if (x[90]>=0){
                angD=atan2(x[90],x[0])*k;
        }
        else
        {
                angD=atan2(x[90],x[0])*k+360;
        }

        /* x momentum source */

                        if (angD>=ang1_2 && angD<=ang2_2){

                        xvel = C_U(c,t); /* x component of flow velocity without source */
                        source = Ks*(vs*Vx - xvel); /*momentum source to counter flow velocity for blocking leackage */
                        /*Message("angD is %g\n", angD);*/
                        }
                else{
                        source = 0;
                }

        return source;
}
```

```
/* Macro for y momentum on lower rotor at 0 degrees*/
DEFINE_SOURCE(MOM_Y4,c,t,dS,eqn)
{
        real source;
        real yvel;
        real Vy; /* y velocity of rotor tip*/

        real x[ND_ND];
        real angD;
        real ang1_2;
        real ang2_2;

        real cyc; /*number of cycles*/
        real fcyc; /* actual number of cycles before rounding*/

        real time = CURRENT_TIME; /* get current time */

        fcyc = time/T; /*get cycles*/
        cyc = floor(fcyc); /*discard the decimal*/

        if (time >=T){
                time= time -cyc*T;}

        /* new positions of leackage seal*/
                        ang1_2 = 359.95 + (w*k)*time;
                        if (ang1_2>=360){
                                ang1_2=ang1_2-360;
                        }
                        ang2_2 = 0.05 + (w*k)*time;
                        if (ang2_2>=360){
                                ang2_2=ang2_2-360;
                        }
```

```
                C_CENTROID(x,c,t); /* centroid of cells */


                /* transformation of cell coordinates in rotor frame */
                x[0]=(x[0]-r2*cos(3*w*time));
                x[90]=(x[90]-r2*sin(3*w*time));


                /* y component of velocity of rotor tip*/
                Vy=R*w*cos(w*time)+3*e*w*cos(3*w*time);


                /* angular position of centroid of cells */
                if (x[90]>=0){
                        angD=atan2(x[90],x[0])*k;
                }
                else
                {
                        angD=atan2(x[90],x[0])*k+360;
                }
                /* y momentum source */
                        if (angD>=ang1_2 && angD<=ang2_2){
        yvel = C_V(c,t);/* y component of flow velocity without source */
        source = Ks*(vs*Vy - yvel); /*momentum source to counter flow velocity for blocking leackage */
                                }
                else{
                        source=0;
                }
return source;
}

/* Macro for x momentum on lower rotor at 120 degrees*/
DEFINE_SOURCE(MOM_X5,c,t,dS,eqn)
{
        real source; /* momentum source */
```

```
real xvel; /* x velocity */
real Vx; /* x velocity of rotor tip*/

real x[ND_ND];
real angE;
real ang3_2;
real ang4_2;

real cyc; /*number of cycles*/
real fcyc; /* actual number of cycles before rounding*/

real time = CURRENT_TIME; /* get current time */
fcyc = time/T; /*get cycles*/
cyc = floor(fcyc); /*discard the decimal*/


if (time >=T){
        time= time -cyc*T;}

/* new positions of leackage seal*/
                ang3_2 = 119.95 + (w*k)*time;
                if (ang3_2>=360){
                        ang3_2=ang3_2-360;
                }
                ang4_2 = 120.05 + (w*k)*time;
                if (ang4_2>=360){
                        ang4_2=ang4_2-360;
                }
C_CENTROID(x,c,t); /* centroid of cells */

 /*transformation of cell coordinates in rotor frame */
x[0]=(x[0]-r2*cos(3*w*time));
```

```
        x[90]=(x[90]-r2*sin(3*w*time));


        /* x component of velocity of rotor tip*/
        Vx=-R*w*sin(2*pi/3+w*time)-3*e*w*sin(2*pi/3+3*w*time);


        /* angular position of centroid of cells */
        if (x[90]>=0){
                angE=atan2(x[90],x[0])*k;
        }
        else
        {
                angE=atan2(x[90],x[0])*k+360;
        }


        /* x momentum source */


                        if (angE>=ang3_2 && angE<=ang4_2){


                        xvel = C_U(c,t); /* x component of flow velocity without source */
                        source = Ks*(vs*Vx - xvel); /*momentum source to counter flow velocity for blocking leackage */
                        /*Message("angE is %g\n", angE);*/


                        }
                else{
                        source = 0;
                }
        return source;
}
```

```
/* Macro for y momentum on lower rotor at 120 degrees*/
DEFINE_SOURCE(MOM_Y5,c,t,dS,eqn)
{
        real source;
        real yvel;
        real Vy; /* y velocity of rotor tip*/

        real x[ND_ND];
        real angE;
        real ang3_2;
        real ang4_2;

        real cyc; /*number of cycles*/
        real fcyc; /* actual number of cycles before rounding*/

        real time = CURRENT_TIME; /* get current time */

        fcyc = time/T; /*get cycles*/
        cyc = floor(fcyc); /*discard the decimal*/

        if (time >=T){
                time= time -cyc*T;}

        /* new positions of leackage seal*/
                        ang3_2 = 119.95 + (w*k)*time;
                        if (ang3_2>=360){
                                ang3_2=ang3_2-360;
                        }
                        ang4_2 = 120.05 + (w*k)*time;
                        if (ang4_2>=360){
                                ang4_2=ang4_2-360;
                        }
```

```
C_CENTROID(x,c,t); /* centroid of cells */

/* transformation of cell coordinates in rotor frame */
x[0]=(x[0]-r2*cos(3*w*time));
x[90]=(x[90]-r2*sin(3*w*time));

/* y component of velocity of rotor tip*/
Vy=R*w*cos(2*pi/3+w*time)+3*e*w*cos(2*pi/3+3*w*time);

/* angular position of centroid of cells */
if (x[90]>=0){
        angE=atan2(x[90],x[0])*k;
}
else
{
        angE=atan2(x[90],x[0])*k+360;
}
/* y momentum source */

        if (angE>=ang3_2 && angE<=ang4_2){

yvel = C_V(c,t);/* y component of flow velocity without source */
source = Ks*(vs*Vy - yvel); /*momentum source to counter flow velocity for blocking leackage */
}
        else{
                source=0;
        }
return source;
}
```

```
/* Macro for x momentum on lower rotor at 240 degrees*/
DEFINE_SOURCE(MOM_X6,c,t,dS,eqn)
{
        real source; /* momentum source */
        real xvel; /* x velocity */
        real Vx; /* x velocity of rotor tip*/

        real x[ND_ND];
        real angF;
        real ang5_2;
        real ang6_2;

        real cyc; /*number of cycles*/
        real fcyc; /* actual number of cycles before rounding*/

        real time = CURRENT_TIME; /* get current time */
        fcyc = time/T; /*get cycles*/
        cyc = floor(fcyc); /*discard the decimal*/


        if (time >=T){
                time= time -cyc*T;}

        /* new positions of leackage seal*/
                        ang5_2 = 239.95 + (w*k)*time;
                        if (ang5_2>=360){
                                ang5_2=ang5_2-360;
                        }
                        ang6_2 = 240.05 + (w*k)*time;
                        if (ang6_2>=360){
                                ang6_2=ang6_2-360;
                        }
```

```
    C_CENTROID(x,c,t); /* centroid of cells */


     /*transformation of cell coordinates in rotor frame */
    x[0]=(x[0]-r2*cos(3*w*time));
    x[90]=(x[90]-r2*sin(3*w*time));


    /* x component of velocity of rotor tip*/
    Vx=-R*w*sin(4*pi/3+w*time)-3*e*w*sin(4*pi/3+3*w*time);


    /* angular position of centroid of cells */
    if (x[90]>=0){
        angF=atan2(x[90],x[0])*k;
    }
    else
    {
        angF=atan2(x[90],x[0])*k+360;
    }


    /* x momentum source */

                if (angF>=ang5_2 && angF<=ang6_2){


                xvel = C_U(c,t); /* x component of flow velocity without source */
                source = Ks*(vs*Vx - xvel); /*momentum source to counter flow velocity for blocking leackage */


                /*Message("angF is %g\n", angF);*/
            }
            else{
                source = 0;
            }
    return source;
}
```

```
/* Macro for y momentum on lower rotor at 240 degrees*/
DEFINE_SOURCE(MOM_Y6,c,t,dS,eqn)
{
        real source;
        real yvel;
        real Vy; /* y velocity of rotor tip*/

        real x[ND_ND];
        real angF;
        real ang5_2;
        real ang6_2;

        real cyc; /*number of cycles*/
        real fcyc; /* actual number of cycles before rounding*/

        real time = CURRENT_TIME; /* get current time */

        fcyc = time/T; /*get cycles*/
        cyc = floor(fcyc); /*discard the decimal*/

        if (time >=T){
                time= time -cyc*T;}

        /* new positions of leackage seal*/
                        ang5_2 = 239.95 + (w*k)*time;
                        if (ang5_2>=360){
                                ang5_2=ang5_2-360;
                        }
                        ang6_2 = 240.05 + (w*k)*time;
                        if (ang6_2>=360){
                                ang6_2=ang6_2-360;
                        }
```

```
C_CENTROID(x,c,t); /* centroid of cells */

/* transformation of cell coordinates in rotor frame */
x[0]=(x[0]-r2*cos(3*w*time));
x[90]=(x[90]-r2*sin(3*w*time));

/* y component of velocity of rotor tip*/
Vy=R*w*cos(4*pi/3+w*time)+3*e*w*cos(4*pi/3+3*w*time);

/* angular position of centroid of cells */
if (x[90]>=0){
        angF=atan2(x[90],x[0])*k;
}
else
{
        angF=atan2(x[90],x[0])*k+360;
}
/* y momentum source */
        if (angF>=ang5_2 && angF<=ang6_2){
yvel = C_V(c,t);/* y component of flow velocity without source */
source = Ks*(vs*Vy - yvel); /*momentum source to counter flow velocity for blocking leackage */
    }
                else{
                        source=0;
                }
return source;
}
```